



Design and Implementation of Dew Point Evaporative Cooler: Theoretical and Experimental Investigation

A Dissertation

Submitted to the Council of the Erbil Technical Engineering
College at Erbil Polytechnic University in Partial
Fulfillment of the Requirements for the Degree of Doctor of
Philosophy (Ph.D.) of Science in Mechanical Engineering

By

Mohammed Abdulqader Sulaiman

B.Sc. in Refrigeration and Air-Conditioning Engineering

M.Sc. in Thermal Power Engineering

Supervised by

Prof. Dr. Ahmed Mohammed Adham

Iraq - Kurdistan - Erbil

May 2024

DECLARATION

I declare that the Ph.D. dissertation entitled: **Design and Implementation of Dew Point Evaporative Cooler: Theoretical and Experimental Investigation** is my own original work, and hereby I certify that unless stated, all work contained within this dissertation is my independent research and has not been submitted for the award of any other degree at any institution, except where due acknowledgment is made in the text.

Signature:

Student Name: Mohammed Abdulqader Sulaiman

Date: / /2024

LINGUISTIC REVIEW

I confirm that I have reviewed the dissertation titled **Design and Implementation of Dew Point Evaporative Cooler: Theoretical and Experimental Investigation** from the English linguistic point of view, and I can confirm that it is free of grammatical and spelling errors.

Signature:

Name of Reviewer:

Date: 7th May 2024

SUPERVISOR CERTIFICATE

This dissertation has been written under our supervision and has been submitted for the award of the degree of Ph.D. of Science in Mechanical Engineering with our approval as supervisors.

	<u>Prof. Dr. Ahmed Mohammed Adham</u>
Signature	Name
Date	

I confirm that all requirements have been fulfilled.

Signature:

Name: Prof. Dr. Ahmed Mohammed Adham

Head of the Department of Technical Mechanical and Energy Engineering

Date:

I confirm that all requirements have been fulfilled.

Postgraduate Office

Signature:

Name: M. Bayad Abdulqader Ahmed

Date:

EXAMINING COMMITTEE CERTIFICATION

We certify that we have read this dissertation: **Design and Implementation of Dew Point Evaporative Cooler: Theoretical and Experimental Investigation**, and as an examining committee examined the student (Mohammed Abdulqader Sulaiman) in its content and what is related to it. We approve that it meets the standards of a dissertation for the degree of Ph.D. in Mechanical Engineering.

Signature

Name: Assist. Prof. Dr. Banipal
Nano Yaqoob

Member

Date

Signature

Name: Assist. Prof. Dr. Ranj
Sirwan Abdullah

Member

Date

Signature

Name: Assist. Prof. Dr. Arkan
Fawzi Saeed

Member

Date

Signature

Name: Assist. Prof. Dr. Omar
Mohammed Hamdoon

Member

Date

Signature

Name: Prof. Dr. Omar Mohammed Ali

Chairman

Date

Signature

Name: Prof. Dr. Ahmed Mohammed Adham

Supervisor

Date

Signature

Name: Prof. Dr. Ayad Zaki Saber

Dean of Erbil Technical Engineering College

Date:

ACKNOWLEDGMENT

In the name of Allah, the only and ultimate source of all knowledge, peace be upon our messenger, leader and guider, Mohammed.

Throughout the years of my study, I was fortunate to have Prof. Dr. Ahmed Mohammed Adham as my supervisor. I genuinely wish to express my deep appreciation and gratitude to him for the guidance, friendship, and support he provided me throughout the hard days of my research. Without his support, nothing I have accomplished would have been possible.

I would like to thank all of my family members, in particular, my mother, my father, my wife, and my sister. Your continuous support and prayers made me strong enough to face the difficulties of this complicated study throughout four years of endeavoring and hard working. Your valuable opinions had positively contributed to my work. Thank you for everything.

Last but not least, I would like to extend my gratitude and appreciation to all of my colleagues and friends, thanks to all for the support and real friendship.

ABSTRACT

This dissertation presents a comprehensive investigation into the development of a neoteric design for the innovative dew point evaporative cooler (DPEC). The DPEC is a groundbreaking cooling device possessing energy efficiency (i.e., coefficient of performance) higher than 20 that makes it super performing cooling machine when compared to the traditional vapor compression refrigeration systems which have energy efficiency of around 3. The DPEC depends only on the evaporative cooling mechanism of water with innovative air flow arrangement inside its heat and mass exchanger which makes it a complicated irreversible thermodynamic machine. The proposed shell and tube design for the DPEC offers further enhancement in its thermal and energy performance with aiming to replace the conventional high energy consuming cooling devices.

The methodology of this research study followed the path of combining theoretical and experimental investigations. This research work started with a thorough review of the existing literatures conducted on DPECs, identifying their limitations and shortcomings. Through a deep leveraging of this process, the novelty for the current work has been identified. At the beginning, to investigate the viability of the proposed notion, a rigorous computational model has been developed. By the help of the dedicated simulation process, the impact of the geometrical aspects and operational conditions on the cooler's performance were investigated. The comprehensive parametrical analysis that has been carried out with the help of the validated numerical simulation, the optimum design parameters were identified and employed for the construction of the unit.

The unit has been constructed with a low cost polycarbonate drinking straw tubes with 5 mm in diameter and 0.15 mm wall thickness. The tubes have been

covered with a dual-layer disposable tablecloth that comprised of a plastic and paper layers both with 0.03 mm thickness. The paper layer of the disposable tablecloth acted as the evaporative surface that helped in effective dispersion and evaporation of water flow. The ultra-thin characteristics of these layers significantly contributed in minimizing the thermal resistance to the heat transfer and improving the overall performance of the cooler. In addition, a dedicated air handling unit has been designed and fabricated for the purpose of the experimentations that was able to regulate the temperature and humidity of the inlet air stream into the unit.

During the experimentations, when the unit operated under the pre-set operational conditions, the system was able to reduce the ambient temperature by up to 34.1 °C (from 53 °C to 18.9 °C), besides, it could achieve a dew-point effectiveness of 99.6% and wet-bulb effectiveness of 135%. This high performance makes the constructed unit to be considered as a super performing cooling device.

Furthermore, the developed numerical model has been validated against the experimental data from the experimentations. The maximum deviation recorded was between $\pm 2.3\%$ and $\pm 5.1\%$. Therefore, the simulation model can predict the thermal and energy performance of the proposed DPEC with high accuracy. On this bases, a deep parametrical analysis has been carried out which enabled testing the system under harsh environmental conditions. Nonetheless, the cooler firmly achieved an energy efficiency ranging between 28 and 66, dew-point effectiveness between 34% and 77%, wet-bulb effectiveness between 62% and 134%, exergy efficiency between 50% and 86%, entropy generation rate between 0.00052 kW/K and 0.0023 kW/K, and sustainability index between 2 and 7, when operated under a wide range of operational and geometrical conditions.

LIST OF CONTENTS

ABSTRACT	VI
LIST OF CONTENTS	VIII
LIST OF FIGURES	XI
LIST OF TABLES	XVIII
NOMENCLATURES.....	XIX
CHAPTER 1	1
1.1 RESEARCH BACKGROUND	1
1.2 ENERGY-EFFICIENT EVAPORATIVE TECHNOLOGIES	4
1.2.1 Direct Evaporative Coolers (DECs).....	6
1.2.2 Indirect Evaporative Coolers (IECs).....	7
1.2.3 Dew Point Evaporative Coolers (DPECs).....	8
1.3 DESCRIPTION OF THE RESEARCH.....	9
1.3.1 Research Aims and Scopes	9
1.3.2 Research Objectives	10
1.3.3 RESEARCH CONTRIBUTIONS	11
1.4 DISSERTATION STRUCTURE	12
CHAPTER 2	14
2.1 INTRODUCTION	14
2.2 REVIEW ON THE TECHNICAL ASPECTS.....	16
2.2.1 Airflow Configurations of DPECs	16
2.2.2 Water-Flow Configurations of DPECs.....	20
2.2.3 Structural Materials of DPECs.....	22
2.3 METHODOLOGIES IN THE CONDUCTED LITERATURES.....	26
2.3.1 Theoretical Studies.....	26
2.3.2 Experimental Studies.....	31
2.3.3 Theoretical and Experimental Studies.....	36
2.4 PERFORMANCE ENHANCEMENT OF DPECS.....	40
2.4.1 Enhancement Through Employed Materials.....	40
2.4.2 Enhancement Through Water Spraying System.....	43

2.4.3 Performance Evaluation Criteria	46
2.5 APPLICATIONS OF DEW POINT EVAPORATIVE COOLERS	51
2.5.1 Applications of DPEC with Solar Panel Systems	51
2.5.2 Applications of DPEC with VCRS Systems	56
2.5.3 Applications of DPEC with Desiccant Wheel.....	59
2.6 CHAPTER SUMMARY AND KEY FINDINGS	65
CHAPTER 3	68
3.1 INTRODUCTION	68
3.2 CONCEPTUAL DESIGN AND WORKING PRINCIPLE	70
3.3 AIR-WATER FLOW CONFIGURATIONS.....	74
3.4 MATHEMATICAL MODELLING	75
3.4.1 Primary Channel Airflow	77
3.4.2 Downward Flowing Water and Channel Wall	78
3.4.3 Working Channel Airflow.....	79
3.4.4 Performance Evaluation Parameters	82
3.5 EXERGY, ENTROPY, AND SUSTAINABILITY ANALYSIS	85
3.6 BOUNDARY CONDITIONS	90
3.6.1 Parallel Flow Configuration.....	90
3.6.2 Counter Flow Configuration	91
3.7 SIMULATION SET-UP AND GRID SENSITIVITY ANALYSIS	92
3.8 MODEL VALIDATION	93
3.9 CHAPTER SUMMARY.....	94
CHAPTER 4	96
4.1 INTRODUCTION	96
4.2 SELECTION OF OPTIMUM DESIGN PARAMETERS.....	96
4.3 STRUCTURAL DESIGN.....	100
4.4 SYSTEM CONSTRUCTION.....	100
4.4.1 Material Selection	100
4.4.2 Primary Channels Construction	103
4.4.3 Evaporative Surface Formation.....	104
4.4.4 Puncturing the Perforations for Air Diversion	106
4.4.5 Water Distribution System Design and Fabrication.....	107
4.5 SYSTEM ASSEMBLY	110
4.6 EXPERIMENT SET-UP.....	115

4.6.1 Air Handling Unit Design and Construction.....	115
4.6.2 Measurement and Instruments.....	117
4.7 UNCERTAINTY ANALYSIS	121
CHAPTER 5	123
5.1 INTRODUCTION	123
5.2 MODEL VALIDATION WITH PREVIOUS STUDIES	123
5.2.1 Validation I.....	124
5.2.2 Validation II	124
5.2.3 Validation III	126
5.3 VALIDATION WITH THE CURRENT CONSTRUCTED UNIT	127
5.3.1 Performance Testing Under Varying Inlet Air Temperature (Test I).....	128
5.3.2 Performance Testing Under Varying Humidity Ratio (Test II)	133
5.3.3 Performance Testing Under Varying Inlet Air Velocity (Test III).....	136
5.3.4 Performance Testing Under Varying Air Ratio (Test IV).....	139
5.4 COMPREHENSIVE PARAMETRICAL ANALYSIS	142
5.4.1 Properties Variation Along the Channels	144
5.4.2 Effect of Operational Parameters	150
5.4.3 Effect of Geometrical Parameters	160
5.5 EXERGY, ENTROPY, AND SUSTAINABILITY ANALYSIS	164
5.5.1 Influence of Inlet Air Conditions	167
5.5.2 Influence of Geometrical Dimentions	174
5.6 CHAPTER SUMMERY	177
CHAPTER 6	179
6.1 CONCLUSIONS	179
6.2 FUTURE WORKS	183
REFERENCES	R1
APPENDIX A1	A1
APPENDIX A2	A14
APPENDIX A3	A18

LIST OF FIGURES

Fig. 1.1 Electricity consumption by sector in Iraq (IEA Iraq, 2021)	1
Fig. 1.2 World's electricity consumption by sector (IEA, 2021)	2
Fig. 1.3 Division of residential electricity consumption (Hossein Motlagh et al., 2020)	3
Fig. 1.4 Nominal COP values of existing refrigeration systems	5
Fig. 1.5 Direct evaporative cooler: (a) air stream inside heat and mass exchanger; (b) cooling process on the psychrometric chart	7
Fig. 1.6 Indirect evaporative cooler: (a) air streams inside heat and mass exchanger; (b) cooling process on the psychrometric chart	8
Fig. 1.7 Dew point evaporative cooler: (a) air streams in the heat and mass exchanger; (b) cooling process on the psychrometric chart	9
Fig. 2.1 Guideline for literature reviewing in Chapter 2.....	15
Fig. 2.2 M-cycle dew point evaporative cooler by Valeriy Maisotsenko (2003)	16
Fig. 2.3 Schematic diagram of two dew point evaporative HMXs: (a) Cross-flow; (b) Counter-flow (Zhan et al., 2011)	17
Fig. 2.4 M-cycle cross-flow HMX (Pandelidis and Anisimov, 2015).....	18
Fig. 2.5 Effect of inlet air temperature on: (a) condensation rate; (b) wet-bulb effectiveness; (c) heat transfer rate (Min et al., 2019).....	19
Fig. 2.6 Eight configurations for air and water flow patterns regarding the HMX of DPEC (Kashyap et al., 2020a)	21
Fig. 2.7 Product air temperature and temperature drop trends under the effect of various inlet air temperatures (Xu et al., 2024).....	23
Fig. 2.8 Felt attachment to the aluminum sheets: (a) primary channel; (b) working channel (Khalid et al., 2016)	24
Fig. 2.9 Working principle on psychrometric process regarding: (a) multi-stage REC; (b) single stage REC (Duan et al., 2017a)	25
Fig. 2.10 Flow-chart of the developed 3-D simulation model (Zhu et al., 2023b)	30

Fig. 2.11 DPEC performance under Arab Gulf climate: (a) cooling capacity; (b) COP (Baakeem et al., 2019).....	31
Fig. 2.12 Performance of the dual-mode evaporative cooler: (a) exergy efficiency; (b) annual operation cost (Kashyap et al., 2022c)	38
Fig. 2.13 Surfaces of the porous materials: (a) basalt paper- like synthetic fiber; (b) synthetic surfactant non-woven; (c) 50% cotton fiber, 30% viscose, 20% polyester; (d) 100% cotton; (e) hydrophilic drainage textile; (f) resin treated kraft paper; (g) rigid kraft paper; (h) original kraft paper (Pandelidis et al., 2021)	41
Fig. 2.14 The test bench for porous materials inspection (Cui et al., 2023)...	42
Fig. 2.15 Microstructure whisker-attained copper tube (Schulz et al., 2005)	42
Fig. 2.16 Available water spraying mechanisms for evaporative cooling (Sun et al., 2020a).....	43
Fig. 2.17 Performance of the system under different water spraying modes: (a) COP; (b) wet-bulb effectiveness (Al-Zubaydi and Hong, 2019)	44
Fig. 2.18 Nozzle types and their water spraying behavior (Sun et al., 2020a)	46
Fig. 2.19 (a) Proposed configuration; (b) conventional configuration; (c) Schematic diagram of PV panel layer (Yang et al., 2024)	54
Fig. 2.20 Solar desiccant air-conditioning (Song and Sobhani, 2020)	54
Fig. 2.21 Schematic diagram of PV/T-PCM solar collector (Wang et al., 2020)	56
Fig. 2.22 (a) Experimental setup; (b) Back-view (Žižak et al., 2022)	56
Fig. 2.23 DPEC- VCRS for air-conditioning (Chauhan and Rajput, 2016) ...	57
Fig. 2.24 (a) First air-conditioning cycle; (b) Second air-conditioning cycle (Zanchini and Naldi, 2019).....	58
Fig. 2.25 Off-grid sustainable air-conditioning system (Olmur et al., 2023).	60
Fig. 2.26 Sustainable air-conditioning cycle (Buker and Riffat, 2016b).....	60
Fig. 2.27 Hourly variation of obtained results (Buker and Riffat, 2016b)	61
Fig. 2.28 Inclusive graphical chart for Chapter 2 regarding all the research aspects conducted on DPECs.....	67
Fig. 3.1 Geometry selection procedure of novel DPEC.....	68

Fig. 3.2 Three-dimensional graphical representation: (a) Novel shell and tube DPEC; (b) Individual primary and working channels pair	72
Fig. 3.3 Air-water flow configurations: (a) parallel flow (PF); (b) counter flow (CF)	74
Fig. 3.4 Differential elements: (a) FPX element (top view); (b) STX element (top view); (c) FPX element (3D illustration); (d) STX element (3D illustration)	76
Fig. 3.5 Differential element applied for heat and mass transfer calculations	78
Fig. 3.6 Total pressure drop within the HMX of DPEC	84
Fig. 3.7 Grid sensitivity analysis for the simulation	93
Fig. 4.1 Effect of channel length on: (a) product air temperature; (b) cooling load	98
Fig. 4.2 Product air temperature and dew point effectiveness variation under influence of: (a) primary channel diameter; (b) working channel height/width	99
Fig. 4.3 Optimum dimensions employed for prototype construction	99
Fig. 4.4 Candidate tubes for HMX formation	101
Fig. 4.5 Selected material for primary channels: (a) drinking straw tubes; (b) tube diameter; (c) tube wall thickness	102
Fig. 4.6 Selected material for evaporative surface: (a) disposable tablecloth role; (b) dual-layer constitution; (c) both layers thickness	102
Fig. 4.7 (a) Tubes placed on metal bar; (b) Bonding of two adjacent tubes; (c) Double-sided translucent paper tape	103
Fig. 4.8 Evaporative surface formation procedures	105
Fig. 4.9 (a) Six perforations in three columns, two per each column; (b) 300 perforated tubes	106
Fig. 4.10 Cellulose sponge tested for water absorption	108
Fig. 4.11 Cellulose+cotton sponge under the test	108
Fig. 4.12 Prepared parts regarding water distribution system	109
Fig. 4.13 (a) Bed plate (upside down); (b) 7mm holes in bed plate; (c) holes made in front and back acrylic sheets for copper tube insertion ..	110

Fig. 4.14 (a) Element framing; (b) Tubes location determination; (c) Aligning top and bottom plates; (d) Perforated plates; (e) Finished plates with referenced dimensions.....	111
Fig. 4.15 (a) Prepared acrylic sheets to compose the cooler's structure; (b) Cooler's structure reinforced with aluminum bars	112
Fig. 4.16 (a) Tubes insertion into the system (upside down); (b) Glued tubes to prevent leakage	113
Fig. 4.17 Dedicated water distribution system for proposed DPEC	113
Fig. 4.18 Air ducting components.....	114
Fig. 4.19 Constructed STX-DPEC	115
Fig. 4.20 Air handling unit prior to the DPEC entrance	116
Fig. 4.21 Parameter measurement instruments organization.....	117
Fig. 4.22 Instruments used for parameters measurement: (a) K-type thermocouple; (b) STC-3028 hygrometer; (c) Pro'sKit MT-4014; (d) VOLTCRAFT K101; (e) Vane Anemometer UNI-T (UT363); (f) Variable area Rotameter; (g) data logger.....	120
Fig. 5.1 Experimental validation of performance parameters under different inlet air temperatures provided by Lin et al. (2018b): (a) product air temperature and cooling capacity; (b) thermal efficiencies.....	125
Fig. 5.2 Experimental validation under the climate conditions of different cities adopted from Xu et al. (2017): (a) product air temperature; (b) thermal efficiencies	125
Fig. 5.3 Experimental validation under diverse ambient air temperature, humidity ratio and velocity provided by Riangvilaikul and Kumar (2010b): (a) product air temperature; (b) dew point efficiency.....	126
Fig. 5.4 Effect of varying inlet air temperature on the temperatures of: (a) product air; (b) exhaust air	132
Fig. 5.5 Effect of varying inlet air temperature on thermal effectiveness	133
Fig. 5.6 Effect of varying inlet air temperature on cooling capacity	133
Fig. 5.7 Effect of varying inlet air humidity ratio on the temperatures of: (a) product air; (b) exhaust air	134
Fig. 5.8 Effect of varying inlet air humidity ratio on thermal effectiveness.	135

Fig. 5.9 Effect of varying inlet air humidity ratio on cooling capacity	136
Fig. 5.10 Effect of varying inlet air velocity on the temperatures of: (a) product air; (b) exhaust air	138
Fig. 5.11 Effect of varying inlet air velocity on thermal effectiveness	138
Fig. 5.12 Effect of varying inlet air velocity on cooling capacity	139
Fig. 5.13 Effect of varying air ratio on the temperatures of: (a) product air; (b) exhaust air	140
Fig. 5.14 Effect of varying air ratio on thermal effectiveness	141
Fig. 5.15 Effect of varying air ratio on cooling capacity	141
Fig. 5.16 Psychrometric presentation of cooling process along the channels	145
Fig. 5.17 Variation of parameters along the channels: (a) airflow temperature; (b) water flow temperature.....	146
Fig. 5.18 Variation of parameters along the channels: (a) humidity ratio and relative humidity; (b) water evaporation rate	147
Fig. 5.19 Variation of parameters along the channels: (a) cooling potential (heat flux); (b) overall heat transfer coefficient.....	149
Fig. 5.20 Variation of parameters along the channels: (a) heat transfer of PF coolers; (b) heat transfer of CF coolers	150
Fig. 5.21 Energy efficiency performance under the effect of inlet air parameters: (a) temperature; (b) humidity ratio.....	151
Fig. 5.22 Variation of cooling capacity under the effect of inlet air parameters: (a) temperature; (b) humidity ratio	152
Fig. 5.23 Variation of product air temperature and dew-point effectiveness by effect of inlet air parameters: (a) temperature; (b) humidity ratio	153
Fig. 5.24 Variation of wet-bulb effectiveness under the effect of inlet air parameters: (a) temperature; (b) humidity ratio.....	154
Fig. 5.25 Variation of drain water temperature and water evaporation under the effect of inlet air parameters: (a) temperature; (b) humidity ratio	155
Fig. 5.26 Variation of product air temperature and thermal effectiveness by effect of: (a) inlet air velocity; (b) working to primary air ratio...	156

Fig. 5.27	Variation of energy efficiency by effect of: (a) inlet air velocity; (b) working to primary air ratio	157
Fig. 5.28	Variation of cooling potential by effect of: (a) inlet air velocity; (b) working to primary air ratio	157
Fig. 5.29	Variation of product air temperature and dew-point effectiveness by effect of feed water parameters: (a) temperature; (b) flowrate.....	158
Fig. 5.30	Variation of drain water temperature and water evaporation by effect of feed water parameters: (a) temperature; (b) flowrate.....	159
Fig. 5.31	Variation of product air temperature by the effect of: (a) channel length; (b) equivalent channel diameter.....	161
Fig. 5.32	Variation of cooling capacity by the effect of: (a) channel length; (b) equivalent channel diameter	162
Fig. 5.33	Variation of dew-point effectiveness by the effect of: (a) channel length; (b) equivalent channel diameter.....	163
Fig. 5.34	Variation of drain water temperature by the effect of: (a) channel length; (b) equivalent channel diameter.....	164
Fig. 5.35	Thermodynamical performance of proposed DPEC: (a) physical properties variation; (b) exergy variation (Grassmann) diagram .	165
Fig. 5.36	(a) Effect of inlet air temperature on exergy flow; (b) Effect of inlet humidity ratio on exergy flow; (c) Variation of exergy flow and total exergy under effect of inlet air temperature; (d) Variation of exergy flow and total exergy under effect of inlet air humidity ratio	168
Fig. 5.37	Variation of exergy destruction and exergy efficiency under the influence of: (a) inlet air temperature; (b) inlet air humidity ratio	169
Fig. 5.38	Variation of entropy generation rate and sustainability index under influence of: (a) inlet air temperature; (b) inlet air humidity ratio	170
Fig. 5.39	(a) Effect of inlet air velocity on exergy flow; (b) Effect of air ratio on exergy flow; (c) Variation of exergy flow and total exergy under effect of inlet air velocity; (d) Variation of exergy flow and total exergy under effect of air ratio.....	172
Fig. 5.40	Variation of exergy destruction and exergy efficiency under the influence of: (a) inlet air velocity; (b) air ratio	173

Fig. 5.41 Variation of entropy generation rate and sustaiabilty index under influence of: (a) inlet air velocity; (b) air ratio	174
Fig. 5.42 (a) Effect of channel length on exergy flow; (b) Effect of equivalent channel diameter on exergy flow; (c) Variation of exergy flow and total exergy under effect of channel length; (d) Variation of exergy flow and total exergy under effect of equivalent channel diameter	175
Fig. 5.43 Variation of exergy destruction and exergy efficiency under the influence of: (a) channel length; (b) equivalent channel diameter	176
Fig. 5.44 Variation of entropy generation rate and sustainability index under influence of: (a) channel length; (b) equivalent channel diameter	177

LIST OF TABLES

Table 2.1 Nominal values of proposed DPECs (Kashyap et al., 2020a)	22
Table 2.2 Detail of the experimental parameters (Khalid et al., 2016).....	25
Table 2.3 Summary of the selected studies regarding the technical aspects (Section 2.2)	27
Table 2.4 Description of the experimental studies regarding DPECs	33
Table 2.5 Summary of the selected studies regarding the methodologies (Section 2.3)	39
Table 2.6 Summary of the selected studies regarding performance enhancement of DPECs (Section 2.4).....	52
Table 2.7 Summary of the selected studies regarding the hybrid DPECs (Section 2.5)	63
Table 3.1 Graphical representation of the proposed HMXs for DPEC	71
Table 3.2 System description according to air-water flow configurations	75
Table 3.3 Induced loss coefficient within HMX (Çengel and Cimbala, 2020)	84
Table 4.1 Pre-set values for numerical simulation.....	97
Table 4.2 Experimental measured parameters and employed instruments... 118	
Table 4.3 Uncertainty of the measured parameters.....	122
Table 4.4 Uncertainty of performance parameters.....	122
Table 5.1 Descriptions of the published experimental studies	124
Table 5.2 Experimental set-up and results	129
Table 5.3 Simulation results under the boundary conditions of experimentations	130
Table 5.4 Pre-set simulation values	143
Table 5.5 Specific exergy variation of air streams at different state points..	167

NOMENCLATURES

AR	working to primary air ratio
c_p	specific heat, kJ/(kg·K)
dz	differential element length, m
D_m	mass diffusivity, m ² /s
DH	hydraulic diameter, m
ex	specific flow-exergy, kJ/kg of air
E	electrical power, kW exergy rate, kW
f	Darcy-Weisbach friction factor
ga	gravitational acceleration, m/s ²
G_L	longitudinal gap between channels, m
G_T	transverse gap between channels, m
Gz	Graetz number
H	height, m
He	equivalent element height, m
i	specific enthalpy, kJ/kg
i_e	latent heat of vaporization, kJ/kg
K	loss coefficient
k	thermal conductivity, W/m·K
L	length, m
Le	Lewis number mass flowrate, kg/s
P	pressure, kPa
Pr	Prandtl number heat transfer, kW cooling capacity/potential, kW
r	radius, m

R_a	specific gas constant of air, kJ/(kg·K)
Re	Reynolds number
R_v	specific gas constant of water vapor, kJ/(kg·K)
s	specific entropy, J/(kg·K)
S	surface area, m ²
SD	standard deviation
	entropy generation rate, kW/K
T	temperature, °C
T_0	dead state temperature, °C
u	velocity, m/s
U_b	Bias uncertainty
U_o	overall uncertainty
U_p	precision uncertainty
v	specific volume, m ³ /kg
V	volume flow rate, m ³ /s
W	width, m

Greek letters

	thermal diffusivity, m ² /s
	thermal resistance, K/W
	thickness, m
	Thermal effectiveness/efficiency
	efficiency
ϵ	energy efficiency
	theta (angular) coordinate
	convective heat transfer coefficient, W/(m ² ·K)
	density, kg/m ³
	wettability factor of wet surface
	humidity ratio, g moisture / kg dry air (g/kg)

convective mass transfer coefficient, m/s
relative humidity, %
water spraying density, kg/(m·s)
water evaporation, kg/s

Subscripts

<i>O</i>	dead state
<i>a</i>	airflow, dry air
<i>atm</i>	atmosphere
<i>db</i>	dry bulb
<i>c</i>	chemical
<i>DP</i>	dew point
<i>ex</i>	exergy
<i>f</i>	water film, water flow
<i>in</i>	inlet condition
<i>lt</i>	latent
<i>m</i>	mechanical
<i>out</i>	outlet condition
<i>s</i>	air-water interface (saturation state)
<i>sat</i>	saturation state
<i>sn</i>	sensible
<i>t</i>	thermal
<i>T</i>	total
<i>v</i>	water vapor
<i>w</i>	channel wall
<i>wi</i>	channel wall's inner surface
<i>wo</i>	channel wall's outer surface
<i>WB</i>	wet bulb

Superscripts

*	denotes the primary channel
**	denotes the working channel
.	denotes the rate of change
<i>mj</i>	major
<i>mn</i>	minor

Abbreviations

CF	counter air-water flow configuration
CFD	computational fluid dynamic
COP	coefficient of performance (i.e., energy efficiency)
CPX	corrugated plate heat and mass exchanger
DEC	direct evaporative cooler
DP	dew point
DPEC	dew point evaporative cooler
DW	desiccant wheel
EACC	evaporative air-cooled condenser
ECT	evaporative cooling tower
EES	engineering equation solver
EWCC	evaporative water-cooled condenser
FPX	flat plate heat and mass exchanger
GHC	gas heating coil
HMX	heat and mass exchanger
HVACR	heating, ventilation, air-conditioning & refrigeration
HX	heat exchanger
ICDW	internally cooled desiccant wheel
IEC	indirect evaporative cooler

LDD	liquid desiccant dehumidifier
M-cycle	Maisotsenko cycle
NTU	number of heat transfer unit
PCM	phase change material
PF	parallel air-water flow configuration
PV	photovoltaic
REC	regenerative evaporative cooler
R&D	research and development
SDD	solid desiccant dehumidifier
STX	shell and tube heat and mass exchanger
TES	thermal energy storage
VCRS	vapor compression refrigeration system
WB	wet bulb

CHAPTER 1

INTRODUCTION

1.1 RESEARCH BACKGROUND

Due to the continuous growth of world's population and the diversification of building appliances, the residential energy consumption has surpassed the proportions dedicated for industrial and public services sectors. For instance, in Iraq, the energy consumption of buildings accounted for 65% which is higher than the industrial and public services combined which are accounted for about 11.2% and 21.6%, respectively, of the total energy use as show in **Fig. 1.1** (IEA Iraq, 2021). This fact reflects the raped increase in the world's total energy demand as reached to more than 20,000 TWh by the end of 2019 as shown in **Fig. 1.2** (IEA, 2021).



Fig. 1.1 Electricity consumption by sectors in Iraq (IEA Iraq, 2021)

Moreover, the portions of residential electricity consumption include appliances, lighting, food preparation (cooking), refrigerating, domestic hot water, air-conditioning systems (HVACR), and other equipment as illustrated

in **Fig. 1.3** (Hossein Motlagh et al., 2020). The electricity consumption in the residential sector is mainly contributed to the air-conditioning systems (i.e., heating, ventilation, air-conditioning & refrigeration (HVACR) systems) (Abbood et al., 2015; Oh et al., 2016).

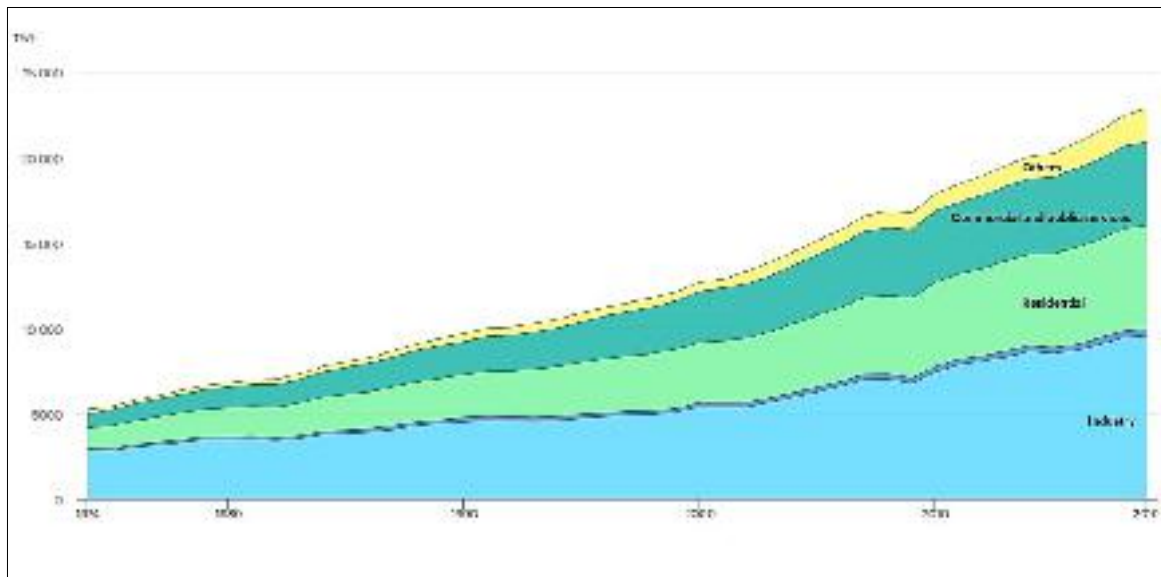


Fig. 1.2 World's electricity consumption by sector (IEA, 2021)

In developed countries, such as United States, the United Arab Emirates, and China, the electricity consumption by HVACR systems has accounted for 41%, 57.5%, and 55% of total residential energy use, respectively (Afshari et al., 2014; California Energy Commission, 2022; International Renewable Energy Agency, 2022). These variations are based on several key factors, such as ambient temperature and humidity, building insulation quality, and how modern the operating systems are. In the meanwhile, in the developing countries, for example Iraq, due to the poor insulation of the buildings and inefficient energy management of air-conditioning systems, the electricity consumption of HVACR systems accounted for 68.99% annually including 42.43% for cooling and 26.56% for heating (Hasan, 2012).

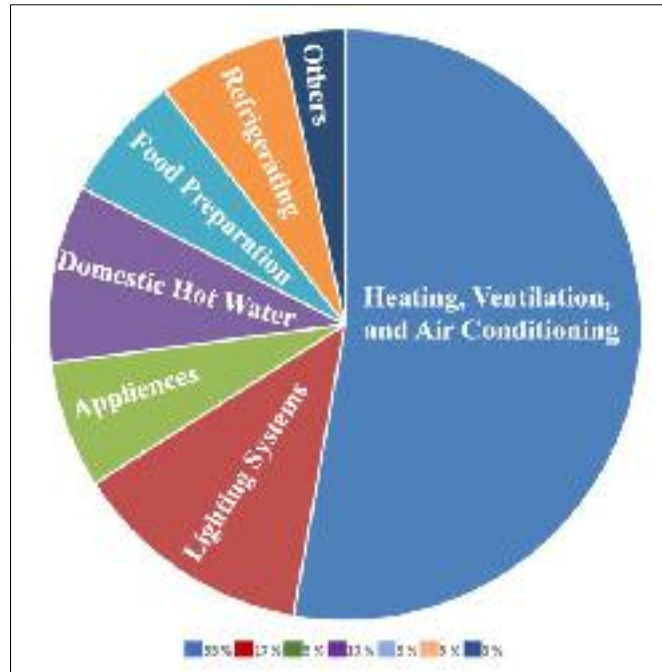


Fig. 1.3 Division of residential electricity consumption (Hossein Motlagh et al., 2020)

Consequently, this high energy consumption by HVACR systems, which is significantly attributes to vapor compression refrigeration system (VCRS) systems, contributes to several environmental and energy crises which are summarized below:

- Environmental crises: six major greenhouse gases, which are stated by the Kyoto Protocol in 1990s (i.e., CO₂, CH₄, NO₂, HFCs, PFCs, and SF₆), are highly contribute to ozone depletion and global warming (United Nations Framework Convention on Climate Change, 1998). Eventually, the utilization of environmentally un-friendly refrigerants and elevated energy demand led to higher emission of greenhouse gases (Lin Jie, 2018).
- Energy crises: in order to attain thermal comfort in buildings environment and world's population rise, the electricity demand by VCRS systems have intensively grown which is the major cause of higher energy demand.

In addition, the utilization of VCRS systems may lead to safety and technical issues. For example, some of the pressurized chlorofluorocarbon (CFC) and hydrofluorocarbon (HFC) refrigerants are toxic and flammable and may cause fire and explosion due to the leakage problems (Goetzler W. et al., 2014). Moreover, most VCRS systems reduce the air temperature to below its dew point temperature and cause de-moisturization and over cooling of the conditioned space that eventually cause higher energy consumption (Lin et al., 2017).

To overcome the above-mentioned disadvantages and achieve the thermal comfort of the conditioned space without utilizing conventional space cooling systems that require enormous amount of electrical energy, thereby, developing an energy-efficient cooling system that is CFC & HFC free, environmentally friendly, and relies on the natural energy sources is indispensable.

1.2 ENERGY-EFFICIENT EVAPORATIVE TECHNOLOGIES

The evaporative cooling technologies can be considered as the main candidate to replace the conventional VCRS systems. The evaporative cooling process is driven by the natural energy source (i.e., water's latent heat of vaporization) (Fouda and Melikyan, 2011). In addition, this technology consumes 80% less energy and reduce up to 44% emission of carbon dioxide when compared to VCRS systems due to lack of compressor and mechanical parts (Duan, 2011). Hence, this technology possesses excellent energy efficiency, in other words, with 10-20 of the coefficients of performance (COP) which is considered the highest among the existing HVACR systems as illustrated in **Fig. 1.4** (Liu et al., 2019b; P. Glanville et al., 2011; REU, 2015).

Over the years, evaporative cooling, in general, has been considered as one of the most sustainable and reliable sources of cooling in buildings and industries owing to its simplicity, low-cost, and ease of access. Besides,

compared to space cooling refrigeration systems, it lacks CFC and HFC coolants that lead to environmental issues. Such working fluids must be pressurized and de-pressurized to transport heat from one zone to another so as to produce cooling.

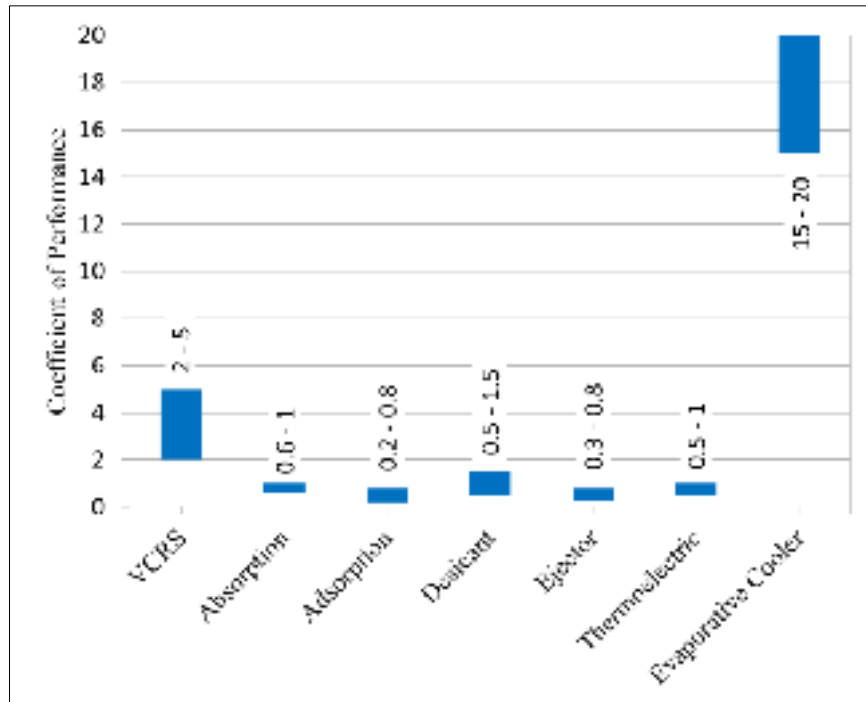


Fig. 1.4 Nominal COP values of existing refrigeration systems

This process consumes high amount of electrical energy that eventually contributes to the global warming phenomenon through the emission of greenhouse gases (Kashyap et al., 2022a; Liu et al., 2018). In consequence, the VCRS systems result in high electricity bills, high initial and maintenance costs, and severe environmental damage (Kashyap et al., 2022b; Shahzad et al., 2021). Therefore, the environmentally friendly characteristics of the evaporative coolers attracted many researchers to study such a system and attempt to improve its performance through many prospects due to the excellency of its thermodynamic process which absorbs the sensible heat of the air stream through the evaporation of water by converting this heat to latent heat without altering its enthalpy (Akhlaghi et al., 2019; Shi et al., 2022a).

In general, the evaporative coolers are categorized into three main types, namely, direct evaporative coolers, indirect evaporative coolers, and dew point evaporative coolers. Each type will be explained in the subsequent sections.

1.2.1 Direct Evaporative Coolers (DECs)

Throughout the history, for thousands of years, the evaporative process of water has been conducted for cooling purposes by hanging wetted objects with high wettability capability over the doors and windows to cool the entrance air stream. The direct evaporative cooler was first invented by Oscar Palmer in 1908 in Arizona with drip type water distribution technique (Cook, 1979; Cooper, 1998). Over the decades, this cooler type came up with other names such as swamp coolers, drip coolers, and desert coolers (Johnston et al., 2022). Dowdy and Karabash (1987) experimentally investigated the DEC by using cellulous as a wetting pad and water dripping technique as water spraying method to moisturize the pads.

Within the DECs, the cooling process occurs when the ambient/outdoor air passes over the wetted pads in direct contact as illustrated in **Fig. 1.5** which represents the evaporation cooling process: (a) air stream inside heat and mass exchanger; (b) cooling process on the psychrometric chart.

When the unsaturated air stream passes over the wetted pad inside the heat and mass exchanger (HMX), it gets moisturized gradually due to the evaporation of the water. As it can be seen on psychrometric chart, the evaporation process occurs along the wet-bulb temperature line, this process is deemed as wet-bulb adiabatic saturation process. The occurrence of this process is attributed to the substantial relationship between the humidity, temperature, pressure, and evaporation process. The applications of DECs are rated for hot areas with low humidity. However, the increased humidity of the

product air is considered as one of the major downgrades of such a system which may cause uncomfortable indoor air condition.

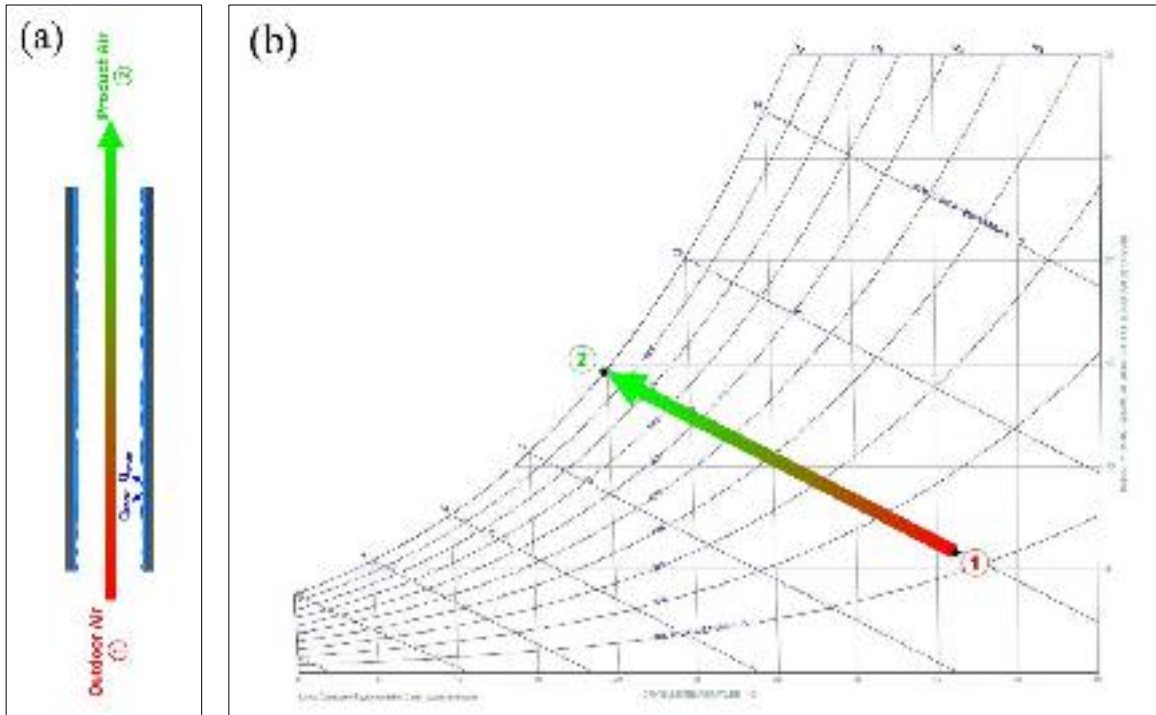


Fig. 1.5 Direct evaporative cooler: (a) air stream inside heat and mass exchanger; (b) cooling process on the psychrometric chart

1.2.2 Indirect Evaporative Coolers (IECs)

The excessive humidity content of the product air from the DEC's has driven the researchers to come up with a new design from which the cooler is separated into the dry and wet channels (Kozubal et al., 2015; R. Chengqin and Y. Hongxing, 2006; Z. Duan et al., 2012). A visual representation of such a process is presented in **Fig. 1.6**. Through this technique, the high humidity issue has been surpassed, yet the cooler faced another impediment, which is the low thermal effectiveness. Similar to the DEC's, the IEC's cannot produce cool air comparable to the wet-bulb temperature of the intake air. The wet-bulb effectiveness is limited, and ranges from 55% to 75% because the airflows of

the dry (i.e., primary) and wet (i.e., working) channels are discrete and only ambient air enters these channels (Duan et al., 2016a; Liu et al., 2019a).

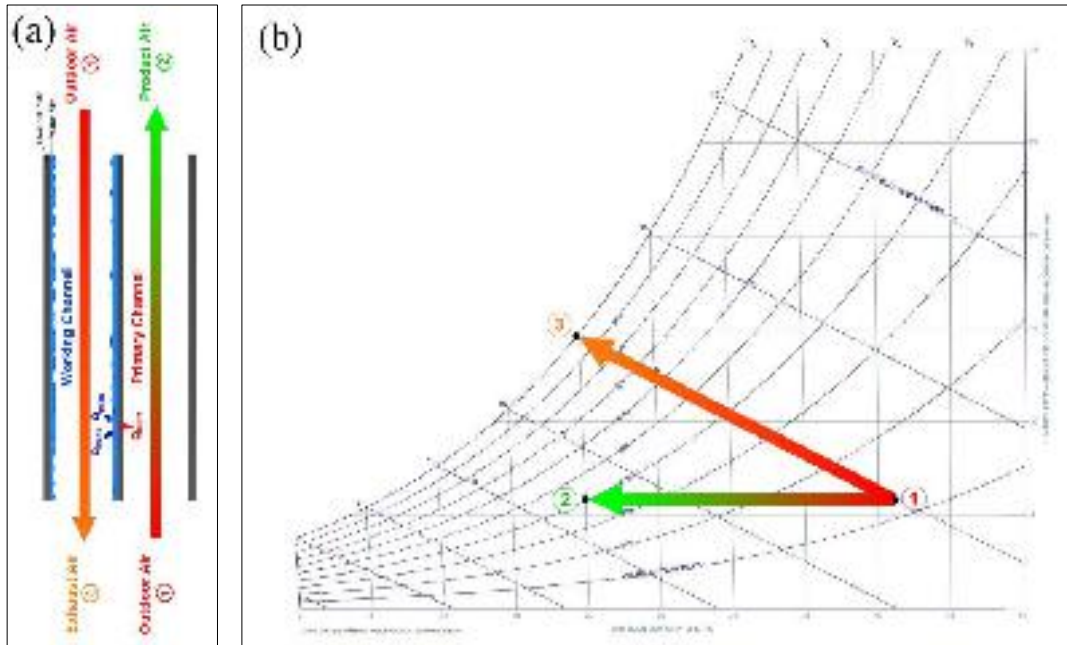


Fig. 1.6 Indirect evaporative cooler: (a) air streams inside heat and mass exchanger; (b) cooling process on the psychrometric chart

1.2.3 Dew Point Evaporative Coolers (DPECs)

The limitation of high humidity content of DEC and the low thermal effectiveness of IECs are two of the common impediments that enthused the researchers to contemplate of a new working technique of air and water streams. Thus, in 2003, Valeriy Maisotsenko was able to overcome these impediments and boost the system's performance when he introduced an evaporative cooling device named Maisotsenko cycle or "M-cycle" that could produce air with a temperature lower than the inlet wet-bulb temperature and towards the dew-point temperature of inlet air (Valeriy Maisotsenko et al., 2003). This phenomenon was achieved by the novel configuration of air and water streams inside the heat and mass exchanger that they proposed from which the air was first pre-cooled inside the dry channels sensibly then diverting

a portion of this cooled air into the wet channel to perform further cooling via evaporation process as illustrated in **Fig. 1.7**.

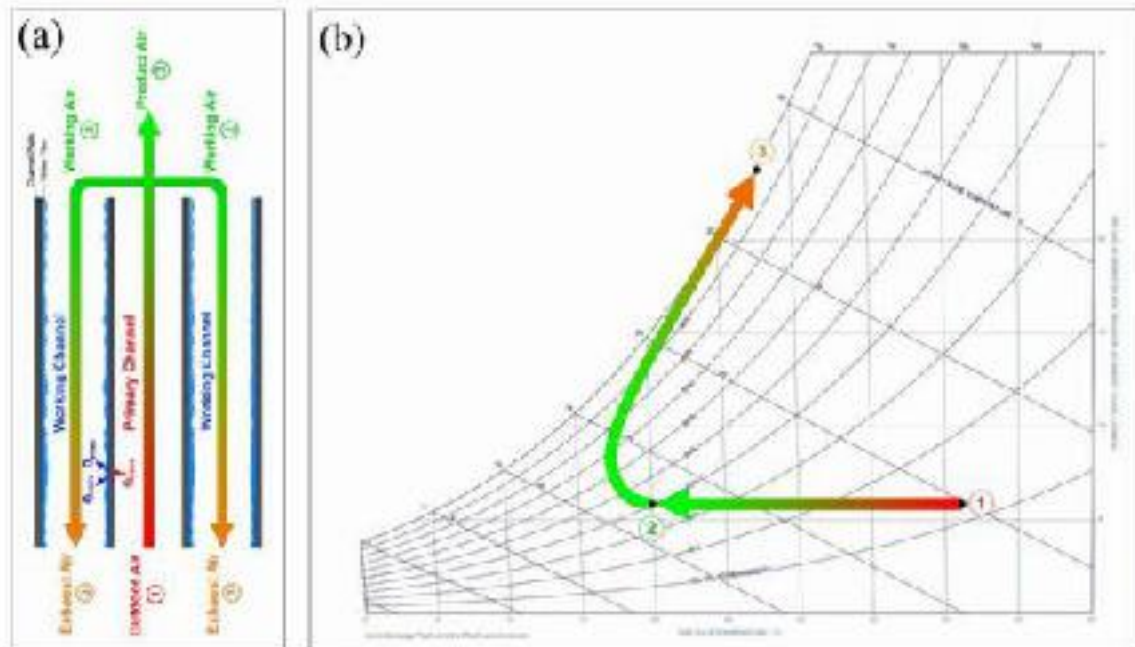


Fig. 1.7 Dew point evaporative cooler: (a) air streams in the heat and mass exchanger; (b) cooling process on the psychrometric chart

This system came up with other names such as dew point evaporative cooler (DPEC) and regenerative evaporative cooler (REC). Since the first innovation, the performance of such a system has been continuously improving through many aspects, including management of better air distribution, utilization of better structural materials, and employing more efficient wetting materials. Therefore, in this study, this evaporative cooling technology will be employed for further investigation and performance improvement.

1.3 DESCRIPTION OF THE RESEARCH

1.3.1 Research Aims and Scopes

The fundamental aim of this research is to introduce a novel dew point evaporative cooler with shell and tube design for its heat and mass exchanger

from which the thermal and energy performance of the cooler deemed to be improved. Since the invention of DPEC, the flat-plate design HMXs have been excessively adopted due to their ease of access, modelling, and manufacturing. In the aspects of heat and mass transfer regarding the flat-plate design, these two convective processes occur perpendicular to the direction of the air stream, in another word, this is a one-dimensional process. Therefore, this deficiency has been considered as one gap through which the performance of the system could be improved. For this, a tubular channel has been proposed from which the process of heat and mass transfer take place around the circumference of the tubes in all directions. The selection of shell and tube design for DPEC will contribute in the following aspects:

- (1) Shell and tube HMX employs a bundle of tubes as primary channels which increases the surface area for heat and mass transfer and makes the process more efficient.
- (2) Shell and tube HMXs can withstand higher pressures which is advantageous and profitable for industrial applications as in DPECs the channels wall of the HMXs must be as thin as possible. Consequently, the cooler will be appropriate to work at higher velocities, thus its cooling capacity improves.
- (3) Shell and tube HMXs result in lower pressure drop. This translates to less energy consumption required by fans to circulate the air through the system.

1.3.2 Research Objectives

To attain the potential aims referred in the forgoing section, this research set several objectives which are addressed below:

- (1) To develop a robust mathematical model that can predict the thermal, energy, and exergy performance of the proposed DPEC. Thereafter, conducting a numerical simulation using Engineering Equation Solver

(EES) environment and compare the cooler's performance to that of flat-plate type DPEC.

- (2) To construct the cooling unit and examining its performance in a controlled lab environment. Then, validating the acquired data from the numerical simulation by comparing it to the experimental data.
- (3) To investigate the coolers' performance under various weather conditions and geometrical configurations to identify the suitable boundary conditions (or feasibility) for the proposed air-conditioning system.
- (4) To carry out first and second laws of thermodynamics based analysis for the proposed DPEC through which a comprehensive perceptiveness about the new cooler can be achieved.

1.3.3 RESEARCH CONTRIBUTIONS

This study records a first endeavor regarding the dew point evaporator by employing a novel shell and tube design for the heat and mass exchanger that enables enhanced thermal and energy performance. Over the decades, the complexity of the HMX of the DPECs is one of the major impediments for the globalization of such a high-performance system, however, through the proposed design, the manufacturing of DPEC made easy, it is time saving and durable. These merits are significantly going to contribute in the globalization issues. To summarize, the proposed system possesses the following novelties:

- I. Innovative structure of HMX:** A unique dew point evaporator heat-mass exchanger with shell and tube design has been proposed that enables heat and mass transfer process occurrence in all transverse directions.
- II. Exclusive numerical simulation model:** Pertinent to the proposed new DPEC, a detailed numerical model has been developed and simulated in EES software which can facilitate the following tasks: (1) selecting the best geometrical parameters for structural optimization, (2) selecting the best

operational condition (, i.e., weather parameters) for ultimate cooling performance, and (3) analyzing the thermal and energy behavior under a wide range of boundary conditions.

- III. **Innovative water distribution system:** the unparalleled water distribution system has been developed for the new cooler that can help in distributing and orienting the water flow sustainably over the tube bundles so as the wetting surfaces of all the tubes getting moisturized evenly.
- IV. **Employment of new materials for the HMX:** the polycarbonate drinking straws have been adopted to serve as the primary channels of the system. The entire HMX has been fabricated from this type of the tube. These tubes come with variety of diameters and characterized by their super thin wall with only 0.15 mm thickness which eventually has insignificant effect on the heat transfer between the primary and working air streams. Regarding the wetting surface, a disposable tablecloth has been adopted which is characterized by high water diffusivity capability alongside with a very shallow thickness (less than 0.03 mm). The utilization of these materials is a new trial in air-conditioning system.

1.4 DISSERTATION STRUCTURE

The prime content of this dissertation has been cleavage into seven chapters. A brief explanation of each chapter is presented below:

CHAPTER 1 this chapter is concisely explain the background, aims, scopes, objectives, and contributions.

CHAPTER 2 this chapter presents a comprehensive literature review carried out for evaporative coolers with shifting the focus towards the development stages pertinent to the DPECs. In addition, this chapter include the theoretical and experimental studies with a detailed review and their key outcomes. Based on the review process, the research gap of this dissertation has been identified.

CHAPTER 3 this chapter is based on the first and second laws of thermodynamics which describes the working mechanism of the proposed novel DPEC alongside with a solid mathematical model development and a numerical simulation scheme that enables testing the system under a variety of operational and geometrical conditions. Through this simulation scheme, the optimum geometrical design for the new cooler has been obtained and thereby harnessed for the construction of the unit.

CHAPTER 4 this chapter inclusively demonstrates the construction procedures of the system, major components design, material selections, prototype assembly, and measuring instruments set-up.

CHAPTR 5 this chapter investigates the thermal, energy, and exergy performance of the new system and shows the effect of the operational and geometrical parameters on the cooler. Further, in this chapter, the constructed system has been tested under a controlled environment by the help of an air handling unit and conducted a series of lab-based experiments to validate the dedicated numerical simulation scheme.

CHAPTER 6 this chapter summarizes the substantial outcomes from this research study, and suggests further recommendations for the potential future works and challenges.

CHAPTER 2

LITERATURE REVIEW

2.1 INTRODUCTION

In this chapter, a comprehensive review regarding the dew point evaporative coolers will be carried out which is based on the ultimate conducted research studies to build a strong scientific foundation for the current study. Since the invention of the dew point evaporative cooler by Valeriy Maisotsenko that patented in United State Patent and Trade Mark Office (Valeriy Maisotsenko et al., 2003), the performance of such a low energy grade system has been continuously improved through many aspects. An overview about all the aspects that have been investigated by the researchers is illustrated in **Fig. 2.1**. A schematic illustration of the patented M-cycle dew point evaporative cooler is presented in **Fig. 2.2**. Through this approach, the research gap has been identified and set as the foundation for the current dissertation, and the future research scopes are suggested. Furthermore, this comprehensive literature review assisted in achieving the following trails:

- i. Obtaining an overall understanding of the research and development (R&D) progresses in this field from which further room for cooler's improvement could be identified that will push the system's performance toward its perfection.
- ii. Introducing new topics for the scientific researches.
- iii. Developing guiding approaches for the subsequent chapters.
- iv. Reducing the risks for any flaws and misconceptions during designing, modelling, manufacturing sessions.

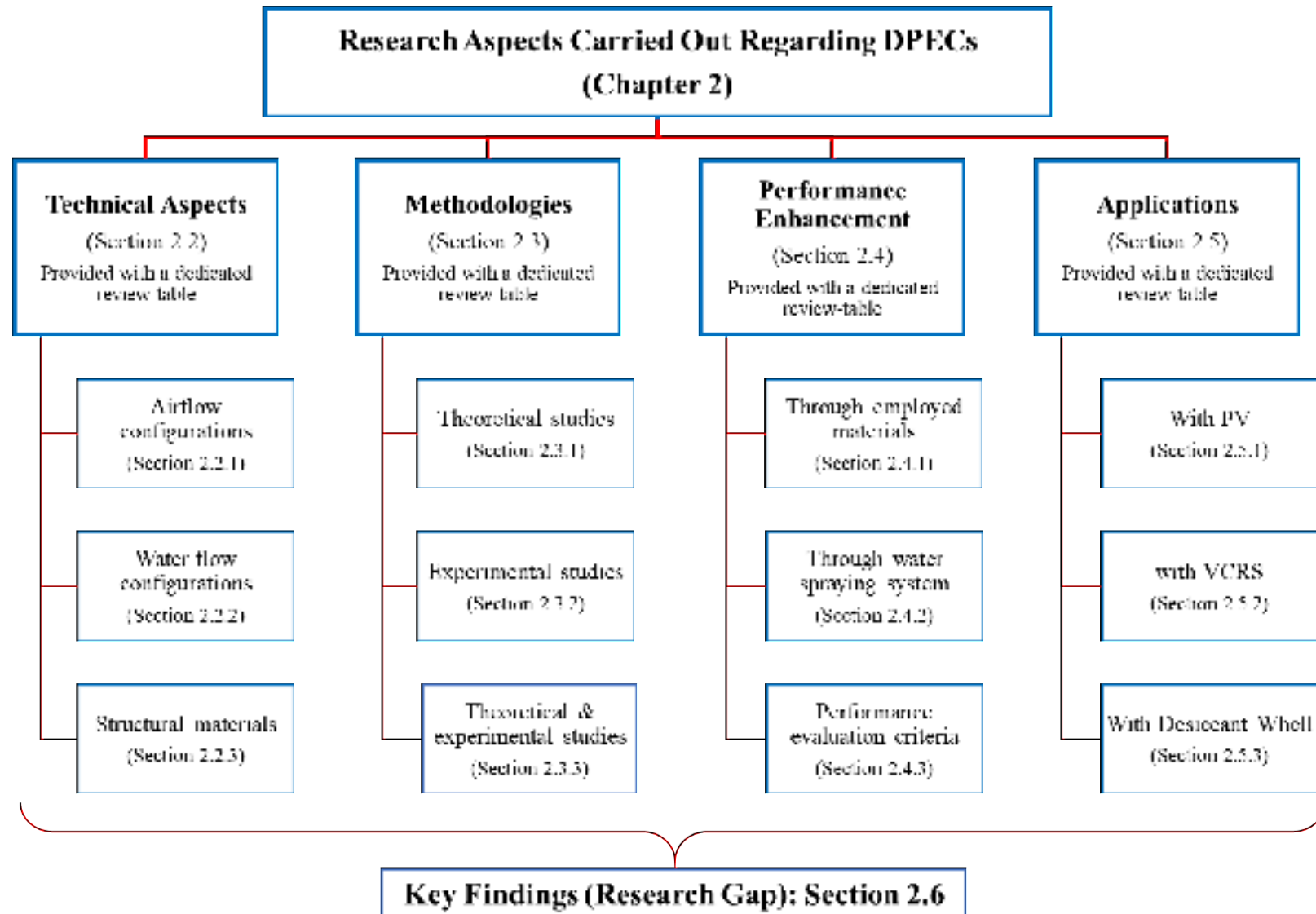


Fig. 2.1 Guideline for literature reviewing in Chapter 2

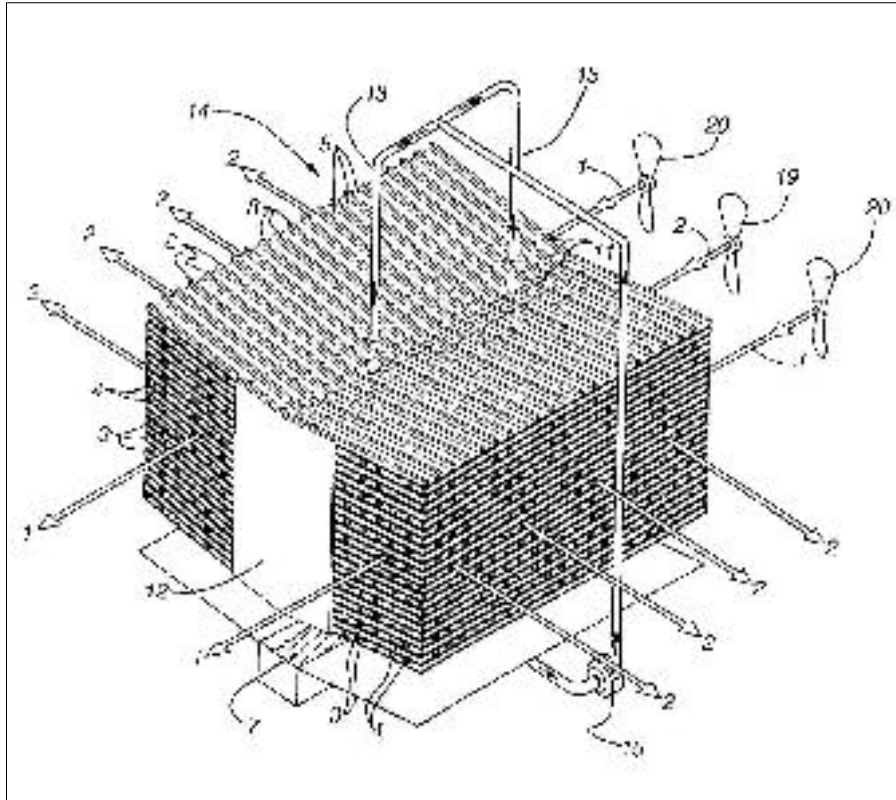


Fig. 2.2 M-cycle dew point evaporative cooler by Valeriy Maisotsenko (2003)

2.2 REVIEW ON THE TECHNICAL ASPECTS

This section presents the theoretical and experimental research studies carried out regarding the arrangement of airflow and water-flow patterns, alongside with the structural materials employed for channels wall, and wet evaporative surfaces. **Table 2.3** presents the literatures regarding this matter.

2.2.1 Airflow Configurations of DPECs

The dew point evaporators are involved with only two generic airflow configurations, namely, the counter-flow and cross-flow. The former, is more preferable to use, because a higher thermal performance could be achieved when compared to the latter configuration. Zhan et al. (2011) carried out a comparative study between the counter-flow and cross-flow dew point evaporative heat-mass exchanger with flat-plate design as illustrated in **Fig.**

2.3. They investigated both configurations theoretically and experimentally under the same exact geometrical and operational boundary conditions. They stated that, in comparison, the counter-flow HMX can achieve about 20% higher cooling capacity and 15%-23% higher wet-bulb and dew-point effectiveness. Consequently, the higher cooling capacity and thermal effectiveness of the counter-flow HMX translates to lower energy consumption, smaller unit size, lower airflow rate, and lower cost. However, they found that the cross-flow HMX had about 10% higher coefficient of performance in comparison to the counter-flow HMX due to lower pressure drop.

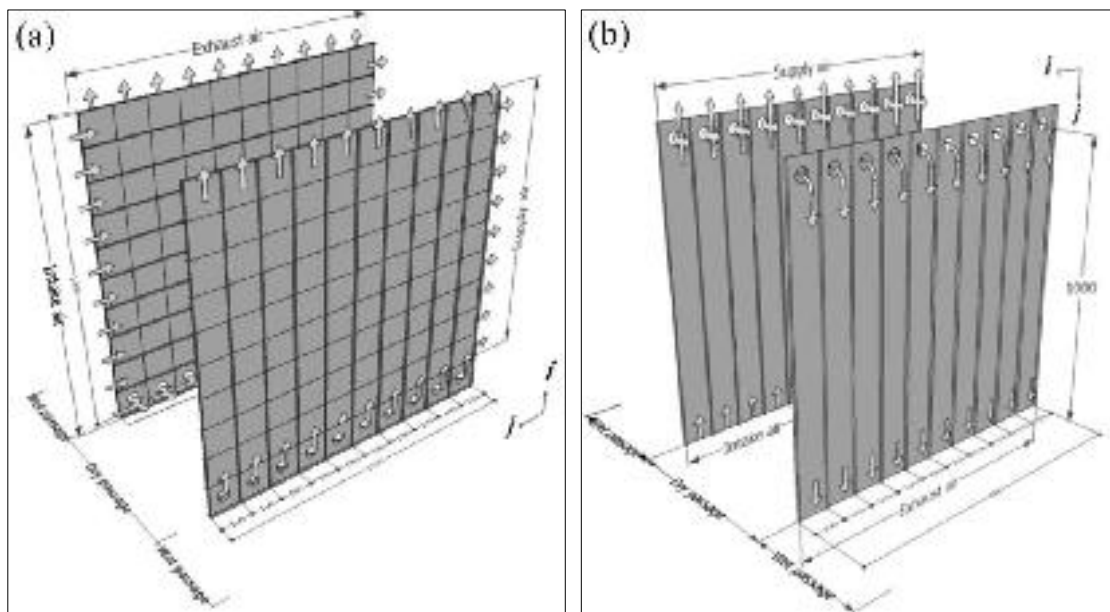


Fig. 2.3 Schematic diagram of two dew point evaporative HMXs: (a) Cross-flow; (b) Counter-flow (Zhan et al., 2011)

The original flat-plate M-cycle dew point cooler was proposed with counter-flow configuration. However, the incipient manufacturing efforts were unsuccessful due to difficulties in identifying the counter-flow region, high pressure drop of the HMX, vertical wetting difficulties of evaporative surface, and immature structural materials (Lee and Lee, 2013; Pandelidis and

Anisimov, 2015; Riangvilaikul and Kumar, 2010a). Subsequently, cross-flow configuration has been selected to replace the counter-flow M-cycle as illustrated in **Fig. 2.4**.

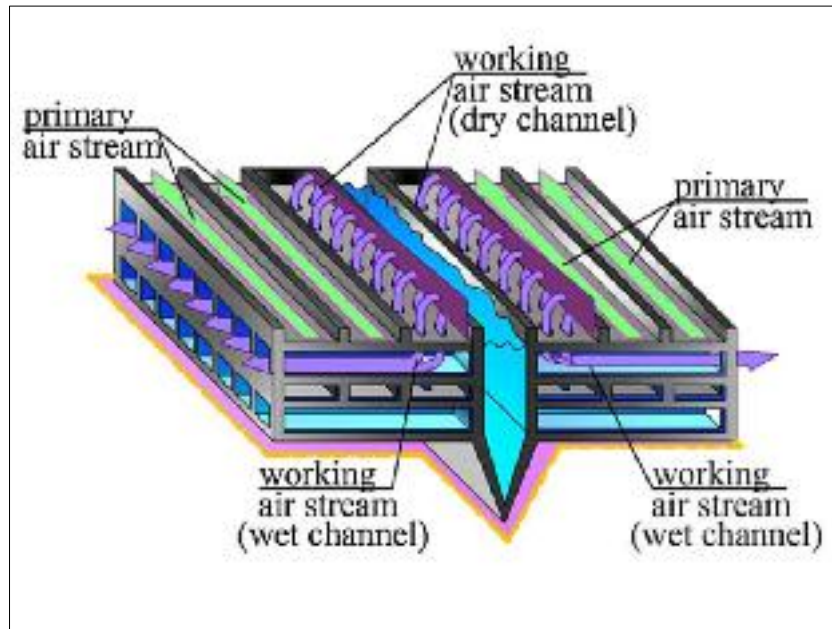


Fig. 2.4 M-cycle cross-flow HMX (Pandelidis and Anisimov, 2015)

Furthermore, Min et al. (2019) developed a 2-D numerical model that can predict the thermal and energy performance for flat-plate cross-flow and counter-flow DPECs. They stated that when using these coolers in hot and humid regions, condensation happens in dry channels due to high humidity content of the air stream. The formation of condensation will reduce the wet-bulb and dew-point effectiveness. As shown in **Fig. 2.5**, under the same operational conditions, results showed that the counter-flow configuration has 2-15% higher condensation rate than cross-flow configuration with 2-7% reduction in wet-bulb effectiveness. As the condensation occurred in the dry-channel, the total heat transfer has boosted by 2-3 times and it is lower in cross-flow by 9% when compared to counter-flow.

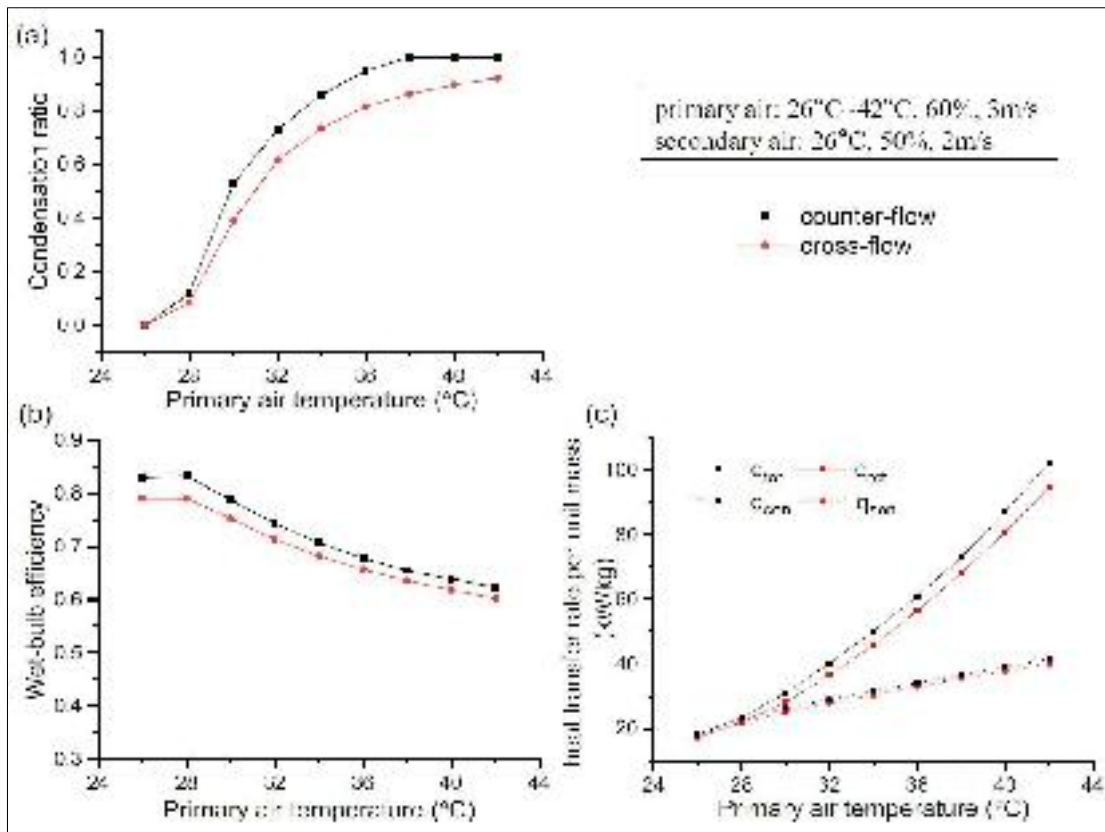


Fig. 2.5 Effect of inlet air temperature on: (a) condensation rate; (b) wet-bulb effectiveness; (c) heat transfer rate (Min et al., 2019)

Furthermore, Jia et al. (2019) constructed two flat-plate dew point evaporative coolers with cross-counter-flow configuration. In the first unit, they used polystyrene and nylon fibers as structural materials. In the second unit, they used aluminum foil. Then, they studied the impact of operational parameters on the thermal performance on both systems. The conducted research reported that the first unit will reduce the size of the cooler due to higher cooling capacity and dew-point effectiveness which was between 46.7% to 78.6%.

Other studies used adopted cross-flow configuration for regenerative air circulating water to achieve lower pressure drop inside the HMX that will lead to reduced airflow and more power efficient (Anisimov et al., 2014; Kashif Shahzad et al., 2018; Pandelidis et al., 2020a). On the other hand, most studies

adopted counter-flow configuration due to a higher cooling capacity, better thermal performance, and lower product air temperature (Duan et al., 2017b; Lin et al., 2020a; Pakari and Ghani, 2019; Wang et al., 2019a; Zhu et al., 2023a).

2.2.2 Water-Flow Configurations of DPECs

Arranging the flow direction of water stream with the air stream has a significant effect on the cooling performance, product air temperature, and drain water temperature. When the direction of water flow is parallel to the airflow direction in dry-channel, both streams simultaneously cool down and result in lower water temperature. In contrast, when the direction between these two streams are counter, the drain water temperature will be higher because as the water approaches the exit point, it approaches the entrance point of the dry-channel's airflow which is at its maximum temperature. Hence, more heat will be transferred to the flowing water.

Kashyap et al. (2020) made a thorough investigation regarding air and water flow patterns with 8 different configurations for flat-plate DPEC, as shown in **Fig. 2.6**. They conducted the numerical simulation under the nominal boundary conditions presented in **Table 2.1**. The comparison of all the configurations were based on cooling capacity, dew-point effectiveness, and COP.

During the investigation, they set the water flow in gravitational-driven (downward) direction. They demonstrated the following outcomes:

- The inlet water mass flow rate and temperature significantly influenced the performance of the DPEC.
- for all configurations, dew-point effectiveness improved when the inlet water temperature was lower than the crossing air temperature.

- When the air-ratio of the secondary air stream increased, the dew-point effectiveness increased. However, this approach reduced the cooling capacity and COP of the coolers.
- When the airflow channels' gap increased, the cooling capacity, dew-point effectiveness and energy efficiency of all the configurations were improved.
- When the primary air velocity increased, it decreased the dew-point effectiveness and COP, while it improved the cooling capacity.
- When the wet-bulb temperature of inlet air raised, it enhanced the dew-point effectiveness, but reduces the cooling capacity.
- For a water-flow of about 5 L/h, configurations A, E, and H had a better performance than the other configurations.

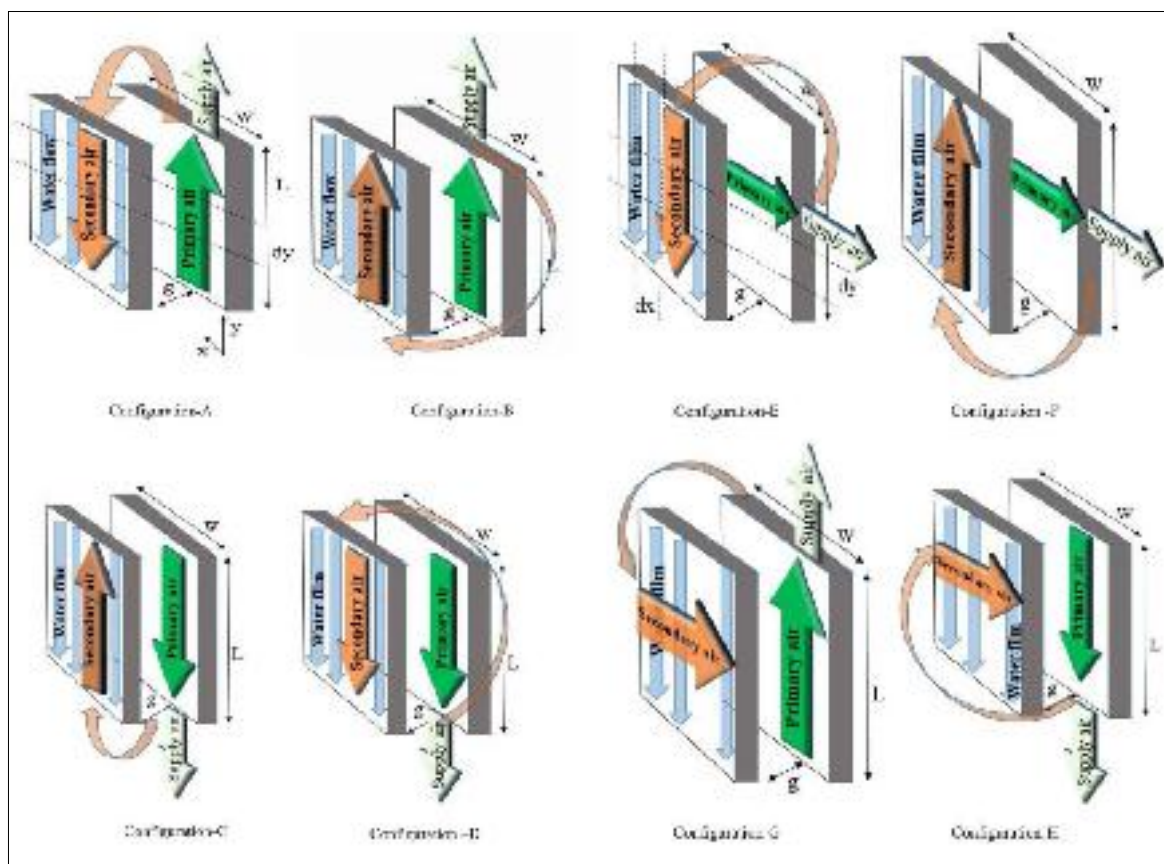


Fig. 2.6 Eight configurations for air and water flow patterns regarding the HMX of DPEC (Kashyap et al., 2020a)

Table 2.1 Nominal values of proposed DPECs (Kashyap et al., 2020a)

Parameter	Value
Length of the evaporative HMX	0.5 m
Width of the HMX	0.5 m
The total height of the HMX	0.7 m
The gap between the primary air channel	0.005 m
The gap between the secondary air channel	0.005 m
The thickness of the plate separating two channels	0.5 mm
The volumetric flow rate of water per channel	5 L/h
The inlet temperature of the water	17 °C
Air extraction ratio	0.3
Total primary airflow rate	0.35 m ³ /s
Total secondary airflow rate	0.105 m ³ /s
Total supply airflow rate	0.245 m ³ /s

Moreover, Ren and Yang (2006) studied the effect of water spray intensity and its direction with the air stream inside the primary and working channels for four different configurations. They found that the cooler gives the best performance when the primary channel's air stream arranged in counter-current to the water-flow direction. They also concluded that, for the same air-water flow pattern, by decreasing the water flowrate, the performance of the cooler improves.

2.2.3 Structural Materials of DPECs

The materials adopted for the DPECs' manufacturing are divided into two main categories; (i) plate material from which the HMX is composed, (ii) wick materials from which the evaporative surface is composed. These materials play a significant role on the system's performance and manufacturing feasibility.

In general, the DPEC is made from flat-plate layers. Several studies utilized aluminum sheets material for these layers due to its ease of handling during the construction and high thermal conductivity. However, this material is not cost efficient. Alternatively, considering low cost, availability, corrosion resistant, and weight, polycarbonate and polyethylene materials have been widely adopted, which are basically plastics. In terms of the wick materials, various types of fiber, cotton, gauze, tissue, and craft paper have been adopted due to their thinness and fast absorbing and spreading of water.

Xu et al. (2024) employed aluminum sheets as flat-plate material and Coolmax® fiber as wick material. Experimental investigations revealed that the fabricated system can reduce the ambient temperature by 18.16 °C (from 43.02 °C to 24.86 °C) as shown in **Fig. 2.7**. In addition, the prototype has a coefficient of performance of 31, and a wet-bulb effectiveness of 93%. Further description with a visual insight of the prototype is presented in **Table 2.4**.

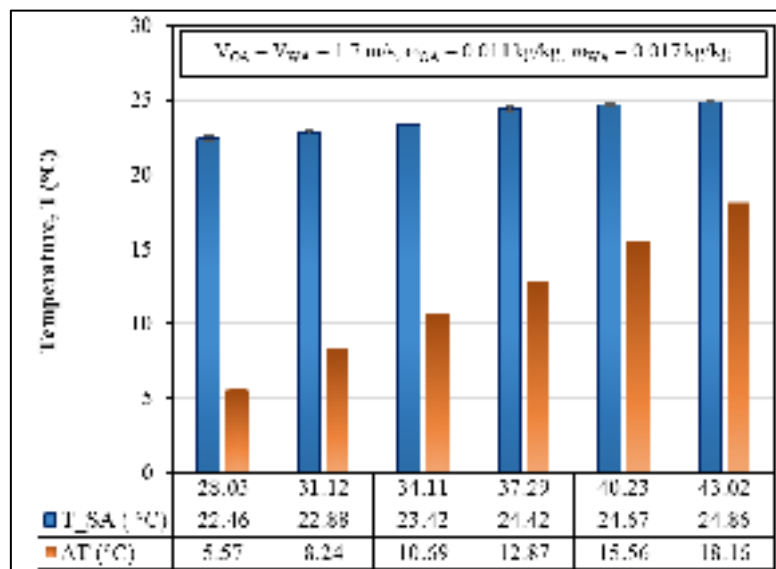


Fig. 2.7 Product air temperature and temperature drop trends under the effect of various inlet air temperatures (Xu et al., 2024)

Similarly, Khalid et al. (2016), employed aluminum sheets coated with felt material to serve as the evaporate surface for cross-flow flat-plate M-cycle, as shown in **Fig. 2.8**. Detail of the parameters used in the fabrication are presented in **Table 2.2**. They concluded that the wet-bulb effectiveness and dew-point effectiveness of the prototype ranged between 92-120% and 62-85%, respectively, under the operational conditions of 25-45 °C ambient temperature and 11-19 g/kg ambient humidity ratio. In addition, similar to (Riangvilaikul and Kumar, 2010a), both studies reported that the proposed prototype can provide a comfort indoor air condition for regions where the ambient temperature and humidity ratio are less than 45 °C and 11.2 g/kg, respectively.

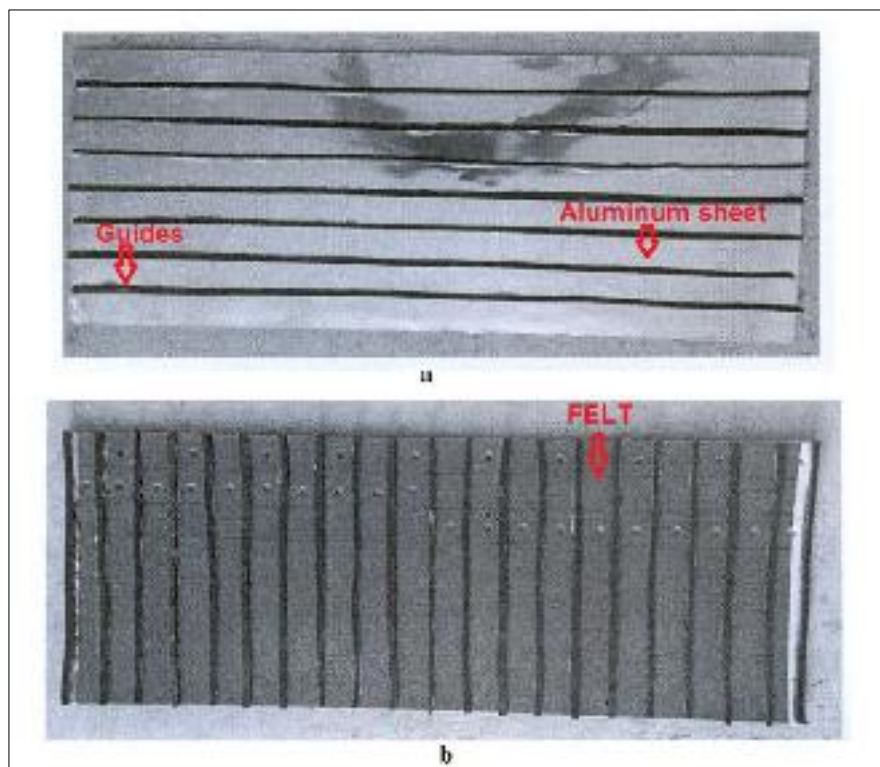


Fig. 2.8 Felt attachment to the aluminum sheets: (a) primary channel; (b) working channel (Khalid et al., 2016)

On the other hand, polymer films and cellulose-blended fiber films has been used by Duan et al. (2017a) as a structural material for a flat-plate REC.

Moreover, each working channel at top has been coated with $0.3 \times 1.0 \times 6.65$ cm aluminum strips that coated with the same wick fiber to serve as the water distribution system. They developed two RECs, one with multi-stage air diversion from primary channel to working channel, and the other one with single stage diversion as illustrated in **Fig. 2.9**.

Table 2.2 Detail of the experimental parameters (Khalid et al., 2016)

Parameter	Design value
Wall material	Aluminum coated fiber (Felt)
Wall thickness	0.5 mm
Length of dry channel	0.508 m
Length of wet channel	0.203 m
Width of channel	25 mm
Channel gap	4 mm
Felt water absorption ability	280 g/m ²
Fabric (Felt) conductivity	0.04 W/m K

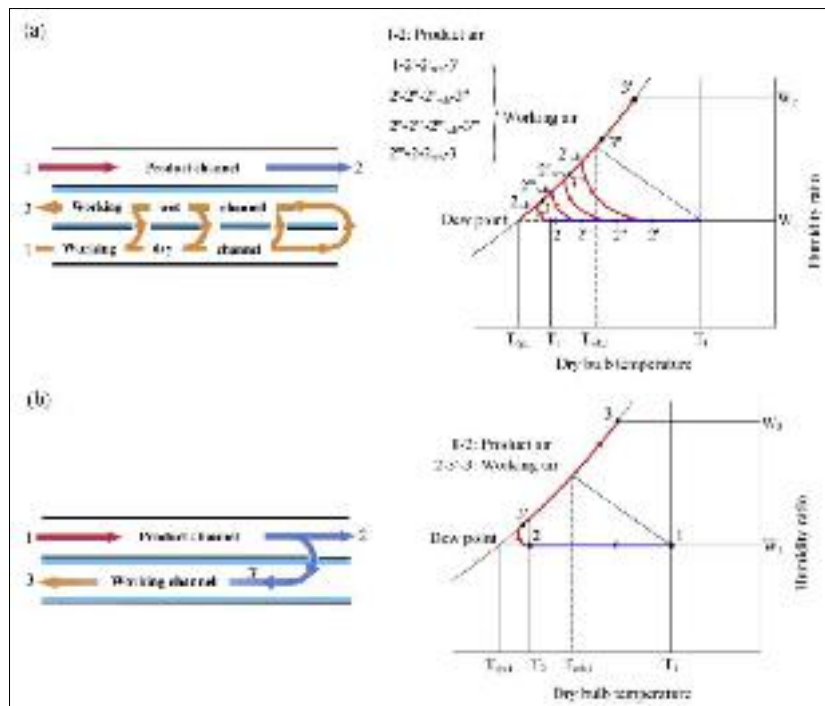


Fig. 2.9 Working principle on psychrometric process regarding: (a) multi-stage REC; (b) single stage REC (Duan et al., 2017a)

They noted, after 5 minutes, the evaporative surfaces were completely moisturized with water. They concluded that the wet-bulb effectiveness, energy efficiency, and cooling capacity of the prototype were ranged between 96% to 107 %, 10.6 to 19.7, and 3.9 kW to 8.5 kW, respectively. Moreover, polycarbonate and polymer materials have been adopted by other researchers as the plate material for the HMX that gave superior low maintenance cost (Lin et al., 2020b; Tejero-González et al., 2013; Velasco Gómez et al., 2012). A summary of the conducted research studies in regard to this section is provided in **Table 2.3**.

2.3 METHODOLOGIES IN THE CONDUCTED LITERATURES

2.3.1 Theoretical Studies

The superior future of the theoretical study is that the proposed system can be examined under a wide range of operational and geometrical conditions, besides, this approach enables to select the optimum design parameters that will later contribute to the system fabrication. For instance, (Pandelidis and Anisimov, 2015) developed a two-dimensional (2-D) heat and mass transfer model to compute the thermal performance of the flat-plate M-cycle. The modified ϵ -NTU has been adopted for mathematical modelling and parametric analysis process. They conducted the simulation under two operational conditions, namely, variable interring air volume flowrate and temperature. Through the simulation, they were able to indicate the optimum operational and geometrical parameters that have the most significant effect on the cooler's performance. On the other hand, Zhu et al. (2023b) developed a three-dimensional (3-D) numerical model to calculate the airflow and moisture content transport for a flat-plate DPEC. They focused on the influence of uneven water distribution in the working channel's evaporative surface and investigated its effect on the system's performance.

Table 2.3 Summary of the selected studies regarding the technical aspects (Section 2.2)

Study	Cooler type	Nature of the work	Airflow configuration	Water-flow configuration	plate material	Wick material	Key finding
(Riangvilaikul and Kumar, 2010a)	Flat-plate DPEC	Experimental	Counter-flow	Downward flowing	polyurethane	Cotton	They obtained that, this system can achieve comfort indoor condition for regions where the temperature and humidity are less than 45 °C and 11.2 g/kg, respectively.
(Zhan et al., 2011)	Flat-plate M-cycle	Theoretical & Experimental	Cross- and counter-flow	Downward flowing	polyurethane	Cotton	They obtained that, counter-flow can achieve higher cooling capacity and thermal effectiveness, but lower COP when compared to cross-flow.
(Lee and Lee, 2013)	Flat-plate REC	Experimental	Counter-flow	Downward flowing	Aluminum	Porous layer coating	They found that the water-flowrate significantly affect the cooling performance which can be improved by reducing the water-flow.
(Anisimov et al., 2014)	Flat-plate M-cycle	Theoretical & Experimental	Cross-flow	Capillary motion	polymer	Porous material	The results showed that the cooler is best suited for hot and dry regions that can reduce the temperature to below wet-bulb.
(Khalid et al., 2016)	Flat-plate M-cycle	Experimental	Cross-flow	Capillary motion	Aluminum	felt	Similar to Riangvilaikul and Kumar (2010), they found that the system can provide comfort indoor condition for regions where the temperature and humidity are less than 45 °C and 11.2 g/kg, respectively.
(Duan et al., 2017b)	Corrugated-plate REC	Numerical & Experimental	Counter-flow	—	polymer	cellulose-blended fiber	They stated that, in order to optimize the performance, the water flow must vary with regard to the intake airflow.

(Kashif Shahzad et al., 2018)	Flat-plate M-cycle	Experimental	Cross-flow	Downward flowing	—	—	Through utilization of desiccant dehumidification wheel, they could reduce humidity and improve the performance.
(Min et al., 2019)	Flat-plate IEC	Theoretical	Cross-flow and counter-flow	Downward flowing	—	—	They showed that, when the systems operated under hot and humid condition, the counter-flow has higher condensation rate that will badly affects the thermal performance.
(Jia et al., 2019)	Flat-plate DPEC	Experimental	Cross-counter flow	Downward flowing	First unit: polystyrene Second unit: aluminum	Nylon fiber	Through this study, they were able to reduce size and weight of the system.
(Wang et al., 2019a)	Flat-plate DPEC	Theoretical	Counter-flow	Downward flowing	—	fiber	They analyzed the entropy generation rate and entropy production number and they proved that these parameters are useful for system optimization.
(Kashyap et al., 2020a)	Flat-plate REC	Theoretical	Cross-flow and counter-flow	Downward flowing	—	—	They investigated eight different air-water flow configurations. Each system showed different characteristics under the investigation.
(Lin et al., 2020a)	Flat-plate DPEC	Theoretical & experimental	Counter-flow	Capillary motion	Polyethylene Terephthalate	Natural fiber	They developed two optimization algorithms and compared the results with experimental data.
(Zhu et al., 2023a)	Flat-plate DPEC	Theoretical	Counter-flow	Capillary motion (stagnant)	Aluminum	—	The numerical simulation showed that higher inlet air temperature and lower humidity lead to higher thermal effectiveness.
(Xu et al., 2024)	Flat-plate REC	Theoretical & experimental	Counter-flow	Downward flowing	Aluminum	Coolmax® fiber	They reported that the sensible heat transfer between dry- and wet-channels becomes effective and rate can be improved by using fins.

A flow-chart of the developed three-dimensional mathematical model is presented in **Fig. 2.10**. Last but not least, on the basis of simulation results, they determined that the 3-D model can improve the simulation accuracy by 5.46% when compared to 2-D models. Furthermore, they found that the uneven water distribution badly effects the cooling performance and water evaporation of the cooler, and they observed that at the entrance and exit of the working channels the water evaporation has the largest driving force which must be considered for practical applications.

One of the leading edges of numerical simulation study for such a system is found in examining the cooler's thermal and energy performance under a wide range of global climate conditions, particularly, at various air temperature and humidity ratio. These two meteorological parameters have the crucial settlement in terms of system's feasibility in particular environments. For instance, Ghosh and Bhattacharya (2021) assessed the performance of hybrid flat-plate DPEC under hot and humid climate to determine its usability for office buildings. Cui et al. (2015) developed a two-dimensional numerical model for a hybrid flat-plate DPEC to lower the cooling load on the VCRS system. They run the simulation under humid tropical climate and found that the developed model can reduce the cooling capacity by 47%.

Moreover, Pandelidis et al. (2018) carried out a numerical investigation for three different hybrid flat-plate M-cycles as recovery systems when used the exhaust air from the conditioned space for moderate climate conditions. They observed that the stated exhaust air can be used as the working air inside the working channels. They indicated a lower product air temperature with 3°K reduction. Further, (Gao et al., 2023) numerically investigated tube in tube design DPEC and compared to flat plate design. They found a noticeable improvements in new coolers performance through employing new geometry. Baakeem et al. (2019) investigated the possibility of using DPEC under the

climate condition of Arab Gulf countries (i.e., Abu Dhabi and Dubai in the United Arab Emirates; Riyadh, Dammam, and Jeddah in Saudi Arabia; Doha, the capital of Qatar; Kuwait, the capital of Kuwait; and Muharraq in Bahrain) with regional relative humidity of about 70%. They stated that the flat-plate DPEC can be considered as a viable choice for all selected cities and can replace the conventional VCRS systems. An illustration of cooling capacity and COP is shown in **Fig. 2.11**.

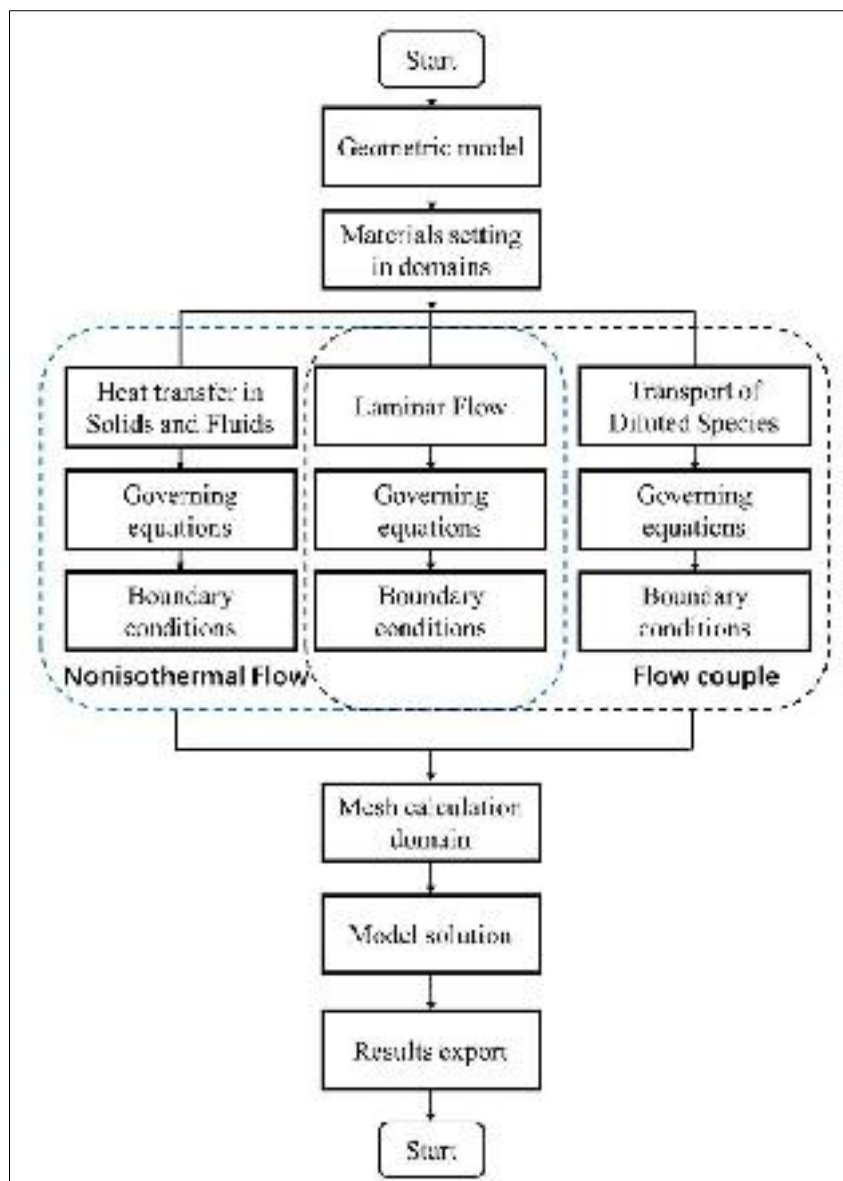


Fig. 2.10 Flow-chart of the developed 3-D simulation model (Zhu et al., 2023b)

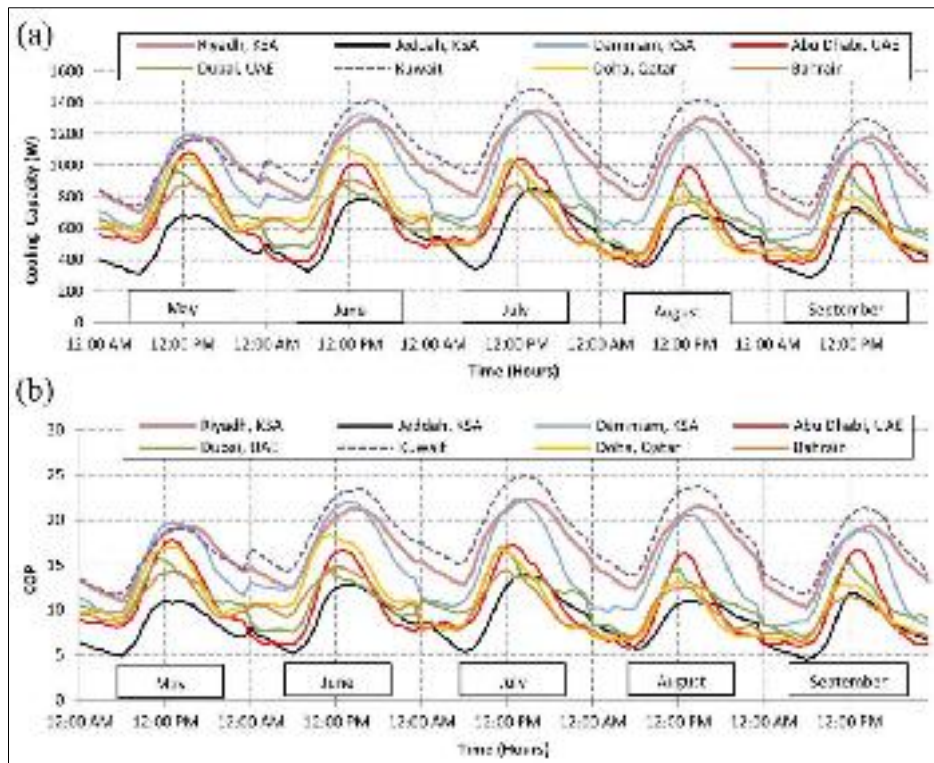


Fig. 2.11 DPEC performance under Arab Gulf climate: (a) cooling capacity; (b) COP (Baakeem et al., 2019)

2.3.2 Experimental Studies

Many researches implemented experimental approach solely without referring to the development of mathematical modelling. Undoubtedly, this approach based on the logical findings from peer reviewed data by published literatures. Hence, the experimental studies establish a foundation for practical applications and mass production. In regard to the DPECs, plastic, aluminum, and fibers have been used frequently as the structural material for heat and mass exchanger. Xu et al. (2017) constructed a dew point evaporative cooler using aluminum sheets and Coolmax[®] fiber as structural materials. They used corrugated aluminum plate rather than the flat aluminum plate so as to increase the heat and mass transfer surface area and give a rigidity to the cooler. An illustration of the prototype is shown in **Table 2.4**. Under the standard test condition (dry-bulb and wet-bulb temperatures of 37.8°C and 21.1°C, respectively), the cooler achieved wet-bulb and dew-point effectiveness of

114% and 75%, respectively, with energy efficiency of 52.5. The experimentations revealed that at lower cooling output, the energy efficiency was increased. Moreover, Duan et al. (2016b) used flat aluminum flat-plates and porous fiber as a structural materials, besides, they inserted triangular air guide into the primary channels to increase the heat transfer surface and increase the cooling capacity as these air guides function as fins which increase the hat transfer rate. They found that the wet-bulb effectiveness and energy efficiency ratio (EER) improved by 31% and 40%, respectively when compared to the conventional IECs. On the other hand, polymer and polypropylene flat-plate sheets with cotton have been used as structural materials by Arun and Mariappan (2019) and Riangvilaikul and Kumar (2010b) with only 0.5 mm thickness. These materials are distinguished by their light weight, availability, corrosion resistance, and low cost alongside with being possible to made in super thin profile. Unlike metals, these super thin plastic layers are able to withstand ripping, cracking or puncturing due to their elasticity feature. These merits are considered highly significant when it comes to mass production as they extend the lifespan of the coolers. In addition, due to extreme thinness, the effect of materials thermal conductivity on heat transfer rate between the primary and working channel air streams will be insignificant, therefore, the heat transfer resistance are generally going to be neglected.

Furthermore, The DPECs can be used for cooling of the electronic units as Dizaji et al. (2021) constructed a mini flat-plate M-cycle cooler to cool down the Graphics processing Unit (GPU) and Control Processing Unit (CPU) of a computer. 3-D printer has been utilized to fabricate the proposed cooler which was made of nylon and tissue. From the experimental investigations, they stated that such a cooler can be employed to decrease the electronic unit's temperature and improve their efficiency. Further description and visual illustration of the conducted experimental studies can be found in **Table 2.4**.

Table 2.4 Description of the experimental studies regarding DPECs

Study	Cooler type	Channel L×H (cm)	Channel gap (cm)	Plate thickness (cm)	Inlet air property	Manufactured unit
(Riangvilaikul and Kumar, 2010b)	Flat-plate DPEC, counter-flow	120×8	0.5	0.05	T= 25–45 °C, = 9.6–26.4 (g/kg), u= 2.4 (m/s), AR= 0.33	
(Duan et al., 2016b)	Flat-plate REC, counter-flow	90×31.4	0.6	0.025	T= 22.7–38.9 °C, T _{wb} = 8.8 19.8 °C, u= 0.75 2.83 (m/s), AR= 0.1–0.7	
(Xu et al., 2017)	Corrugated-plate DPEC, counter-flow	100×80	0.28×1.16 (corrugated wave)		T= 26–37.8 °C, = 8.8 19.8 (g/kg), V= 750 (m ³ /h), AR= 0.44	

2.3.3 Theoretical and Experimental Studies

The studies that gather theoretical research aided by the experimental validation plays a remarkable role in scientific investigations and provides a valuable understanding for cause-and-effect relationship. Additionally, through the designed experiments under a controlled lab environment by the aid of air handling units, a deeper understanding of the causality for different factors effecting study outcomes can be acquired. The key significance of such approach can be explained further:

- (1) **Causality comprehending:** This approach allows the researcher to intentionally manipulate the effective parameters. In our case, it incorporates the manipulation of operational and geometrical variables and observe their impact on thermal and energy performance of the system.
- (2) **Control over effective parameters:** In this approach, the researcher has a high level of control over the experimentation variables, from which particular variables can be isolated and their influence can be evaluated. This level of control ensures the direct connection between the observed variation and manipulated parameters.
- (3) **Specific results:** This approach yields a precise and specific results by focusing on the parameter of interest and observing the outcomes when the researcher examined the designed prototype under a controlled lab experiment.
- (4) **Cause-and-effect identification:** By testing the hypothesis, the relationship between the cause-and-effect is made possible and can be identified. This approach grants a foundation for parametric analysis and exploration.
- (5) **Regional assessment:** The obtained results from this approach will apply to similar ideas and situations in real-life circumstances that contributes to evidence-based operations in different regional conditions.

(Pakari and Ghani, 2019) developed a one-dimensional and three-dimensional heat and mass transfer model for a flat-plate DPEC with counter-flow configuration. In order to validate the developed model, they build a physical model based on the optimum geometrical parameters obtained from the numerical simulation as shown in **Table 2.4**. The agreement between the developed 1-D and 3-D modes and the experimental data, with regard to the product air temperature, was 10% and 8.5%, respectively. Besides, they found that the product air temperature is 1.86% lower for 1-D model than 3-D model. However, the computational time was three times higher for 3-D model. In addition, Wan et al. (2018) developed two models to simulate a flat-plate DPEC. First, they formulated an $NTU-Le$ R model to calculate heat and mass transfer coefficients within exchanger. Then, a two-dimensional CFD model has been developed to simulate the heat and mass transfer process. Afterwards, they manufactured the DPEC prototype to validate the developed models. They reported that the developed models can obtain accurate results while simplifies the computational scheme.

Kashyap et al. (2022c) designed and constructed an evaporative cooler working in dual-modes: first, as DEC; and second, as a flat-plate REC. They carried out exergy and economic analysis for cooling seasons under the controlled lab climate condition of five different cities to examine the potential benefits of employing such a system in diverse climatic conditions. The selected cities were, Delhi, Brisbane, Brasilia, Shanghai, and Seoul. The obtained results regarding the exergy efficiency and annual operating cost for both operating modes are presented in **Fig. 2.12**. They stated that, the exergy efficiency is superior for REC than that of the DEC, and the running cost is higher for REC under all climate zones.

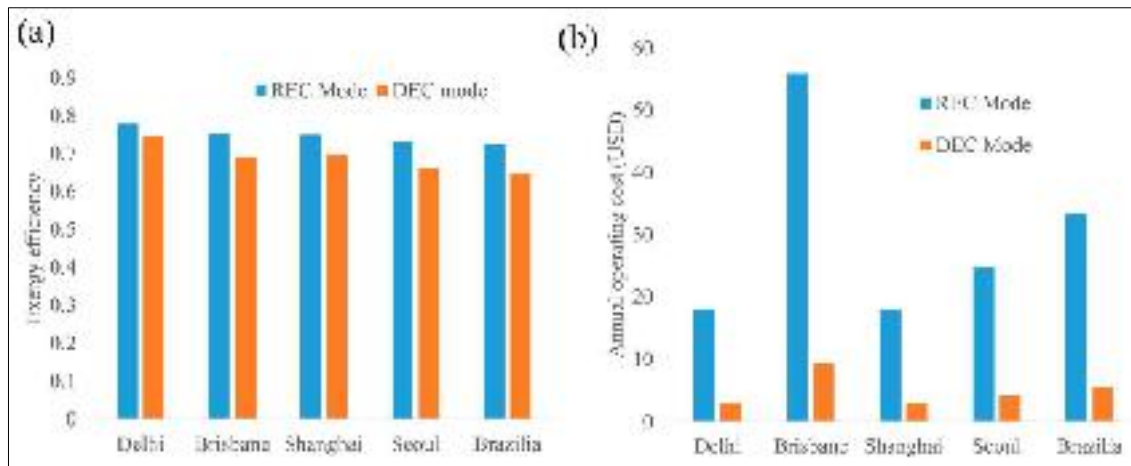


Fig. 2.12 Performance of the dual-mode evaporative cooler: (a) exergy efficiency; (b) annual operation cost (Kashyap et al., 2022c)

Kousar et al. (2022) carried out numerical and experimental analysis for counter- and cross-flow DPEC with flat-plate HMX under wide range of climate conditions (refer to **Table 2.4**). They utilized the experimental results for energy, exergy, environmental, and cost analysis. They found that, the highest and lowest exergy efficiency for cross- and counter-flow configurations were 52%, 21.58%, and 46%, 18.23%, respectively. Moreover, they reported that under low, medium, and high operating condition, the counter-flow arrangement consumed more water and electricity by 39% and 2.7%, 24.65% and 35%, 21.4%, and 38%, respectively.

The numerical/experimental approach has been adopted by many other researchers in their research studies. For instance, Sadighi Dizaji et al. (2020) conducted a sensitivity analysis of effective geometrical and operational parameters for multi-stage flat-plate M-cycle. Their analysis was based on the novel wet-surface theory. This theory enables the observation of the evaporative surface temperature alongside with the distribution of the temperature and humidity along the HMX's channels that will imitate the real working condition. Then the developed model was experimentally validated with respect to the manufactured test-rig. more details are shown in **Table 2.4**.

Table 2.5 Summary of the selected theoretical studies regarding the methodologies (Section 2.3)

Study	Nature of the work	Developed model	Numerical approach	Utilized software	Cooler configuration	Structural materials	Key finding
(Cui et al., 2015a)	Theoretical	2-D mathematical model	—	COMSOL Multiphysics	Hybrid Flat-plate DPEC, counter-flow	—	The proposed system can aid VCRS by reducing the cooling capacity by 47%.
(Pandelidis and Anisimov, 2015)	Theoretical	2-D mathematical model	Modified - NTU	—	Flat-plate M-cycle, cross-flow	Polyethylene & Cellulose fiber	They stated that uneven airflow inside wet-channels leads to reduction in cooling performance.
(Pandelidis et al., 2018)	Theoretical	4-D mathematical model	Runge-Kutta	Wolfram Mathematica	Hybrid Flat-plate M-cycle, cross-flow	—	They stated when using the exhaust air from conditioned space, the product air can be reduced by 3 K.
(Wan et al., 2018)	Theoretical & experimental	2-D mathematical model	NTU-Le R & CFD	COMSOL Multiphysics	Flat-plate DPEC, counter-flow	Polyethylene & fiber	They developed NTU-Le-R model and two dimensional CFD model that can predict the heat and mass transfer coefficients.
(Baakeem et al., 2019)	Theoretical	Steady-state energy and mass conservation model	—	MATLAB	Flat-plate DPEC, counter-flow	—	The DPEC is a suitable choice for Arab Gulf cities and can be considered as an alternative to VCRSs.
(Ghosh and Bhattacharya, 2021a)	Theoretical	—	—	Java	Flat-plate Hybrid REC, counter-flow	polypropylene Hilflow®	The proposed system can prevent the indoor air overheating and provide thermal comfort throughout the cooling seasons.
(Kashyap et al., 2022c)	Theoretical & Experimental	Steady-state energy and mass conservation model	Finite difference scheme	EES	Flat-plate REC, counter-flow & DEC	Aluminum & cotton	They concluded that, the exergy efficiency is superior for REC than that of the DEC, and the running cost is higher for REC.
(Zhu et al., 2023b)	Theoretical	3-D mathematical model	CFD	COMSOL Multiphysics	Flat-plate DPEC, counter-flow	Aluminum	Compared to 2-D models, the 3-D model improved the simulation accuracy by 5.46%

2.4 PERFORMANCE ENHANCEMENT OF DPECS

2.4.1 Enhancement Through Employed Materials

The core materials of heat and mass exchangers of dew point evaporative coolers have been investigated through many literatures. Due to insignificant effect of the plat material because of their super-thin profile (between 0.2 to 0.5 mm thickness in most studies) on heat transfer process, consequently, most research studies focused on examining wick materials (i.e., porous materials), due to their direct effect on the water dispersion and evaporation. Typically, there are two groups of porous materials, namely, craft papers, and fibers. The fibers are classified into three categories: (1) natural fibers (such as cellulose pad, aspen pad, and coconut pad), (2) polymer fibers (such as nylon fiber), and (3) fabric fibers (such as coolpass, topcool spandex, and bamboo charcoal with Coolmax active) (Lv et al., 2021). The wick materials have a crucial effect on the cooler performance as it contributes to the absorption, diffusion, and evaporation rates of water. These three merits are remarkably indicating the heat and mass transfer process inside the working channels.

Pandelidis et al. (2021) experimentally examined eight different types of porous materials, including the synthetic and natural fibers, to be used as evaporative surface as shown in **Fig. 2.13**. They observed that, when compared to the natural fibers, the synthetic fibers are more capable of water distribution rate. Among the adopted materials, the basalt paper-like synthetic fiber had the highest dispersion capability that was able to vertically elevate the water to 40 cm by the capillary effect. Besides they stated that the synthetic fibers are more durable than the natural fibers. Moreover, several more different types of fabrics weaved from different fibers have been investigated and compared to the craft paper in term of absorption capability, evaporation rate, and diffusion rate by (Xu et al., 2016). They reported that, in comparison to the craft paper,

some of the adopted fibers had 171-182% more absorption capability, 77-93% more evaporation rate, and 298-396% more diffusion rate.

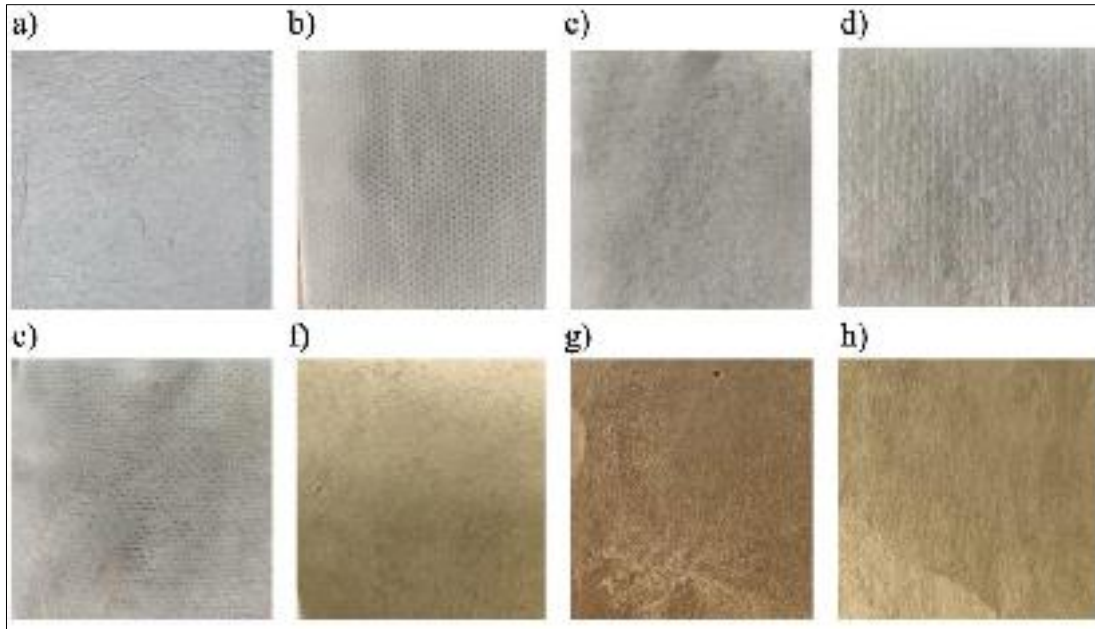


Fig. 2.13 Surfaces of the porous materials: (a) basalt paper- like synthetic fiber; (b) synthetic surfactant non-woven; (c) 50% cotton fiber, 30% viscose, 20% polyester; (d) 100% cotton; (e) hydrophilic drainage textile; (f) resin treated kraft paper; (g) rigid kraft paper; (h) original kraft paper (Pandelidis et al., 2021)

More materials have been investigated by other literatures as a potential to be used for evaporative surfaces (Boukhanouf et al., 2014; Y. Chen et al., 2021a; Guilizzoni et al., 2019; Jradi and Riffat, 2016; Min et al., 2021). They used the same experiment-procedure to test the proposed porous materials. One experiment set-up is illustrated in **Fig. 2.14**.

On the other hand, a different approach has been carried out by (Zhao et al., 2008) from which, alongside with fibers, they investigated metals to be used as evaporative media. In this regard, as recommended by Schulz et al. (2005), a wick (whiskers, meshes, sintered, or grooves) are structured on the surface of the metal plate (aluminum and copper). A sample of the whisker-attained

refined surface of copper tube is shown in **Fig. 2.15**. Thus, the wick-attained metals are compared to the fibers, ceramics, zeolite, and carbon on the bases of water holding ability, durability, water-proof coating, and cost. They found that the wick-attained metals are the most adequate material over other adopted materials and the wick-attained aluminum plates are cheaper than the wick-attained copper tubes. From the conducted tests, for all the adopted materials, they observed that the evaporation rate was in the range of 0.57-0.58 l/m²·h and the heat transfer rate was in the range of 392-399 W/m².

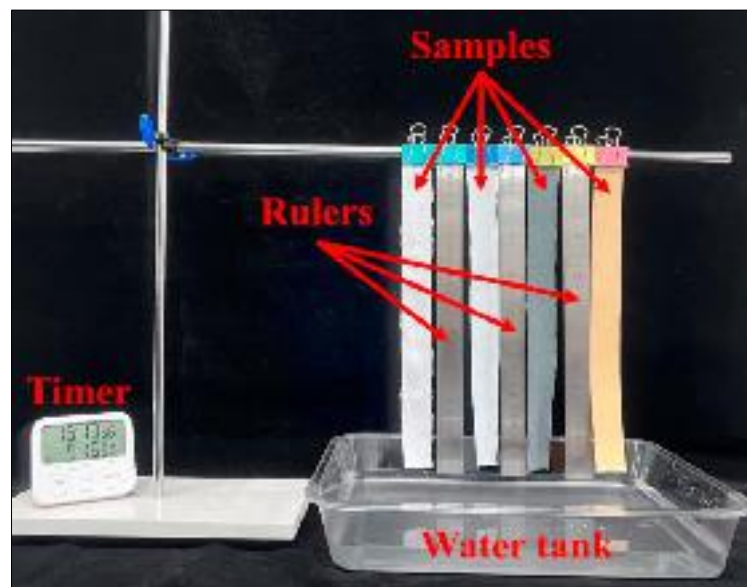


Fig. 2.14 The test bench for porous materials inspection (Cui et al., 2023)



Fig. 2.15 Microstructure whisker-attained copper tube (Schulz et al., 2005)

2.4.2 Enhancement Through Water Spraying System

One of the key factors to the heat and mass transfer process inside the wet-channel is the wettability of the evaporative surface (wick material). The water spray system has a significant role regarding this matter. Many efforts have been made to enhance the uneven water distribution by the evaporative surface. Conducted literatures focused on investigating different materials for better diffusion and evaporation of water (as discussed in **Section 2.4.1**) and optimizing water spraying mechanism. Most of the studies regarding this matter have implemented experimental approach. Throughout the experimentations, different types of water spraying mechanisms were utilized as shown in **Fig. 2.16**.

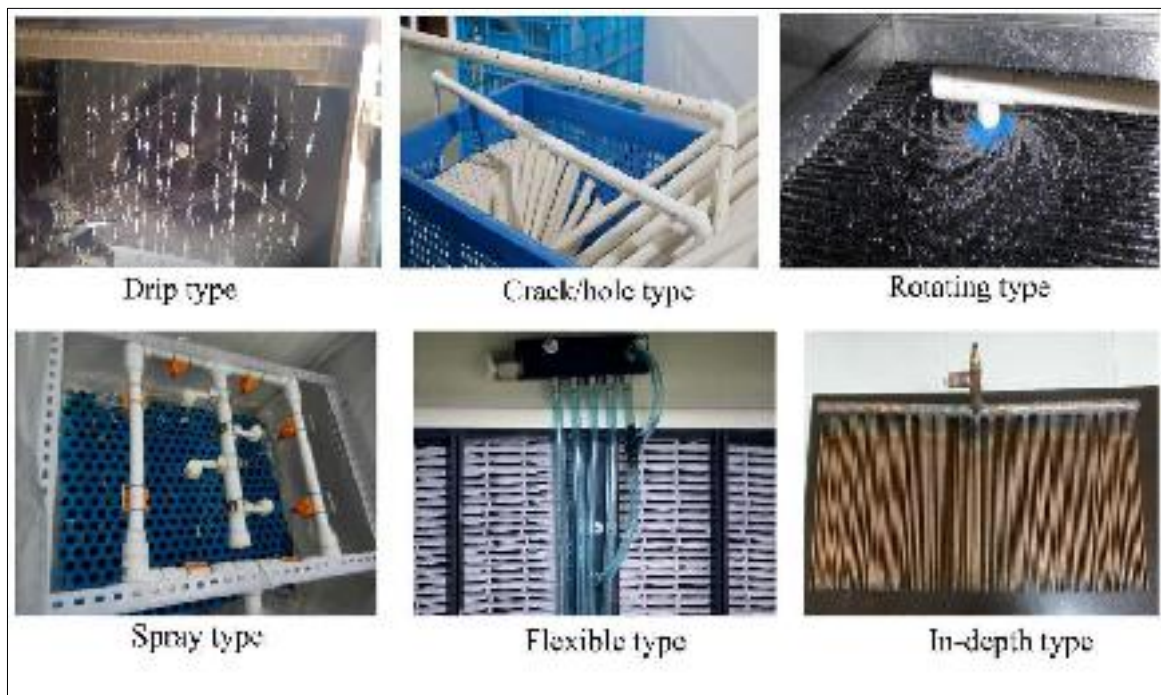


Fig. 2.16 Available water spraying mechanisms for evaporative cooling (Sun et al., 2020a)

De Antonellis et al. (2019) experimentally investigated six air-water flow configurations with different water nozzle arrangement focusing on limiting the

water consumption issue. They designed the water to working channel airflow ratio to be ranged between 1.4-4%. The results showed that a wet-bulb effectiveness as high as 82-84% can be obtained with the horizontal and top plate orientation with water flowing at top. Al-Zubaydi and Hong (2019) employed three water spraying modes (external, internal, and mixed) and analyzed their effect on six types of the water spraying configuration on three cooler's performances. They evaluated the cooler's performance based on the wet-bulb efficiency, COP, and cooling capacity. They found that the cooler had the best performance with mixed water spray mode, and with the internal mode the cooler performed better when compared to the external mode as depicted in Fig. 2.17.

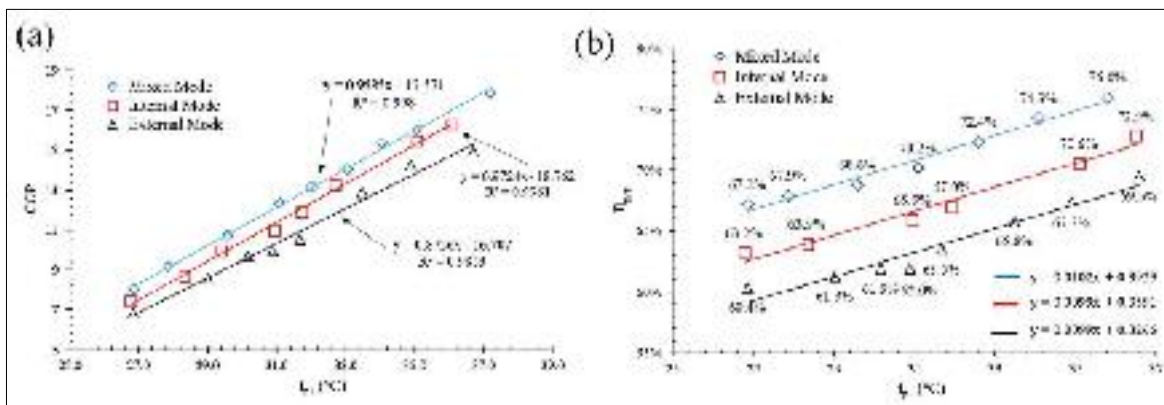


Fig. 2.17 Performance of the system under different water spraying modes: (a) COP; (b) wet-bulb effectiveness (Al-Zubaydi and Hong, 2019)

Lin et al., (2018b) experimentally studied the water spray effect for two plate orientations (horizontal and vertical). In this regard, they showed the water temperature distribution for each test. During the investigation, they noted that when the water is rapidly applied to the evaporative surfaces, the temperature distribution along the evaporative surface is disrupted and needed longer time to reach the steady state.

Generally, in theoretical studies, the evaporative surfaces are assumed to be fully saturated. Yet this condition is hard to achieve in practical applications for DPECs. Therefore, many researchers tried to design an effective water spraying system to obtain higher performance and reduce deviation between the numerical and experimental data. However, with regard to theoretical investigations, Lacour et al. (2018) and Montazeri et al. (2015) developed a 3-D CFD model and identified the water particles size to observe their behavior and impact inside evaporative cooling devices.

On the other hand, many researchers used intermittent water supply to reduce the water flowrate. This approach yields power saving by water pump and improved cooling performance (Golizadeh Akhlaghi et al., 2020; Ma et al., 2023; Shi et al., 2022b; Wang et al., 2017). During the intermittent water supply, the fully wetted evaporative surface can be achieved via the capillary motion of water. This mechanism avoids the issues like unsteady water flow, formulation of unnecessary thick water layer, flow resistance to heat transfer between primary and working channels airflow, and continuous energy consumption (Y. Chen et al., 2021b).

Sun et al. (2020b) examined five different nozzles under the influence of intermittent and continuous water spraying modes. Different water spraying nozzles were utilized, such as spiral, conical, square, sector, and target types as shown in **Fig. 2.18**. They conducted a series of experimentations to indicate a nozzle type with lower water consumption and higher wet-bulb effectiveness. They were able to achieve lower water consumption by balancing between the amount of water flowing on the evaporative surface and the rate of evaporation for each individual experiments. The amount of water flowing was based on the water consumption rate by the cooler under the specified boundary conditions. They recommended the spiral type nozzle due to its acceptance water spraying rate, wide area coverage, and good uniformity.

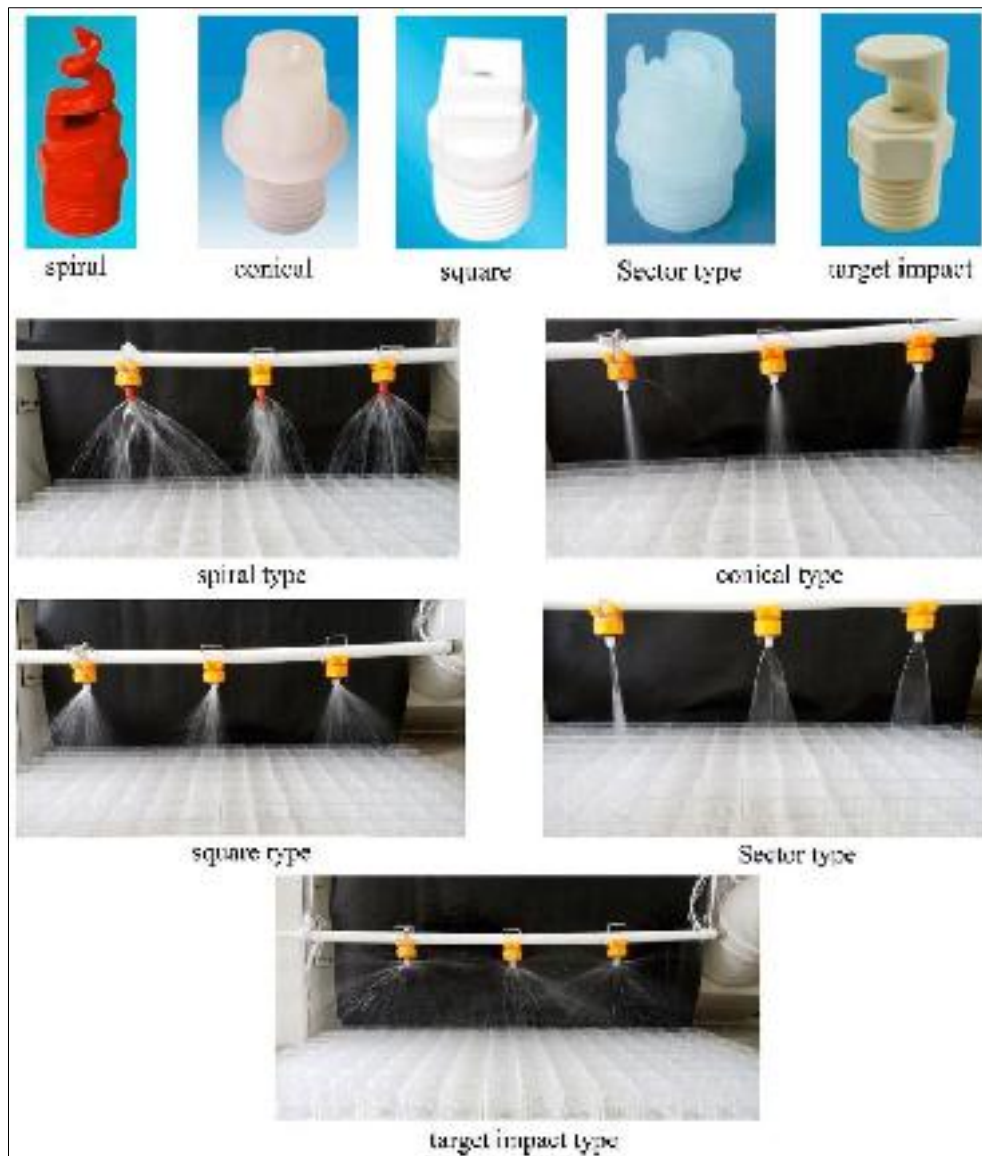


Fig. 2.18 Nozzle types and their water spraying behavior (Sun et al., 2020a)

2.4.3 Performance Evaluation Criteria

To evaluate and indicate the thermal, energy, and exergy performance of the DPEC, the globally accepted standards from American Society of Heating, Refrigeration, and Air-conditioning Engineers (ASHRAE) are considered as the most comprehensive and accurate criterias to be adopted for assessing and testing the cooling systems. In particular, ANSI/ASHRAE Standard 143 (2015) and ANSI/ASHRAE Standard 55 (2017) provides precise measurement procedures and

guided practices under a controlled laboratory environment for testing IECs. Thus, the following key performance parameters have been adopted to rate and evaluate the performance of the proposed DPEC.

2.4.3.1 Temperature Drop

This parameter indicates the temperature difference between the inlet air and product air. At first glance, it is a substantial parameter to indicate the thermal performance of the system that provides how much the cooler has reduced the temperature of inlet air. Furthermore, it is considered as a base parameter from which other performance evaluation parameters will be calculated.

2.4.3.2 Wet-Bulb and Dew-Point Effectiveness

The cooling efficiency of DPEC depends on wet-bulb and dew-point effectiveness. The wet-bulb effectiveness is responsible for indicating how much the product air dry bulb temperature is approaching or exceeding the wet bulb temperature of ambient air that can be expressed as

$$= (t_{db,2} - t_{wb,1}) / (t_{db,1} - t_{wb,1}) \quad (2.1)$$

where,

ϵ : is the wet-bulb effectiveness;

$t_{db,1}$: is the dry bulb temperature of inlet/ambient air, °C;

$t_{db,2}$: is the dry bulb temperature of outlet/product air, °C;

$t_{wb,1}$: is the wet bulb temperature of inlet/ambient air, °C.

In the meanwhile, the dew-point effectiveness is a demonstration of the cooler's thermal effectiveness in terms of dew point depression that indicates

how much the product air dry bulb temperature is approaching the dew point temperature of the inlet air which can be expressed as

$$= (t_{d,p} - t_{d,i}) / (t_{d,i} - t_{d,a}) \quad (2.2)$$

where,

ϵ : is the dew-point effectiveness;

$t_{d,i}$: is the dew point temperature of inlet/ambient air, °C.

2.4.3.3 Cooling Potential/Capacity

In a DPECs, the cooling potential or cooling capacity is pertinent to the sensible heat loss of primary air inside primary channels. Therefore, it is a function of temperature drop of the primary air flow that can be demonstrated as follows

$$= \dot{Q}_{c,p} \cdot (1 - \epsilon) \cdot \dot{m}_p \cdot (t_{p,i} - t_{p,o}) \quad (2.3)$$

where,

$\dot{Q}_{c,p}$: is the cooling potential of the HMX, kW;

\dot{m}_p : is the mass flowrate of the primary air, kg/s;

ϵ : is the working to primary air ratio;

$c_{p,p}$; is the specific heat of primary airflow at constant pressure, (kJ/kg·K);

$t_{p,i}$: is the temperature of inlet air, °C;

$t_{p,o}$: is the temperature of product air, °C.

2.4.3.4 Energy Efficiency

Energy efficiency or coefficient of performance is a common evaluation metric for air-conditioning systems. It is a ratio of cooling potential of the

system to the total electrical power consumed by the cooler. For DPECs, it can be expressed as

$$= \frac{P_{fan} + P_{pump}}{\eta} \quad (2.4)$$

where,

η : is the energy efficiency;

P_{fan} : is the electrical power consumed by the fan, kW;

P_{pump} : is the electrical power consumed by the water pump, kW.

The electrical power required by the fan and pump are highly contributed by the pressure drops occurred as a result of fluid flow inside the pipes (friction/major resistance) and fluid flow inside the components (local/minor resistance) that can be expressed as

$$P_{total} = P_{major} + P_{minor} \quad (2.5)$$

$$= (0.5 \cdot \rho \cdot L \cdot v^2 \cdot \lambda^{-1}) + (0.5 \cdot \rho \cdot v^2 \cdot \sum K) \quad (2.6)$$

where,

P_{total} : is the total pressure drop, kPa;

P_{major} : is the major pressure loss, kPa;

P_{minor} : is the minor pressure loss, kPa;

λ : is the Darcy-Weisbach friction factor;

L : is the length, m;

ρ : is the density, kg/m³;

v : is the fluid flow velocity, m/s;

D_h : is the hydraulic diameter, m;

$\sum K$: is the local loss coefficient.

2.4.3.5 Water Evaporation Rate

The evaporation of water is the driving force of the heat and mass transfer inside the HMX of DPEC. The water evaporation take place when the water molecules absorb the heat from their surroundings and discharge into the working air through latent heat transfer, by which, the humidity ratio of the working air increases. It can be calculated by the following equation

$$= \dots \cdot \dots \cdot \dots \cdot (\dots - \dots) \quad (2.7)$$

where,

- : is the water evaporation rate, kg/s;
- : is the convective mass transfer coefficient of working channel air, m/s;
- : is the wettability factor of wet surface;
- : is the surface area of water surface, m²;
- : is the density of working air, kg/m³;
- : is the humidity ratio at air-water interface, kg/kg;
- : is the humidity ratio of working airflow, kg/kg;

2.4.3.6 Exergy Efficiency and Entropy Generation Rate

The exergy analysis is considered as the essence of second law of thermodynamics analysis from which it can be identified how much exergy the system can harness from the total exergy available. Whereas the entropy generation rate by the system indicates how much the system approaches the irreversibility, they can be expressed as

$$= \text{---} \quad (2.8)$$

$$= \frac{\text{---}}{0} \quad (2.9)$$

where,

η : is the exergy efficiency;

\dot{E}_{out} : is the total output exergy, kW;

\dot{E}_{in} : is the total input exergy, kW;

\dot{S}_{gen} : is the entropy generation rate, kW/K;

\dot{E}_{D} : is the exergy destruction, kW;

T_0 : is the dead state temperature, °C.

2.5 APPLICATIONS OF DEW POINT EVAPORATIVE COOLERS

2.5.1 Applications of DPEC with Solar Panel Systems

The generated heat from the solar photovoltaic (PV) panels are the leftover heats from the received solar radiation photons that did not transformed into electrical energy. This excess heat critically reduces the energy transformation process by the PV cells and reduces the panel's efficiency. Therefore, it is substantial to cool down the PV panels. There are several methods for cooling off the solar PV collectors, such as: (a) thermoelectric coolers, (2) phase change materials, (3) evaporative cooling, (4) fins-aided air-cooling channels, and (5) closed-loop underground cooling.

Regarding the evaporative cooling approach, it can be carried out through three essential evaporative technologies, namely, the direct evaporative cooling (DEC), indirect evaporative cooling (IEC), and dew point evaporative cooling (DPEC). The DPEC is considered as the most significant choice for cooling of the PV panels and improving their energy conversion efficiency due to its high thermal and energy efficiency that can produce the lowest product air temperature compared to other evaporative cooling types.

Table 2.8 Summary of the selected studies regarding performance enhancement of DPECs (Section 2.4)

Study	Nature of the work	Enhancement method	Employed materials	Water distribution mechanism	Key findings
(Zhao et al., 2008)	Experimental	wick (whiskers, meshes, sintered, or grooves) are structured on the surface of the metal plate and compared to other materials on the bases of water holding ability, durability, water-proof coating, and cost.	fibers, ceramics, zeolite, carbon, copper, aluminum	Downward flowing	They found that the wick-attained metals are the most adequate material over other adopted materials and the wick-attained aluminum plates are cheaper than the wick-attained copper
(Xu et al., 2016)	Experimental	On the bases of absorption capability, evaporation rate, and diffusion rate, several types of fabrics weaved from different fibers have been investigated and compared to the craft paper.	They used seven types of fabrics and craft paper for the purpose of experimentation	Capillary motion	They stated that, in comparison to the craft paper, some of the adopted fibers had 171-182% more absorption capability, 77-93% more evaporation rate, and 298-396% more diffusion rate.
(Al-Zubaydi and Hong, 2019)	Experimental	analyzed the effect of three water spraying modes on six types of the water spraying configuration on three cooler's performances.	PVC plastic	Downward flowing	They cooler had the best performance with mixed water spry mode, and it performed better with internal mode than the external mode
(De Antonellis et al., 2019)	Experimental	Investigated six air-water flow configurations with water nozzle arrangement in view of reducing the water consumption issue	Aluminum alloy	Downward flowing	It was found that, with water flowing at top, a wet-bulb effectiveness as high as 82-84% can be obtained with the horizontal and top plate orientation
(Sun et al., 2020a)	Experimental	investigated five different nozzles under the influence of intermittent and continuous water spraying modes.	porous ceramics	Downward flowing	The spiral type nozzle had the best capability for water volume flowrate, wide area coverage, and good uniformity.
(Pandelidis et al., 2021)	Experimental	Investigated eight different materials to be used as the evaporative surface for evaporative air coolers.	Eight types of synthetic and natural materials	Capillary motion	They found that, when compared to the natural fibers, the synthetic fibers are more capable of water distribution rate. The basalt paper-like synthetic fiber had the highest dispersion capability.

Moreover, occasionally there is another application when integrating the photovoltaic/thermal (PV/T) collector with desiccant wheel integrated DPEC which is used to improve the in-door air quality when this configuration is operated under humid climates. These methods come with passive and active cooling techniques. The passive cooling method uses natural convection and conduction heat transfer process to dissipate the generated heat into the environment, while active cooling method dispose that heat using forced circulating coolants, such as water, air, or nanofluids (Kozak-Jagięła et al., 2023; Reddy et al., 2015; Zhang et al., 2020).

However, the active cooling is more advantageous due to the potential of harnessing this excess heat and utilizing it for other applications. Such applications include the domestic hot water production (Habchi et al., 2024; Hazi et al., 2014; Mi et al., 2020), heat recovery ventilation for domestic and industrial processes under a particular weather condition (Choi et al., 2023; Irshad et al., 2024; Sarvar-Ardeh et al., 2024), and desalination of seawater to produce tap and clean water (He et al., 2023; Isah et al., 2024; Ravajiri et al., 2024).

This section focuses on the configurations integrating DPEC with solar PV panels, and brings all the outcome aspects from such a performance elevating hybrid system. Many configurations and approaches have been adopted for this regard. Yang et al. (2024) developed a flat-plate DPEC integrated PV panel with two working channels, one is located in the DPEC that can produce a product air temperature lower than the wet-bulb temperature of ambient air, and the other one is located at the bottom of the solar panel as shown in **Fig. 2.19**. They compared the performance of the proposed configuration to previous configurations and noticed 16.4% improvement in the performance of the PV panel efficiency when simulated under two summer weather conditions.

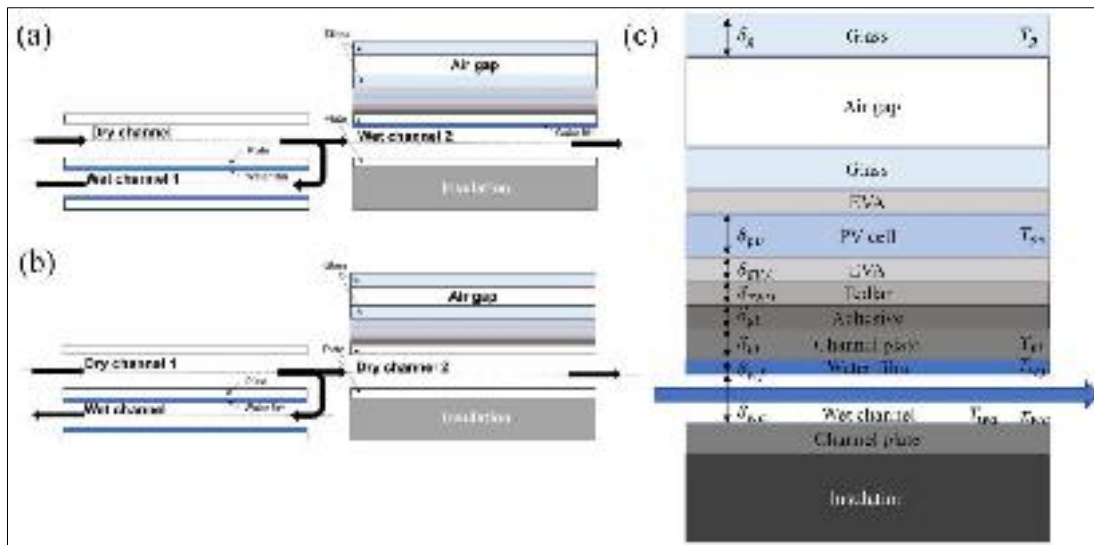


Fig. 2.19 (a) Proposed configuration; (b) conventional configuration; (c) Schematic diagram of PV panel layer (Yang et al., 2024)

Song and Sobhani (2020) investigated the transient performance of flat-plate M-cycle integrated solar desiccants air cooling system with phase change material (PCM) as illustrated in **Fig. 2.20**. The PV/T collector employed to provide the required heat at daytime, while during the nighttime, the PCM thermal energy storage utilized in this regard.

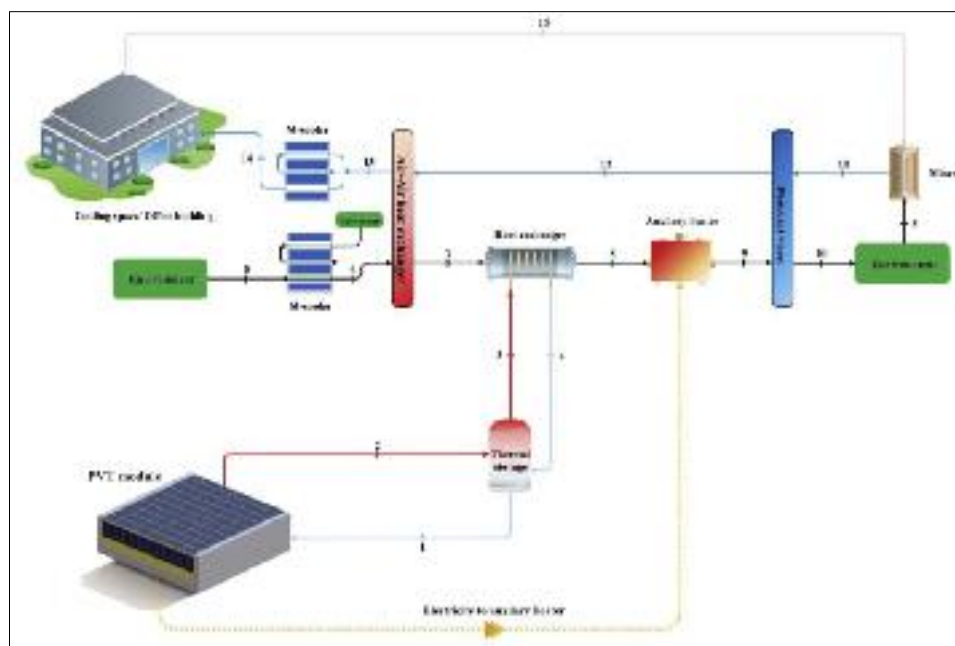


Fig. 2.20 Solar desiccant air-conditioning (Song and Sobhani, 2020)

The required heat is the essence of the desiccant wheel (DW) operation that function as the air dehumidifier to enhance the thermal performance of DPEC. The proposed system has been investigated under hot and humid climate condition for a small office building for five cooling months (from June to October). Afterwards, the performance of the M-cycle investigated with respect to in-door air thermal comfort acquisition. They found that the total COP obtained from the proposed system was 0.404. In addition, they concluded that the utilization of PCM can increase the overall efficiency of the system.

Similarly, Wang et al. (2020) utilized the same configuration as Song and Sobhani (2020), this time they added a humidification-dehumidification desalination unit (HDDU) to the configuration benefited from the waste heat from the desiccant wheel for the purpose of freshwater production from seawater. Both studies added a PCM material to the PV/T collector which is located beneath the panel to store heat at daytime and restoring it at nighttime simultaneously with the stored heat in the thermal storage tank (**Fig. 2.21**).

The hybrid PV/T based DPEC has been adopted by many literatures as effective air-conditioning system to bring thermal comfort in high humidity weather condition regions (Buker and Riffat, 2016a; Harrouz et al., 2021). Furthermore, many literatures potentially cooled the solar PV panel through direct evaporation method using water spray mechanisms by sparkling the ejected water on top of the PV panel via different types of nozzles due to simplicity and low cost of this cooling method (Benato et al., 2021; Mahdi and Ali Aljubury, 2021; Nateqi et al., 2021). Regarding the passive cooling method, Žižak et al. (2022) experimentally investigated the potential of using passive evaporative cooling for PV solar collector under various weather conditions of eight cities as illustrated in **Fig. 2.22**. The experiments reported that about 20.1°C reduction and 9.6% increase in both PV peak temperature a electricity generation could be achieved with the proposed cooling method.

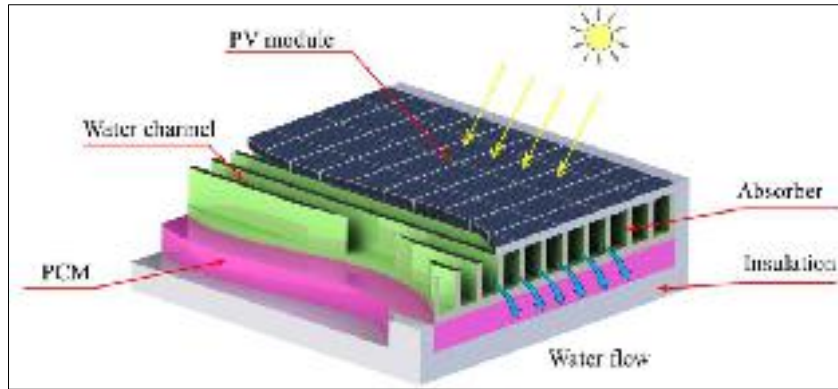


Fig. 2.21 Schematic diagram of PV/T-PCM solar collector (Wang et al., 2020)

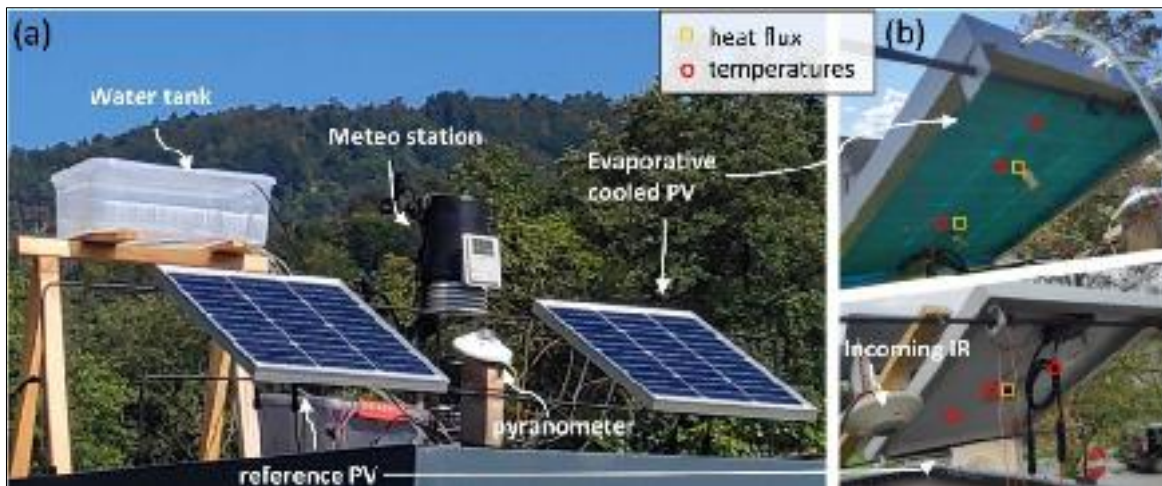


Fig. 2.22 (a) Experimental setup: (b) Back-view (Žižak et al., 2022)

2.5.2 Applications of DPEC with VCRS Systems

The intensive power consumption of VCRS systems is the greatest downside of such system. Consequently, this type of air-conditioning system possesses the significantly low energy efficiency ratio (COP) compared to the evaporative based air-conditioning systems in general. Several factors affecting the degradation of this COP, such as sub-cooling and superheating of the working fluid, compressor efficiency, refrigerant type, and discharge and suction pressures. The efficiency of VCRS systems can be notably increased through the improvement of the above-mentioned factors. Operating this

They pre-cooled the ambient fresh air first in the DPEC before entering the VCRS system in order to produce a desired supply air under a wide range of climate conditions. It was found that the proposed configuration was able to achieve 192.31 kWh of average net monthly power consumption when operated under hot and dry climate, while the amount of saving reduced to 124.38 kWh for hot and moderate humid climate. Similarly, Zanchini and Naldi (2019) combined a flat-plate M-cycle with VCRS system (refer to **Fig. 2.24**) to provide a thermal comfort for an office building during July and August in north Italy. The simulation conducted for hourly energy consumption, dehumidifying, and ventilation. They proposed two air flow management configurations for the cycle and compared them to the traditional cycle. In the first configuration, they employed the out-door air to be pre-cooled in the M-cycle, while in the second configuration, they employed the recirculated air from conditioned space to be pre-cooled in the M-cycle. They found that the second configuration reduced the total energy consumption by 38%.

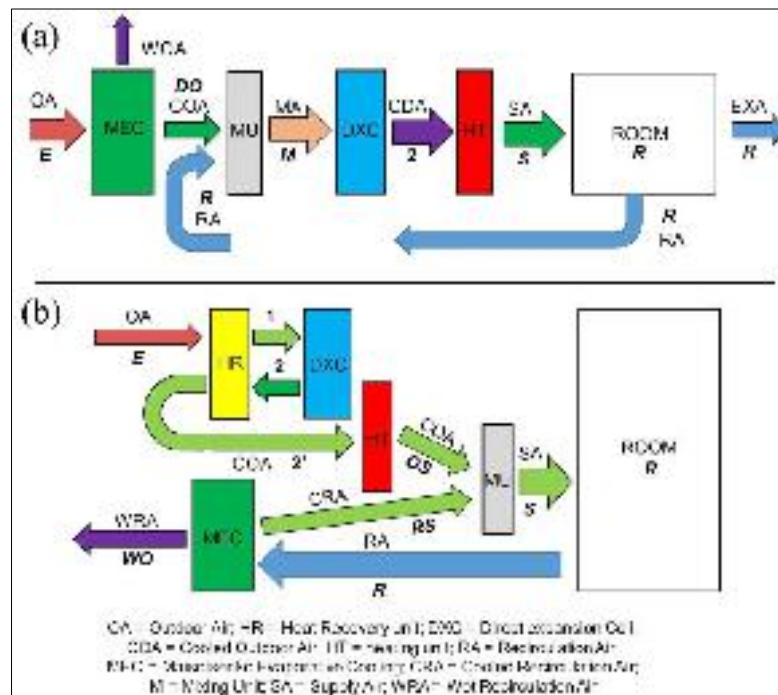


Fig. 2.24 (a) First air-conditioning cycle; (b) Second air-conditioning cycle (Zanchini and Naldi, 2019)

Similar approach has been adopted by other researchers in the light of providing energy saving, performance improvement, and indoor thermal comfort condition (Chen et al., 2022; Q. Chen et al., 2021; Cui et al., 2015b; Duan et al., 2019).

2.5.3 Applications of DPEC with Desiccant Wheel

The application of DPEC combined with desiccant wheel is usually used for regions with hot and humid climate condition. This type of combination has a broad implementation due to its efficient ability to remove the moisture from ambient air and reducing its dew-point temperature significantly as the dew-point temperature is the most effective key parameter for DPEC systems. The desiccants are hygroscopic materials capable of absorbing and releasing the moisture when exposed to the air. In general, there are two types of desiccant materials, namely, liquid desiccants (such as, lithium chloride solution, calcium chloride solution, and ionic liquid) and solid desiccants (such as, metal-organic framework, zeolite, and silica gel). On the bases of their application in air-conditioning systems, they are available as: liquid-desiccant dehumidifiers (LDD), and solid-desiccant dehumidifiers (SDD).

Olmur et al. (2023) assessed the performance of an off-grid sustainable solid desiccant air-conditioning system for a building under the weather condition of Adana, Turkey. In their proposed configuration, they used solid desiccant wheel to dehumidify the flowing air prior to the flat-plate DPEC and the required heat and electrical energy of the cycle were provided by a water-cooled PV/T system as illustrated in **Fig. 2.25**. They stated that the electrical, thermal, and total COP were respectively 4.09, 0.46, and 0.42. Besides, the net energy consumption for the cooling season was computed to be -102.82 kWh, the negative sign indicates the self-energized sustainable cycle.

Zhou (2021) studied the potential of flat-plate DPEC that integrated with solar-driven DW and compared the results with the conventional VCRS systems. They investigated the thermal and energy performance of such a system to provide cooling and heating demand for a building under the climate condition of three cities of Australia with tropical, subtropical, and temperature climate conditions. The results indicated that, under the tropical weather climate, the cycle could not achieve 28.36% of cooling and heating demands, while it could achieve 98% of such demands when the cycle operated under subtropical and temperature weather climates. Ghosh and Bhattacharya (2021b) Carried out design methodology and thermal analysis of flat-plate DPEC assisted by LDD under hot and humid climate. They set the indoor design temperature to about 25 °C based on ASHRAE Standard 55-2017 (2020) recommendation. It was reported that the thermal COP of the cycle varied between 0.32 to 0.96 for a year-round operating period.

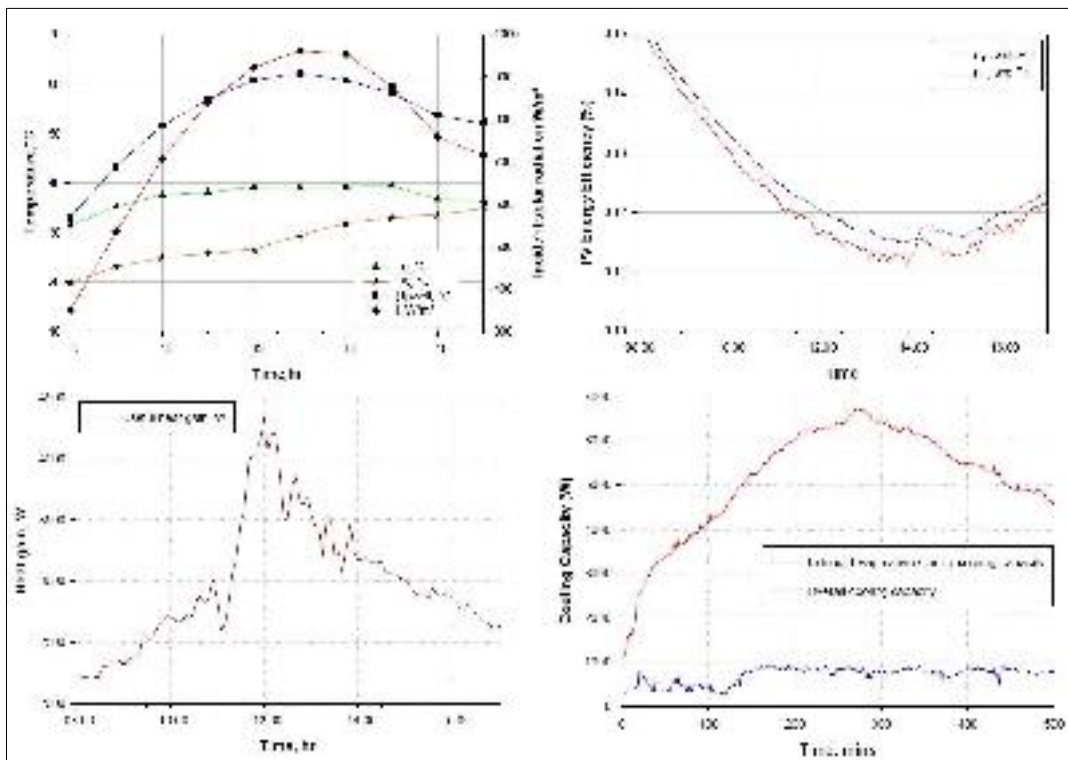


Fig. 2.27 Hourly variation of obtained results (Buker and Riffat, 2016b)

Many researchers adopted the similar idea of desiccant wheel assisted flat-plate DPEC through various airflow configurations, equipment placements, and integrated devices in the light of improving the thermal and energy performance and maintaining the indoor thermal comfort under a wide range of regional climates (Chen et al., 2018; Delfani and Karami, 2020; Elsarrag et al., 2016; Lai et al., 2022; Pandelidis et al., 2020b, 2016; Woods and Kozubal, 2013).

One study (Lai et al., 2022) considered freshwater production alongside with cooling process by adding humidification-dehumidification desalination unit (HDDU) to the flat-plate M-cycle integrated SDD air-conditioning cycle under three air circulation modes: ventilation, half-circulation, and re-circulation. The exhaust air from the M-cycle has been used by the HDDU to improve the water generation. From the conducted simulations they found that the water production rates were similar for all air circulation modes of around 52 kg/h. on the other hand, the recirculation mode showed the best cooling performance of 7.91 kW which could maintain the temperature of the supply air lower than 20.85 °C. More details about the selected studies in this regarding can be found in **Table 2.7**.

Table 2.9 Summary of the selected studies regarding the hybrid DPECs (Section 2.5)

Study	Nature of the work	Integrated modules	Region	Weather condition	Key finding
(Woods and Kozubal, 2013)	Theoretical & experimental	DPEC+DEC+LDD		Hot-humid, hot-dry, moderate-humid	They presented numerical modelling and experimental testing of two stage desiccant enhanced DPEC with 8 independent variables. They proposed a future installation for the system to study the energy saving potential.
(Buker and Riffat, 2016b)	Theoretical & experimental	DPEC+LDD+HX+TES+DEC+PV/T		Hot-humid	A prototype of the proposed configuration was fabricated and tested. They analyzed the electrical and heat generation from the PVT. The proposed cycle can deliver 5 kW of cooling and 3 kW of heating.
(Chauhan and Rajput, 2016)	Theoretical	DPEC+VCRS		Hot and dry, hot and moderate humid	It was found that, when the proposed cycle operated at 46 °C and 6 g/kg specific humidity, the maximum net monthly power saving was 240.28 kW h indicating 7.2 years of payback period.
(Chen et al., 2018)	Theoretical	REC+CT+LDD+TES+HX+PV/T		Hot-humid	For each unit, they internally calculated the heat and mass transfer and concluded that the required energy for the cycle can be saved by 22.4-53.2% under various air conditions.
(Duan et al., 2019)	Theoretical	DPEC+VCRS	Beijing, China	Hot-humid	It was stated that combined DPEC with VCRS able to save energy by up to 38.2%. They developing a dynamic model based on Energy Plus for the hybrid system.
(Zanchini and Naldi, 2019)	Theoretical	M-cycle+VCRS+HX	Milan, Italy	Hot-humid	They conducted hourly energy consumption, dehumidification, and ventilation using two different airflow configurations. They were able to save up to 38% of energy consumption.

(Song and Sobhani, 2020)	Theoretical	M-cycle+PV/T+DW+TES+heater+HX	Bandar Abbas, Iran	Hot-humid	They used integrated PV/T-TES to provide the heat for DW during daytime and nighttime to improve the supply air quality from the M-cycle. The total obtained COP was 0.404.
(Wang et al., 2020)	Theoretical	M-cycle+PV/T+DW+TES+heater+HX+HDDU	Bandar Abbas, Iran	Hot-humid	They used similar system as (Song and Sobhani, 2020) but this time they added HDDU to produce freshwater from seawater alongside with providing a thermal comfort.
(Ghosh and Bhattacharya, 2021b)	Theoretical	DPEC+ECT+LDD+HX	Kolkata, India	Hot-humid, moderate-humid	They proposed a desiccant assisted DPEC which can maintain the indoor thermal comfort specified by ASHRAE.
(Zhou, 2021)	Theoretical	DPEC+DW+GHC+TES+PV/T	Darwin; Brisbane; Melbourne, Australia	tropical, subtropical and temperate	The proposed solar-driven air-conditioning was able to deliver 98% of cooling and heating load under Brisbane and Melbourne climates, while it could not deliver 28.36% of such demand when operated under Darwin climate.
(Lai et al., 2022)	Theoretical	M-cycle+SDD+heater+HDDU		Hot-humid	By the insertion of HDDU into the SDD+M-cycle cycle, they were able to generate about 52 kg/h of freshwater alongside with 7.91 kW of cooling under hot-humid climate.
(Olmü et al., 2023)	Theoretical	DPEC+DEC+SDD+ PV/T	Adana, Turkey	Hot-humid	The proposed configuration was able to provide the required cooling for the building and electricity generation for the cycle.
(Yang et al., 2024)	Theoretical	DPEC+PV	Fukuoka, Japan		They cooled the PV panel directly by adding a DPEC to the bottom of the panel and noticed 16.4% improvement in the performance.

2.6 CHAPTER SUMMARY AND KEY FINDINGS

In this chapter, a comprehensive and detailed literature review has been carried out covering all the aspects studied by the researchers, such as technical aspects, methodology, performance enhancement, and DPEC's applications with other systems for various purposes. A detailed chart for all the aspects that have been investigated by the enormous number of literatures, which have been reviewed in this chapter, has been established and presented in Fig. 2.28. After a thorough review of the available literatures, it was indicated that majority of the researchers employed flat plate and corrugated plate type heat and mass exchangers. Consequently, a clear gap has been indicated and considered as the research gap for this PhD project. The current PhD work intends to achieve breakthroughs in cooling technologies and energy saving through introducing multiple innovations for the dew point evaporative cooler that haven't been addressed previously. Therefore, it is decided to conduct a deep-dive investigation into this headline by implementing the following objectives:

- (1) Proposing a novel shape for the DPEC that will improve the heat and mass transfer process and enhances the overall performance of the cooler. Further, it was aimed through employing a new geometry the fabrication of such a system made easy which was one of the biggest impediments for globalization of such a high-performance cooling system for years due to its complex design. For this reason, a shell and tube design DPEC has been proposed.
- (2) Developing an innovative water distribution system to distribute the water flow evenly over the tube bundle of the heat and mass exchanger. For this reason, cloth-sponge with perforated copper tubes have been proposed.
- (3) Employing a new material for the evaporative surface that possess effective water absorption and distribution characteristics. For this reason, a synthetic ultra-thin disposable tablecloth is proposed.

- (4) Establishing a dedicated numerical simulation scheme, first by formulating a mathematical model that can predict the complicated heat and mass transfer process in tandem within the HMX with least amount of assumption to elevate the model's accuracy. For this reason, the energy and mass balance equations will be employed and the governed differential equations will be discretized by the finite difference method with forward difference scheme inside the Engineering Equation Solver environment using newton iteration method.
- (5) Validating the acquired data from the numerical simulation against the experimental data to indicate the reliability of the numerical simulation with the view of deploying the dedicated numerical model for the future applications.
- (6) Assessing the performance of the proposed system under a wide range of operational and geometrical conditions so as to assess the cooler's performance and to identify the optimum geometrical sizes to be adopted for the manufacturing process of the system.

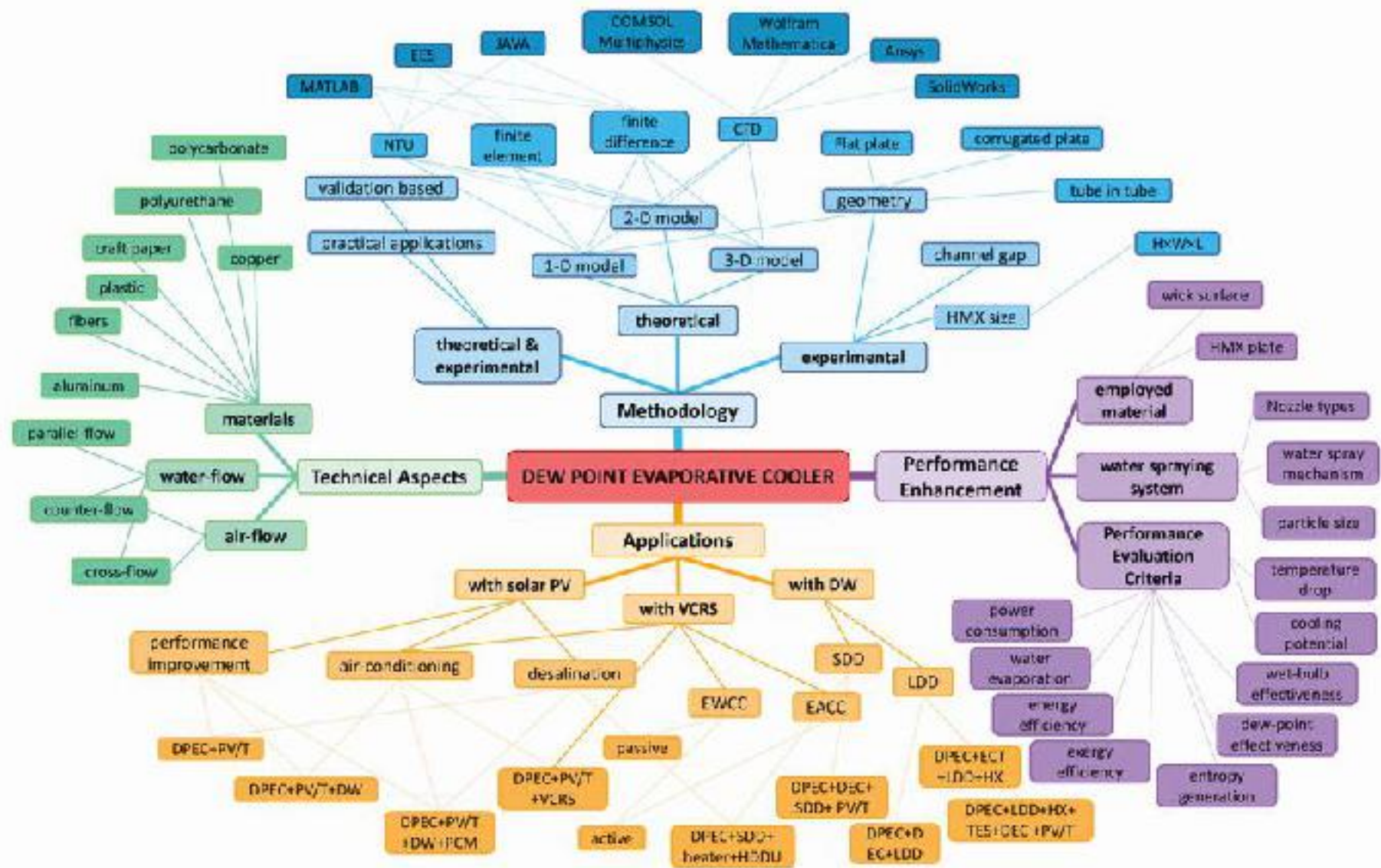


Fig. 2.28 Inclusive graphical chart for Chapter 2 regarding all the research aspects conducted on DPECs

CHAPTER 3

MATHEMATICAL MODELLING

3.1 INTRODUCTION

This chapter presents the inception for the geometry-development concept regarding the dew point evaporative cooler based on the intensive numerical investigation conducted with regard to the key performance parameters. **Fig. 3.1** shows the selection procedures for the best performing DPEC.

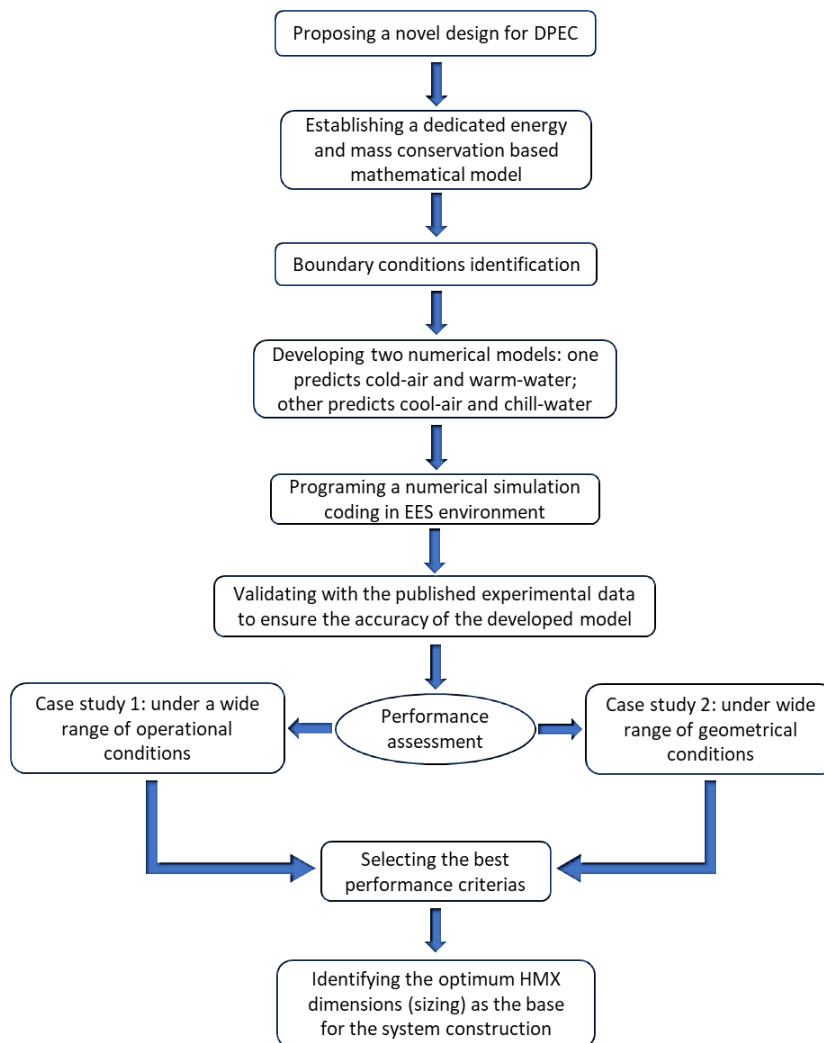


Fig. 3.1 Geometry selection procedure of novel DPEC

In addition, the following objectives will be carried out in this chapter:

- (1) A novel design for DPEC will be proposed, sketched, and compared to the conventional flat-plate type DPECs.
- (2) Describing the working principle of the physical models.
- (3) A robust mathematical model will be formulated based on the energy and mass balance equations.
- (4) Dedicated numerical model will be developed and computerized that enables the prediction of heat and mass transfer process within the HMXs.
- (5) The numerical model will be validated against the published experimental data so as to ensure the accuracy of the developed model.
- (6) A series of numerical simulations will be conducted so as to assess the performance of the proposed system under different operational conditions and geometrical configurations so as to identify the optimum dimensions for the novel DPEC which will be employed for the manufacturing of the system.

Moreover, the developed numerical simulation model should be able to carry out the following tasks:

- (I). Predicting cooler's thermal and energy performance.
- (II). Executing exergy, entropy, and sustainability analysis of the proposed DPEC.
- (III). Determining the optimum sizing for the proposed DPEC and finalizing the physical design of the HMX so as to be employed for the construction of the unit.

The results obtained from the numerical simulation will be double validated with the experimental data from the fabricated unit in **Chapter 5**.

3.2 CONCEPTUAL DESIGN AND WORKING PRINCIPLE

After a thorough review of the existing literatures that has been carried out in **Chapter 2**, it was noticed that most of the studies employed flat plates as the base design for HMX. Therefore, so as to investigate other possible geometries for DPEC, four new designs were proposed and compared to the conventional flat-plate and corrugated-plate type DPECs. A 3-D graphical sketching alongside with 2-D front shapes of the HMX are presented in **Table 3.1**. Throughout the investigation, the concentric-tube design heat and mass exchanger showed the best thermal performance among all the HMX types (more explanations discussed in **Chapter 5**). Consequently, the concentric-tube type has been selected and further improved with regard to feasibility for easy construction. Therefore, it has been substituted with shell and tube design in lights of easy manufacturing (i.e., design complexity reduction), maintenance, and rigidity of the practical unit.

The flat-plate type DPECs has an impediment of limited heat and mass transfer potential due to occurrence of heat transfer only in one direction from primary channel to working channel (i.e., perpendicular to the flat plate), unlike the proposed design from which the potential of heat and mass transfer has been significantly increased as they occur in all radial directions. On that base, we proposed a shell and tube design for HMX of DPEC, which has not been studied previously. The proposed novel HMX consists of one shell (works as a single working channel) and a preferred number of tubes (work as primary channels). The selection of tubes number is based on the designed cooling capacity of the system. Such a design made the construction of complex HMX very easy, and the complexity impediment can be overcome. Besides, it could save time during mass production owing to the simplicity of shell and tube configuration. During the analysis, the energy and thermal performances of the novel DPEC

ware investigated and compared to that of flat-plate DPEC under two air-water flow configurations and different operational and geometrical conditions.

Table 3.1 Graphical representation of the proposed HMXs for DPEC

HMX type	Two-dimensional shape of channels	Three-dimensional shape of channels
Concentric tube (HMX-1)		
Square tube (HMX-2)		
Rectangular tube (HMX-3)		
Triangular tube (HMX-4)		
Flat plate (HMX-5)		
Corrugated plate (HMX-6)		

That being so, the formulation of the mathematical model and the working principle of the proposed novel cooler will be demonstrated in this chapter, thereafter, the development of the numerical model will be described. A 3-D schematic representation of the novel shell and tube DPEC is presented in **Fig. 3.2(a)** with deeper illustration of individual primary and working channels pair in **Fig. 3.2(b)**.

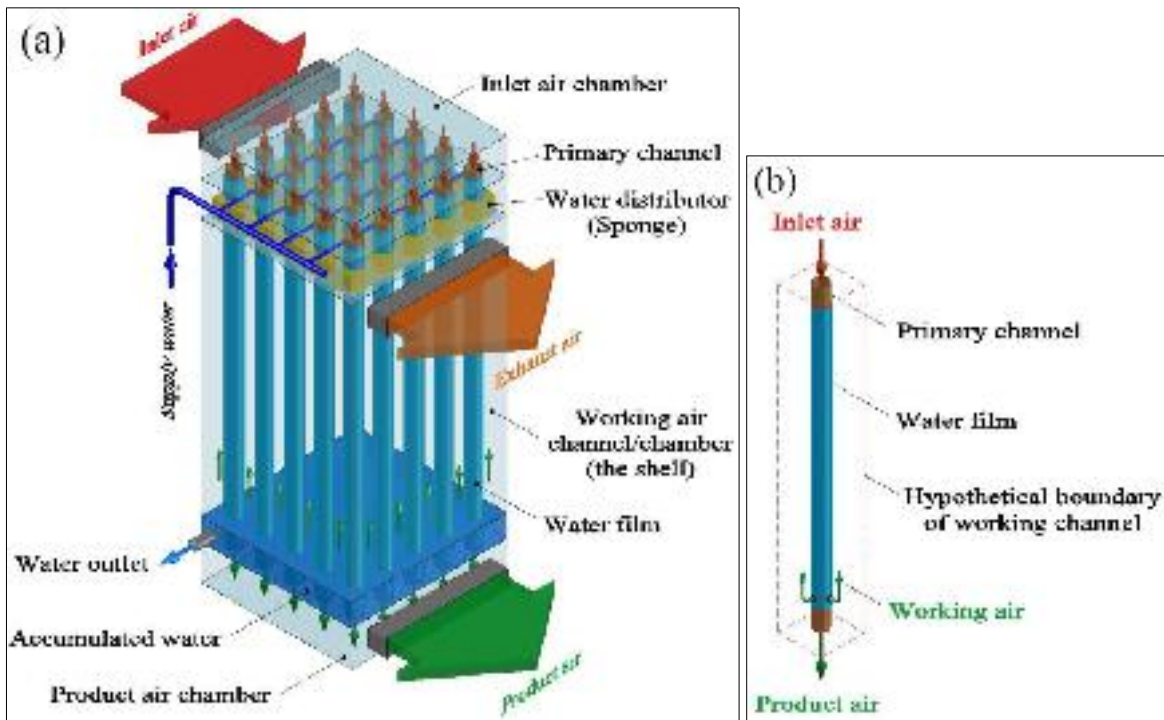


Fig. 3.2 Three-dimensional graphical representation: (a) Novel shell and tube DPEC; (b) Individual primary and working channels pair

As illustrated in **Fig. 3.2**, the proposed shell and tube type DPEC consists of one shell and preferred number of tubes (depends on the designed cooling load). The cooler is divided into three chambers, namely, inlet air chamber, working air chamber and product air chamber. The utilization of these chambers contributes in uniform air distribution (at entrance) and accumulation (at exit), alongside with facilitating the manufacturing process. At the beginning, the unsaturated air enters the system from side/top of the inlet air

chamber and distributed uniformly onto the primary channels. This ensures each channel earns equal amount of airflow. After these air streams been cooled, the product air chamber accumulates the flowing air from each channel and directs them out of the unit from side/bottom of the chamber.

Regarding the working air chamber, it houses the working air streams, evaporative surfaces, and water spraying system. Once all the primary channels covered with wick film (evaporative surface), then they are compiled and enclosed by a transparent acrylic sheet to form the shell, which works as a single working channel. Due to the absence of a working channel boundary wall for each primary channel, a hypothetical boundary is considered for each channel for the purpose of mathematical modeling, as illustrated in **Fig. 3.2(b)**. A portion of the unsaturated cooled air from the primary channel diverts to the working channel/chamber through the perforations made in the tubes wall (six perforations per each primary channel) prior to the product air chamber. Each tube is covered by a wicking film that guarantees efficient absorption, diffusion, and uniform flow of water.

For the proposed DPEC, a dedicated water distribution system has been developed as shown in **Fig. 3.2(a)**. It consisted of perforated plate, perforated fabric-sponge, copper tubes, water pump, and rotameter (more description is presented in **Chapter 4**). The water is fed to the fabric-sponge via perforated copper tubes on top and flowing downward around the evaporative surface by the effect of the gravitational force. A part of the downward flowing water will be evaporated as it passes through the working air chamber due to mass transfer phenomenon (i.e., evaporation process) and accumulated in the water sink to be dripped out of the system. At the end, after the working air been processed and nearly fully saturated via the evaporation process, it leaves the working air chamber as exhaust air.

3.3 AIR-WATER FLOW CONFIGURATIONS

The configuration of air and water flows inside HMX significantly affects the system's performance. As illustrated in **Fig. 3.3**, two configurations are proposed for both exchanger types. In **Fig. 3.3(a)**, which represents the first configuration, the flow directions of the primary air and downward flowing water are parallel (cocurrent). However, in **Fig. 3.3(b)**, which represents the second configuration, the flow directions of the primary air and downward flowing water are counter. Yet, the direction between the primary and working air streams is kept counter for both configurations, and the water is always flowing downward, as described in **Table 3.2**.

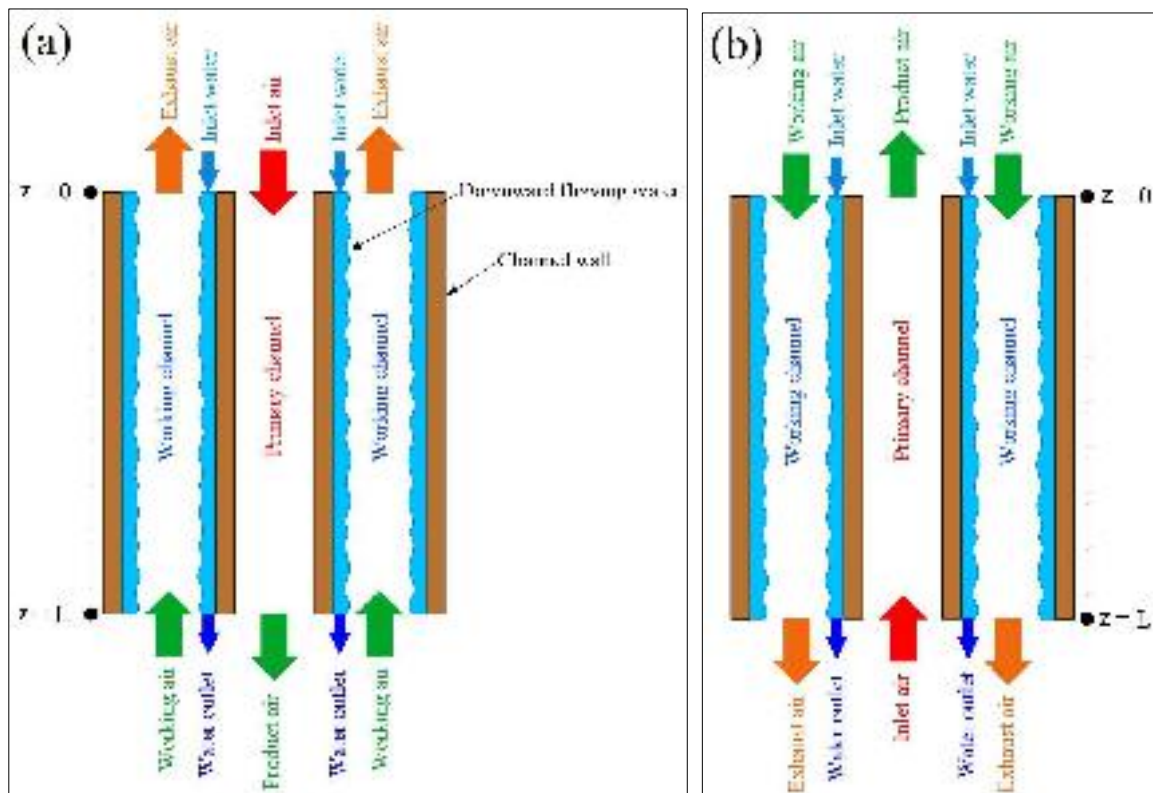


Fig. 3.3 Air-water flow configurations: (a) parallel flow (PF); (b) counter flow (CF)

Table 3.2 System description according to air-water flow configurations

DPEC type	Air-water flow configuration	System Name	Description
Shell and tube exchanger (STX)	Parallel flow (PF)	STX-PF	The primary and working airflows are always kept in counter direction. However, the directions between the primary air and water flow are investigated in two cases. In the first case, they are in cocurrent flow (i.e., parallel flow), while in the second case, they are in opposite direction (i.e., counter flow)
	Counter flow (CF)	STX-CF	
Flat plate exchanger (FPX)	Parallel flow (PF)	FPX-PF	
	Counter flow (CF)	FPX-CF	

3.4 MATHEMATICAL MODELLING

This section is based on the first law of thermodynamics analysis deeming the energy and mass balance equations as they have been employed to develop the mathematical model which can predict the heat and mass transfer for both STX and FPX type dew point evaporative coolers. Each primary and working channel (refer to **Fig. 3.2(b)**) is divided into numerous amounts of differential elements, explained in **Section 3.6**. The illustrations for each differential element of both DPEC types are depicted in **Fig. 3.4**.

During the simulation, to conduct a fair comparison study, the volumes of HMX of both systems are fixed, and the cross-section area for each differential element of both systems is equally sized; besides, the primary channel's cross-section area is equated to that of the working channel. For the model's accuracy to be improved, within each differential element, conduction and convection heat transfer through the channel wall and by downward flowing water are considered, respectively, alongside with the thermal entry region consideration for both primary and working air channels. The key assumptions of the developed model are as follows:

- i. The surface of the wet film is considered to be completely wetted ($\phi = 1$).
- ii. The velocities of air and water flows are considered uniform within each differential element.
- iii. The system's circulating air is considered incompressible gas.
- iv. The physical interaction between the exchanger and the surroundings is assumed adiabatic.
- v. Variation of thermophysical properties in x direction are neglected, while in z direction they continuously varying from entrance and exit of each element.
- vi. The heat and mass transfer are in steady state.
- vii. The fully developed region is considered to be at constant surface temperature.

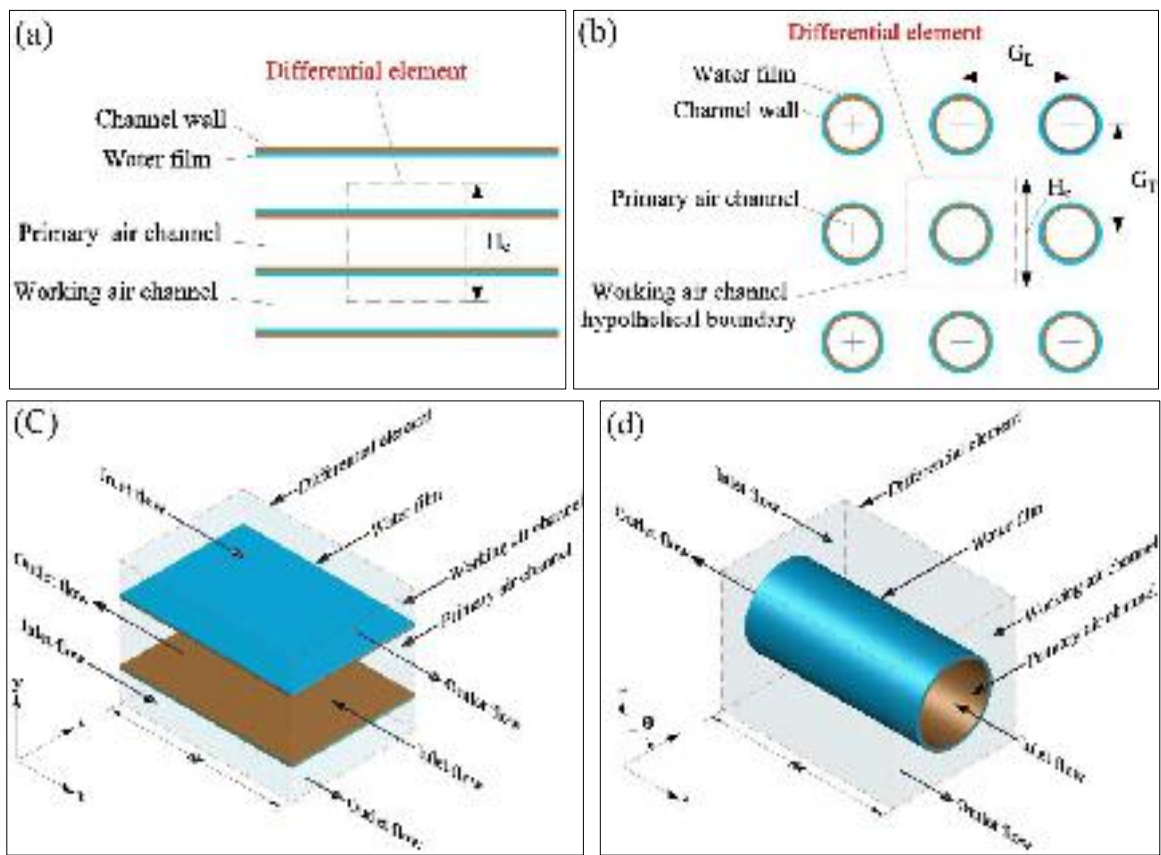


Fig. 3.4 Differential elements: (a) FPX element (top view); (b) STX element (top view); (c) FPX element (3D illustration); (d) STX element (3D illustration)

Overall, within the heat and mass exchanger, heat is transferring from primary air to the channel wall and thereafter from channel wall to the downward flowing water, which is then released to the working air flow through convection and evaporation processes. **Fig. 3.5** shows the controlled differential element, based on which, the changes in thermophysical properties and the heat and mass transfer processes have been illustrated. For each differential element, the governing equations are outlined below:

3.4.1 Primary Channel Airflow

The airflow inside the primary channel loses heat sensibly to the inner wall surface by convection. Hence, the humidity ratio of the air remains unchanged. In terms of heat balance, the total heat lost from primary air can be expressed as

$$\dot{m}_a \cdot c_p \cdot (T_{a,i} - T_{a,e}) = \dot{m}_w \cdot (h_{w,i} - h_{w,e}) \quad (3.1)$$

where d denotes the rate of change of any parameters at inlet and exit of a differential element. The convective heat transfer coefficient (h_c) of each element varies based on the location of the element in the flow path, which depends on the flow regions. Concerning the thermal consideration for flow inside a channel, two regions are available: namely, the thermal entrance region and the fully developed region. Regarding the Reynolds number (Re), the flow inside the primary and working channels were examined under a wide range of temperatures, air flow velocity, and channel sizes, and it was found that the Re in all the cases were below 2300. This implies that the flow is consistently laminar. Thus, the thermal entry region (Z_t) for laminar flow can be calculated from (Cengel et al., 2022)

$$Z_t = (0.05 \cdot Re) / 20 \quad (3.2)$$

For the primary channel, the corresponding Nusselt number at the entrance region is calculated with the following correlation (Baehr and Stephan, 2006; Bergman et al., 2017):

$$= \frac{\frac{7.54}{\tanh(2.264 \cdot \frac{1}{Gz} - 1/3 + 1.7 \cdot \frac{1}{Gz} - 2/3)} + 0.0499 \cdot \tanh(\frac{1}{Gz})}{\tanh(2.432 \cdot \frac{1}{Gz} - 1/6 - 1/6)} \quad (3.3)$$

where Gz is the Graetz number, $Gz = DH \cdot Z^{-1} \cdot Re \cdot Pr$. On the other hand, in fully developed region, the Nusselt number is constant. This region is characterized by being either at a constant heat flux state or at constant surface temperature state. For the current study, a constant surface temperature is considered owing to continuous phase transition of water (i.e., evaporation) at the outer channel wall (Bergman et al., 2017).

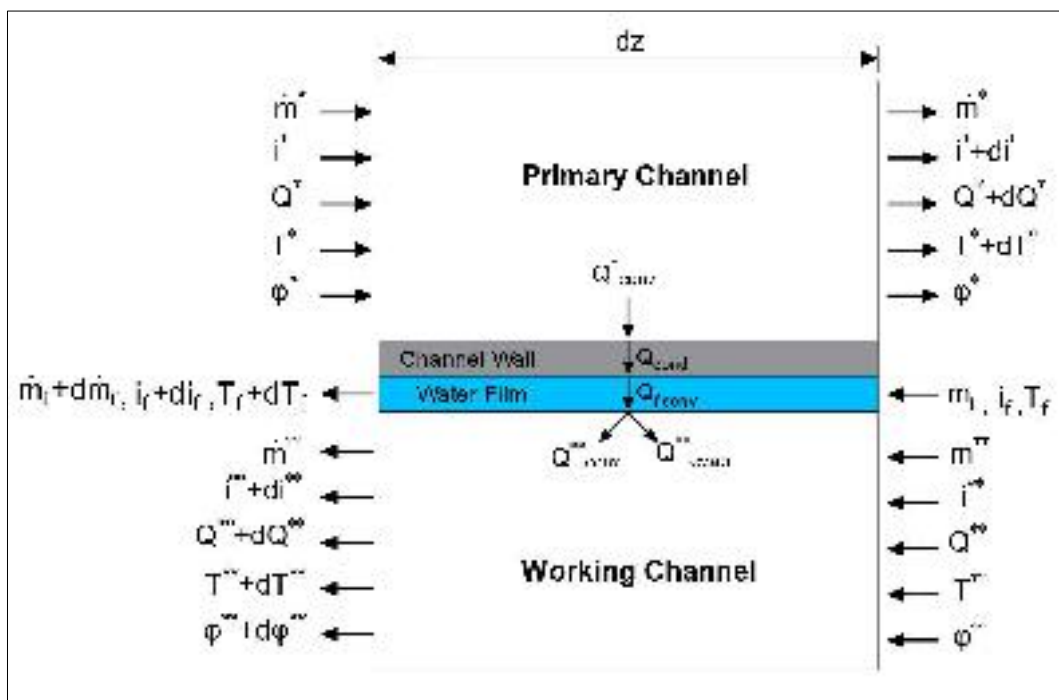


Fig. 3.5 Differential element applied for heat and mass transfer calculations

3.4.2 Downward Flowing Water and Channel Wall

The rate of transferred heat from the air stream in primary channel to the inner surface of the channel wall is the same amount of transferred heat from

outer surface of the wall to the downward-flowing water. In terms of heat balance, the above statement can be expressed as

$$\frac{(T_{air} - T_{wall})}{R_{t,air}} = \frac{(T_{wall} - T_{water})}{R_{t,water}} = \frac{(T_{air} - T_{water})}{R_{t,tot}} \quad (3.4)$$

where $R_{t,air}$ is the thermal resistance faced by heat transfer from air stream in primary channel to downward flowing water for each computational element, which can be expressed as

$$R_{t,air} = \left(\frac{1}{h_{air} \cdot 2 \cdot \Delta x} \right)^{-1} + \ln \left(\frac{r_{out}}{r_{in}} \right) \cdot \left(\frac{1}{2 \cdot \Delta x} \right)^{-1} + \left(\frac{1}{h_{water} \cdot 2 \cdot \Delta x} \right)^{-1} \quad (3.5)$$

$$R_{t,tot} = \left(\frac{1}{h_{air} \cdot \Delta x} \right)^{-1} + \left(\frac{1}{h_{water} \cdot \Delta x} \right)^{-1} + \left(\frac{1}{h_{wall} \cdot \Delta x} \right)^{-1} \quad (3.6)$$

As it is affected by gravity, the downward flowing water film is highly contributing in transferring heat between channel wall and working airflow through evaporation and convection. Its thickness and convective coefficient can be computed from (Stoitchkov and Dimitrov, 1998)

$$\delta = \sqrt[3]{\frac{3 \cdot \mu \cdot \Delta x}{g \cdot \rho \cdot \Delta T}} \quad (3.7)$$

$$h_{water} = 1.88 \cdot \delta^{-1} \quad (3.8)$$

3.4.3 Working Channel Airflow

For the current study, the analysis of the working channel airflow for the flat plate type cooler is differentiated from the shell and tube type cooler. The working airflow inside the flat plate exchanger is treated as internal flow inside individual channels having rectangular profile, while the working air-flow inside the shell and tube exchanger is treated as external flow with the consideration of flow along a bank of tubes with the aligned-arrangement, unlike the primary air channels, where the flowing air inside both cooler types

was considered as internal flow. Accordingly, the Nusselt number varies for each type as it can be calculated for shell and tube type exchanger with the following correlation (Bergman et al., 2017)

$$Nu = \begin{cases} 0.36 \cdot (G_T / G_L)^{0.25} & \text{if } G_T / G_L > 0.7 \\ 0.27 & \text{if } 0.27 < G_T / G_L < 0.7 \\ 0.63 & \text{if } G_T / G_L < 0.27 \end{cases} \quad (3.9)$$

where G_T and G_L are transverse and longitudinal gaps between the channels (refer to **Fig. 3.4(b)**), and the Pr_s is evaluated at surface temperature. Meanwhile, for flat-plate type, the Nusselt number can be computed with **Eq. 3.10**, which differs from the one used for the primary air channel owing to the evaporation process inside the working air channel (Dowdy and Karabash, 1987; Heidarinejad et al., 2010; Lin et al., 2016)

$$Nu = 0.10 \cdot (L_c / \delta)^{0.12} \cdot 0.8 \cdot Pr_s^{1/3} \quad (3.10)$$

where L_c is the characteristic length and is equal to volume over area. Along the working channel, heat and mass transfer occur simultaneously through convection and evaporation, i.e., sensible and latent heat transfer. For working air inside each differential element, its total energy change equates the sum of latent and sensible heat gain from the water film which can be expressed as

$$\dot{Q}_{total} = \dot{Q}_{latent} + \dot{Q}_{sensible} = (h_e \cdot A \cdot (T_s - T_a)) + (h_c \cdot A \cdot (T_s - T_a)) \quad (3.11)$$

$$= \dot{Q}_{latent} + \dot{Q}_{sensible} \quad (3.12)$$

$$(h_e) = h_c + \frac{\dot{Q}_{latent}}{A \cdot (T_s - T_a)} \quad (3.13)$$

Regarding **Eq. 3.11**, the first term of the right-hand side indicates the latent heat transfer by evaporation, while the second term is the sensible heat transfer by convection. Further, i_e is the latent heat of vaporization which depends on

the pressure at which the evaporation occurs. At the air-water interface on evaporative surface, the air is considered fully saturated and its pressure is equivalent to that of the saturation (P_s). Moreover, ω_s is the humidity ratio of airflow near air-water interface where the saturation is dominant, and it can be calculated from (Baehr and Stephan, 2006)

$$\omega_s = 0.622 \cdot (P_s) / (P - (P_s)) \quad (3.14)$$

The saturation pressure of air stream near air-water interface can be calculated by using the Goff-Gratch formula for $T > 273.16$ K, as referenced in (Junzeng et al., 2012)

$$\log(P_s) = X_1 \cdot (T - 273.16) + X_2 \cdot (T - 273.16)^2 + X_3 \cdot (10^{4 \cdot (T - 273.16)^{-1}} - 1) + X_5 \cdot (10^{6 \cdot (T - 273.16)^{-1}} - 1) + X_7 \quad (3.15)$$

where $T = 273.16 \times T_s^{-1}$, and the coefficients ($X_1 - X_7$) are as follows:

$$X_1 = -7.90298, X_2 = 5.02808, X_3 = 1.3816 \times 10^{-7}, X_4 = 11.344, X_5 = 8.1328 \times 10^{-3}, X_6 = -3.49149, X_7 = 1013.246$$

Regarding the amount of heat transfer by the water flow to the outside of each differential element boundary, it is equivalent to the total energy change of downward flowing water for that element. In other words, it can be expressed as subtracting the total primary air heat loss from the total working air heat gain that yields the following equation

$$\dot{Q} = \dot{m}_a (h_{a2} - h_{a1}) - \dot{m}_w (h_{w2} - h_{w1}) \quad (3.16)$$

As a result of latent heat transfer, a portion of flowing water is partially discharged into the working air through evaporation. Consequently, diminution occurs in the flowing water quantity that deems the evaporated water which can be expressed in terms of mass balance as

$$= \dots \cdot (\dots - \dots) = \dots \cdot (\dots - \dots) \quad (3.17)$$

Regarding the mass transfer coefficient (h_m), based on the analogy between the heat and mass transfer, it can be computed as

$$h_m / h_c = \dots \cdot \dots^{2/3} \quad (3.18)$$

$$= \dots \cdot (\dots \cdot \dots)^{-1} \quad (3.19)$$

3.4.4 Performance Evaluation Parameters

The performance of the proposed DPEC has been evaluated using thermal efficiency, water consumption, cooling potential/capacity, and energy efficiency. The thermal efficiency is typically characterized as dew-point effectiveness (ϵ_{dp}) and wet bulb efficiency (ϵ_{wb}) that can be expressed as

$$\epsilon_{dp} = (t_{d,p} - t_{d,e}) / (t_{d,p} - t_{d,s}) \quad (3.20)$$

$$\epsilon_{wb} = (t_{wb,p} - t_{wb,e}) / (t_{wb,p} - t_{wb,s}) \quad (3.21)$$

The water consumption (i.e., water evaporation rate) can be calculated using **Eq. 3.17**. Besides, the cooling capacity (Q) and energy efficiency (ϵ) of the systems can be computed as

$$Q = \dots \cdot (1 - \dots) \cdot \dots \cdot (\dots - \dots) \quad (3.22)$$

$$\epsilon = \dots / (\dots + \dots) \quad (3.23)$$

The electrical power (E) required by the fan can be estimated using the following formula

$$E = \dots \cdot \dots / \dots \quad (3.24)$$

where ΔP_{total} is the circulating air's total pressure drop within the HMX that can be expressed in terms of the major loss (ΔP_{major}) and minor loss (ΔP_{minor}) as (Cengel et al., 2022)

$$\Delta P_{total} = \Delta P_{major} + \Delta P_{minor} \quad (3.25)$$

$$= 0.5 \cdot \left(\frac{L}{D} \right) \cdot \left(\frac{\rho \cdot V^3}{2} \right) + \sum K \cdot \left(\frac{\rho \cdot V^3}{2} \right) \quad (3.26)$$

$$= 0.5 \cdot \left(\frac{L}{D} \right) \cdot V^2 \quad (3.27)$$

The value of the Darcy-Weisbach friction factor (f) relies on the rate of airflow and channel's geometry, $f=N/Re$, where N value is dependent on the geometry, for instance, with regard to laminar flow, $f=64/Re$ for circular pipe and $f=96/Re$ for a wide rectangular pipe (Çengel Y. A. and Cimbala J. M., 2020).

In addition, K is the loss coefficient, and its value depends on the type of the component the air passes through. **Fig. 3.6** illustrates the corresponding pressure drops along the airflow paths within the HMX of DPEC. As illustrated, the induced airflow from the supply fan is equally distributed onto the primary channels, thus all the primary channels assumed to have similar air flowrate. When the air enters the primary channel, a sudden contraction loss (K_1) is produced. By passing the inlet airflow through the primary channel, friction loss (f_1) is occurred due to viscous effect, then a fraction of the primary airflow exit at the end of the primary channel as a product airflow from which sudden expansion loss (K_3) is produced. The remaining of the inlet airflow is diverted to the adjacent working channel through the perforations as working airflow. Tee-line flow loss (K_2), Tee-branch flow loss (K_4), and diversion loss (K_5) are caused owing to the diversion of the airflow through the perforations to the adjacent channel. Moreover, the friction loss (f_2) is produced when the working air passes through the working channel. Finally, due to exhaust of the working

air to the environment, a sudden expansion loss (K_6) is produced (Çengel and Cimbala, 2020). All abovementioned loss coefficients provided in **Table 3.3**.

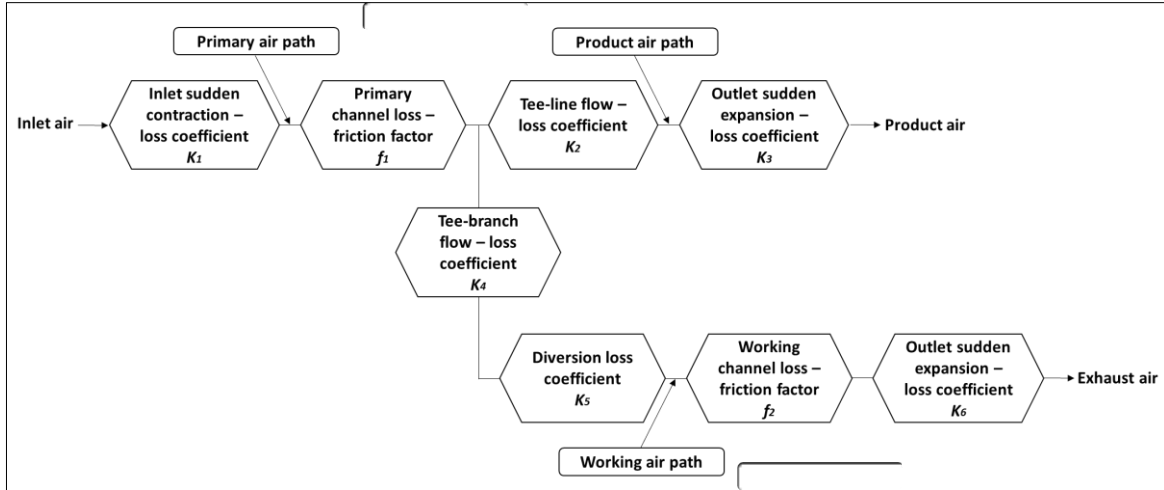


Fig. 3.6 Total pressure drop within the HMX of DPEC

Table 3.3 Induced loss coefficient within HMX (Çengel and Cimbala, 2020)

Loss coefficient	Value	Description
K_1	0.8	Sudden contraction loss of dry channel entrance
K_2	0.9	Tee-line flow loss of dry channel
K_3	2	Sudden expansion loss of dry channel exit
K_4	2	Tee-branch flow loss of the perforations
K_5	1.5	Diversion loss
K_6	2	Sudden expansion loss of wet channel exit

The required electrical power by the water pump can be calculated as

$$= \quad \cdot \quad / \quad (3.28)$$

The pressure loss of the water flow () is considered for the water line that connects the pump to the water distributor inside the cooler. According to Çengel Y. A. (2020), the estimated fan and pump efficiencies can be considered between 50% and 85%.

3.5 EXERGY, ENTROPY, AND SUSTAINABILITY ANALYSIS

This section is based on the second law of thermodynamics deeming the exergy and entropy analysis of the shell and tube design DPEC which relies on the temperature (T) and pressure (P) of the cooling process and the environment. These two parameters (i.e., T and P) are considered as the state properties, and to obtain them, firstly, the analysis of the first law of thermodynamics must be conducted to formulate the energy and mass balances equations for the DPEC. Regarding this matter, the energy and mass balances-based system of equations has been developed for the proposed DPEC as pervasively explained. Subsequently, the state properties of the working fluids (air and water) at any point inside the heat and mass exchanger channels were acquired from the solution of the numerical simulation that been implemented by EES software.

The prime distinction between the first and second laws of thermodynamics can be found in their essence statement about the energy. While the former law concerns about the amount of energy and its conservation notion, the latter law focuses on the quality and the flow direction of energy. The second law also demonstrates the irreversibility of energy systems and the natural tendency of any thermodynamical process towards the chaos and disorder (i.e., entropy generation).

According to the second law of thermodynamics, within an energy system, the available amount of thermal energy can be transformed to work only when temperature gradient exists between the hot source and cold sink. However, not all the available thermal energy can be 100% converted due to energy dissipation and entropy increase which prevents the 100% efficiency of the actual systems. The aforementioned statement of the second law of thermodynamics is the key aspect of the irreversibility of any thermodynamic

process. Within a system, the irreversibility leads to reduction in exergy, while it increases the entropy.

So as to prescribe the working potential of the hot source, the grade or the quality of the pertinent thermal energy must be indicated, which is highly depends on its temperature. This can be achieved by dictating the potential exergy for the system. Both energy properties (exergy and entropy), can be computed by the help of the second law of thermodynamics. Firstly, the exergy is considered as a physical property of a thermodynamic system that uncovers the available amount of its thermal energy with regard to a dead state. Commonly, the dead state, or in another word the zero state, is refer to the ambient or environment state.

For the flow streams of the cooler, the total amount of potential work is acquainted as the flow-exergy (Bejan A., 2016; Y. A. Çengel et al., 2019). The flow-exergy regarding the working fluids of the DPEC is separated for moist air stream and liquid water stream. For moist air stream, the total specific flow-exergy ($\dot{e}x_{a,T}$) include thermal ($\dot{e}x_t$), mechanical ($\dot{e}x_m$), and chemical ($\dot{e}x_c$) exergies which can be expressed as follows (Bejan A., 2016; Chengqin et al., 2002a; Dincer I. and Rosen M.A., 2020)

$$\dot{e}x_{a,T} = \dot{e}x_t + \dot{e}x_m + \dot{e}x_c \quad (3.29)$$

$$\dot{e}x_t = (c_{p,a} + \phi c_{p,v})T_0 \left(\frac{T}{T_0} - 1 - \ln \frac{T}{T_0} \right) \quad (3.30)$$

$$\dot{e}x_m = (1 + 1.608\phi)R_a T_0 \ln \frac{P}{P_0} \quad (3.31)$$

$$\dot{e}x_c = R_a T_0 \left[(1 + 1.608\phi) \ln \frac{1 + 1.608\phi_0}{1 + 1.608\phi} + 1.608\phi \ln \frac{1.608\phi_0}{1.608\phi} \right] \quad (3.32)$$

where T_0 , ϕ_0 , and P_0 are temperature, humidity ratio, and pressure with reference to dead state, $c_{p,u}$ and $c_{p,v}$ are respective specific heats of dry air and

water vapor, and R_a is the dry-air's specific gas constant. On the other hand, the total specific flow-exergy for liquid water stream can be expressed as (Blanco-Marigorta et al., 2022; Caliskan et al., 2012a)

$$\dot{e}x_{f,T} = (i_{f(T)} - i_{v(T_0)}) - (s_{f(T)} - s_{v(T_0)})T_0 + (P - P_{sat(T)})v_{f(T)} - R_v T_0 \ln(\Phi_0) \quad (3.33)$$

where i_f , i_v , s_f and s_v are enthalpy and entropy of saturated water liquid and water vapor as a function of temperatures, respectively, P_{sat} is the saturated water vapor pressure, v_f is the saturated liquid water's specific volume, R_v is water-vapor's specific gas constant, and Φ_0 is the relative humidity at dead state condition.

Under a particular environment, while the exergy defines the amount of available energy in a thermodynamic process, the dead state is deemed as a key parameter to define the exergy amount and energy quality. The dead state comes with other variant names, such as zero state and reference state. This key parameter has been considered differently by the researchers. Some studies considered the ambient condition as the dead state (Chengqin et al., 2002b; Taufiq et al., 2007), while others considered saturated state (100% humidity) of the ambient as the dead state (Kashyap et al., 2020b; Lin et al., 2018c; Wang et al., 2018), in addition, autonomous (random) boundary condition has also been considered as the dead state by some studies (Caliskan et al., 2011; Sadighi Dizaji et al., 2019a).

Subsequently, the exergy balance equation for the proposed dew point evaporative cooler can be written as

$$\dot{E}x_{input} = \dot{E}x_{output} + \dot{E}x_{destruction} \quad (3.34)$$

$$\dot{E}x_{input} = \dot{E}x_{a,in}^* + \dot{E}x_{f,in} = \dot{e}x_{a,in}^* \dot{m}_{a,in}^* + \dot{e}x_{f,in} \dot{m}_{f,in} \quad (3.35)$$

$$\begin{aligned} \dot{E}x_{output} = \dot{E}x_{a,out}^* + \dot{E}x_{a,out}^{**} + \dot{E}x_{f,out} = \dot{e}x_{a,out}^* \dot{m}_a^* + \dot{e}x_{a,out}^{**} \dot{m}_a^{**} \\ + \dot{e}x_{f,out} \dot{m}_{f,out} \end{aligned} \quad (3.36)$$

$$\begin{aligned} \dot{E}x_{destruction} = \dot{e}x_{a,in}^* \dot{m}_a^* + \dot{e}x_{f,in} \dot{m}_{f,in} - \dot{e}x_{a,out}^* \dot{m}_a^* - \dot{e}x_{a,out}^{**} \dot{m}_a^{**} \\ - \dot{e}x_{f,out} \dot{m}_{f,out} \end{aligned} \quad (3.37)$$

where $\dot{E}x_{a,in}$ and $\dot{E}x_{f,in}$ are total exergy input rate of inlet air and water streams, respectively, $\dot{E}x_{a,out}^*$, $\dot{E}x_{f,out}$, and $\dot{E}x_{a,out}^{**}$ are exergy output rate of product air, exhaust air, and drain water, respectively. In addition, $\dot{E}x_{destruction}$ is the exergy destruction in the thermodynamic process during heat and mass transfer inside HMX. Moreover, the specific exergies of unsaturated air inlet ($\dot{e}x_{a,in}^*$), product air outlet ($\dot{e}x_{a,out}^*$), and exhaust air outlet ($\dot{e}x_{a,out}^{**}$) are can be calculated with the following correlations as

$$\dot{e}x_{a,in}^* = c_{p,a}^* T_0 \left(\frac{T_{a,in}^*}{T_0} - 1 - \ln \frac{T_{a,in}^*}{T_0} \right) + R_a T_0 \ln \frac{P_{a,in}^*}{P_0} + R_a T_0 \ln(1 + 1.608\phi_0) \quad (3.38)$$

$$\dot{e}x_{a,out}^* = c_{p,a}^* T_0 \left(\frac{T_{a,out}^*}{T_0} - 1 - \ln \frac{T_{a,out}^*}{T_0} \right) + R_a T_0 \ln \frac{P_{a,out}^*}{P_0} + R_a T_0 \ln(1 + 1.608\phi_0) \quad (3.39)$$

$$\begin{aligned} \dot{e}x_{a,out}^{**} = (c_{p,a}^{**} + \phi_{a,out}^{**} c_{p,v}^{**}) T_0 \left(\frac{T_{a,out}^{**}}{T_0} - 1 - \ln \frac{T_{a,out}^{**}}{T_0} \right) + (1 + 1.608\phi_{a,out}^{**}) R_a T_0 \ln \frac{P_{a,out}^{**}}{P_0} \\ + R_a T_0 \left[(1 + 1.608\phi_{a,out}^{**}) \ln \frac{1 + 1.608\phi_0}{1 + 1.608\phi_{a,out}^{**}} + 1.608\phi_0 \ln \frac{1.608\phi_{a,out}^{**}}{1.608\phi_0} \right] \end{aligned} \quad (3.40)$$

It can be observed that from **Eq. (3.38)** and **Eq. (3.39)**, the humidity ratio (ϕ) is set to zero, because the humidity ratio along the primary channel is constant and not vary (Caliskan et al., 2012b; Sadighi Dizaji et al., 2019b; Taufiq et al., 2007). On the other hand, the specific exergy of inlet water ($\dot{e}x_{f,in}$) and drain water ($\dot{e}x_{f,out}$) are calculated with the following correlations as

$$\begin{aligned} \dot{e}x_{f,in} = (i_f(T_{f,in}) - i_v(T_0)) - (s_f(T_{f,in}) - s_v(T_0)) T_0 + \\ (P_{in}^{**} - P_{v,sat}(T_{f,in})) v_f(T_{f,in}) - R_v T_0 \ln(\phi_0) \end{aligned} \quad (3.41)$$

$$\begin{aligned}
ex_{f,out} = & \left(i_{f(T_{f,out})} - i_{v(T_0)} \right) - \left(s_{f(T_{f,out})} - s_{v(T_0)} \right) T_0 + \\
& \left(P_{out}^{**} - P_{v,sat}(T_{f,out}) \right) v_{f(T_{f,out})} - R_v T_0 \ln(\Phi_0)
\end{aligned} \quad (3.42)$$

So as to assess the exergetic performance of the proposed DPEC, the exergy efficiency needs to be demonstrated and analyzed. In an ideal thermodynamic process, the exergy efficiency is unity and can be as high as 1.0 owing to absence of exergy destruction. However, in an actual process, inside DPEC, the irreversibility is unavoidable due to inevitable exergy destruction occurrence during heat transfer and water evaporation. According to Ratlamwala and Dincer (2013), the exergy efficiency can be defined through three different approaches. The first approach states that the exergy efficiency is the ratio of exergy gained by the cooler to the exergy provided to the cooler. In this regard, the gained exergy is considered as the rate of exergy change in the primary airflow, while the provided exergy is considered as the input exergy by the air stream and the exergy of the water. The second approach states that the exergy efficiency is the ratio of the exergy content of the product air to the exergy content of the interring water. The third approach states that the exergy efficiency is the ratio of the combined exergy of the outlets to the combined exergies of inlets regarding the air and water streams. All three approaches have been adopted by different literatures to demonstrate the exergetic performance of the system. For the current study, the third approach has been adopted as this approach reduce the effect of the dead state conditions and empowers the results to vary more extendedly due to the consideration of the input parameters as expressed below (Caliskan et al., 2012a; Kashyap et al., 2022c; Kousar et al., 2022; Sadighi Dizaji et al., 2019b)

$$\eta_{ex} = \frac{\dot{Ex}_{a,out} + \dot{Ex}_{w,out} + \dot{Ex}_{f,out}}{\dot{Ex}_{a,in} + \dot{Ex}_{f,in}} \quad (3.43)$$

Pertinent to the exergetic efficiency, the sustainability index plays a significant role in the management and utilization of resources (i.e., water and

electricity) efficiently. The sustainability index (*SI*) of DPEC is a function of exergetic efficiency and it can be expressed as (Caliskan et al., 2011; Kashyap et al., 2020b; Kousar et al., 2022)

$$SI = \frac{1}{1-\eta_{ex}} \quad (3.44)$$

Regarding the entropy, it is considered as a fundamental parameter in any thermodynamical processes which indicates the scale of disorder. In general, entropy demonstrates how much disorganized the energy inside a system and it increases overtime. Inside the HMX of DPEC, some of the heat will be lost due to irreversibility which is eventually contributes to the generation of entropy. In another word, the entropy generation inside DPEC is the escalation of entropy as a result of irreversible cooling, evaporation, and pressure reduction processes (Farmahini-Farahani et al., 2012; MAHJOUR et al., 2014; Wang et al., 2019b). Entropy generation is a remarkable indicator for thermodynamical optimization of DPEC. The entropy generation (\dot{S}_{gen}) is the function of destroyed exergy to the temperature of dead state which can be expressed as

$$\dot{S}_{gen} = \frac{\dot{E}_{x_{destruction}}}{T_0} \quad (3.45)$$

3.6 BOUNDARY CONDITIONS

3.6.1 Parallel Flow Configuration

The boundary conditions for the parallel air-water flow configuration inside the HMX are as follows (refer to Fig. 3.3 and Fig. 3.4)

Primary air channel:

$$T_a^*|_{z=0} = T_{a,in}^*, \varphi^*|_{z=0} = \varphi_{in}^*, \dot{m}_a^*|_{z=0} = \dot{m}_{a,in}^* \quad (3.46)$$

$$T_a^*|_{z=L} = T_{a,out}^*, \varphi^*|_{z=L} = \varphi^*|_{z=0}, \dot{m}_a^*|_{z=L} = \dot{m}_{a,in}^* \cdot (1 - AR) \quad (3.47)$$

$$\frac{\partial T_a^*}{\partial r} = 0, \frac{\partial \dot{m}_a^*}{\partial r} = 0, \frac{\partial \varphi^*}{\partial r} = 0 \quad (3.48)$$

Channel wall:

$$\frac{\partial T_w}{\partial \theta}|_{z=0} = 0, \frac{\partial T_w}{\partial \theta}|_{z=L} = 0 \quad (3.49)$$

Downward flowing water:

$$T_f|_{z=0} = T_{f,in}, \dot{m}_f|_{z=0} = \dot{m}_{f,in}, \dot{m}_f|_{z=L} = \dot{m}_{f,in} - \dot{\psi} \quad (3.50)$$

Working air channel:

$$T_a^{**}|_{z=0} = T_{a,out}^{**}, \varphi^{**}|_{z=0} = \varphi_{out}^{**}, P_a^{**}|_{z=0} = P_{atm} \quad (3.51)$$

$$T_a^{**}|_{z=L} = T_{a,in}^{**} = T_{a,out}^*, \varphi^{**}|_{z=L} = \varphi^*|_{z=L}, \dot{m}_a^{**}|_{z=L} = \dot{m}_{a,in}^* \cdot AR \quad (3.52)$$

3.6.2 Counter Flow Configuration

The boundary conditions for the counter air-water flow configuration inside the HMX are as follows (refer to **Fig. 3.3** and **Fig. 3.4**)

Primary air channel:

$$T_a^*|_{z=0} = T_{a,out}^*, \varphi^*|_{z=0} = \varphi^*|_{z=L}, \dot{m}_a^*|_{z=0} = \dot{m}_{a,in}^* \cdot (1 - AR) \quad (3.53)$$

$$T_a^*|_{z=L} = T_{a,in}^*, \varphi^*|_{z=L} = \varphi_{in}^*, \dot{m}_a^*|_{z=L} = \dot{m}_{a,in}^* \quad (3.54)$$

$$\frac{\partial T_a^*}{\partial r} = 0, \frac{\partial \dot{m}_a^*}{\partial r} = 0, \frac{\partial \varphi^*}{\partial r} = 0 \quad (3.55)$$

Channel wall:

$$\frac{\partial T_w}{\partial \theta}|_{z=0} = 0, \frac{\partial T_w}{\partial \theta}|_{z=L} = 0 \quad (3.56)$$

Downward flowing water:

$$T_f|_{z=0} = T_{f,in}, \dot{m}_f|_{z=0} = \dot{m}_{f,in}, \dot{m}_f|_{z=L} = \dot{m}_{f,in} - \dot{\psi} \quad (3.57)$$

Working air channel:

$$T_a^{**}|_{z=0} = T_{a,in}^{**} = T_{a,out}^{**}, \phi^{**}|_{z=0} = \phi^{**}|_{z=0}, \dot{m}_a^{**}|_{z=0} = \dot{m}_{a,in}^{**} \cdot AR \quad (3.58)$$

$$T_a^{**}|_{z=L} = T_{a,out}^{**}, \phi^{**}|_{z=L} = \phi_{out}^{**}, P_a^{**}|_{z=L} = P_{atm} \quad (3.59)$$

3.7 SIMULATION SET-UP AND GRID SENSITIVITY ANALYSIS

The governing differential equations for the developed model were discretized by applying the finite difference method (FDM), and the forward difference scheme was utilized as the inlet conditions were known. These discrete equations are then solved with the help of Newton iteration method. The system of simultaneous non-linear equations was implemented in engineering equation solver (EES) environment. The coding of the model can be found in **Appendix A** that can predict the thermal, energy, and exergy performance of the proposed DPEC under variety of geometrical and operational conditions.

The thermodynamic properties of air, water, and water vapor have been computed using inbuilt functions of EES. After that, the grid sensitivity analysis was investigated on various cell element numbers (from 50 to 750 elements for each individual channel) as shown in **Fig. 3.7**. It was found that the changes in product air temperature and thermal efficiency are within 2.38% when increasing the element number from 50 to 450, while they were within 0.12% when increasing the element number from 450 to 750. Therefore, considering the time and accuracy of the trial computational results, 450 differential elements were adopted for each flow channel.

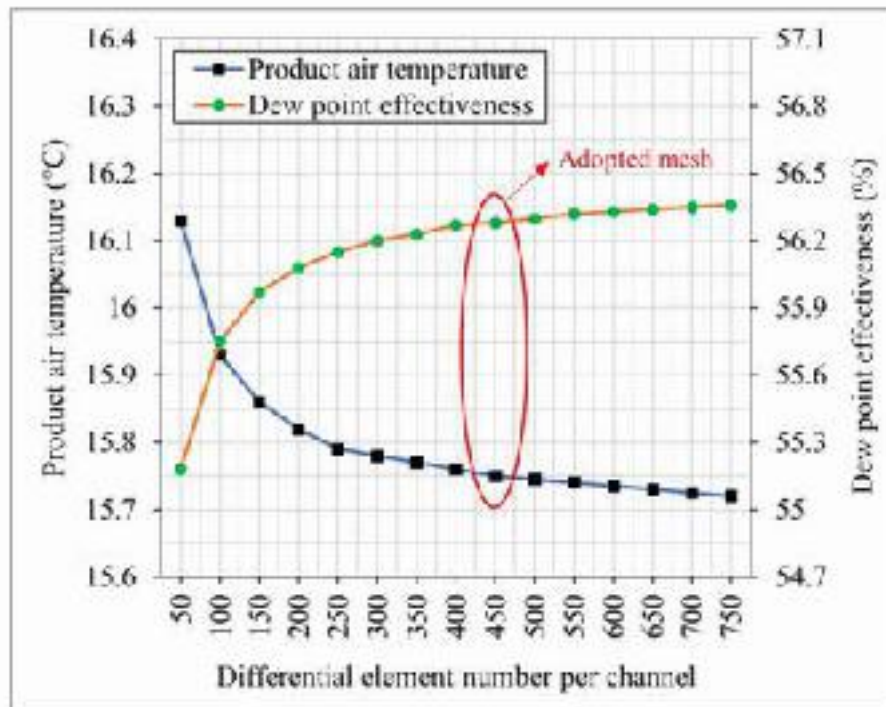


Fig. 3.7 Grid sensitivity analysis for the simulation

3.8 MODEL VALIDATION

Regarding model accuracy, it was validated using two approaches. In the first approach, the developed model was validated against three sets of experimental results from the published literatures (Lin et al., 2018b; Riangvilaikul and Kumar, 2010b; Xu et al., 2017). However, due to lack of experimental research studies on shell and tube type DPEC, therefore, the developed model's accuracy has been validated by comparing it with flat plate type DPECs, which is fairly adequate because similar heat and mass balance equations have been employed for both shell and tube type and flat plate type coolers in the current comparative study. Moreover, in the field of evaporative coolers in general, the circular tubes have been considered by several studies (Cui et al., 2023; Sun et al., 2023, 2020b; Wang et al., 2017), but they all considered indirect evaporative coolers with cross-flow rather than dew point evaporative cooler, which have a completely different working principle from

DPEC. During the validation, identical geometrical and operational specifications have been adopted from the experimental studies.

The utilization of the first approach of validation is crucial as it ensures the credibility of the developed numerical model and enables assessing the proposed DPEC under a wide range of geometrical and operational conditions, from which the optimum geometrical dimensions will be selected to be employed for the manufacturing of the system prior to the experimental work.

In the second approach of validation process, the developed numerical model was validated against the obtained results from the constructed unit (i.e., novel shell and tube design DPEC unit). The exact same geometrical dimensions, weather conditions, and operational circumstances of the experiments have been employed in the numerical simulation model. A detailed explanation for the simulation set-up and the validation of the developed numerical model with the experimental data from both approaches are demonstrated and discussed in **Chapter 5**.

3.9 CHAPTER SUMMARY

In this chapter, a novel design for DPEC was proposed. The new geometry includes shell and tube design for heat and mass exchanger of DPEC that will improve the heat and mass transfer process and surpasses the design complexity of the conventional DPEC. Eventually, this contribution helps in future manufacturing and mass production of such a high energy and thermal performance system. The working principle of the cooler alongside with the physical processes inside the HMX were explained in detail.

To demonstrated the full capability of the proposed system, two different air-water flow arrangements were studied from which chilled water and cold air can be obtained: first, primary air stream and water flow arranged in counter

direction to produce cold air and warm water; second, primary air stream and water flow arranged in parallel direction to produce chiled water and cool air. In both cases, the direction between the primary and working airflows was fixed to counter, and the water always flowed downward.

In addition, a dedicated mathematical model has been developed which was based on the heat and mass balance notions. The governing equations for the physical model were discretized using finite difference method and coded into the Engineering Equation Solver software so as to perform the numerical simulation. Prior to the construction of the cooler, it was crucial to make sure of the accuracy of the developed numerical mode results, because the size of the manufactured system is totally dependent on the optimum dimensions acquired from the theoretical model. This approach prevents the under-sizing or over-sizing the airflow channels that will significantly cause the degradation of the cooler's performance. Therefore, the experimental validation was conducted for the developed model by comparing it with three experimental data from published literatures under a wide range of geometrical and operational circumstances.

Furthermore, the model is able to carry out a comparative analysis between the proposed DPEC and the flat-plate type DPEC with regard to the key performance parameters, such as cooling capacity, energy consumption, dew-point effectiveness, wet-bulb effectiveness, energy efficiency, product air temperature, outlet water temperature, water consumption, exergy destruction, entropy generation, and cooler's sustainability. The theoretical comparative investigation between these two coolers is mandatory to show the superiority of the neoteric DPEC.

CHAPTER 4

EXPERIMENTAL WORK

4.1 INTRODUCTION

This chapter is established on the acquired optimum design parameters from the numerical simulation. These parameters will be employed in the construction of the proposed novel dew point evaporative cooler. The detailed analysis for the selection of each design parameters will be discussed in the subsequent section. Despite the selected materials and the equipment which are available commercial products, the designed heat and mass exchanger and the water distribution system are original and innovative. The main tasks carried out in this chapter are as follows:

- i. Structural design demonstration for the proposed DPEC.
- ii. Materials selection for tubes wall and evaporative surface.
- iii. Step-by-step procedure of the fabrication of the HMX.
- iv. Prototype assembling, and sensors allocation.
- v. Measuring instruments calibration
- vi. Experiments set-up preparation.

At last, the uncertainty analysis of the experimental results will be carried out. The obtained results from the experiments will be presented and discussed in **Chapter 5**.

4.2 SELECTION OF OPTIMUM DESIGN PARAMETERS

The construction of the physical prototype will be implemented based on the optimum sizes of the channel gap/height, channel width, tube diameter, and

exchanger length which have been obtained from the numerical simulation. A set of numerical simulations were carried out based on the pre-set parameters showed in **Table 4.1**. During the simulation, thermal performance of the proposed cooler has been investigated under a wide range of geometrical sizes.

Table 4.1 Pre-set values for numerical simulation

Parameter	Unit	Value
Ambient air temperature	°C	35,40,45
Ambient air moisture content	kg/kg	0.005
inlet air velocity	m/s	1.2
Ratio of working to primary air	–	0.4
Inlet water temperature	°C	23
Inlet water flowrate	l/h	10
Wall and film thickness	cm	0.03
Primary channel diameter	cm	0.5
Working channel width/height	cm	1
Channel length	cm	85

Regarding the channel length, the variation of product air temperature and cooling load potential of the cooler under the influence of varying channel length from 0.2 m to 1.5 m are illustrated in **Fig. 4.1** at three different inlet air temperatures. As it can be seen, the product air temperature reduced dramatically when the channel length increased from 0.2 m to 0.7 m due to increased surface area for heat and mass transfer process. Afterwards, when the channel length increased from 0.7 m to 0.9 m, the product air temperature moderately reduced and this reduction rate became least effective when the length increased more than 1 m. On the other hand, the impact of channel length on cooling load trend is significantly lower than its impact on product air temperature. Therefore, a channel length of 0.85 is deemed to be the optimum length considering the size, weight, and cost of the system.

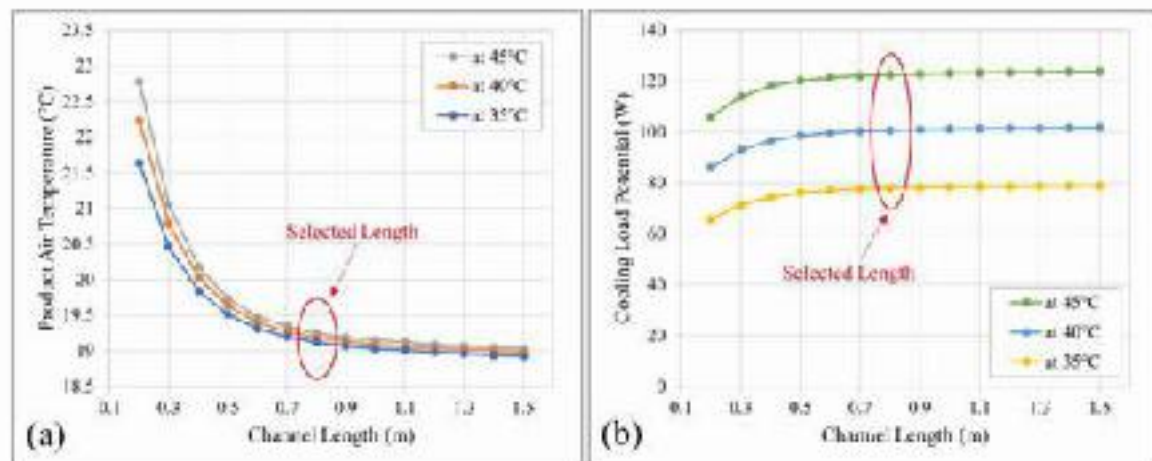


Fig. 4.1 Effect of channel length on: (a) product air temperature; (b) cooling load

Regarding the influence of primary channel tube diameter and working channel height/width on the cooler's performance, they both presented in Fig. 4.2. Both design parameters are demonstrated in Fig. 3.4 back in Chapter 3. As illustrated in Fig. 4.2(a), the product air temperature is gradually decreased with increasing the tube diameter until the tube diameter reached 6.5 mm, thereafter, the temperature started increasing substantially. The temperature difference between 5 mm and 6.5 mm diameter tubes is only 0.3 °C. Consequently, a tube with 5 mm diameter has been selected as optimum choice considering the size and weight of the cooler. Moreover, the working channels are considered to have hypothetical square boundary layer (as illustrated in Fig. 4.3), thus, the height and width of these channels are equal. Fig. 4.2(b) shows the effect of working channels height and width on coolers performance. It can be observed that the product air temperature continuously increases with increasing the height or the width of these channels, while the dew point effectiveness trend is less affected. However, when increasing working channel's height and width, the size of the system significantly increases, therefore, the middle option (10 mm) has been selected as the product air temperature varies by ± 1 °C when compared with the maximum and minimum

considered width. Therefore, the final selected optimum design dimensions to be used for the manufacturing process are shown in Fig. 4.3. Moreover, the identification of channel numbers is only affecting the cooling load of the cooler, while it does not have any effect on the product air temperature and drained water temperature. Accordingly, 300 channels have been selected for the cooler that arranged in 15 rows and 20 columns.

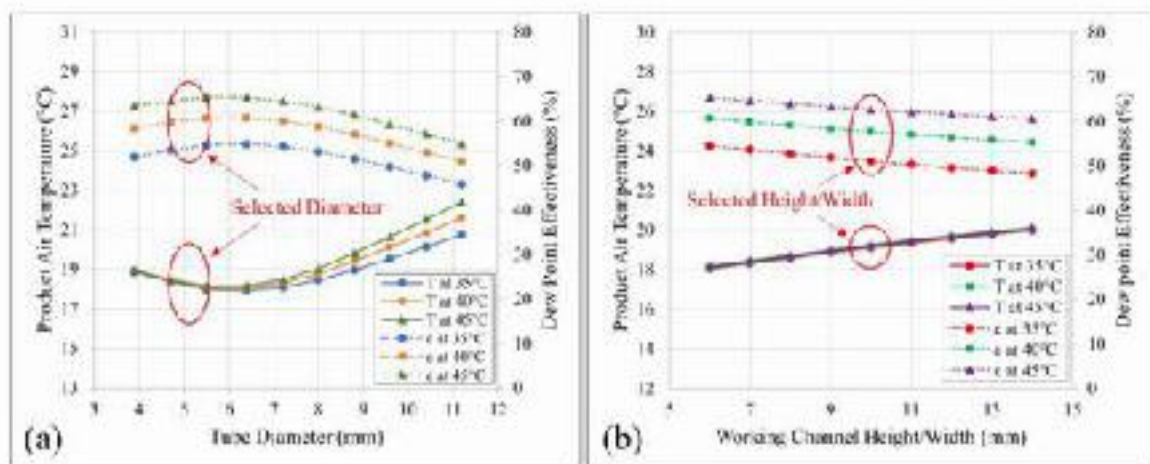


Fig. 4.2 Product air temperature and dew point effectiveness variation under influence of: (a) primary channel diameter; (b) working channel height/width

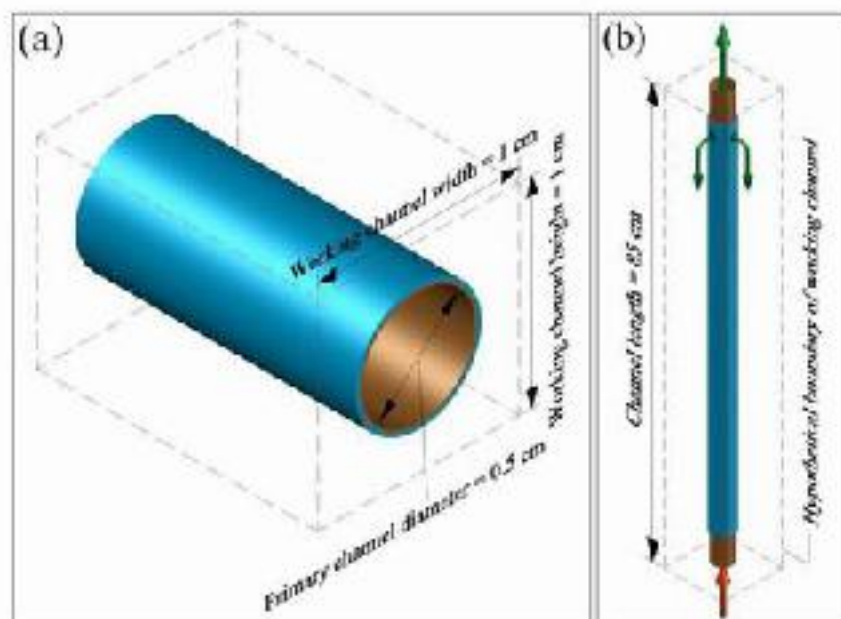


Fig. 4.3 Optimum dimensions employed for prototype construction

4.3 STRUCTURAL DESIGN

The proposed DPEC is mainly consisted of a quintessential heat and mass exchanger, supply air axial fan, exhaust air axial fan, water pump, and water distributor. The supply axial fan drags the ambient air into the primary channels. Inside the primary channels the air will be processed by sensible cooling process and loss the heat to the tubes wall. The processed air is then supplied to the conditioned space for the purpose of the air-conditioning. The extracted heat from the primary air is then transported through the tubes wall to the evaporative surfaces, afterwards this heat deployed into three parts. Two parts of it absorbed by working air via sensible and latent heat transfer and leave the cooler by the exhaust air, while the third part is absorbed and carried out of the cooler by the flowing water as drain water. In addition, the working air is a diverted air from the primary channels to the working channel through circular perforation by a specified ratio (called air ratio) to perform further cooling. This mechanism is what distinguishes the DPEC from other types of evaporation based cooling machines (i.e., direct and indirect evaporative coolers) and pushes the DPEC to its furthest potential and bring the ambient dry-bulb temperature towards its dew-point temperature.

4.4 SYSTEM CONSTRUCTION

After the determination of the optimum design parameters by the numerical simulation, i.e., primary channel diameter, working channel height and width, and channel length, they have been employed for the subsequent stages of constructing the cooler.

4.4.1 Material Selection

Due to the extreme thinness of the channel wall, the heat effortlessly transfer from primary channel to the working channel. Hence, the material type

is futile when it comes to the heat transfer resistance. In this regard, a polycarbonate drinking straw tubes have been nominated for building the heat and mass exchanger as shown in Fig. 4.4. Eight different tube types have been investigated, each has different hardness level and wall thickness. The one marked in a red rectangle has been chosen which has thinnest wall with 0.15 mm and most appropriate diameter of about 5 mm, and they are characterized by light weight, rigidity, and low cost as illustrated in Fig. 4.5.

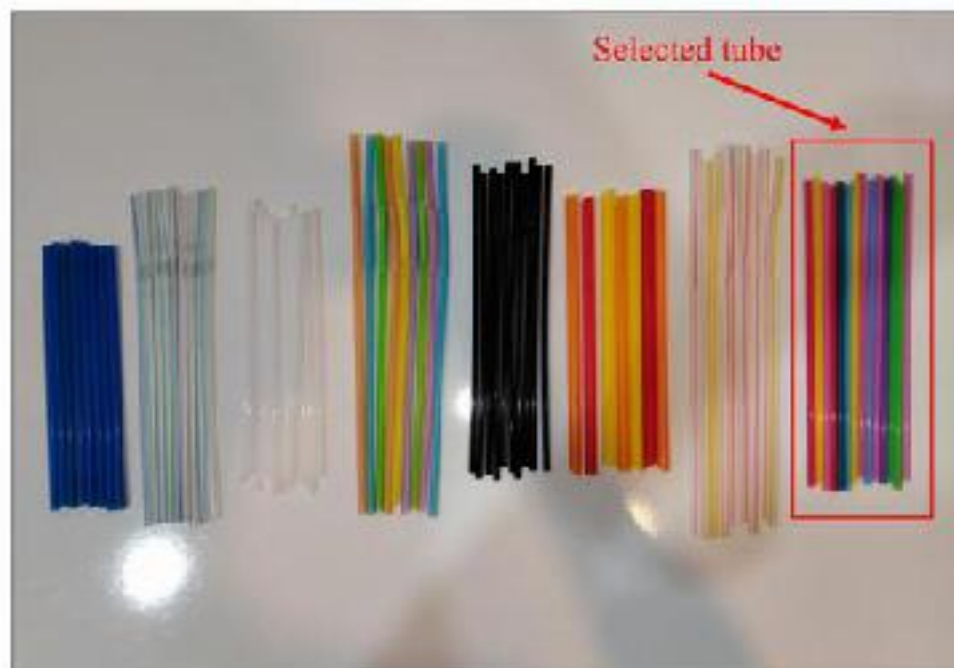


Fig. 4.4 Candidate tubes for HMX formation

In addition, the utilized materials for the evaporative surfaces required to has high absorptivity and diffusivity capabilities, alongside with ultra-thin profile. For this reason, after a deep search for appropriate material, disposable tablecloth has been chosen. The selected disposable tablecloth is consisting of two distinct layers with only 0.03 mm thickness. The first layer is a super thin plastic layer that is significantly soft to touch. This softness ensures minimum air gap formation when wrapped around the tube. While the second layer is made of paper which has a high water absorption and diffusion characteristics. Fig. 4.6 Shows the employed tablecloth for evaporative surface. These two

layers are strongly bonded together, and the plastic layer avoids the destruction and removal of the paper layer.

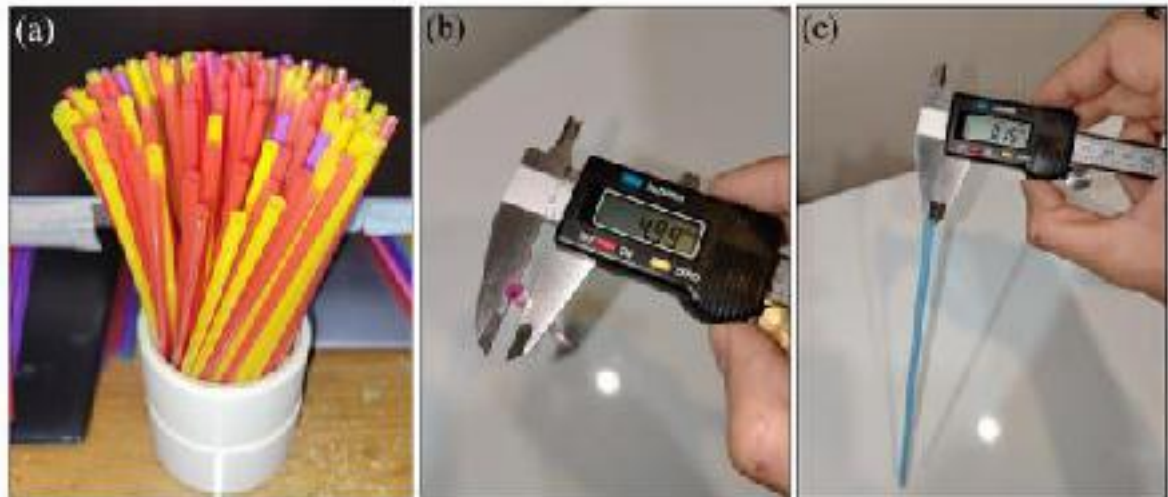


Fig. 4.5 Selected material for primary channels: (a) drinking straw tubes; (b) tube diameter; (c) tube wall thickness

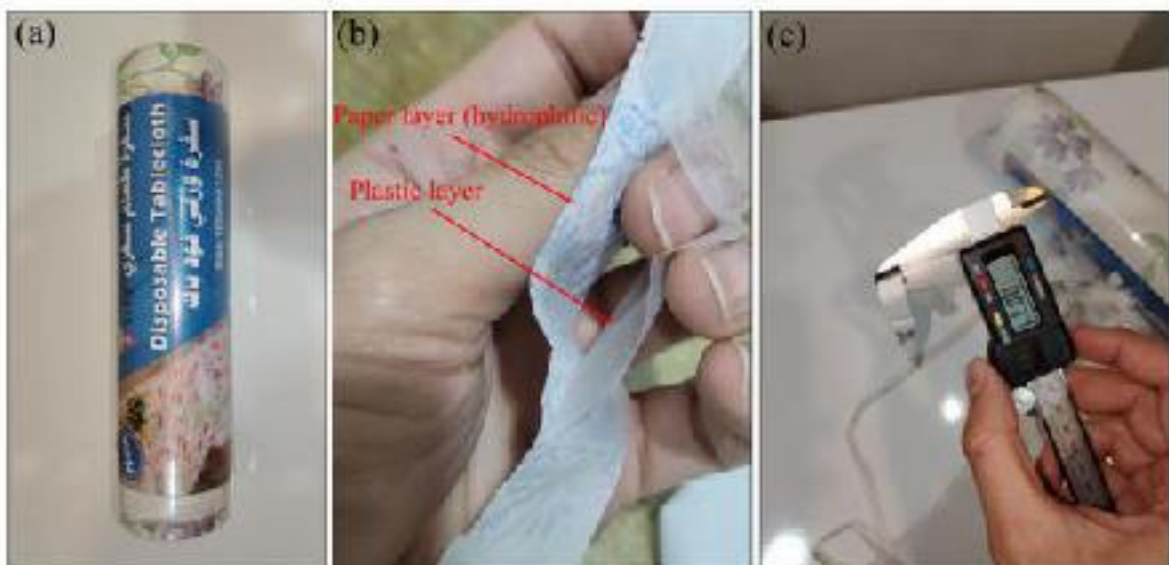


Fig. 4.6 Selected material for evaporative surface: (a) disposable tablecloth role; (b) dual-layer constitution; (c) both layers thickness

Regarding the tape type used for joining two neighboring tubes and to affix the evaporative surfaces to the tubes, several types have been investigated and the double-sided translucent paper tape has been selected for its ultra-thin

profile. The HMX has been enclosed by transparent acrylic sheets to prohibit the heat and mass transfer with the surrounding ambient air and to give rigidity to the cooler.

4.4.2 Primary Channels Construction

The primary channels are basically formed by connecting the drinking straw tubes. Each straw has a length of 21.75 cm and it requires the attachment of 4 tubes to form one primary channel with 87 cm length. Nevertheless, only 85 cm remain from that length as 1 cm of top and bottom of each tube inserted into the inlet air and product air chambers for welding purpose, respectively (see Fig. 3.2).

So as to prevent the curvature of the connected tubes and ensure their straightness, the tubes have been placed onto a circular metal bar with 4.8 cm diameter as shown in Fig. 4.7(a). Afterwards, the four tubes are connected with each other by a double-sided translucent paper tape having 1 cm width (refer to Fig. 4.7(b)). The utilized paper tape is characterized by ultra-thin profile, super adhesive, and hard to rip (presented in Fig. 4.7(c)).

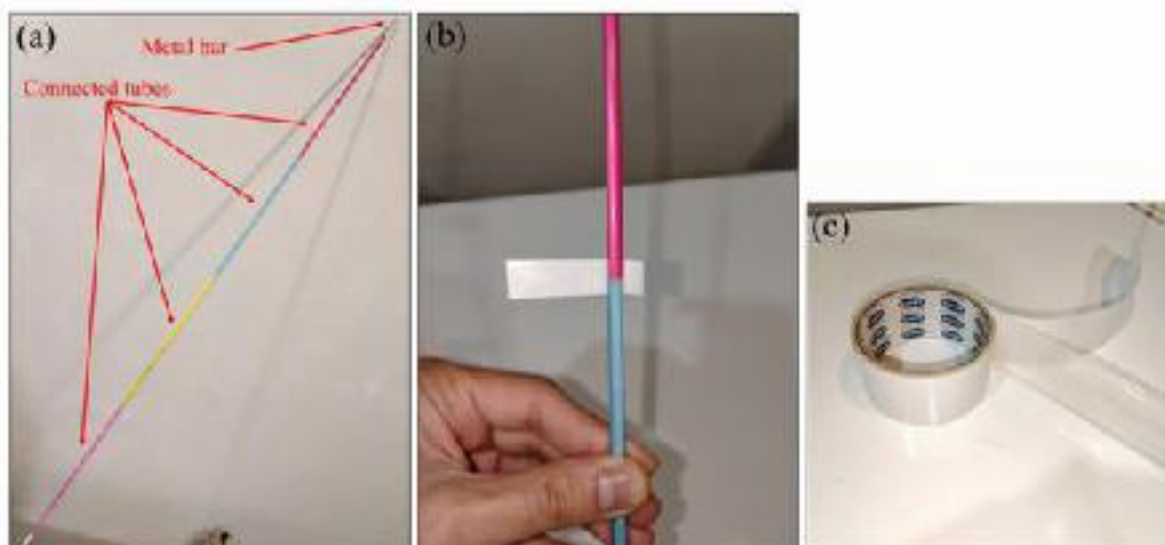


Fig. 4.7 (a) Tubes placed on metal bar; (b) Bonding of two adjacent tubes; (c) Double-sided translucent paper tape

4.4.3 Evaporative Surface Formation

The procedures of evaporative surfaces formation on top of the primary channels are illustrated in **Fig. 4.8** and the steps are as follows:

- (1) So as to rap the dual-layer tablecloth around the tubes, the tablecloth sheets have been sliced into narrow stripes with 1 cm width as shown in **Fig. 4.8(a)** and **(b)**. Similar to tablecloth sheets' length, each strip has 100 cm length, while the connected tubes require 130 cm long stripes to be covered entirely.
- (2) Thus, two stripes (100 cm and 30 cm) have been attached with a small 1×1 cm² paper tape (refer to **Fig. 4.8(c)**).
- (3) The rapping process started from top of the tubes to bottom so as to give a spiral shape to the evaporative surface. This will help in seamless water flow along the strips. To do so, first a 1 cm paper tape has been stick to the top and bottom of the tube to mount in place the strip as can be seen in **Fig. 4.8(d)**. Then, the strip stuck to the tape and started rapping (see **Fig. 4.8(e)** and **(f)**). In between the top and bottom stuck strip, the strip stuck to three more 1 cm tapes at tube bonding joints. This gives extra grip to the evaporative surface with the tube which guarantees overcoming the issues like removal or waging of the evaporative surface during the operation of the system.
- (4) After rapping the strip, the evaporative surface integrated primary channel is finally manufactured as presented in **Fig. 4.8(g)**. This process repeated 300 times for all 300 tubes to be prepared for the next stage which is the deployment of these tubes over the precisely perforated plates to compose the heat and mass exchanger.

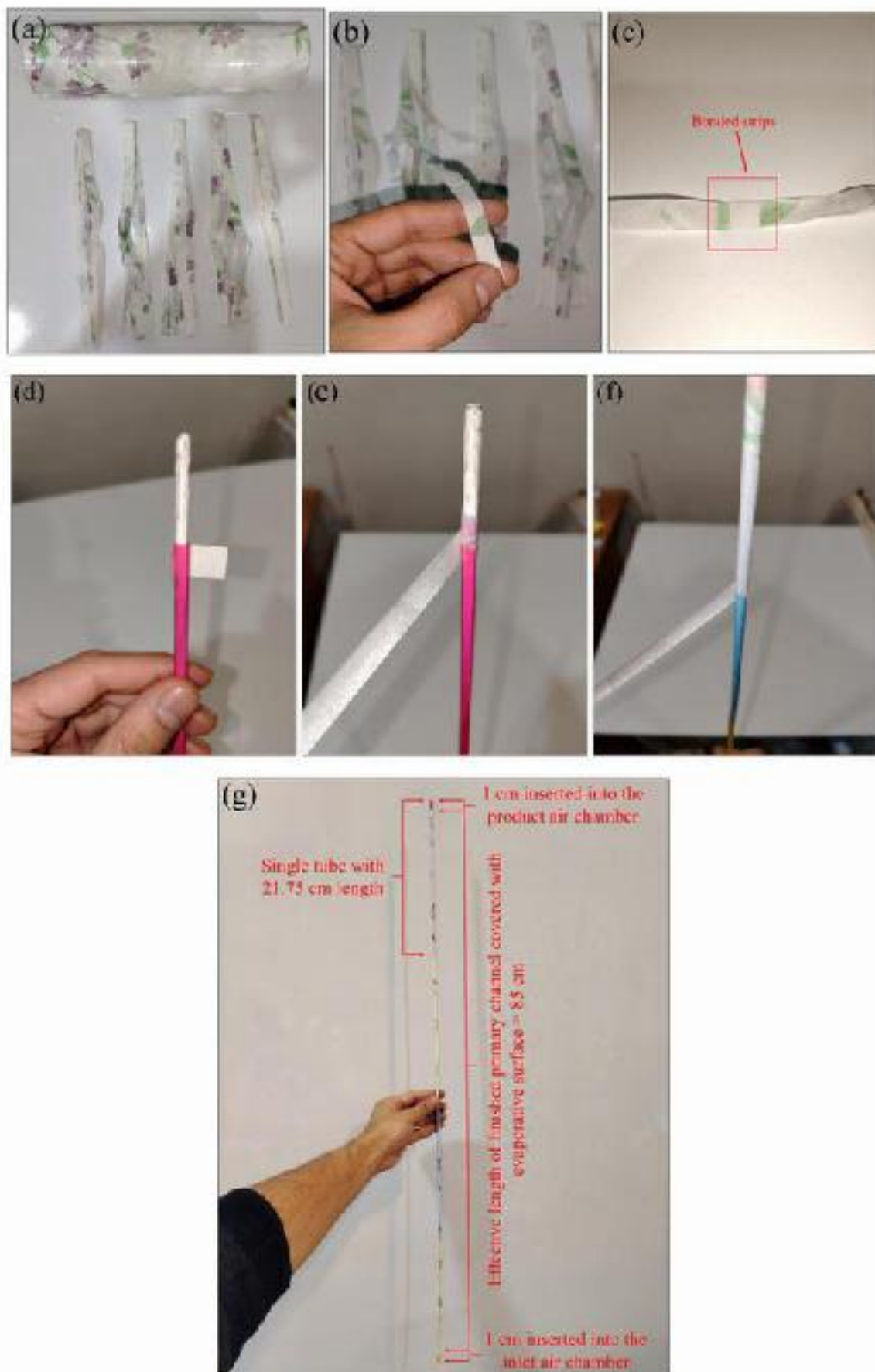


Fig. 4.8 Evaporative surface formation procedures

4.4.4 Puncturing the Perforations for Air Diversion

Inside the working channels, for the working airflow to be available, a part of the primary airflow in the primary channels needs to be diverted to the working channels before it leaves the primary channels to primary air chamber as product air. For this to happen, six perforations have been made in each tube prior to the water distribution location.

The reasons behind selecting six holes rather than lower numbers were to permit seamless air diversion and to reduce pressure drop occurrence through these perforations. Each hole has a circular shape with 2 mm diameter which was made by a soldering device as illustrated in Fig. 4.9. The six holes divided on to three columns around each tube, and each column holds two perforations. The distinct feature about using soldering device rather than other punctuators is that during punching process, due to the high temperature of the device's tip, both the tube wall and tablecloth are fused together which gave an extra grip to the evaporative surface.

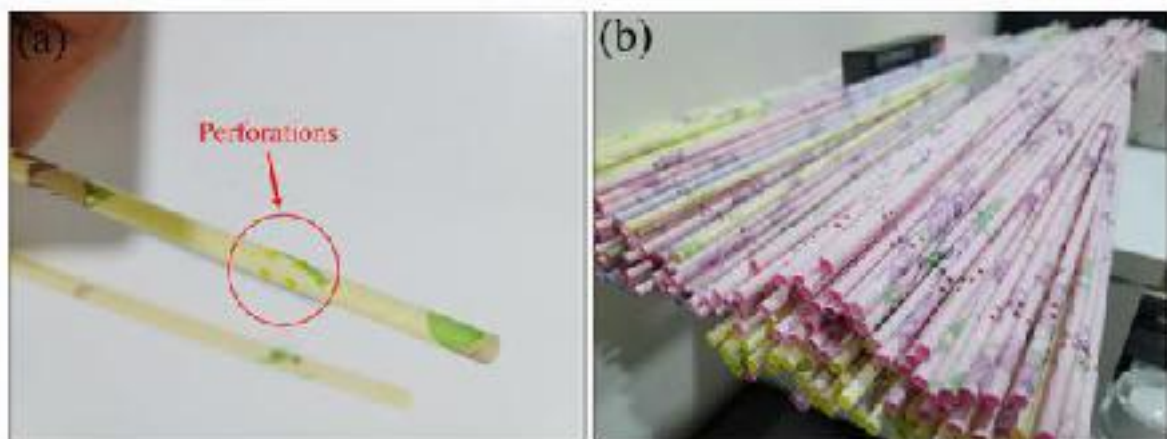


Fig. 4.9 (a) Six perforations in three columns, two per each column; (b) 300 perforated tubes

4.4.5 Water Distribution System Design and Fabrication

For the proposed DPEC, a dedicated water distribution system has been designed which is able to distribute water evenly over the 300 evaporative surface integrated primary channels. The innovative water distribution system made sure to bring adequate water for each evaporative surface and wet the entire surface of the outer tube. The first water distribution system was made from plastic (polycarbonate), but it was a failure attempt as it was fragile and could not with stand the weight of the water inside the system, besides, making a numerous small holes in the tubes all with same diameter as water dripping points was unattainable. Therefore, in the second attempt, copper tubes have been utilized in this regard and it fixed all the aforementioned issues. The proposed water system is consisted of one copper header, eighteen copper tubes, sponge cloth sheet, one bed plate, a water pump, and a flow regulator (rotameter). Each copper tube contains 14 small holes with 0.75 mm diameter. It was made sure that all the holes have the exact same diameter so as every tube permit the same amount of water flow. The holes have been made with a drilling machine. The distance between each two holes was 1 cm to meet the designed distance where each hole provides water to in between 4 exterior surfaces of the tubes.

Moreover, a sponge has been used to spread the water evenly in between the tubes. Several types of sponges have been put into the investigation. However, many of these sponges possessed serios problems, for example, the cellulose sponge naturally could not absorb the water, it must be pressurized and depressurized so as to absorb the water as shown in **Fig. 4.10**. As can be seen, a water droplet placed on top of the sponge for 30 minutes, yet it remained stationary without being absorbed by the sponge.

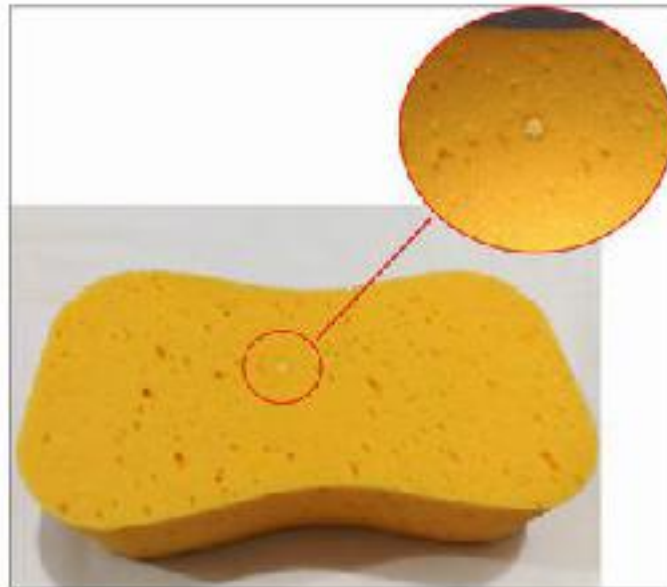


Fig. 4.10 Cellulose sponge tested for water absorption

In the second attempt, a super absorbent cellulose+cotton sponge has been tested. This type was able to absorb the water naturally, however, its major problem was that it got hardened and shrank by 15% after it went dry as shown in **Fig. 4.11**. This issue led the tubes of the HIMX to bend.

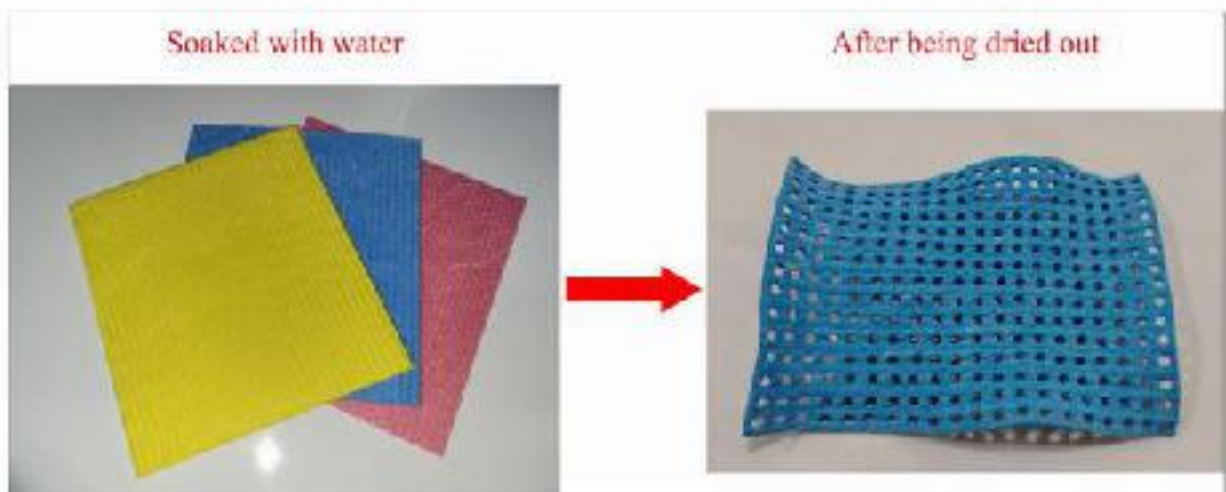


Fig. 4.11 Cellulose+cotton sponge under the test

In the last attempt, a super absorbent 50% polyester 50% viscose cloth sponge has been tested. This type could overcome all the above-mentioned

problems and was able to naturally absorb and distribute water instantly. It has been employed for the water distribution system. First, it was resized to 20 cm × 15 cm to fit the HMX and perforated by office paper perforator. The size of each perforation was 5 mm which was enough to let the tubes go through. Fig. 4.12 shows the prepared parts for the water distribution system construction.

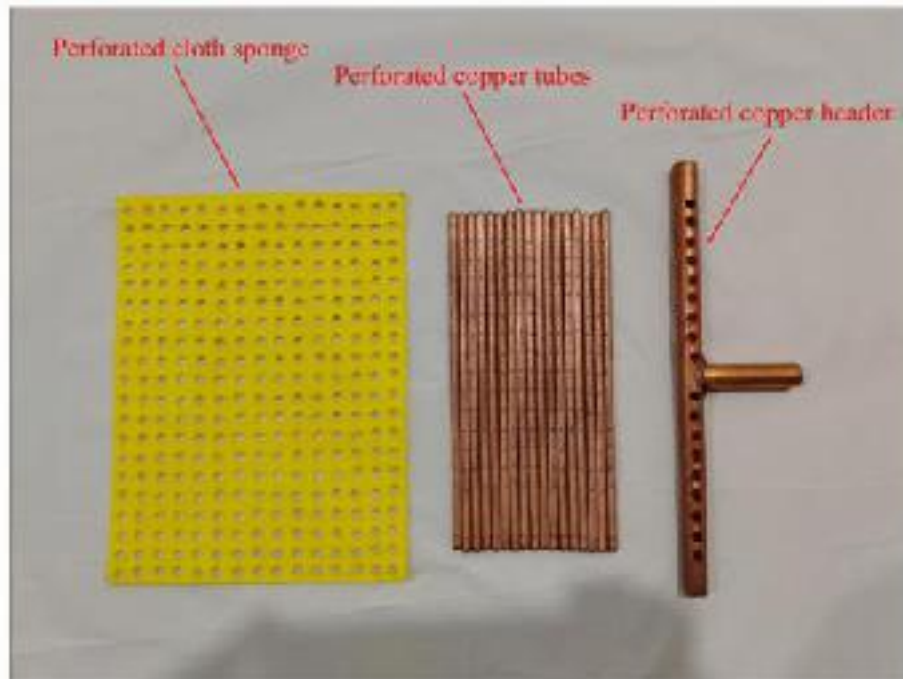


Fig. 4.12 Prepared parts regarding water distribution system

After the employed sponge has been perforated with 300 holes, it was placed on the bed plate. The bed plate was perforated with the same number of holes in a way that each hole from the sponge and the plate aligns. Besides, the holes in the bed plate were larger (about 7 mm) to let the water passes through them by the effect of the gravitational force. The implemented holes in the bed plate for system construction relative to the water distribution system are presented in Fig. 4.13. That being so, the water dripping from the copper tubes holes onto the cloth sponge, the cloth sponge distributes the water evenly among the tubes and when it gets fully soaked, the excess water falls down

through the bed plate's perforations alongside the evaporative surface. Finally, the remained water (unevaporated) drops down into the water sink at the bottom of the HMX to be discharged out of the system.

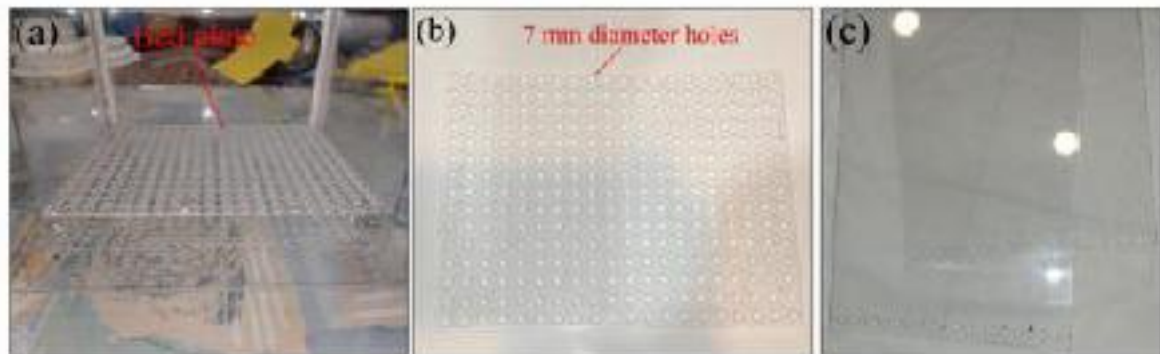


Fig. 4.13 (a) Bed plate (upside down); (b) 7mm holes in bed plate; (c) holes made in front and back acrylic sheets for copper tube insertion

4.5 SYSTEM ASSEMBLY

The fabricated tubes must be installed with 10 mm apart so as to produce hypothetical working channels boundary in between them. This is made possible by top and bottom plates that are perforated with 300 holes and these holes are perfectly aligned to ensure the primary channels straightness. The process of puncturing has been conducted through several stages. First, the designed dimensions of each square element (1 cm \times 1 cm) were sketched on a paper as shown in Fig. 4.14(a) (the blue squares) and the placement of each perforation was precisely marked as shown in Fig. 4.14(b) (the red intersected lines).

Fig. 4.14(c) illustrates the aligned top and bottom plates prior to the perforation process which was made by a drilling machine, and the final look of the perforated plates are shown in Fig. 4.14(d) and (e). Likewise, the perforations regarding the bed plate of the water distribution system were made with the same procedures.

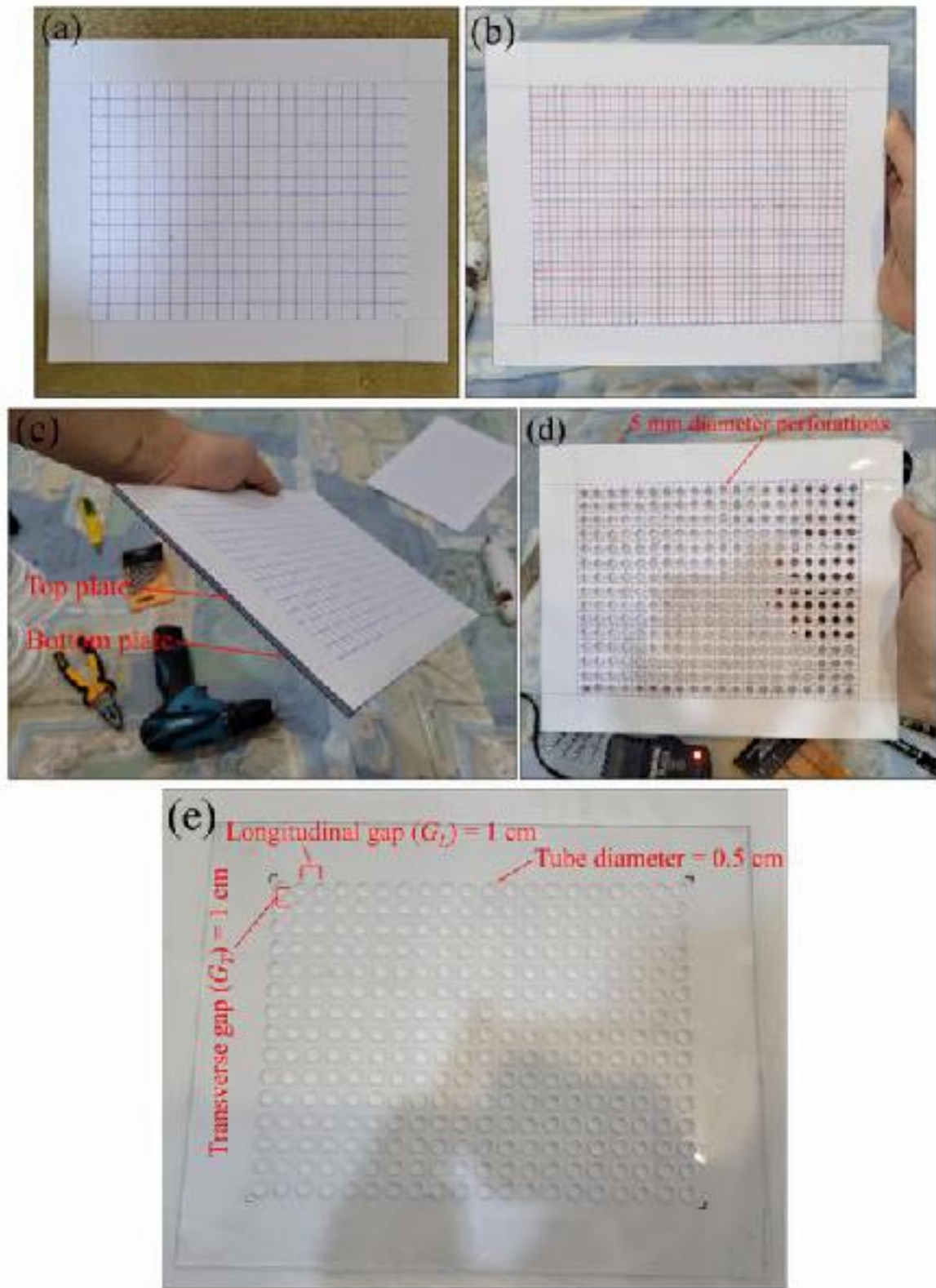


Fig. 4.14 (a) Element framing; (b) Tubes location determination; (c) Aligning top and bottom plates; (d) Perforated plates; (e) Finished plates with referenced dimensions

Afterwards, the acrylic sheet has been designed and cut in to pieces according to the HMX dimensions to compose the structure of the system as shown in Fig. 4.15(a). In addition, aluminum bars were employed to hold the plates in place and to give the cooler's structure an extra rigidity as can be seen in Fig. 4.15(b). All the acrylic sheets, including the aluminum bars, have been welded together using a super adhesive glue which was characterized by instant solidification and high bonding strength; besides, bolts and nuts have been used as well regarding this matter.



Fig. 4.15 (a) Prepared acrylic sheets to compose the cooler's structure; (b) Cooler's structure reinforced with aluminum bars

Thereafter, the perforated cloth sponge has been placed on top of the bed plate, then the fabricated tubes were inserted into the system one by one (as shown in Fig. 4.16(a)), and they have been glued to the plate to avoid the displacement and fluctuation. The outer circumference of each tube that has been inserted into the inlet air chamber was glued all over to ensure the sealing so as the accumulated water at the sink does not leak (refer to Fig. 4.16(b)). Subsequently, when all the tubes have been placed in the cooler to form the

HMX, then the water distribution system has been integrated into the system by inserting the perforated copper tubes in between the mounted primary channels/tubes on top of the cloth sponge. All the insertion points of the copper tubes have been sealed with transparent silicon glue to prevent any air exchange between the HMX and the surrounding. The final shape of the water distribution system is presented in Fig. 4.17.

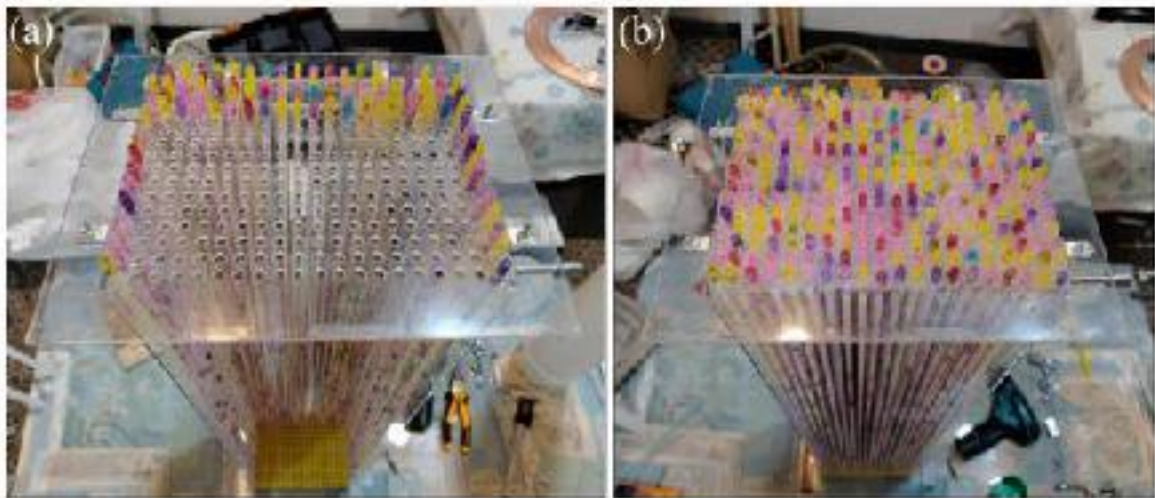


Fig. 4.16 (a) Tubes insertion into the system (upside down); (b) Glued tubes to prevent leakage



Fig. 4.17 Dedicated water distribution system for proposed DPEC

Regarding the air ducting system that delivers the airflow into and carries it away from the HMX, several components have been purchased, and others have been hand made as presented in **Fig. 4.18**. The utilized components include different sized fittings, T-joints, elbows, air dampers, and reduced duct wedges. They were designed in a way that all the channels receive the equivalent amount of airflow which is fundamental to ensure each primary and working channels pair produce the similar thermal performance.



Fig. 4.18 Air ducting components

Eventually, after preparing and constructing all the required parts, they have been assembled together to form the final cooling unit as can be seen from **Fig. 4.19**. To acquire the accurate results and to minimize the heat exchange with the surrounding, all the ducting system have been coated with a thermal insulation layer during the test.

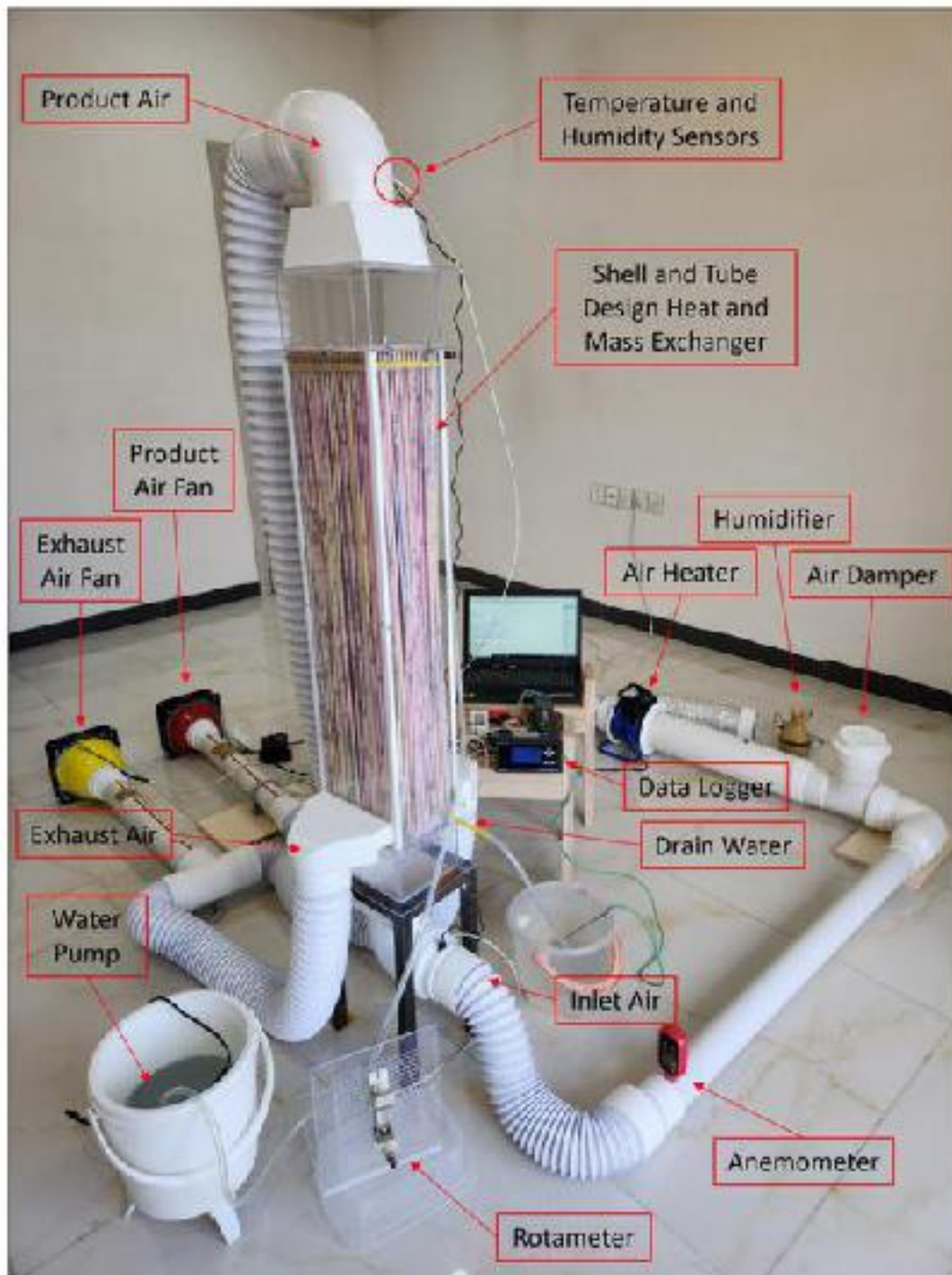


Fig. 4.19 Constructed STX-DPEC

4.6 EXPERIMENT SET-UP

4.6.1 Air Handling Unit Design and Construction

So as to conduct the experimentations under a wide range of ambient conditions, therefore, an air handling unit (AHU) were designed and

manufactured to generate a desired weather condition for the cooler. A schematic diagram of the AHU is shown in Fig. 4.20. The constructed AHU includes one electrical heater, one humidifier, two air dampers, two air filters, and several ducting components. Thus, the fabricated AHU could produce a summer-like condition for the cooler, besides, it can simulate the inlet air to a desired humidity ratio for the purpose of testing the unit under humid climate condition.

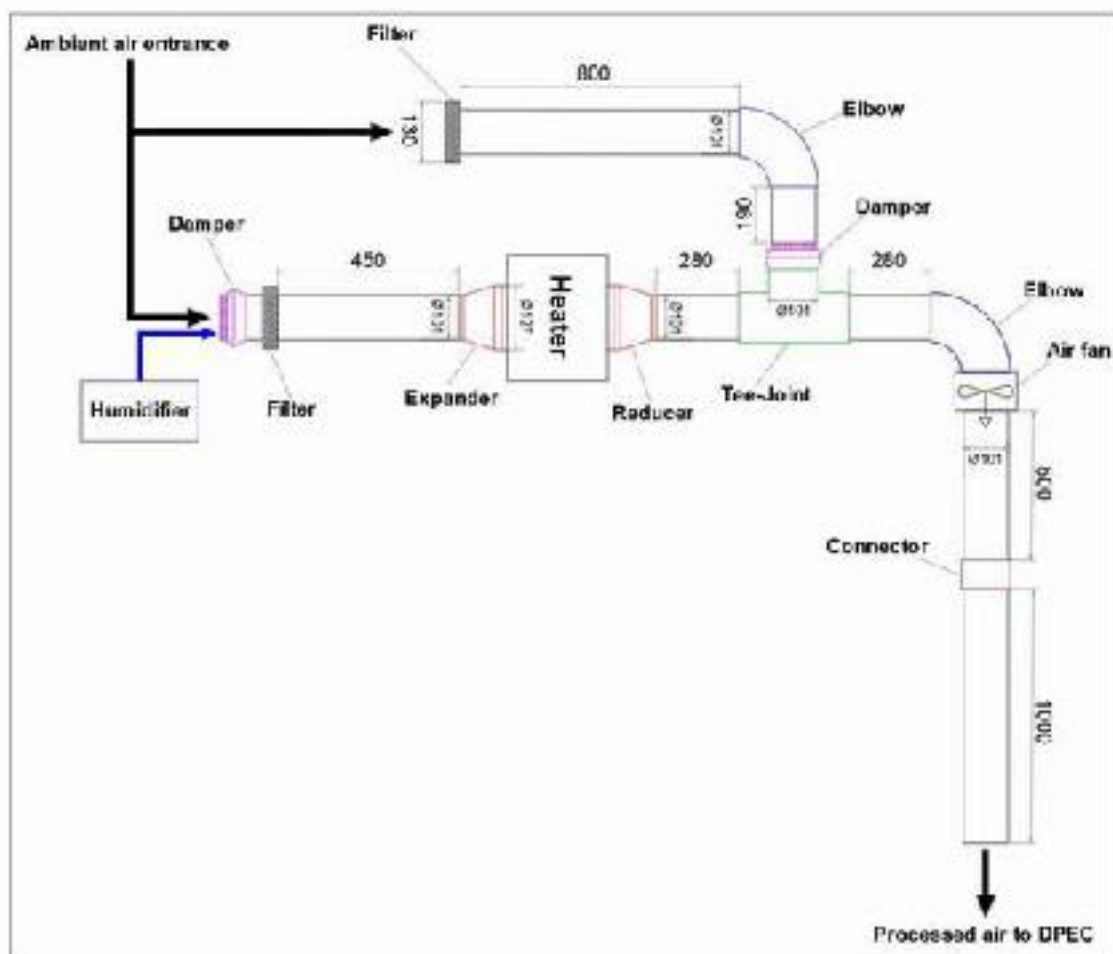


Fig. 4.20 Air handling unit prior to the DPEC entrance

The dew-point temperature was selected as the base parameter for the experimentations as it is the crucial parameter for indicating the thermal performance of the DPEC. Moreover, the precise air temperature obtained through the organization of the air dampers. The first air damper is placed prior

to the heater, and the second one is placed after the heater to regulate the amount of intake air through which the air temperature can be controlled to the desired limit. In addition, a 1500 mm pipe has been utilized in the AHU prior to the DPEC which is enough length to yield a fully developed air flow to emphasize an even air distribution over the primary channels of the HMX (Xu et al., 2017). The purpose of using the air fan inside the AHU was to compensate a part of the pressure lose caused by the ducting.

4.6.2 Measurement and Instruments

The deployment of the parameter measurement instruments is illustrated in Fig. 4.21. This schematic diagram is the exact replicant of the experimental set-up for the measuring instruments.

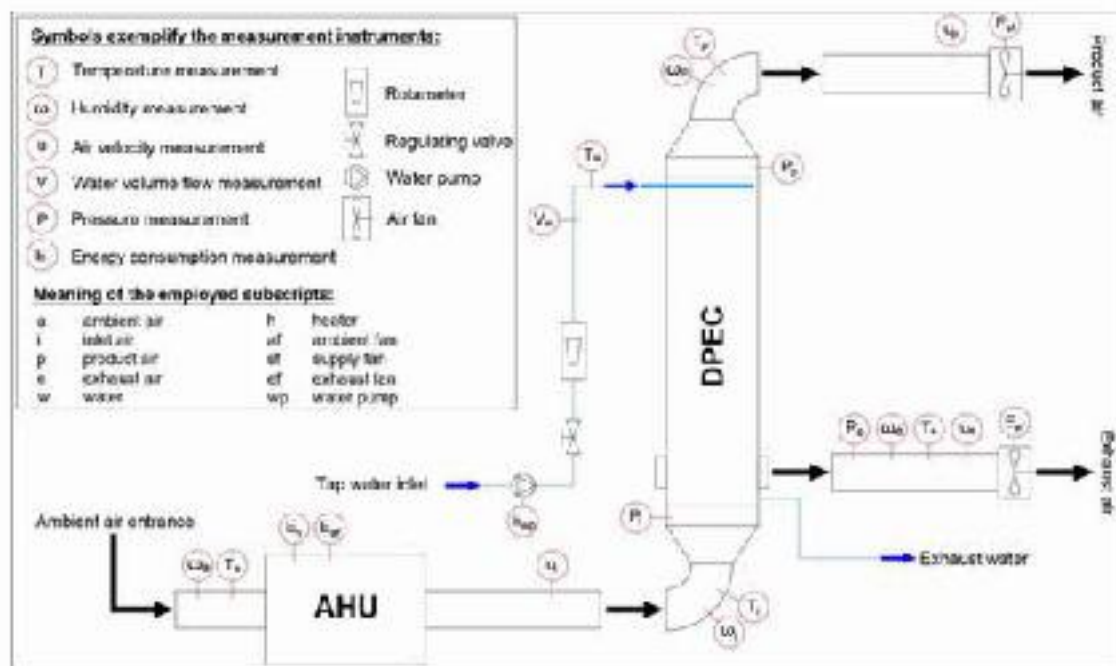


Fig. 4.21 Parameter measurement instruments organization

As it shown, the inlet, product, and exhaust air temperature and humidity measurement sensors were located right at the entrance and exit points to acquire a precise measurement before the air potentially exchange any heat with the ambient. Details of the measured parameters alongside with the employed

instruments for their measurements have been presented in **Table 4.2**. The table also includes the measuring range, resolution, and accuracy of each instrument.

Table 4.2 Experimental measured parameters and employed instruments

Parameter	Employed instrument	Measuring range	Resolution	Accuracy
Ambient air dew-point and dry-bulb temperature	Pro'sKit MT-4014	-10~50 °C	0.1 °C	±1 °C
Ambient air relative humidity	Pro'sKit MT-4014	0-100% RH	0.1% RH	±3% RH
Inlet air dry-bulb temperature	K-type thermocouple	0-400 °C	0.1 °C	±0.5%
Inlet air relative humidity	STC-3028 hygrometer	0~100% RH	0.1% RH	±0.1% RH
Inlet air velocity	Vane-Anemometer UNI-T (UT363)	0~30 m/s	0.1 m/s	±0.5 m/s or ±5% of reading
Product air dry-bulb temperature	K-type thermocouple	0-400 °C	0.1 °C	±0.5%
Product air relative humidity	STC-3028 hygrometer	0-100% RH	0.1% RH	±0.1% RH
Product air velocity	Vane-Anemometer UNI-T (UT363)	0~30 m/s	0.1 m/s	±0.5 m/s or ±5% of reading
Exhaust air dry-bulb temperature	K-type thermocouple	0-400 °C	0.1 °C	±0.5%
Exhaust air relative humidity	STC-3028 hygrometer	0~100% RH	0.1% RH	±0.1% RH
Exhaust air velocity	Vane-Anemometer UNI-T (UT363)	0~30 m/s	0.1 m/s	±0.5 m/s or ±5% of reading
Feed water temperature	VOLTCRAFT K101	-200~1370 °C	0.1 °C	±0.3%
Drain water temperature	VOLTCRAFT K101	-200~1370 °C	0.1 °C	±0.3%
Feed water flowrate	Variable area Rotameter (FTI SERIES 630)	100~1000 ml/min	—	±5% of reading

Moreover, **Fig. 4.22** demonstrates the visual representation of the utilized instruments for the experimentations. The measuring instruments were calibrated prior to their usage for data acquisition. For the experimentation, regarding the temperature measurements, K-type thermocouples (PT100) has

been used to measure the inlet, product, and exhaust air dry-bulb temperatures as shown in **Fig. 4.22(a)**. The utilization of this type of temperature measuring instruments is accurate enough for such application and it has been widely used to monitor the thermal performance of DPECs. For humidity measurement, STC-3028 hygrometer has been employed to monitor the relative humidity variation at inlet, product, and exhaust vents of the cooler (refer to **Fig. 4.22(b)**). Furthermore, a hand held Pro'sKit MT-4014 has been utilized to measure the thermophysical properties of the ambient air, such as dry-bulb temperature, dew-point temperature, and relative humidity (see **Fig. 4.22(c)**). Similarly, for feeding and drain water temperatures, a hand held VOLT CRAFT K101 thermocouple has been employed as illustrated in **Fig. 4.22(d)**.

The velocity measurement carried out at a location where the length of the tubes were about 13 times the diameter of the tube to emphasize the fully developed air stream (Xu et al., 2017). This way, accurate velocity measuring process can be obtained and a Vane Anemometer (UNI-T (UT363)) has been employed for this matter as shown in **Fig. 4.22(e)**. For water flow measurement, a variable area acrylic tube Rotameter has been utilized that features the integrated flow regulation valve to precisely adjust the water flowrate to desired scale (demonstrated in **Fig. 4.22(f)**). The K-type thermocouples were connected to the data logger (refer to **Fig. 4.22(g)**) which was programmed to read and save the data each 5 seconds interval. Thereafter, the acquired data were transferred to the computer for future analysis. During the experimentation, the operating parameters, such as temperature, humidity, and velocity, of the inlet air were controlled via adjusting the heater, humidifier, fan, and air dampers to the designed condition for each test, more explanation can be found in **Chapter 5**. All the measuring instruments were calibrated prior to the experimental work, more detail about the calibration of the sensors can be found in **Appendix A2**.

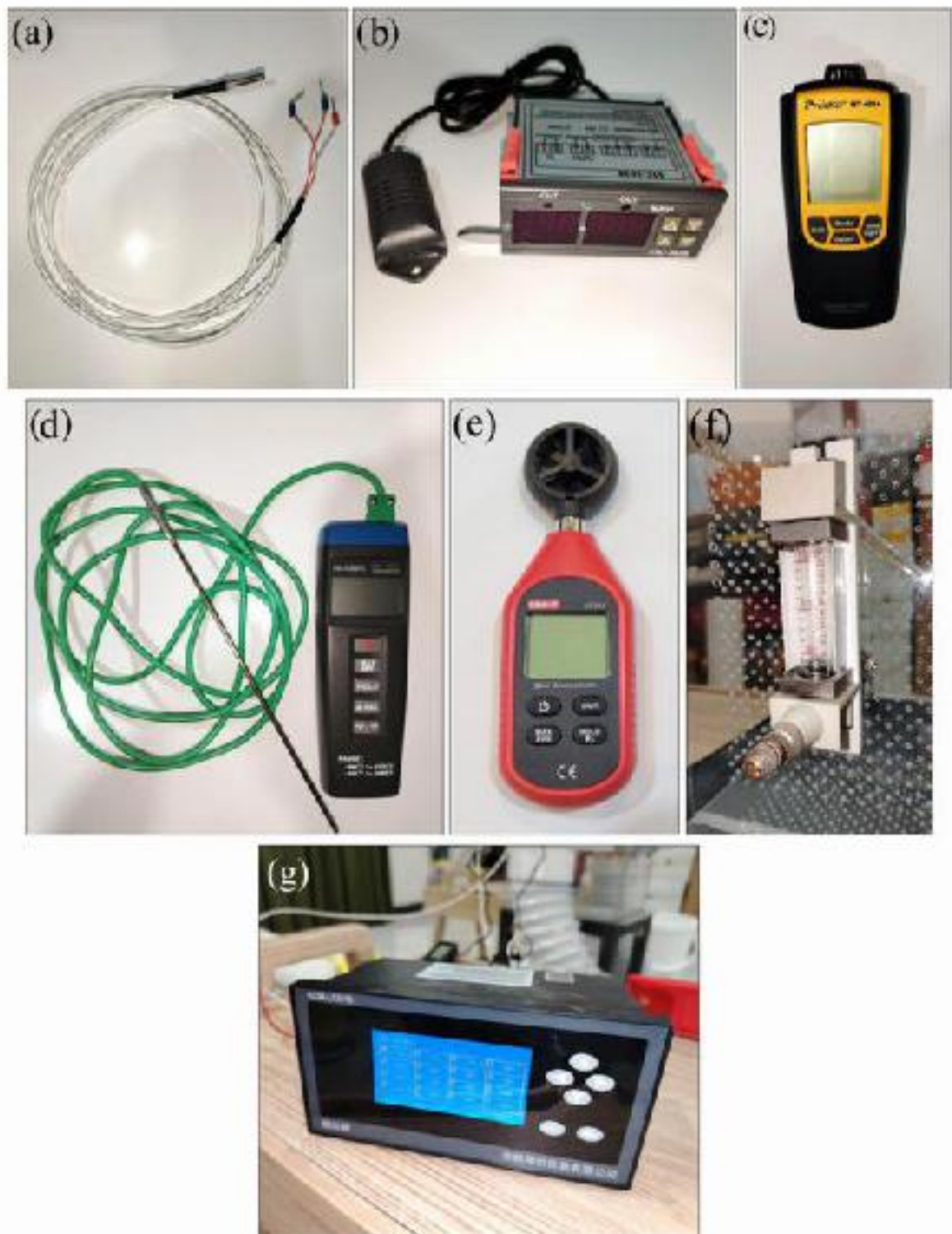


Fig. 4.22 Instruments used for parameters measurement: (a) K-type thermocouple; (b) STC-3028 hygrometer; (c) Pro'sKit MT-4014; (d) VOLTcraft K101; (e) Vane Anemometer UNI-T (UT363); (f) Variable area Rotameter; (g) data logger

4.7 UNCERTAINTY ANALYSIS

During the data acquisition in the experimental work, the uncertainty of the measured data is inevitable which is potentially caused by various sources, such as human factor, measuring instruments, and experimental environment. Therefore, conducting the uncertainty analysis for the experimental data is imperative. In the current research study, the uncertainty of the measured data caused by the measuring instruments error factor. One of the main objectives of the uncertainty analysis is to quantify the accuracy of the measuring process.

For the purpose of overall uncertainty calculation for the measured data, both types of potential errors from the sensors have been considered, namely, the systematic error and random error which are occurred from the physical measurement, connections, and data processing systems (Willink, 2022; Xu et al., 2024). The overall uncertainty (U_o) was calculated by Eq. (4.1)

$$U_o = \sqrt{U_p^2 + U_b^2} \quad (4.1)$$

where U_p is the random or precision uncertainty, and U_b is the systematic or Bias uncertainty. The precision uncertainty is a function of standard deviation (SD) that can be calculate as

$$SD = \sqrt{\frac{\sum_{i=1}^N (x_i - \bar{x})^2}{N-1}} \quad (4.2)$$

$$U_p = SD \cdot N^{-0.5} \quad (4.3)$$

where x_i is measured parameter, \bar{x} is the mean value of the measured parameter, and N is the number of measurement times. Moreover, the Bias uncertainty, which is claimed as the resolution or error of the measuring instrument, can be calculated as

$$U_b = E_{max} \cdot 3^{-1} \quad (4.4)$$

where E_{max} is the maximum error which is permanently given by the manufacturer. The results from the uncertainty calculation are presented in **Table 4.3**.

Table 4.3 Uncertainty of the measured parameters

Independent parameter	Mean value \bar{x}	Random uncertainty U_p	Standard deviation SD	Bias uncertainty U_b	Overall uncertainty U_o
Inlet air temperature (°C)	40.4	0.109	0.245	0.166	± 0.198 °C $\pm 0.49\%$
Product air temperature (°C)	21.18	0.085	0.192	0.166	± 0.186 °C $\pm 0.88\%$
Exhaust air temperature (°C)	26.7	0.134	0.300	0.166	± 0.213 °C $\pm 0.79\%$
Inlet air relative humidity (%)	23.76	0.143	0.321	0.033	± 0.146 % $\pm 0.61\%$
Product air relative humidity (%)	69.06	0.211	0.473	0.033	± 0.213 % $\pm 0.31\%$
Exhaust air relative humidity (%)	99.62	0.111	0.249	0.033	± 0.116 % $\pm 0.116\%$
Inlet air velocity (m/s)	1.36	0.024	0.054	0.0226	± 0.033 m/s $\pm 2.42\%$
Product air velocity (m/s)	1.26	0.025	0.055	0.0220	± 0.032 m/s $\pm 2.54\%$
Exhaust air velocity (m/s)	0.86	0.027	0.060	0.0143	± 0.031 m/s $\pm 3.61\%$
Inlet water flowrate (L/h)	10.16	0.151	0.338	0.169	± 0.181 L/h $\pm 1.78\%$

Table 4.4 Uncertainty of performance parameters

Performance parameter	Overall uncertainty U_o
Wet-bulb effectiveness (%)	$\pm 0.865\%$ or $\pm 0.76\%$ of ε_{WB}
Dew-point effectiveness (%)	$\pm 0.764\%$ or $\pm 0.978\%$ of ε_{DP}
Cooling capacity (W)	± 4.657 W or $\pm 4.43\%$ of Q_c

CHAPTER 5

RESULTS AND DISCUSSION

5.1 INTRODUCTION

In this chapter, first, the developed numerical simulation model will be validated against the obtained experimental results from the published literatures. The results from the comparison will be presented and the deviation rates will be demonstrated. Thereafter, regarding the manufactured unit, the obtained results from the experimentations will be presented, analyzed, and discussed by comparing them to the results from the simulations executed under the identical boundary conditions as the experimentations, thus the accuracy of the developed mathematical model can be further assessed. Moreover, a thorough numerical investigation will be carried out so as to dive deep into the parametrical analysis and extensively investigating the effect of each geometrical, climatical, and operational parameters on the thermal and energy performances of the innovative DPEC. Furthermore, to show the superiority of the proposed DPEC, its performance compared to the widely used flat-plate type DPEC for both possible air-water flow configurations. For this reason, the first and second laws of thermodynamical analysis have been adopted to demonstrate and compare all the performance aspects of the proposed DPECs.

5.2 MODEL VALIDATION WITH PREVIOUS STUDIES

In this approach, the developed numerical model was validated against three sets of experimental results from the published literatures, namely, Lin et al. (2018b) , Xu et al. (2017), and Riangvilaikul and Kumar (2010b). During the

validation process, identical geometrical and operational specifications have been adopted from the experimental studies as shown in **Table 5.1**.

Table 5.1 Descriptions of the published experimental studies

Parameter	Unit	(Lin et al., 2018b)	(Xu et al., 2017)	(Riangvilaikul and Kumar, 2010b)
Study Method	—	Experimental	Experimental	Experimental
System type	—	DPEC-FPX	DPEC-CPX	DPEC-FPX
Channel length	cm	60	100	120
Channel width	cm	15	80	8
Channel height/gap	cm	0.3	—	0.5
H×W of each corrugated wave	cm	—	0.28×1.16	—
Ambient air temperature	°C	30–40	26–37.8	25–45
Ambient air humidity ratio	g/kg	10.5–12	8.8–19.8	6.9–26.4
Ambient air velocity	m/s	2.0	—	2.4
Inlet air flowrate	m ³ /h	—	750	—
Ratio of working to primary air	—	0.33	0.44	0.33

5.2.1 Validation I

Under the same operational and geometrical conditions (**Table 5.1**) from Lin et al. (2018b), the acquired results were validated against their experimental data, as shown in **Fig. 5.1**. It was found that the maximum discrepancy for cooling potential and product air temperature in **Fig. 5.1(a)** are about 3.3 W (2%) and 0.3 °C (1.7%), respectively. In addition, as depicted in **Fig. 5.1(b)**, the discrepancy is less than 2% when the model predicts the thermal efficiency of the cooler.

5.2.2 Validation II

The current model was further validated against the experimental data from Xu et al. (2017). They mainly used corrugated plate rather than the typical flat

plate HMX to remove the need for channel guides and increase the surface area. The inlet air conditions and geometrical specifications are given in **Table 5.1**. The validation was performed under the environment of six different cities with different climates as shown in **Fig. 5.2**, and the discrepancies were all within 4.4% when comparing the results of current model and their experimental data.

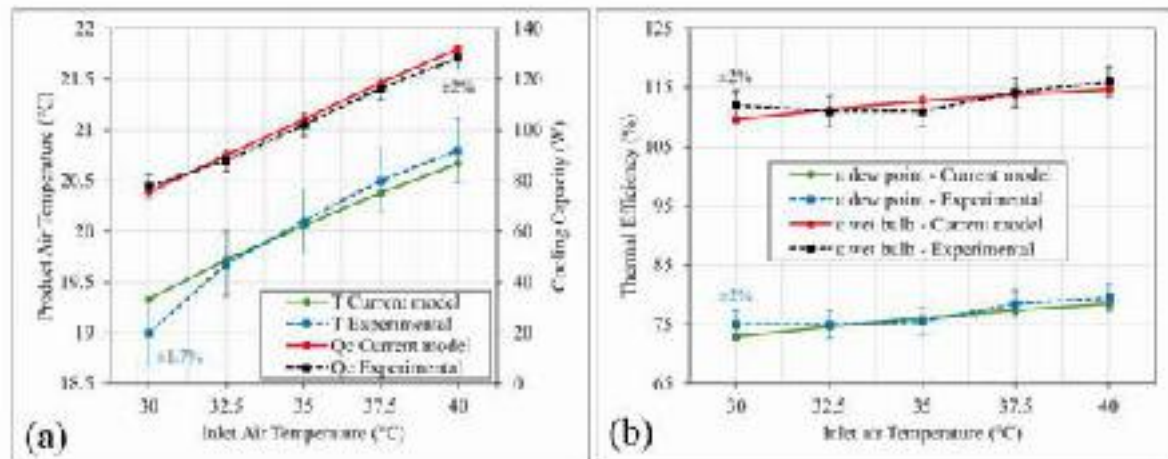


Fig. 5.1 Experimental validation of performance parameters under different inlet air temperatures provided by Lin et al. (2018b): (a) product air temperature and cooling capacity; (b) thermal efficiencies

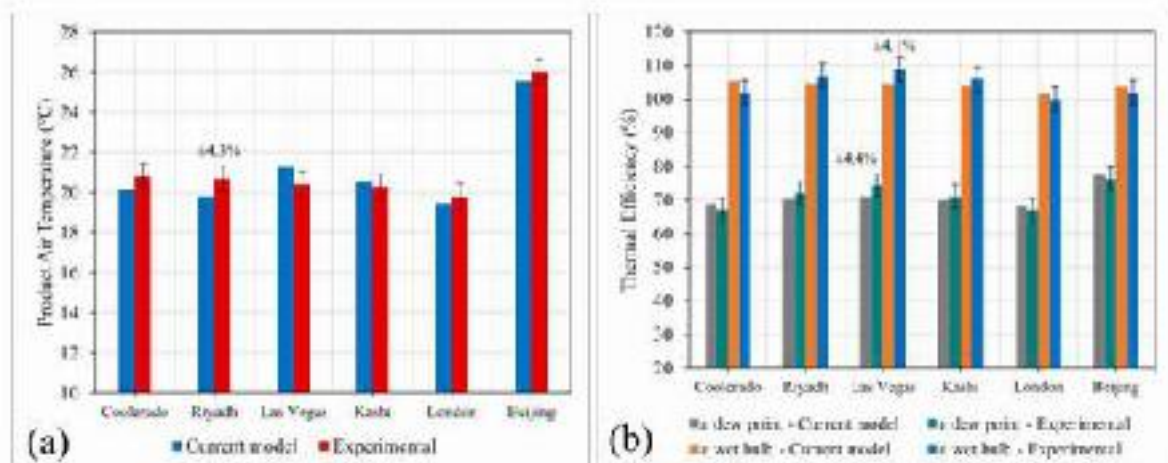


Fig. 5.2 Experimental validation under the climate conditions of different cities adopted from Xu et al. (2017): (a) product air temperature; (b) thermal efficiencies

5.2.3 Validation III

Finally, the experimental results from Riangvilaikul and Kumar (2010b) have been adopted for the validation under diverse inlet air velocity, temperature, and humidity ratio. The highest recorded discrepancy for the product air temperatures was nearly within 0.6 °C (3%) at an ambient temperature of 45 °C and humidity ratio of 6.9 g/kg, as depicted in Fig. 5.3(a), while the maximum discrepancy was accounted for 3.3% when predicting the dew point effectiveness under inlet air velocity of 1.5 m/s and humidity ratio of 19 g/kg as depicted in Fig. 5.3(b).

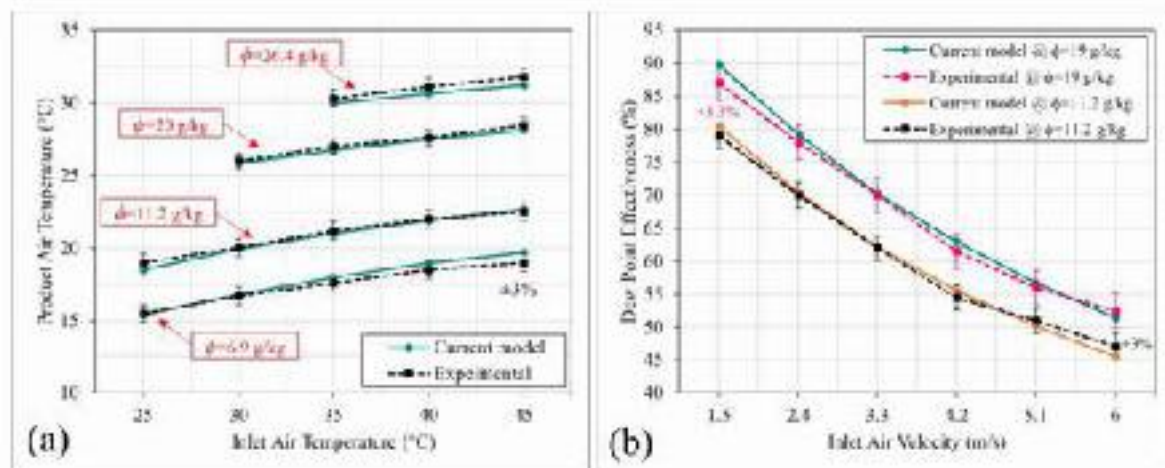


Fig. 5.3 Experimental validation under diverse ambient air temperature, humidity ratio and velocity provided by Riangvilaikul and Kumar (2010b): (a) product air temperature; (b) dew point efficiency

From the above analysis, the agreement between the developed numerical model and the experimental data is relatively high, and due to the analogy between the developed model for both flat plate and shell and tube exchangers, therefore, the current model can provide a credible result with high accuracy at predicting the performance of shell and tube type DPEC. Conducting the validation process using this approach is significant to enable assessing the performance of the proposed cooler under a wide range of geometrical, climatical, and operational conditions, from which the optimum geometrical dimensions can be selected for

the manufacturing of the unit as a preparation for the experimental work as demonstrated and explained in **Section 4.2**. Furthermore, this approach makes the investigation possible to execute a comprehensive parametrical analysis (explained in detail in **Section 5.4**), otherwise it wouldn't be attainable through the experimentations.

5.3 VALIDATION WITH THE CURRENT CONSTRUCTED UNIT

With the help of the numerical investigation, the optimum geometrical dimensions were selected as the base for construction of the shell and tube design heat and mass exchanger of DPEC as explained intensively in **Chapter 4**. The constructed unit has been operated and put under the experimentations. So as to widely evaluate the unit's performance, various operational related parameters have been investigated under laboratory experiments. The measuring instruments and sensors were attentively configured and located so as to enable accurate data measuring and recording of temperature, relative humidity, and air flow velocity of three air streams, namely, entrance, product, and exhaust air streams (more detail can be found in **Section 4.6**).

During the experimentation, the performance of the unit has been evaluated under varying inlet air temperature, inlet air humidity ratio, inlet air flowrate, and air ratio. These four parameters have a critical effect on DPEC's performance. Therefore, they have been considered as varying parameters for the experimentations for the current study. The experimental results are presented in **Table 5.2** and the simulation results under the exact boundary conditions of the experimentations are presented in **Table 5.3**.

The results were obtained by carrying out the following experimental procedures:

- (1) Power on the cooling unit, air handling unit, and measuring instruments.
- (2) Regulating the product air and exhaust air fans speed to coincide the required air flowrate inside the primary and working channels to meet the pre-set air ratio.
- (3) Adjusting the water flowrate via integrated rotameter and regulating valve in the water distribution system as well as the water temperature to achieve the pre-set water flowrate and temperature.
- (4) Regulating the electrical air heater to obtain the pre-set temperature of entrance air.
- (5) During the experimentation, the data were recorded when the system reached to steady state condition, for each measurement, it has been waited for about 10 to 15 minutes to let the operating condition stabilize when regulating for a new measurement, i.e., less than 0.5% alteration per minute for each parameter measurement.

5.3.1 Performance Testing Under Varying Inlet Air Temperature (Test I)

In this test, a series of experiments were carried out under different inlet air temperatures ranging from 25°C to 50°C. The variation of air temperature was achieved by regulating the electrical air heater inside the AHU alongside with adjusting intake air streams through both air dampers (see Fig. 4.20). During the test, the product air flowrate was adjusted to 17.78 m³/h and the exhaust air flowrate was adjusted to 11.87 m³/h to yield the pre-set air ratio of 0.4 and pre-set entrance air flowrate of 29.65 m³/h. Further operational conditions of the inlet air regarding Test I can be found in Table 5.2. In addition, the inlet water temperature and water flowrate were regulated to 23 °C and 10 L/h, respectively.

Table 5.2 Experimental set-up and results

Test condition	Operational conditions of entrance air				Experimental (measured) results						
	Temperature (°C)	Humidity ratio (g/kg)	Air flowrate (m ³ /h)	Air ratio	Product air temperature (°C)	Product air RH (%)	Exhaust air temperature (°C)	Exhaust air RH (%)	η_{wh} (%)	η_{dp} (%)	Q_c (W)
Test I: varying air temperature	25	10.815	29.673	0.4	20.4	71.9	21.9	99.7	72.24	47.12	27.45
	30	10.815	29.673	0.4	20.8	70.2	23.7	99.8	94.05	62.32	53.97
	35	10.815	29.673	0.4	20.9	69.7	24.7	99.8	106.1	71.35	81.38
	40	10.815	29.673	0.4	21.1	68.9	26.3	100	112	76.33	107.4
	45	10.815	29.673	0.4	21.2	68.5	27.6	99.9	115.9	79.97	133.1
	50	10.815	29.673	0.4	21.4	68.0	28.9	100	117.9	82.27	157.5
Test II: varying humidity ratio	40	5.2	29.673	0.4	17.0	43.2	22.6	99.7	109.9	64.71	129.7
	40	8.22	29.673	0.4	19.9	56.6	23.9	99.8	107.7	69.55	113.8
	40	10.5	29.673	0.4	21.1	66.9	26.3	99.8	112	76.33	107.4
	40	12.1	29.673	0.4	21.3	76.0	26.9	100	116.6	81.18	106.4
	40	14.5	29.673	0.4	21.3	90.7	27.3	100	128.5	92.52	106.7
	40	16.7	29.673	0.4	22.1	99.1	27.9	100	135	99.6	102.4
Test III: varying air flowrate	40	11.780	21.200	0.4	21.9	71.4	27.1	99.7	111.4	77.19	73.52
	40	11.780	25.434	0.4	21.8	71.8	26.9	99.7	112.1	77.61	88.71
	40	11.780	29.673	0.4	21.5	73.1	26.8	99.4	113.9	78.89	105.2
	40	11.780	33.912	0.4	21.4	73.6	26.3	99.6	114.5	79.32	120.9
	40	11.780	38.151	0.4	21.3	74.0	27.1	99.2	115.1	79.75	136.7
	40	11.780	42.390	0.4	21.4	73.6	27.3	99.2	114.5	79.32	151.1
	40	11.780	46.630	0.4	21.5	73.1	27.3	99.1	113.9	78.89	165.3
Test IV: varying air ratio	40	12.50	29.673	0.2	22.2	74.3	28.9	100	112.8	79.00	135.1
	40	12.50	29.673	0.3	21.9	75.6	27.2	100	114.7	80.33	120.2
	40	12.50	29.673	0.4	21.5	77.5	26.9	99.8	117.2	82.11	105.3
	40	12.50	29.673	0.5	21.4	77.9	25.6	99.4	117.9	82.55	88.22
	40	12.50	29.673	0.6	21.3	78.5	24.7	99.6	118.5	82.99	70.96
	40	12.50	29.673	0.7	21.2	78.9	24.5	99.2	119.1	83.44	53.5
	40	12.50	29.673	0.8	21.1	79.4	23.9	99.2	119.8	83.88	35.86

Table 5.3 Simulation results under the boundary conditions of experimentations

Test condition	Operational conditions of entrance air				Simulation results						
	Temperature (°C)	Humidity ratio (g/kg)	Air flowrate (m ³ /h)	Air ratio	Product air temperature (°C)	Product air RH (%)	Exhaust air temperature (°C)	Exhaust air RH (%)	η_{wb} (%)	η_{ap} (%)	Q_c (W)
Test I: varying air temperature	25	10.815	29.673	0.4	20.24	72.66	21.53	100	74.75	48.76	28.39
	30	10.815	29.673	0.4	20.31	72.35	23.14	100	99.09	65.66	56.86
	35	10.815	29.673	0.4	20.36	72.13	24.67	100	110.2	74.06	84.48
	40	10.815	29.673	0.4	20.41	71.91	26.12	100	116.1	79.1	111.3
	45	10.815	29.673	0.4	20.45	71.72	27.5	100	119.5	82.47	137.2
	50	10.815	29.673	0.4	20.49	71.55	28.8	100	121.6	84.89	162.5
Test II: varying humidity ratio	40	5.2	29.673	0.4	16.8	43.73	23.79	100	110.8	65.27	130.8
	40	8.22	29.673	0.4	19.04	59.75	25.2	100	112.3	72.51	118.6
	40	10.5	29.673	0.4	20.41	69.84	26.12	100	116.1	79.1	111.3
	40	12.1	29.673	0.4	20.92	77.80	26.49	100	119	82.81	108.5
	40	14.5	29.673	0.4	21.87	87.63	27.17	100	124.7	89.73	103.5
	40	16.7	29.673	0.4	22.71	95.56	27.79	100	130.4	96.22	98.93
Test III: varying air flowrate	40	11.780	21.200	0.4	21.15	74.72	25.79	100	116	80.37	76.55
	40	11.780	25.434	0.4	20.94	75.69	26.12	100	117.3	81.27	92.89
	40	11.780	29.673	0.4	20.8	76.34	26.4	100	118.2	81.89	109.2
	40	11.780	33.912	0.4	20.72	76.72	26.64	100	118.7	82.21	125.3
	40	11.780	38.151	0.4	20.71	76.77	26.83	100	118.8	82.26	141
	40	11.780	42.390	0.4	20.77	76.47	26.99	100	118.4	82.03	156.3
	40	11.780	46.630	0.4	20.86	76.06	27.12	100	117.8	81.61	171
Test IV: varying air ratio	40	12.50	29.673	0.2	21.84	75.92	29.6	100	115.1	80.6	137.8
	40	12.50	29.673	0.3	21.4	77.99	27.87	100	117.9	82.57	123.5
	40	12.50	29.673	0.4	21.08	79.54	26.6	100	119.9	83.96	107.7
	40	12.50	29.673	0.5	20.85	80.67	25.63	100	121.4	85	90.84
	40	12.50	29.673	0.6	20.66	81.62	24.86	100	122.5	85.82	73.37
	40	12.50	29.673	0.7	20.52	82.33	24.35	100	123.5	86.47	55.45
	40	12.50	29.673	0.8	20.4	82.93	23.83	100	124.2	87.01	37.19

The selection of water temperature was based on the natural temperature of the tap water, in another word, the underground water temperature in a typical day which was measured practically for the current study. On the other hand, most studies ((Kashyap et al., 2022a; Rasheed et al., 2022; Sverdlin et al., 2011; Xu et al., 2024)) utilized lower water temperatures (between 7°C to 20°C) for the purpose of decreasing product air temperature and increasing cooling capacity of the system, nonetheless, this approach does not consider practical as the water need to be precooled before interring the system. Consequently, using tap water is more reasonable as it always available in moderate temperature without needing for precooling.

The obtained results from Test I are presented in **Table 5.2**. The experimental results are compared to the numerical results by implementing the exact boundary conditions of experimentations in the simulation program, hence, the obtained simulation results are presented in **Table 5.3**. Moreover, **Fig. 5.4** depicts the effect of varying inlet air temperature on the product and exhaust air temperatures both in experimental and simulation. As can be noted in **Fig. 5.4(a)**, with altering the inlet air temperature from 25 °C to 50 °C, the product air temperatures of both experimental and simulation were marginally affected accounting for 1°C change in experimental data, while 0.25°C change in simulated data, yielding a maximum deviation of ±4.2% at inlet air temperature of 50°C. This can be attributed to stability in performance of the proposed DPEC under wide range of ambient temperatures.

On the other hand, the exhaust temperatures were significantly affected by the inlet air temperature (refer to **Fig. 5.4(b)**), increasing from 21.9°C and 21.53°C to 28.9°C and 28.8°C respectively for both experimental and simulation due to the occurrence of simultaneous heat and mass transfer process inside working channel. However, the exhaust air temperature recorded less deviation than the product air temperature between the experimental and

simulated data. In this regard, the maximum deviation of $\pm 2.3\%$ was recorded at 30°C entrance air temperature.

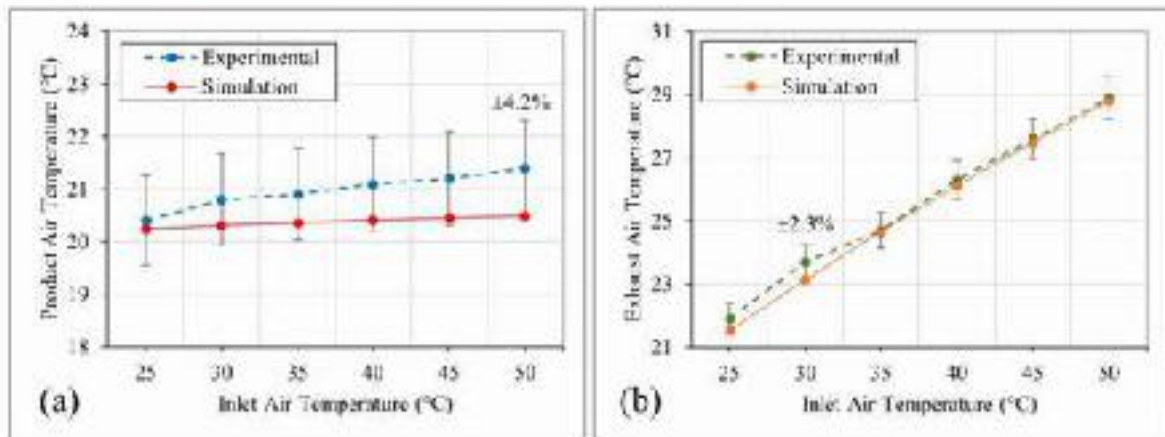


Fig. 5.4 Effect of varying inlet air temperature on the temperatures of: (a) product air; (b) exhaust air

Regarding the impact of inlet air temperature on wet-bulb and dew-point effectiveness, as illustrated in **Fig. 5.5**, they are continuously increasing with increasing the temperature. As can be seen, the theoretical thermal effectiveness was slightly better than the experimental owing to the slightly higher temperature of the experimental results. The highest deviation recorded was $\pm 5\%$ for wet-bulb effectiveness and $\pm 3\%$ for dew-point effectiveness. Besides, the wet-bulb effectiveness can reach to as high as 117.9% for the experimentation and as high as 121.6% for the simulation at ambient temperature of 50°C . Likewise, at the same temperature, the highest dew-point effectiveness was 82.27% and 84.89% for experimental and simulation, respectively. The improved thermal effectiveness at higher temperatures is the indication of more efficient thermal management by the DPEC at hotter ambient conditions. Similar to thermal efficiency, the cooling capacity of the cooler was significantly improved with increasing inlet air temperature (see **Fig. 5.6**) spanning from 27.43 W to 157.5 W for the experimental and 28.39 W to 162.5 W for the simulation yielding a maximum deviation of $\pm 3\%$ at 50°C .

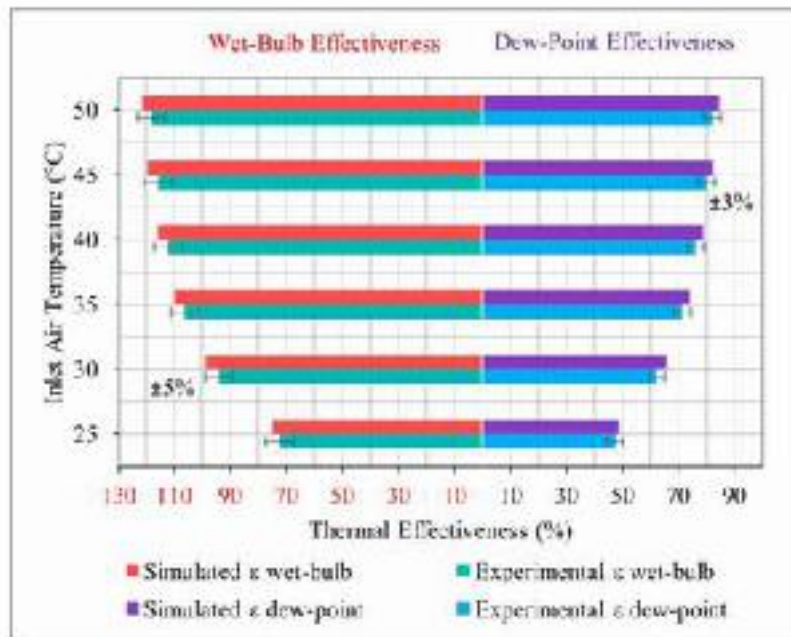


Fig. 5.5 Effect of varying inlet air temperature on thermal effectiveness

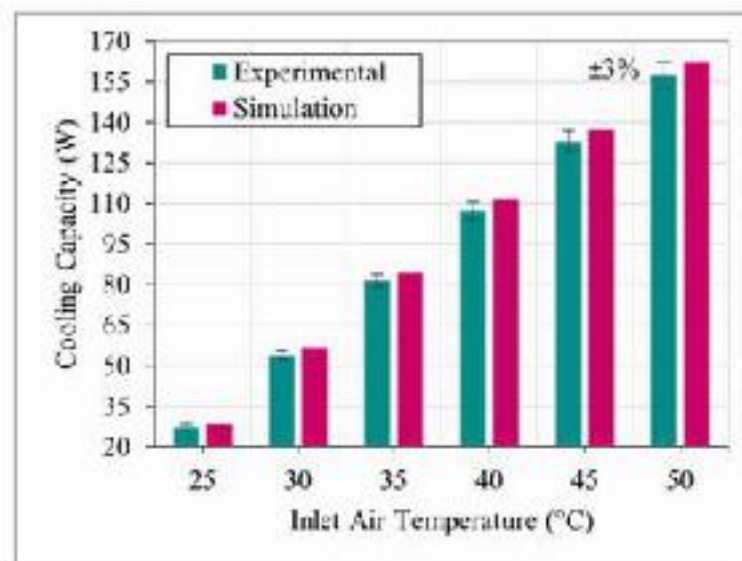


Fig. 5.6 Effect of varying inlet air temperature on cooling capacity

5.3.2 Performance Testing Under Varying Humidity Ratio (Test II)

In this test, the constructed system has been tested under varying inlet air humidity ratio spanning from dry to humid air conditions at humidity ratio of 5.2, 8.22, 10.5, 12.1, 14.5, and 16.7 gram moisture per kg dry air (g/kg). The variation of inlet air humidity ratio was achieved by the help of the humidifier

which was integrated into the AHU as illustrated in Fig. 4.20. Other operational parameters were kept similar to Test I except for the inlet air temperature which was fixed to 40°C during conducting Test II.

Unlike the effect of varying inlet air temperatures, varying inlet air humidity ratio noticeably effect the temperature of product air, as illustrated in Fig. 5.7(a), while it acted similarly regarding the exhaust air temperature, as illustrated in Fig. 5.7(b).

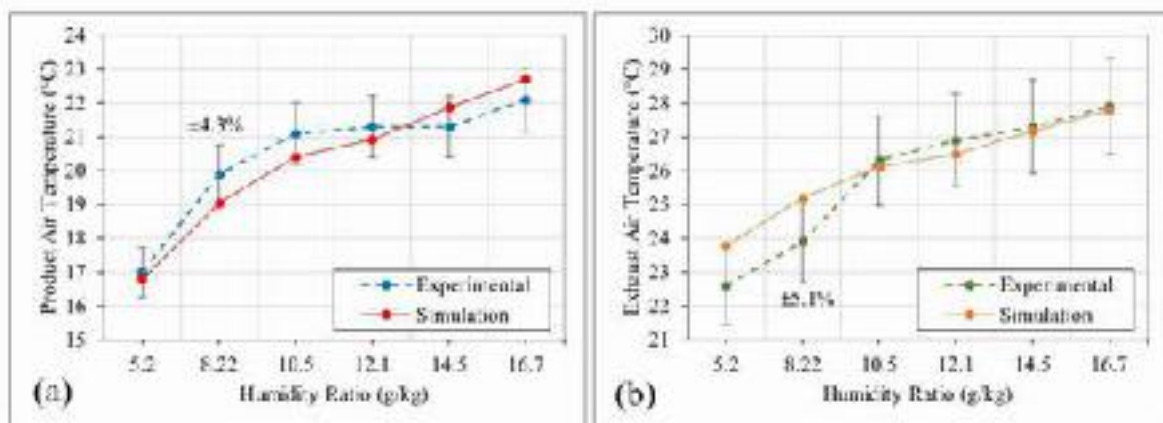


Fig. 5.7 Effect of varying inlet air humidity ratio on the temperatures of: (a) product air; (b) exhaust air

The experimental product air temperature was slightly higher than the simulation till the humidity ratio of 14.5 g/kg, thereafter, the simulation became higher than the experimental. While for the exhaust air temperature, at the beginning, the simulation temperatures were higher till the humidity ratio of 10.5 g/kg, afterwards, the experimental surpassed the simulation. The occurrence of this phenomenon can be related to the interaction of the temperature measuring instrument with the humidity. According to this statement, among all the measured data of all four tests, the ones with varying humidity ratio had the highest fluctuation rate. Nonetheless, throughout all the varying humidity ratio experimentations, when the cooler tested under the dry,

moderate, and humid air conditions, the maximum deviation recorded between the experimental and simulation data was about $\pm 4.3\%$ for product air temperature, and about $\pm 5.1\%$ for exhaust air temperature both at the humidity ratio of 8.22 g/kg. Experimentally, among all the conducted experimentations of all 4 sets of tests, the system could achieve the lowest product air temperature of 17 °C when operated under humidity ratio of 5.2 g/kg and inlet air temperature of 40°C.

Pertinent to the alteration between the experimental and simulated product air temperatures that occurred when the humidity ratio increased from 12.1 g/kg to 14.5 g/kg, similarly, the thermal efficiency and cooling capacity trends acted in the same manner, as shown in Fig. 5.8 and Fig. 5.9.

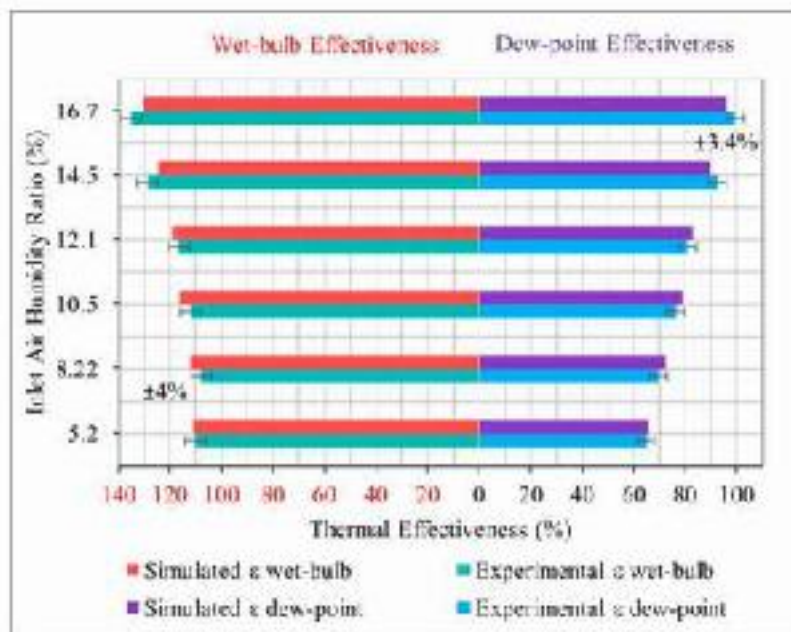


Fig. 5.8 Effect of varying inlet air humidity ratio on thermal effectiveness

These three performance parameters, i.e., wet-bulb effectiveness, dew-point effectiveness, and cooling potential, are strongly bonded to the product air temperature. Experimentally, when the unit operated under hot and humid air condition (40°C and 16.7 g/kg), the cooler could reach to 99.6% of dew-

point effectiveness which is relatively very high, as the highest dew-point effectiveness could be reached is 100% theoretically. This indicates that the system can produce a chill air with its temperature almost equates the dew point temperature of inlet air. Regarding the experimental wet-bulb effectiveness, under the same aforementioned operating conditions, the cooler could achieve a significantly high wet-bulb effectiveness of 135%. In this regard, the highest deviations recorded were $\pm 3.4\%$ and $\pm 4\%$ for dew-point and wet-bulb effectiveness, respectively. On the other hand, the cooling potential of the cooler acts in opposite manner to that of the thermal effectiveness as it produces more cooling in drier weather conditions as depicted in Fig. 5.9. Of all the recorded data, the maximum cooling capacity deviation was $\pm 4\%$ at humidity ratio of 8.22 g/kg.

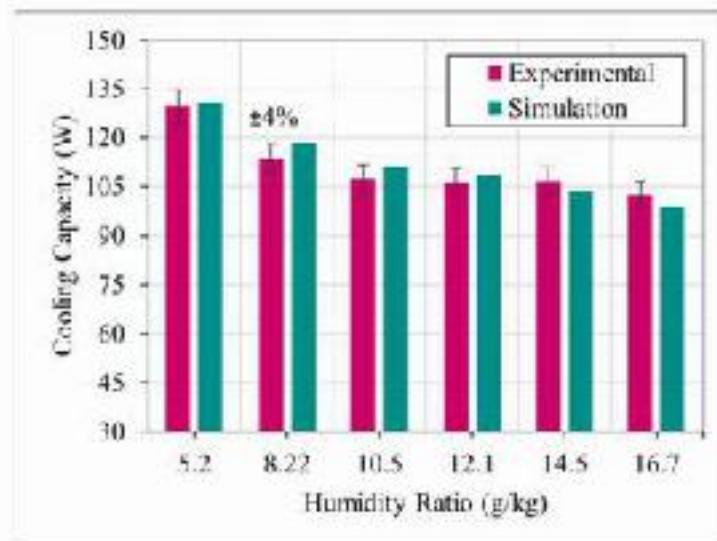


Fig. 5.9 Effect of varying inlet air humidity ratio on cooling capacity

5.3.3 Performance Testing Under Varying Inlet Air Velocity (Test III)

The variation of inlet air velocity was adjusted via three air velocity measuring instruments, referring to u_i , u_p , u_e in Fig. 4.21. The inlet air anemometer was utilized to measure the pre-set inlet air flowrate into the

system, and both the product and exhaust anemometers were utilized to measure the air flowrates at both exits of the unit and the amount of the air flowrates were adjusted via variable speed fans to coincide the pre-set inlet air flow and air ratio for the experimentation each time when altering the inlet air velocity. The inlet air velocity was varied from 1 m/s to 2.2 m/s at each dry channel entrance. By a simple calculation, each time when varying the inlet air velocity, the total amount of inlet air flowrate was found alongside with the corresponding air flow at both exits of the cooler to achieve the required air ratio.

As illustrated in **Fig. 5.10**, variation of inlet air velocity has insignificant effect on product air temperatures which was accounted for 0.4 °C experimentally and 0.29 °C numerically when inlet air velocity increased from 1 m/s to 2.2 m/s. Furthermore, as shown in **Fig. 5.10(a)**, the experimental and simulated product air temperatures agreed well as both sets of data have similar acting trends. Likewise, the exhaust air temperature acted similarly except in experimental data, the trend was slightly decreased by 0.25 °C and increased again. This occurrence is related to the temperature measuring instrument as this phenomenon did not happen in the simulation results, nevertheless, the rate of fluctuation is marginal and accounted for only 0.5 °C (or 1.8%). The highest deviation calculated for product air temperature was about $\pm 3.9\%$ and for exhaust air temperature was about $\pm 4.8\%$.

The system achieved nearly same wet-bulb and dew-point effectiveness over the span of inlet air velocity (refer to **Fig. 5.11**). This indicates the insignificant effect of inlet air velocity/flowrate on the thermal efficiency of the DPEC. The cooler could achieve in average about 113.6% and 78.7% of experimental wet-bulb and dew-point effectiveness, respectively. The wet-bulb effectiveness of more than 100% indicates the superiority of the unit which can

produce an air with its temperature lower than the ambient wet-bulb temperature and towards its dew point temperature.

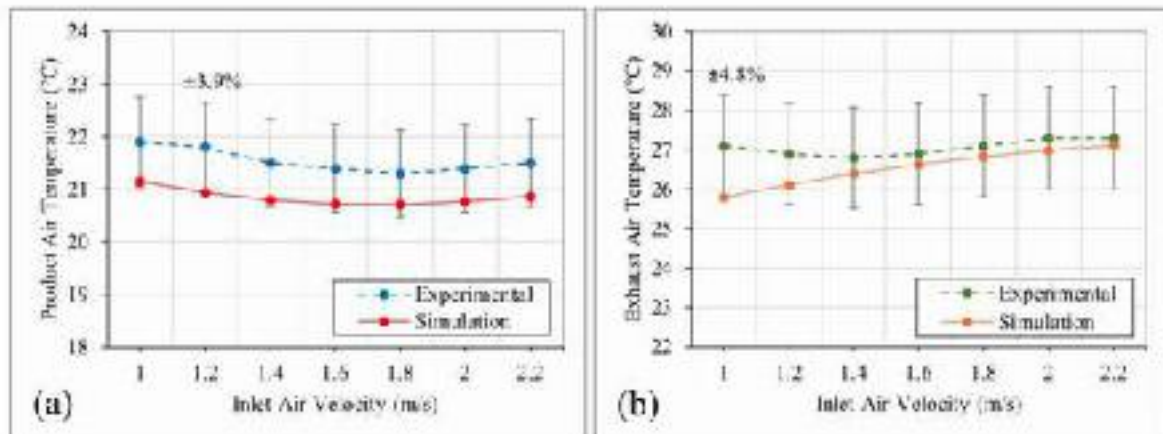


Fig. 5.10 Effect of varying inlet air velocity on the temperatures of: (a) product air; (b) exhaust air

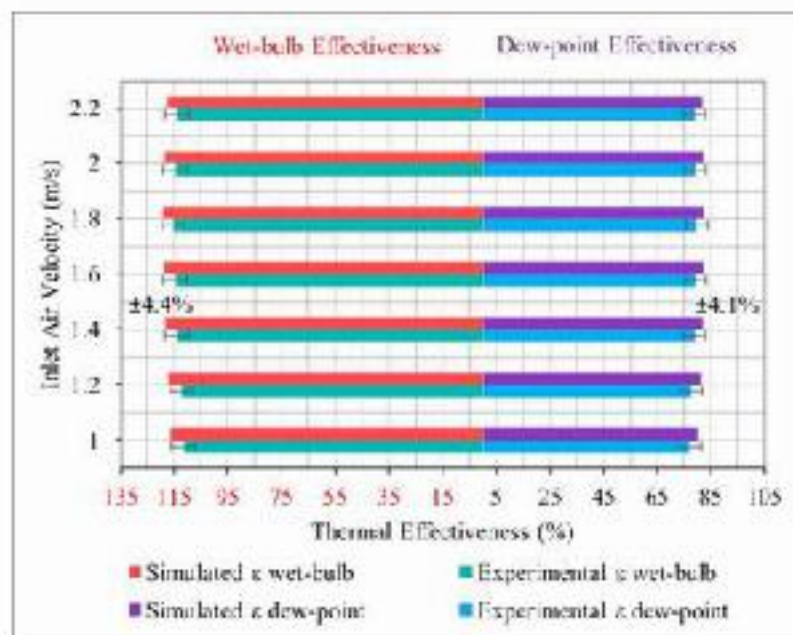


Fig. 5.11 Effect of varying inlet air velocity on thermal effectiveness

Contrast to the thermal efficiency, the cooling capacity of the DPEC is highly affected by the air velocity/flowrate, as shown in Fig. 5.12. The impact of the air velocity on the cooling potential is crucial as the cooling capacity of the constructed unit increased from 73.52 W at air velocity of 1 m/s to 165.3 W

at air velocity of 2.2 m/s which is accounted for 124% increase in cooling capacity. In addition, the maximum deviation recorded between the experimental and simulated cooling capacity was $\pm 3.3\%$.

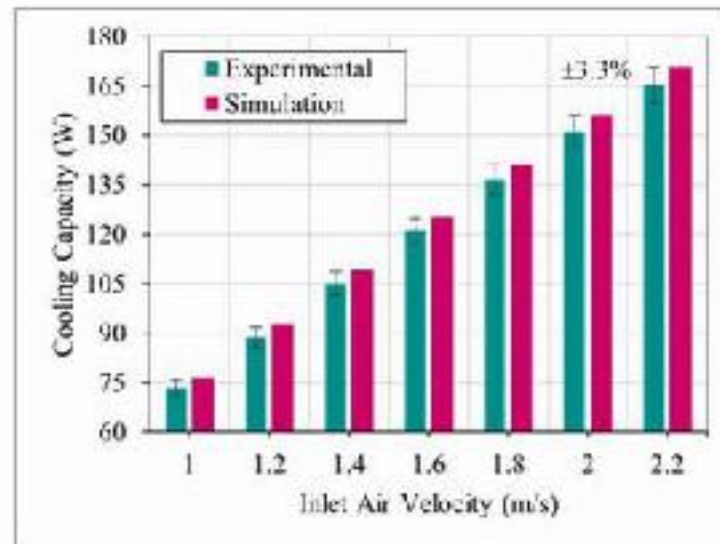


Fig. 5.12 Effect of varying inlet air velocity on cooling capacity

5.3.4 Performance Testing Under Varying Air Ratio (Test IV)

The variation of working to primary air ratio can be achieved through two methods: either by using air dampers at both exits of the DPEC so as to increase or decrease the resistance to the air flow, or by using variable speed fans. In former method, the air fan run at a constant speed (mostly at highest pre-set speed) which does not considered power friendly. In latter method, the amount of air flow inside the primary and working air channels are adjusted by regulating fan speed. In this case, less power will be consumed by the fans. Therefore, for the current study, the second method have been adopted to adjust the pre-set air ratio for the experimentation. Same method for measuring the speed of air flows in Test III has been adopted for Test IV. The pre-set operational conditions for the current test are presented in **Table 5.2**.

Regulating the air ratio results in variation of the air flowrate inside primary and working air channels. Lower air ratio indicates higher primary air flow and lower working air flow, and vice versa for higher air ratio. In this regard, as the air ratio increased, the product air temperature gradually decreased (refer to **Fig. 5.13(a)**) that lead to higher wet-bulb and dew-point effectiveness of the cooler as illustrated in **Fig. 5.14**. The fact behind this occurrence is owed to that at higher air velocity inside the working channel, more evaporation (i.e., mass transfer) occurs, and higher evaporation result in higher cooling of the working air flow. Therefore, as illustrated in **Fig. 5.13(b)**, the exhaust air temperature decreased noticeably with increasing air ratio which was accounted for 5°C reduction in experimental exhaust temperature when air ratio increased from 0.2 to 0.8. From the recorded and simulated data, the maximum deviation recorded was $\pm 3.3\%$ for product air temperature and $\pm 2.3\%$ for exhaust air temperature.

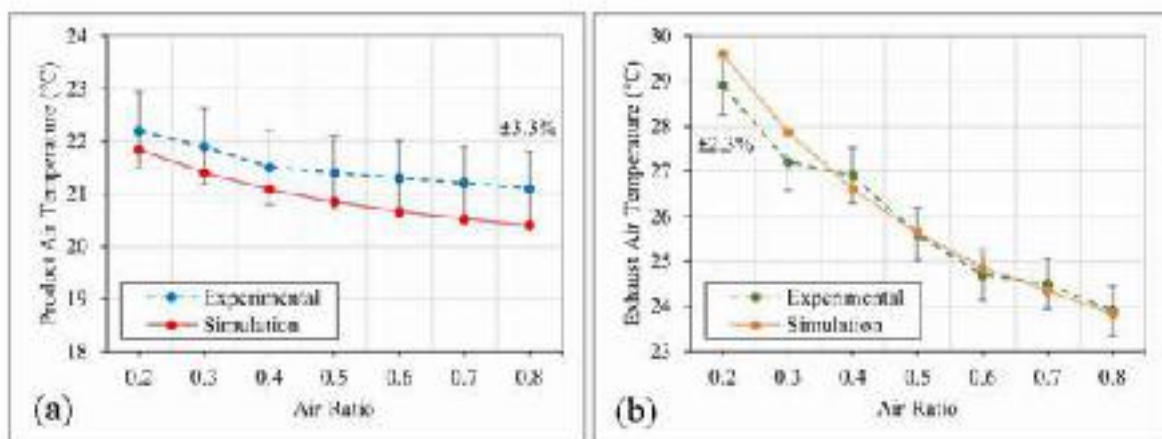


Fig. 5.13 Effect of varying air ratio on the temperatures of: (a) product air; (b) exhaust air

Under all air ratios, the experimental wet-bulb effectiveness was higher than 112% which is a good indication of superiority of the constructed system. Moreover, the working to primary air ratio is critical parameter regarding the cooling capacity of the cooler (see **Fig. 5.15**) due to the direct relation between

the cooling capacity and primary air flowrate. As explained earlier, higher air ratio means lower product air flowrate that eventually reduces cooling potential of the cooler. For instance, when the air ratio increased from 0.2 to 0.8, the experimental cooling capacity of the system was reduced from 135.1 W to 35.86 W, or in another word, 73.4% reduction in cooling potential of the cooler.

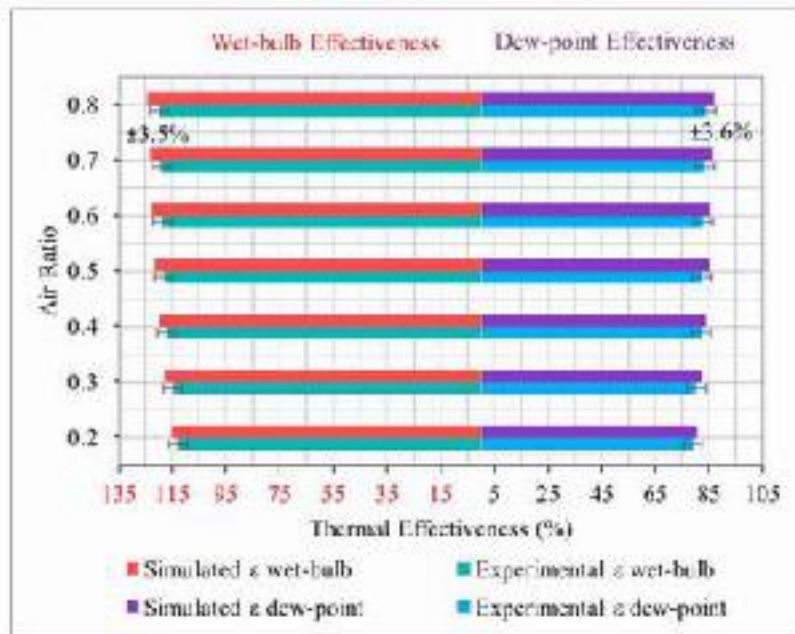


Fig. 5.14 Effect of varying air ratio on thermal effectiveness

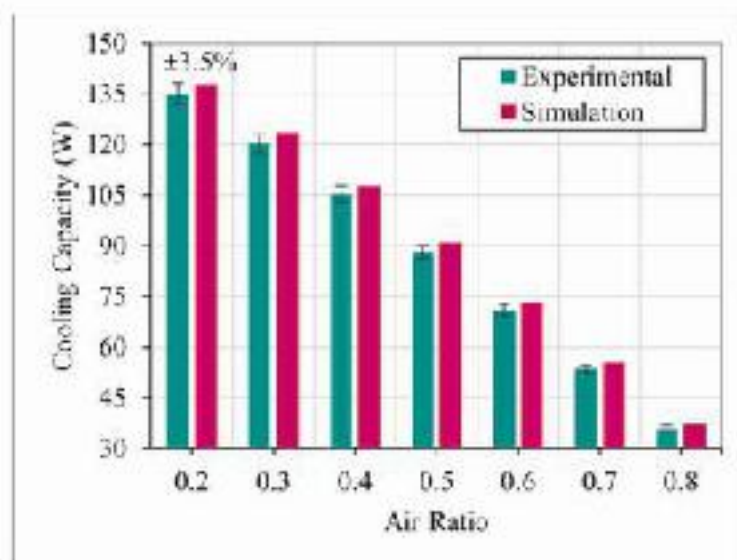


Fig. 5.15 Effect of varying air ratio on cooling capacity

Moreover, despite the experimental results presented in **Table 5.2**, a solo experiment has been carried out so as to test the cooler under extreme hot and dry ambient air condition. In the experiment, the inlet air temperature and humidity ratio were adjusted to 53°C and 5.2 g/kg, respectively, with fixing other parameters similar to that of **Table 5.2**. Under this operational condition, the system was able to reduce the product air temperature to 18.9°C (18.3°C numerically), that accounted for 34.1°C reduction in ambient temperature. With this thermal performance, the system experimentally achieved dew-point and wet-bulb effectiveness of 71.56% and 115.5%, respectively.

5.4 COMPREHENSIVE PARAMETRICAL ANALYSIS

After the developed numerical model being intensively validated with the experimental data from the published literatures and the experimental data from the current constructed unit, the model showed a good agreement when compared with the experimental data, the maximum recorded deviation was between $\pm 2.3\%$ to $\pm 5.1\%$ for different experimental data. This indicates that the simulation model can predict the performance of the proposed DPEC with a high accuracy. Therefore, the simulation model can confidently be utilized for conducting a comprehensive parametrical analysis that otherwise could not be done experimentally.

Furthermore, as the mathematical model been developed for both types of the DPECs, namely, the shell and tube type and flat-plate type, therefore, in the upcoming sections, the results from both models have been compared to each other so as to show the superiority of the proposed novel DPEC (explained in detail in **Chapter 3**). In addition, the developed models can obtain the thermal and energy performances of both cooler types in two air-water flow configurations, i.e., counter and parallel air-water flow configurations as described in **Section 3.3 (Fig. 3.3 and Table 3.2)**. The purpose for considering

these two air-water flow configurations is that the counter configuration can produce chill air with moderate water temperature, while the parallel configuration can produce cool air with chill water temperature.

Moreover, one of the most distinct feature of the dedicated simulation model is that it can obtain the variation of the physical properties along the channels of the cooler. In particular, at any point along the primary and working channels, the model can compute the air flow temperature, water flow temperature, humidity ratio, relative humidity, evaporation rate, cooling potential, latent heat transfer, sensible heat transfer, and heat and mass transfer coefficients. The comprehensive parametrical analysis of all subsequent sections are conducted under the pre-set conditions presented in Table 5.4. For the purpose of fair comparison between the two DPECs, the volumes of both exchangers are fixed, and the cross-section areas of both primary and working channels are fixed and equated for both DPECs and within each HMX to each other. For the current study, 3025 tubes were selected as with this number nearly one ton of refiguration (3.517 kW) could be achieved. The deep dive parametrical analysis are presented in the following sections.

Table 5.4 Pre-set simulation values

Parameter	Unit	Shell and tube HMX	Flat plate HMX
Exchanger size: W×D×L	cm	55×55×120	55×55×120
Cross-section area of the exchanger	cm ²	3025	3025
Cross-section area of primary channel	cm ²	0.5	0.5
Cross-section area of working channel	cm ²	0.5	0.5
Primary channel diameter/height	cm	0.798	0.5
Working channel width	cm	1.0	1.0
Channel length	cm	120	120
Ambient air temperature	°C	35	35
Ambient air moisture content	g/kg	4.0	4.0
Inlet air velocity	m/s	1.5	1.5
Ratio of working to primary air	–	0.35	0.35
Inlet water temperature	°C	23	23
Inlet water flowrate	L/h	60	60
Wall and film thickness	mm	0.2	0.2

5.4.1 Properties Variation Along the Channels

The direction of properties variation of air and water are according to flow paths along the channels. As illustrated in **Fig. 3.3**, the water always flows downward for both air-water flow configurations, entering at $z=0$ cm and leaving at $z=120$ cm. Regarding the parallel flow (PF) configuration (refer to **Fig. 3.3(a)** and **Table 3.2**), the outdoor air enters the primary channel at $z=0$ cm and leaves at $z=120$ cm, while the diverted chilled air enters the working channel at $z=120$ cm and leaves at $z=0$ cm. On the other hand, for counter flow (CF) configuration (refer to **Fig. 3.3(b)**), the state points of airflow are opposite to those of PF configuration. The above statements are reflected in the upcoming analysis with reference to pre-set conditions in **Table 5.4**.

5.4.1.1 Cooling Process on Psychrometric Chart

In this section, by utilizing the initial conditions referred to in **Table 5.4**, the change of states of airflow along the primary and working channels are depicted on the psychrometric chart as can be seen in **Fig. 5.16**. Each line was comprised from a series of 900 data (or nodes) from which 450 of primary channel and 450 of working channel, capturing the real time physical process inside the HMX. The state point S1 indicates the state of air entering the system, while the state points S2-5 indicate the air states at the primary channels exit (i.e., product air). Furthermore, the state points S6-9 indicate the state of exhaust air at the working channels exit. It can be noticed that the shell and tube type cooler in both air-water flow configurations (i.e., PF and CF) produced a better cooling and lower temperature than the flat-plate type cooler. Besides, for both STX and FPX, the counter air-water flow configuration produced a colder product air than the parallel air-water flow configuration. Further explanations regarding these phenomenon are presented in the upcoming sections.

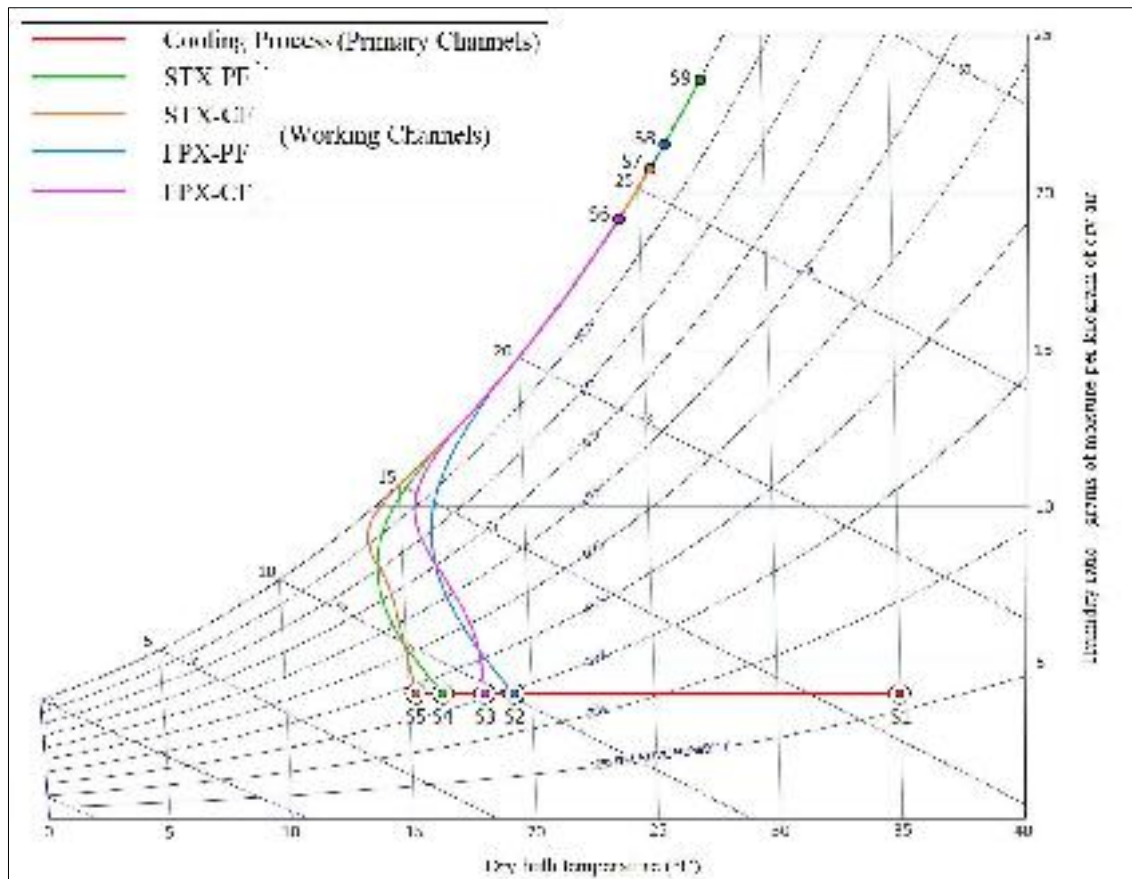


Fig. 5.16 Psychrometric presentation of cooling process along the channels

5.4.1.2 Temperature Variation Along the Channels

The variation in temperatures of air and water flows along the channels for both coolers with both air-water flow configurations are illustrated in **Fig. 5.17(a)** and **(b)**, respectively. As can be noticed, for all exchanger types, the primary air temperatures are gradually decreasing in the flow direction, where primary air enters at $z=0$ cm for PF and $z=120$ cm for CF, owing to sensible heat transfer to the channel wall, but the decreasing rate is significantly higher for the STX when compared to the FPX, which is accounted for more than 3°C at the end of the primary channels for both air-water flow configurations.

This clearly indicates FPX being outperformed by the STX with a noticeable difference. However, the temperature variation of working air is pertinent to that of water flow (refer to **Fig. 5.17(b)**). In PF configuration, the

working air enters at $z=120$ cm where water leaves the system. At the working channel entrance, due to intense evaporation, at first, the air temperature gradually decreased in the flow direction until the evaporation stabilized (refer to **Fig. 5.18(a)**); thereafter, the air temperature started increasing continuously up to $z=5$ cm, subsequently, owing to lower temperature of water than the air, the air temperature decreased again. Regarding the CF configuration, working air enters the channel at $z=0$ cm, where water enters the system as well. Here, owing to sensible heat transfer from water to working air, there is a slight increase in the temperature of working air. Similarly, the temperature of working air started to decrease at channel entry due to intense evaporation, and then it began to rise again as evaporation stabilized.

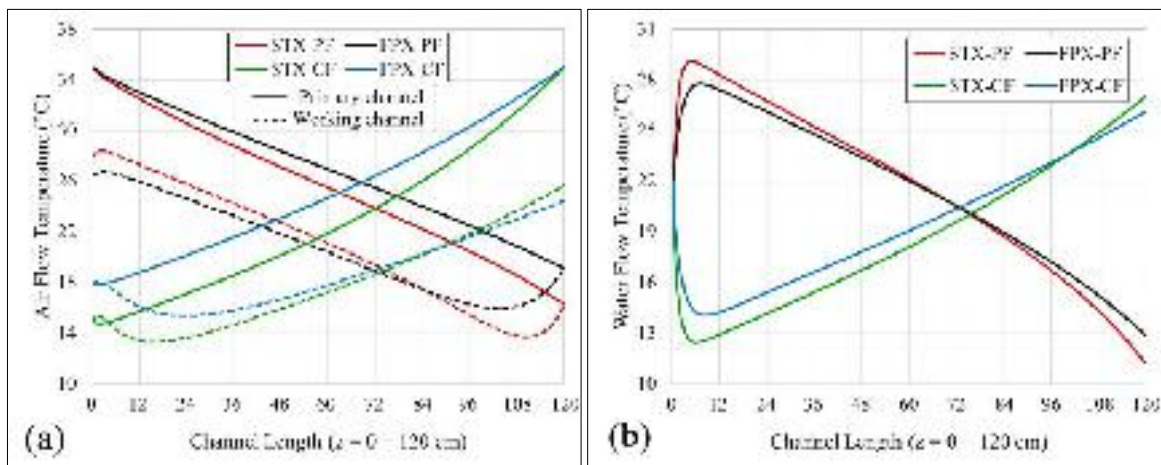


Fig. 5.17 Variation of parameters along the channels: (a) airflow temperature; (b) water flow temperature

Moreover, from **Fig. 5.17(b)**, the water temperatures are sharply increased in PF configuration, while oppositely decreased in CF configuration for both coolers (STX and FPX) due to significant difference between the air and water temperatures at water entrance location (i.e., $z=0$ cm). From the analysis, with reference to the pre-set conditions in **Table 5.4**, it was found that the STX always produced a lower product air temperature than the FPX, which was

accounted for about 2.83 °C lower for PF configuration and 3.1 °C lower for CF configuration, this indicates the superiority of the new design in terms of performance. In the meanwhile, for both coolers, it is apparent that the PF configuration always produced a much lower water temperature than the CF configuration, which was about 15.76 °C (140%) lower for STX and 13.18 °C (101%) lower for FPX.

5.4.1.3 Humidity and Evaporation Variation Along the Channel

Along the working channel, the variations of humidity ratio and relative humidity are depicted in **Fig. 5.18(a)**. The humidity ratio of working air continuously increases owing to the continuous evaporation of water film. As evidence, the working air of STX in both air-water flow configurations requires a shorter distance to reach the saturation state when compared to FPX, as demonstrated by relative humidity trends. This denotes more efficient heat and mass transfer in STX.

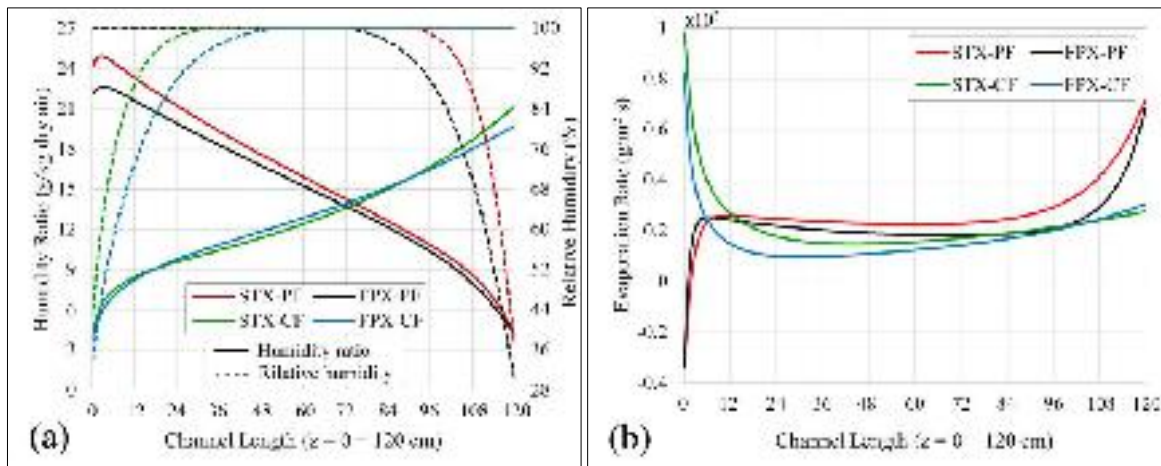


Fig. 5.18 Variation of parameters along the channels: (a) humidity ratio and relative humidity; (b) water evaporation rate

Moreover, regarding the PF configuration in both systems, a slight decrease in humidity ratio trends can be noticed near the channel end (z=5 cm). This

indicates the potential for condensation of water vapor that can be confirmed by the occurrence of negative evaporation seen from **Fig. 5.18(b)** at the exact location near the channel end, this phenomenon relates to higher working air's dew point temperature when compared to the surface temperature, or in another word, the surface temperature of the channel wall is lower than the dew point temperature of working air. **Fig. 5.18(b)** shows a high water evaporation rate for all proposed systems at the entrance of working channels, mainly because the humidity ratio is lowest at the working channels entrance. After that, the evaporation rate decreases gradually up until the occurrence of the saturation state (refer to **Fig. 5.18(a)**, dotted lines). Although the working air attains saturation, yet the water film's evaporation continuous due to the consistent heating of water film by primary air along the channel that will eventually maintain the necessary difference in saturation pressure for evaporation between water vapor and working air at air-water interface.

5.4.1.4 Heat Transfer Along the Channel

Along the primary channel, the cooling potential flux is shown in **Fig. 5.19(a)** under the operational and geometrical conditions presented in **Table 5.4**. As the air enters the primary channel (at $z=0$ cm for PF and $z=120$ cm for CF), the cooling begins at its maximum rate due to highest difference in temperature between the air and wall alongside with the effect of thermal and hydrodynamic boundary layer development. In addition, near the end of primary channels, a dramatic decrease in cooling flux could be noticed in the CF configuration. This occurrence is deemed reasonable because the primary air temperature at channel end is lower than that of the channel wall owing to low water temperature at the entrance, as shown in **Fig. 5.17(a)** and **(b)**; this results in heating the primary air which represented as negative sensible heat transfer in **Fig. 5.19(a)**.

Fig. 5.19(b) illustrates the overall heat transfer coefficients of air flows along the working channels for the proposed systems. Inside the working channels, heat transfers by convection and evaporation process, i.e., sensible and latent heat transfer, respectively, as illustrated in **Fig. 5.20(a)** and **(b)**.

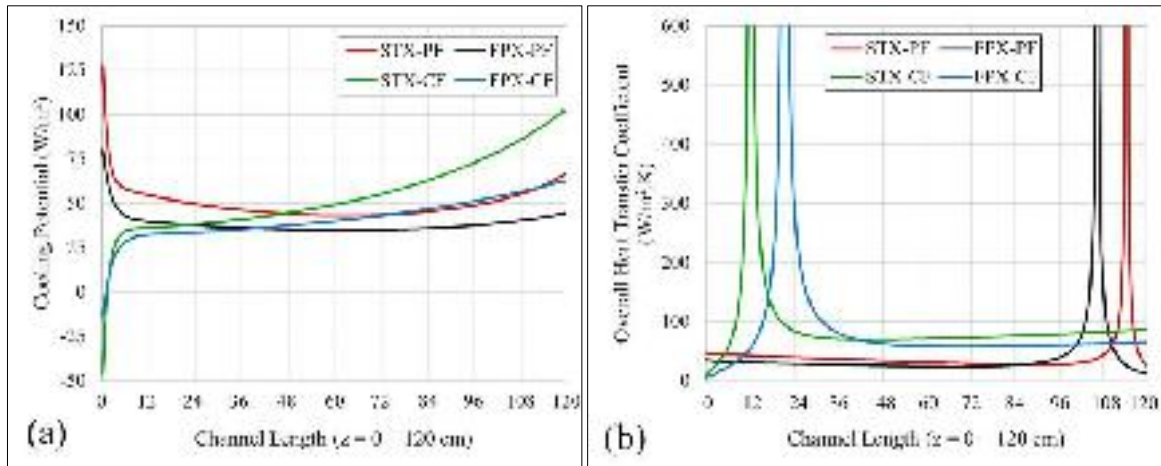


Fig. 5.19 Variation of parameters along the channels: (a) cooling potential (heat flux); (b) overall heat transfer coefficient

Inside each working channels, for convection heat transfer to happen, the temperature difference between air and water must be tangible; otherwise, the heat will only transfer via evaporation. Consequently, due to the equilibrium state where the working air and water film temperatures equates, thereby, in this location, the overall heat transfer coefficient proceeds to infinity, as depicted in **Fig. 5.19(b)**.

Based on the computed results, near the entrance of the working channels in both air-water flow configurations of both coolers, the latent heat transfer is at its peak, as illustrated in **Fig. 5.20(a)** and **(b)**, because the air that has been diverted from the primary channel is relatively dry, as a result, the highest evaporation rate occurs. Meanwhile, regarding the PF configuration for both exchangers (refer to **Fig. 5.20(a)**), despite the higher temperature of working air than the water film, but nonetheless, the trends of sensible and latent heat

transfer near the exit of working channels ($z=5$ cm) experience a dramatic fall due to the effect of condensation that has been explained previously. On the other hand, regarding the CF configuration depicted in **Fig. 5.20(d)**, at the working channels entrance ($z=0$ cm), the higher inlet water temperature than that of the working air resulted in negative sensible heat transfer.

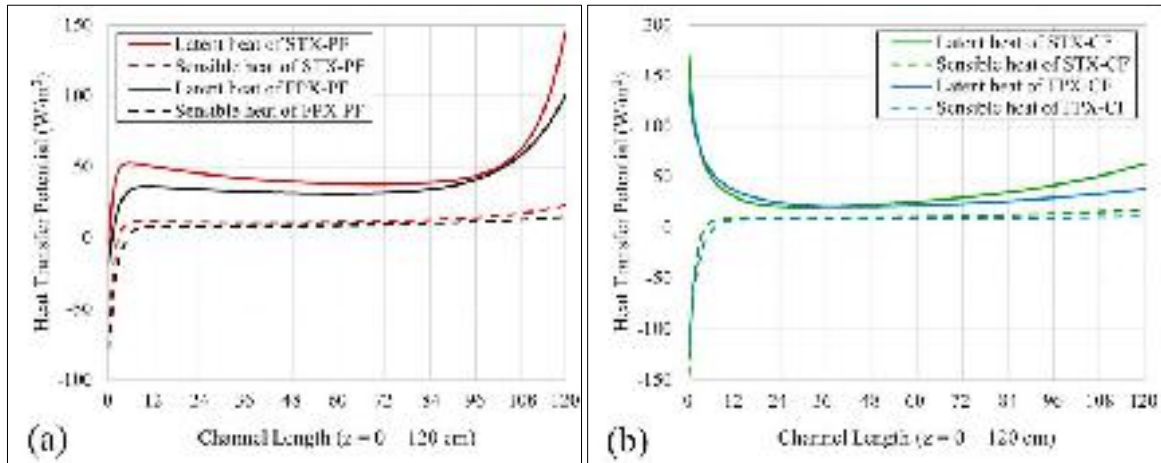


Fig. 5.20 Variation of parameters along the channels: (a) heat transfer of PF coolers; (b) heat transfer of CF coolers

5.4.2 Effect of Operational Parameters

5.4.2.1 Effect of Inlet Air Temperature and Humidity Ratio

Among all the operational and geometrical parameters, temperature and humidity of inlet air flow have the most crucial effect on system's performance when compared to other parameters. Therefore, these two parameters will be investigated more extensively than other operational and geometrical parameters. In this section, the performance of the proposed DPECs are evaluated under various temperature and humidity ratio of inlet air while keeping other operational and geometrical parameters constant as listed in **Table 5.4**. The energy efficiency (i.e., COP) of the proposed systems under wide range of inlet air temperature and humidity ratio are illustrated in **Fig.**

5.21(a) and **(b)**. The variations in these two operational parameters have the opposite effect on energy efficiency as it substantially improved when the inlet air temperature raised. At the same time, it decreased with increasing humidity ratio. The reason behind this phenomenon relates to the cooling characteristic of the exchangers, which is improved with increased temperature while deteriorated with increased humidity (refer to **Fig. 5.22(a)** and **(b)**).

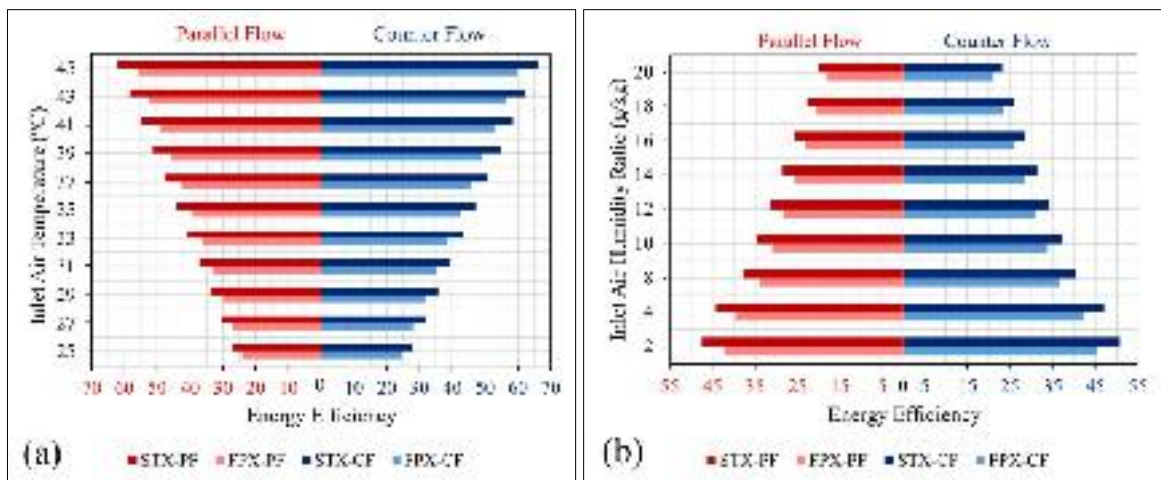


Fig. 5.21 Energy efficiency performance under the effect of inlet air parameters: (a) temperature; (b) humidity ratio

The reason behind this occurrence is pertinent to the evaporation process which is the fundamental operating principle of DPEC. The driving force of evaporation is the difference between the vapor pressure at air-water interface and the partial vapor pressure of water vapor in the working air flow. When the liquid water is heated, the water molecules gain kinetic energy and the vapor pressure at the air-water interface increases which yields a larger driving force for evaporation (i.e., water diffusion). Moreover, the humidity ratio of the air affects the partial vapor pressure of the water vapor in the working air flow. At higher humidity, the difference between the partial pressure and vapor pressure reduces, hence the evaporation reduces. Therefore, higher temperature promotes the evaporation, while higher humidity inhibits the evaporation.

Consistently, the STX showed a higher energy efficiency than that of FPX, which accounted for 12.2% in average, owing to better cooling potential of STX than that of FPX.

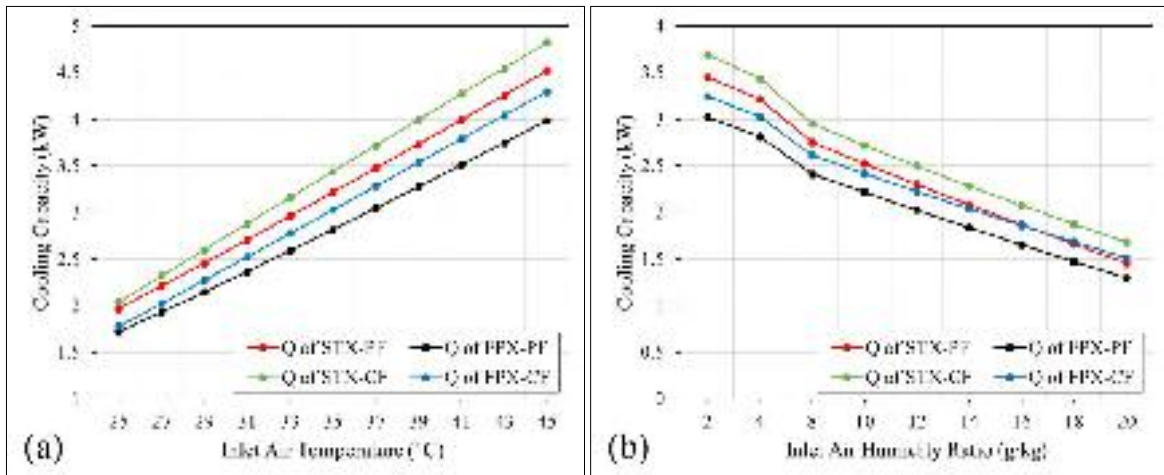


Fig. 5.22 Variation of cooling capacity under the effect of inlet air parameters: (a) temperature; (b) humidity ratio

In the meanwhile, as depicted in **Fig. 5.23**, the product air temperature and dew-point effectiveness are gradually increased when inlet air temperature raised from 25°C to 45°C and humidity ratio raised from 2 g/kg to 20 g/kg. However, the increasing rate in product air temperature for STX is lower when compared to that of FPX, which indicates more effective cooling in favor of STX, which continuously produced colder air with 3.1°C in case of inlet air temperature variation (see **Fig. 5.23(a)**) and 2.78°C in case of inlet air humidity ratio variation (see **Fig. 5.23(b)**) in average for both parallel and counter air-water flow configurations.

As its evidence, in both coolers, the CF configuration always produced lower product air temperature (as low as 13°C at inlet air temperature and humidity of 35°C and 2 g/kg, respectively) than the PF configuration, with a difference as high as 11.6% for STX and 9.9% for FPX under the inlet air temperature and humidity ratio of 45°C and of 4 g/kg, respectively. Moreover,

regarding the dew-point effectiveness, the STX always recorded the higher rate under both operational conditions with the highest rate recorded in CF configuration, which accounted for 78% in average under the case of humidity ratio variation.

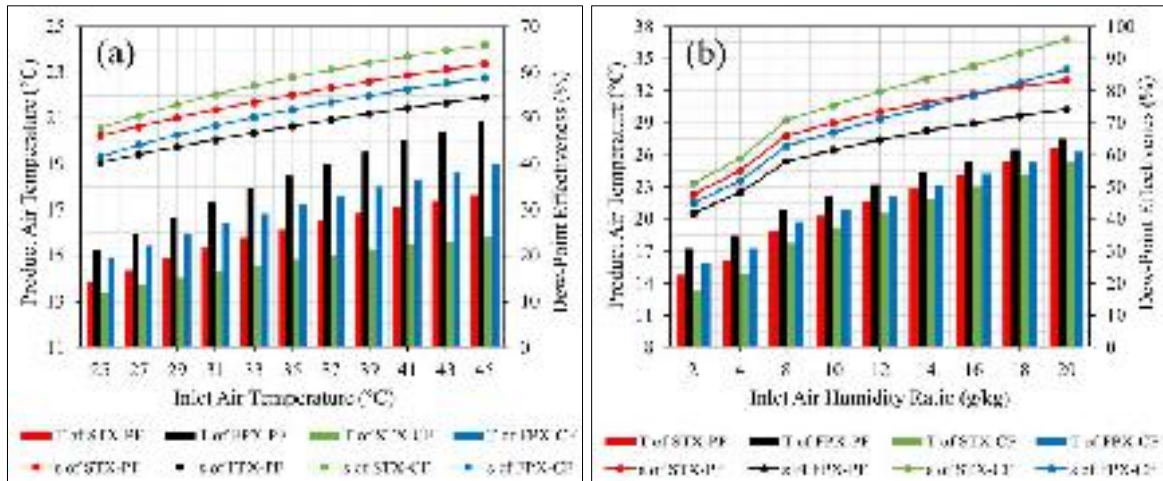


Fig. 5.23 Variation of product air temperature and dew-point effectiveness by effect of inlet air parameters: (a) temperature; (b) humidity ratio

Furthermore, regarding the wet-bulb effectiveness, under the variation of inlet air temperature and humidity, the STX continuously outperformed the FPX in both air-water flow configurations as illustrated in **Fig. 5.24**. The wet-bulb effectiveness of STX exceeded 100% when the inlet temperature raised above 29°C for CF configuration and 35°C for PF configuration, while for FPX, it exceeded 100% only when the inlet temperature raised above 41°C for CF configuration and it never reached 100% over the span of the considered temperature and humidity for PF configuration. On the other hand, the wet-bulb effectiveness for STX was persistently above 100% over the span of the humidity ratio for both air-water flow configurations. This is owing to the superiority of STX design over the FPX design which resulted in improved heat and mass transfer process inside the HMX.

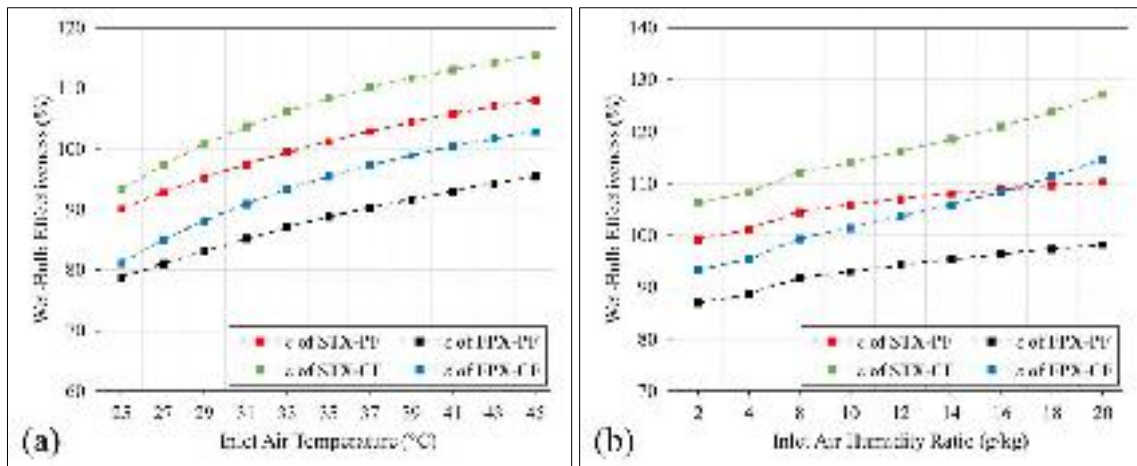


Fig. 5.24 Variation of wet-bulb effectiveness under the effect of inlet air parameters: (a) temperature; (b) humidity ratio

Fig. 5.25(a) and **(b)** depicts noticeable superiority of PF configuration over CF configuration when it comes to chill drain water temperature. Both DPEC types were able to produce a chill water temperature at low inlet air humidity ratio, regardless of the temperature of inlet air. For instance, the STX and FPX type DPECs could reduce the drain water temperature to about 9.2°C and 10.7°C, respectively, under the inlet air temperature and humidity of 35°C and 2 g/kg, respectively.

Regarding the water evaporation, i.e., water consumption rate, the rate for STX was persistently higher than that of the FPX owing to a better mass transfer process by STX that eventually result in better cooling performance. It is worth notice that at higher temperature and lower humidity, the evaporation rate significantly elevated due to the fact that the evaporation potential increases with increasing temperature and diminishes with increasing humidity as previously explained. In average, the evaporation rate for the considered cases in **Fig. 5.25(a)** and **(b)** has boosted by up to 106% when the temperature increased from 25°C to 45°C, while it has diminished by up to 66% when the inlet air humidity increased from 2 g/kg to 20 g/kg. This phenomenon will badly affect the cooling performance of the system as explained earlier.

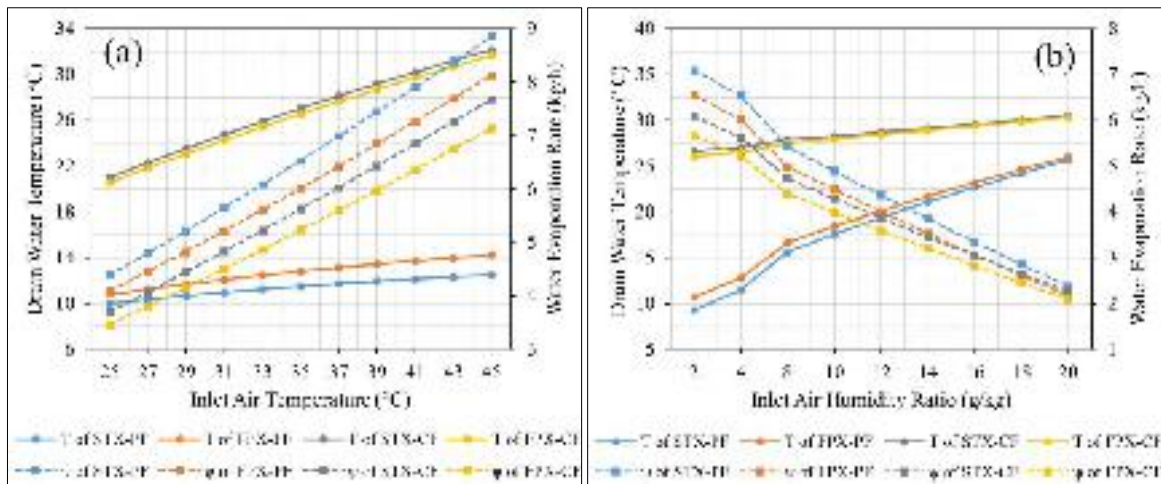


Fig. 5.25 Variation of drain water temperature and water evaporation under the effect of inlet air parameters: (a) temperature; (b) humidity ratio

5.4.2.2 Effect of Inlet Air Velocity and Air Ratio

The performance of DPEC is strongly bonded to the inlet air velocity and working to primary air ratio due to their direct impact on Reynolds number and convection coefficients inside the channels. In this section, the performance of the proposed DPECs were investigated under varying inlet air velocity from 1 m/s to 3 m/s, and the air ratio from 0.1 to 0.9. For this set-up, the flow is still in laminar state with Reynolds number computed to alter between 170 and 1873, and the convective heat transfer coefficients were computed to be around 27 W/m²·K under the initial conditions presented in **Table 5.4**. **Fig. 5.26(a)** and **(b)** illustrate the influence of product air temperature and dew-point effectiveness by inlet air velocity and air ratio, respectively. As its evidence, at lower inlet air velocity and higher air ratio, the proposed coolers performed better as they can obtain colder air and higher dew-point effectiveness. The former is related to higher heat transfer occurrence between primary channel airflow and channel wall when air flow is reduced that yields in lower product air temperature, and the latter is related to more air will flow inside working channels at higher air ratios that eventually results in more heat and mass transfer which cause a dramatic reduction in product air temperature.

Moreover, the STX consistently performed better than FPX for both air-water flow configurations, continuously producing air with about 14.5% colder in temperature and 19% higher in dew-point effectiveness, in average. In addition, when the air ratio was 0.1, the STX with CF configuration produced the coldest air and highest dew-point effectiveness, but while the air ratio increased to 0.9, similarly, the coldest air and highest dew-point effectiveness were achieved by the same HMX type but this time with PF configuration.

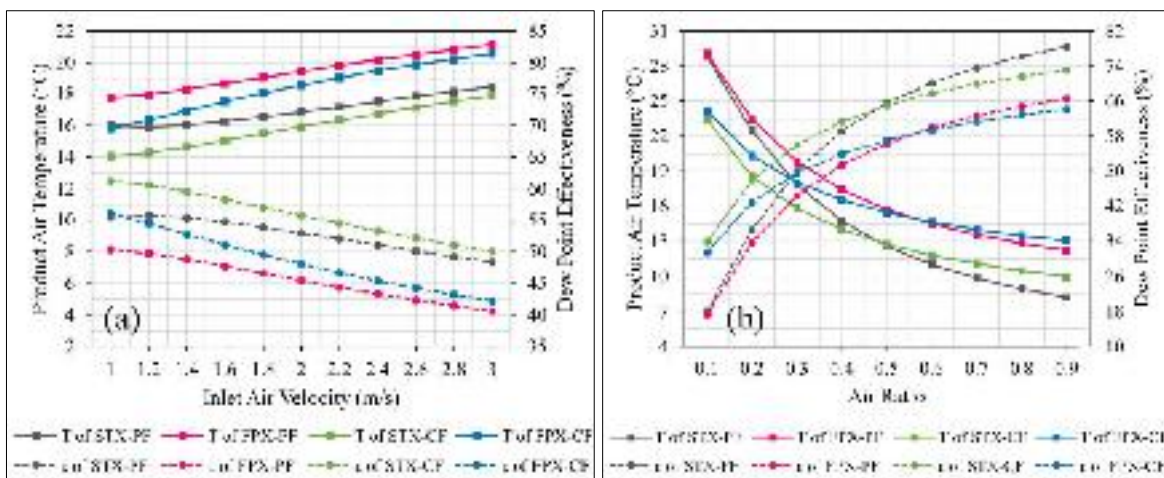


Fig. 5.26 Variation of product air temperature and thermal effectiveness by effect of: (a) inlet air velocity; (b) working to primary air ratio

Regarding the coefficient of performance (i.e., energy efficiency), as illustrated in **Fig. 5.27**, all DPEC types acted in the same manner. It is apparent that the variation of air ratio had significantly more effect on the energy performance of the coolers than the variation of inlet air velocity. For all the coolers, in general, when the inlet air velocity gradually increased from 1 m/s to 3 m/s, the highest energy efficiency obtained at air velocities between 1.4 m/s to 2.2 m/s. Likewise, regarding the air ratio, all the coolers achieved the best energy efficiency at working to inlet air ratio of 0.3 to 0.4. This case is pertinent to the cooling capacity of the coolers as they achieved the highest cooling capacity at air ratio of 0.3 to 0.4 as depicted in **Fig. 5.28(b)**. The above

statement indicates that the air ratio of 0.3 to 0.4 gives the best proportion between the cooling capacity and power consumption for the cooler through which the highest and most stable performance efficiency can be achieved. Furthermore, it can be notice that when air ratio increased from 0.3 to 0.9, the cooling capacity of the coolers were dramatically decreased that can be accounted for 2.51 kW reduction in average for all coolers.

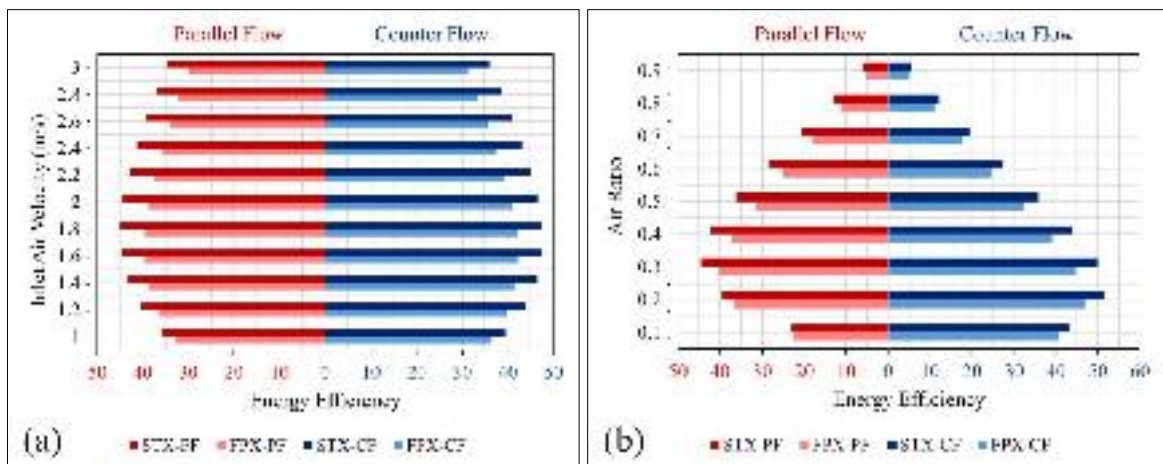


Fig. 5.27 Variation of energy efficiency by effect of: (a) inlet air velocity; (b) working to primary air ratio

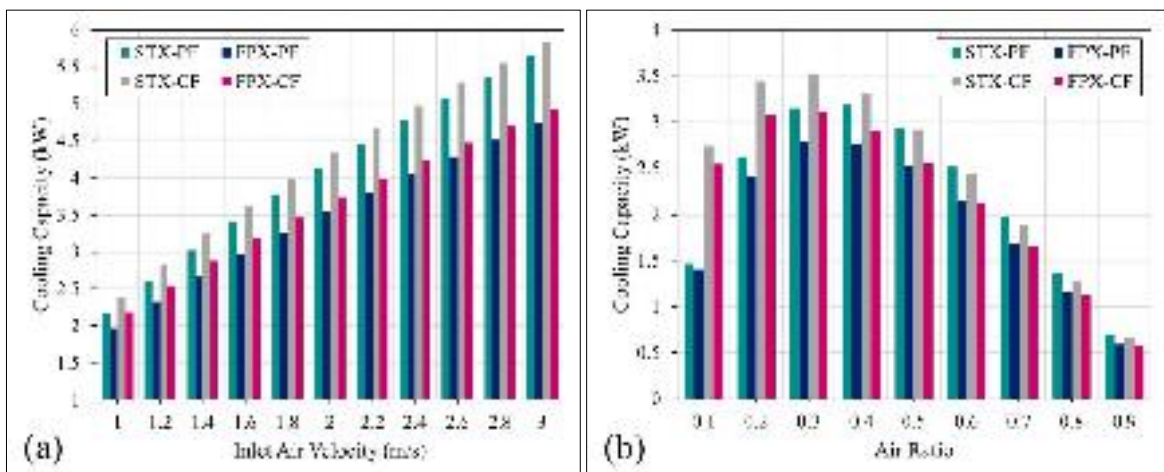


Fig. 5.28 Variation of cooling potential by effect of: (a) inlet air velocity; (b) working to primary air ratio

On the other hand, with increasing the inlet air velocity, the cooling capacity of the DPECs linearly increased (refer to **Fig. 5.28(a)**). However, the

STX of both air-water flow configurations were uninterruptedly outperformed the FPX with a prominent difference owing to the ability of STX type DPEC to produce a noticeably colder air. Besides, the CF configuration steadily achieved higher cooling capacity than PF configuration over the entire range of considered inlet air velocity and air ratio.

5.4.2.3 Effect of Feed Water Temperature and Flowrate

The variations of product air temperature and dew-point effectiveness by the effect of feed water temperature and flowrate are depicted in **Fig. 5.29(a)** and **(b)**, respectively. It was found that the feed water temperature has insignificant effect on the performance of both coolers when they were arranged in PF configuration; in contrast, for CF configuration, the product air temperatures were gradually increased while the dew-point effectiveness were decreased because in CF configuration, at the point where $z=0$ mm the primary air exits the system whereas the water enters the system, and owing to higher water temperature at this location, heat transferred from water film to primary air that eventually leads to higher product air temperature.

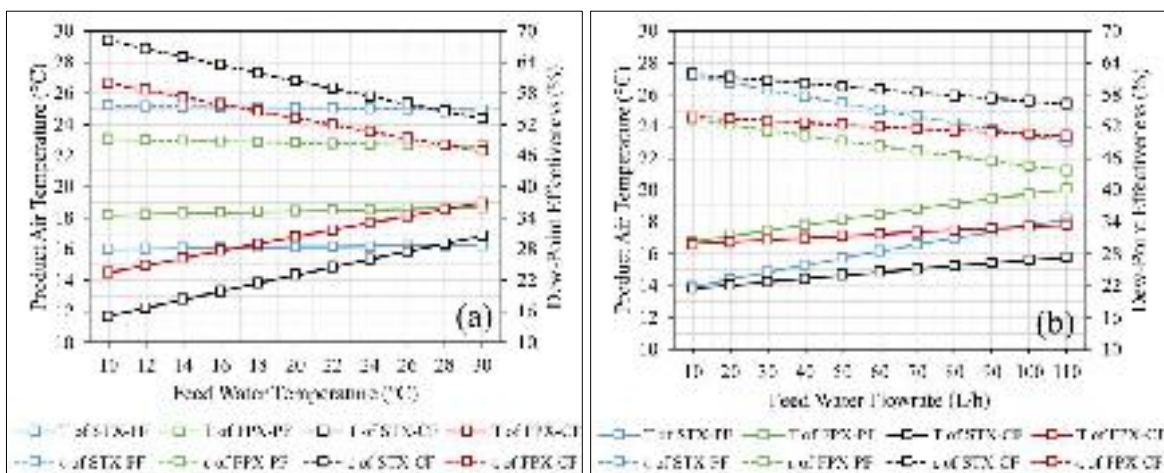


Fig. 5.29 Variation of product air temperature and dew-point effectiveness by effect of feed water parameters: (a) temperature; (b) flowrate

Meanwhile, the effect of feed water flowrate acted similar to that of feed water temperature, but this time with a higher impact on PF configuration. It can be easily seen that at low feed water flowrate, e.g., 10 L/h, both coolers of the same air-water flow configuration obtained similar results (refer to **Fig. 5.29(b)**), but the difference has increased with increasing the flowrate (in favor of counter flow configuration). In both cases of feed water analysis, the STX showed a better performance than that of FPX, and the difference between the trends of the same cooler was almost kept constant along the variation of feed water temperature and flowrate, which accounted for about 2.4°C and 8.9% regarding the product air temperature and coolers effectiveness trends, respectively.

Regarding the drain water temperature and water evaporation rate, they both have been affected somewhat marginally by the effect of water temperature and flowrate as can be seen from **Fig. 5.30(a)** and **(b)**. However, in this regard, the rate of change is more noticeable by the effect of water flowrate, while the effect of water temperature can be considered trivial. Overall, the performance characteristics of the proposed DPECs are observed to be more sensitive to inlet water flowrate than inlet water temperature.

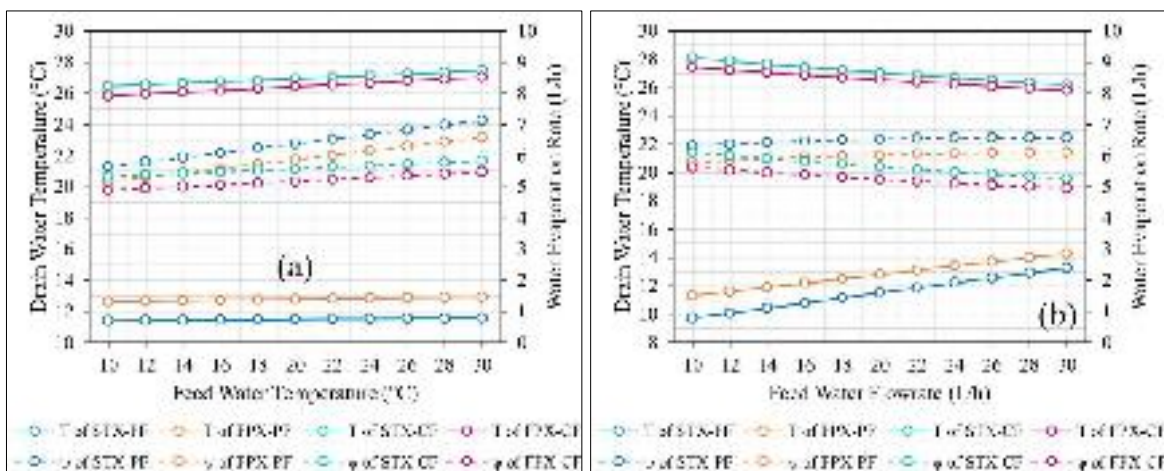


Fig. 5.30 Variation of drain water temperature and water evaporation by effect of feed water parameters: (a) temperature; (b) flowrate

5.4.3 Effect of Geometrical Parameters

In this section, the effect of geometrical aspects (i.e., channel length and channel diameter/height) on performance parameters will be investigated. As explained in **Chapter 3**, in particular **Section 3.4**, the comparative analysis between the STX and FPX was based on fixed volume of the exchangers as well as fixed cross-section area of all differential elements. Moreover, the cross-section area of the primary channels is kept equal to that of the working channels. Therefore, to study the effect of channel height/diameter, each time by increasing or decreasing the primary channel diameter of STX type, the hypothetical working channel height (H_e) of STX and the primary and working channels height of the FPX are simultaneously changed to match the corresponding dimension for fixed cross-section area analogy (refer to **Fig. 3.4**). Thus, for the purpose of terminology simplification, the analysis of channel height/diameter is presented in terms of “equivalent channel diameter” of STX. Accordingly, as the size of all the HMXs were fixed, thus each time with increasing equivalent channel diameter, the number of channels decreased as well.

It is observed that the effect of equivalent channel diameter is opposite to that of the channel length regarding the performance of the coolers. As illustrated in **Fig. 5.31(a)**, when the channel length increased from 40 cm to 240 cm, the product air temperatures of the proposed coolers are gradually reduced due to increased surface area that contributed in higher heat and mass transfer rate. It is worth mentioning that the performance of the proposed DPECs were more sensitive to the variation of length when it increased from 0.4 m to 1 m, whereas the sensitivity was noticeably reduced when the length increased from 1 m to 2.4 m.

The STX type DPEC with CF configuration continuously produced the coldest air under the entire variation of channel length and equivalent channel

diameter as illustrated in **Fig. 5.31(a) and (b)**, respectively. **Fig. 5.31(b)** shows that with increasing the equivalent channel diameter from 0.39 cm to 1.11 cm, the product air temperature significantly increased which was accounted for about 7.8°C increase for STX with both air-water flow configurations and 8.8°C increase for FPX with both configurations, in average.

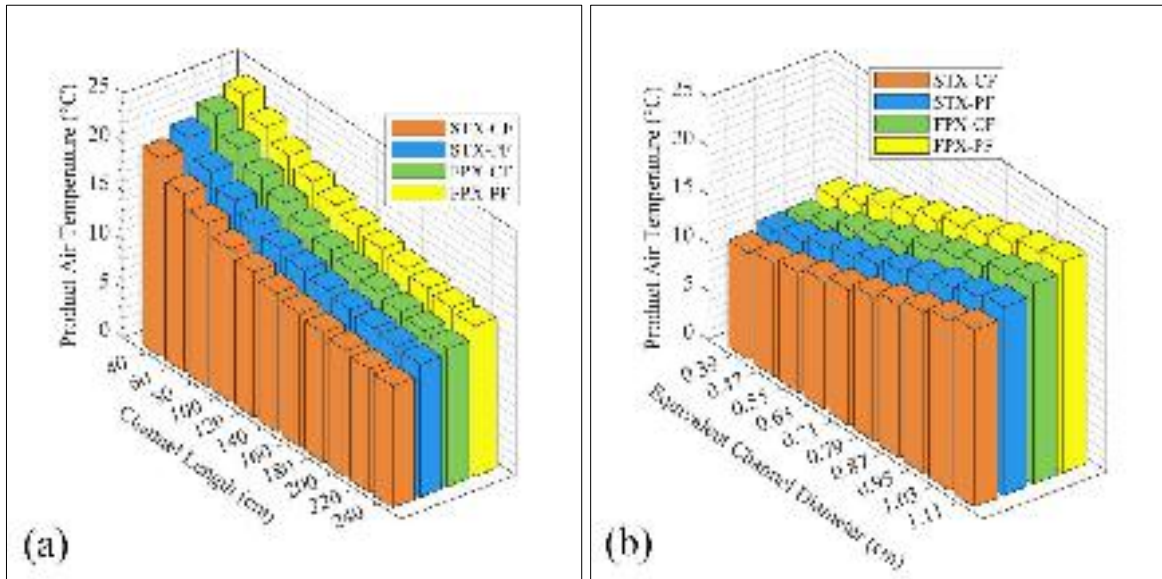


Fig. 5.31 Variation of product air temperature by the effect of: (a) channel length; (b) equivalent channel diameter

This situation happened due to the fact that when the channels diameter/height increased, the air velocity reduces which affects a chain of physical processes inside the HMX of DPEC. More precisely, by the reduction of air velocity, the convective heat transfer coefficient decreases which is a function of Reynolds number and Nusselt number that eventually results in lowering the potential for heat transfer process. In addition, due to direct relation (analogy) between heat and mass transfer coefficients, consequently, mass transfer coefficient reduces as well. This parameter greatly impact the mass transfer (i.e., water evaporation) rate. That being so, lower cooling take place inside the HMX as can be seen from **Fig. 5.32(b)**. In contrast, similar to the effect of inlet air temperature, when channel length increased, the cooling

capacity of the coolers were prominently improved, and the rate of improvement is higher for channel length spanning from 0.4 m to 1 m than spanning from 1 m and above, refer to **Fig. 5.32(a)**.

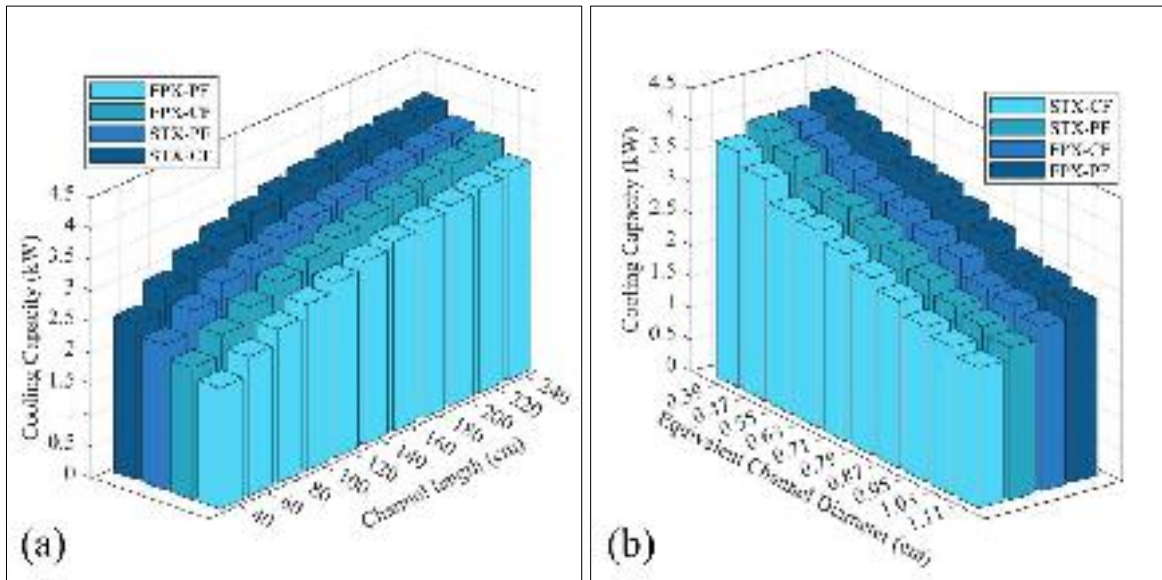


Fig. 5.32 Variation of cooling capacity by the effect of: (a) channel length; (b) equivalent channel diameter

Fig. 5.33(a) and **(b)** shows the variation of dew-point effectiveness under the effect of channel length and equivalent channel diameter, respectively. For the dew-point effectiveness to be as high as possible, the system need to be operated under a higher humidity air condition, as the air with high humidity has a higher dew point temperature. This means the system can easier produce an air with its temperature closer to inlet air's dew point temperature that eventually results in higher dew-point effectiveness (according to **Eq.3.20** in **Chapter 3**). Therefore, under the operational condition of the current investigation (humidity ratio of 0.004 kg/kg) which is considered as dry air, the proposed STX with both air-water flow configurations could achieve a dew-point effectiveness higher than 60%, which is acceptable considering a harsh operational condition for dew-point effectiveness.

The air-water flow configurations highly impact the outlet water temperature as shown in **Fig. 5.34**. In particular, the drain water temperature in PF configuration was significantly lower than that of CF configuration, accounting for about 17°C lower in average for both coolers. To be more specific, the STX with PF configuration achieved the lowest temperature, ranging between 10°C to 14°C under the variation of channel length (see **Fig. 5.34(a)**), while ranging from 9.3 °C to 13.4 °C under the variation of equivalent channel diameter (see **Fig. 5.34(b)**).

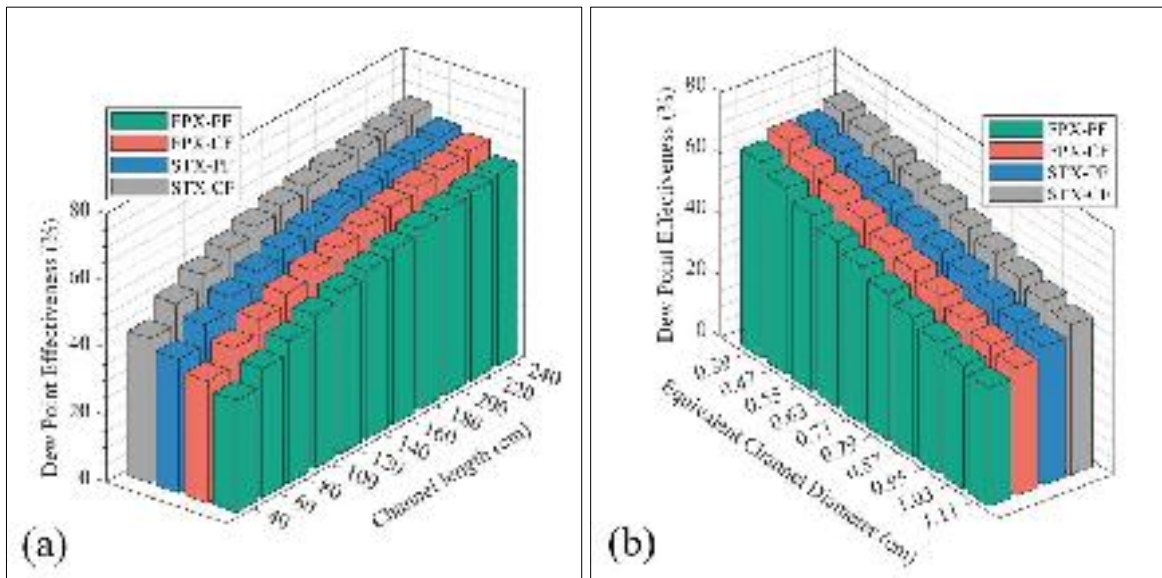


Fig. 5.33 Variation of dew-point effectiveness by the effect of: (a) channel length; (b) equivalent channel diameter

When the equivalent channel diameter increased from 0.39 cm to 1.11 cm, the drain water temperature increased by up to 4°C for PF configuration and decreased by 0.8°C for CF configuration. The reason for this phenomenon has been explained earlier in **Section 5.4.1.2**. Furthermore, despite the superiority of CF configuration over the PF in terms of thermal and energy performance, yet it continuously produced warm water (between 21°C to 32°C) under the entire ranges of considered parameters for the purpose of extensive parametric analysis. Again, this phenomenon has been explained in **Section 5.4.1.2**.

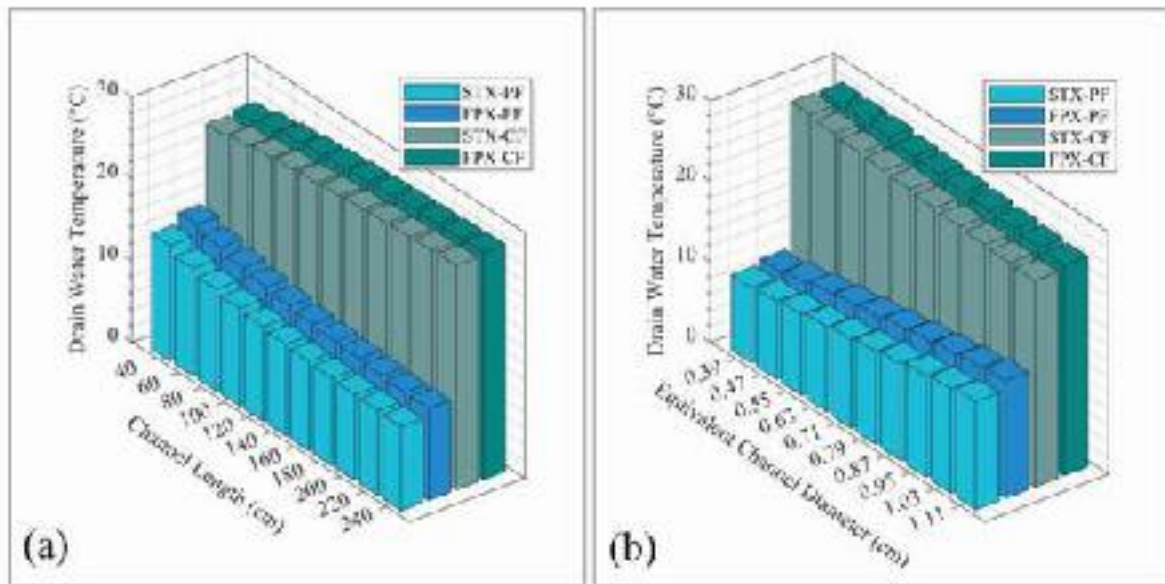


Fig. 5.34 Variation of drain water temperature by the effect of: (a) channel length; (b) equivalent channel diameter

5.5 EXERGY, ENTROPY, AND SUSTAINABILITY ANALYSIS

In this section, the exergy, entropy, and sustainability analysis for the innovative DPEC will be thoroughly analyzed and discussed based on the second law of thermodynamics. Owing to the superiority of shell and tube design DPEC paradigm with CF configuration in terms of product air temperature, cooling capacity, and energy efficiency, therefore, it has been decided to conduct the second law of thermodynamics analysis with regard to the above-mentioned system. The significance of this approach lies in its capability for demonstrating a comprehensive evaluation for thermal and energy performance of any irreversible systems. In particular, the first law of thermodynamics assists in identifying the energy efficiency and thermal performance of a thermodynamic process, while the second law of thermodynamics is further sophisticated method where it helps to evaluate the energy quality and irreversibility of energy transfer within a thermodynamic system.

The current analysis has been carried out based on the pre-set nominal values presented in **Table 5.4** and considering the ambient air at saturated state as the dead state condition for exergy analysis. Similar to **Section 5.4**, the second law of thermodynamics analysis has been undertaken covering a wide range of operational and geometrical conditions. **Fig. 5.35** illustrates the exergy flow variation diagram (Grassmann diagram) of the proposed STX-DPEC with CF configuration.

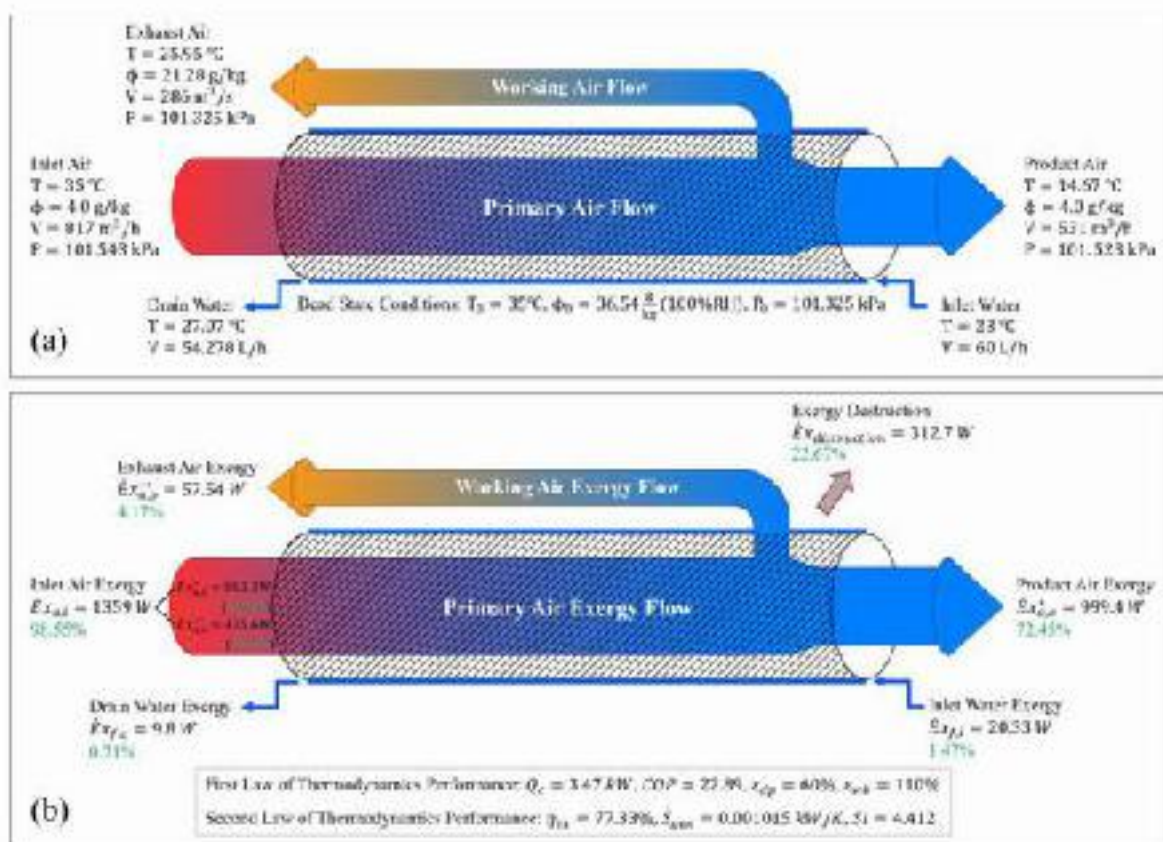


Fig. 5.35 Thermodynamical performance of proposed DPEC: (a) physical properties variation; (b) exergy variation (Grassmann) diagram

The thermal performance of the cooler is shown in **Fig. 5.35(a)** alongside with the dead state conditions. On the other hand, the exergy, entropy, and sustainability index performance of the cooler are shown in **Fig. 5.35(b)**. As indicated, for the inlet air temperature of 35°C , humidity ratio of 4 g/kg , and

air flow of $817 \text{ m}^3/\text{h}$, the total available inlet air exergy was 1359 W and the exergy from the product air and exhaust air were respectively 999.4 W and 57.54 W , while the destruction exergy was 312.7 W , yielding an exergetic efficiency of 77.33% .

Moreover, the inlet air exergy can be further divided into product air's inlet exergy (883.3 W) and working air's inlet exergy (475.6 W) in accordance to working to product air ratio ($AR=0.35$). It can be observed that, after the cooling of product air, its exergy portion from the total inlet exergy of air and water combine has increased from 64.0% to 72.45% that accounted for 8.45% improvement in its exergy. This occurrence is attributed to the reduction in working air's exergy (from 34.4% to 4.17%) in which 22.67% of the total inlet exergy was destroyed to convert 116.1 W of exergy for cooling of product air. In addition, the entropy generation rate was 0.001015 kW/K and the sustainability index for the cooler was 4.412 .

Furthermore, the exergy breakdown of the air streams at different state points inside the heat and mass exchanger is presented in Table 5.5. The exergy brake down of the air streams include thermal exergy (Eq. (3.30)), mechanical exergy (Eq. (3.31)), and chemical exergy (Eq. (3.32)). It can be notice that the thermal exergy of the inlet air is zero due to equivalent temperatures of dead state and ambient air. Likewise, the mechanical exergy of the exhaust air is zero as the exhaust air eventually ejected to the atmosphere with its pressure matching that of the atmosphere. The chemical exergy, on the other hand, remains constant for inlet air and product air, because inside the primary channels, the cooling process take place sensibly without the variation in air stream's humidity content.

Table 5.5 Specific exergy variation of air streams at different state points

Air State Point	Specific Exergy		
	Thermal Exergy (J/kg)	Mechanical Exergy (J/kg)	Chemical Exergy (J/kg)
Inlet Air	0.0	0.1903	5.049
Product Air	0.7056	0.1728	5.049
Exhaust Air	0.1418	0.0	0.492

In addition, at primary channel's entrance (inlet air) and exit (product air), the mechanical exergy decreased owing to the reduction of the air pressure (i.e., flow resistance), while the thermal exergy increases due to the cooling effect. The cooling effect achieved at the cost of the conversion of chemical exergy inside the working channel, therefore, a dramatic decrease occurred in its magnitude (from 5.049 J/kg to 0.492 J/kg). Overall, it is obvious that the chemical exergy possesses the biggest share of the total exergy, and due to the dependency of the chemical exergy majorly on the humidity of the air, therefore, as explained in Section 5.4.2.1, the performance of the DPEC is highly bonded with the humidity content of the ambient air. While the mechanical exergy has the least contribution on the exergetic performance due to low pressure drop by the cooler.

5.5.1 Influence of Inlet Air Conditions

The thermodynamic performance of DPEC is noticeably influenced by the operational conditions, with some parameters having more significant effect than the others. In this regard, the effect of inlet air temperature and humidity ratio is depicted in Fig. 5.36. The inlet air temperature and humidity ratio individually ranged between 25°C to 55°C and 2 g/kg to 20 g/kg, respectively. Other parameters kept constant according to Table 5.4. Fig. 5.36(a) and (b) illustrate the variation of exergy flow (i.e., product air exergy, exhaust air exergy, drain water exergy, and destructed exergy) and total available inlet

exergy under the effect of inlet air temperature and humidity ratio, respectively. Each circle of the donut-pie figures represents the total input exergy, and from within, it has been divided into product air exergy, exhaust air exergy, drain water exergy, and exergy destruction, which are the entire components of the total available exergy, each provided with its magnitude and percentage contribution to that total exergy. Similarly, Fig. 5.36(c) and (d) illustrate the exergy flow variation, only this time with total available exergy included for each condition.

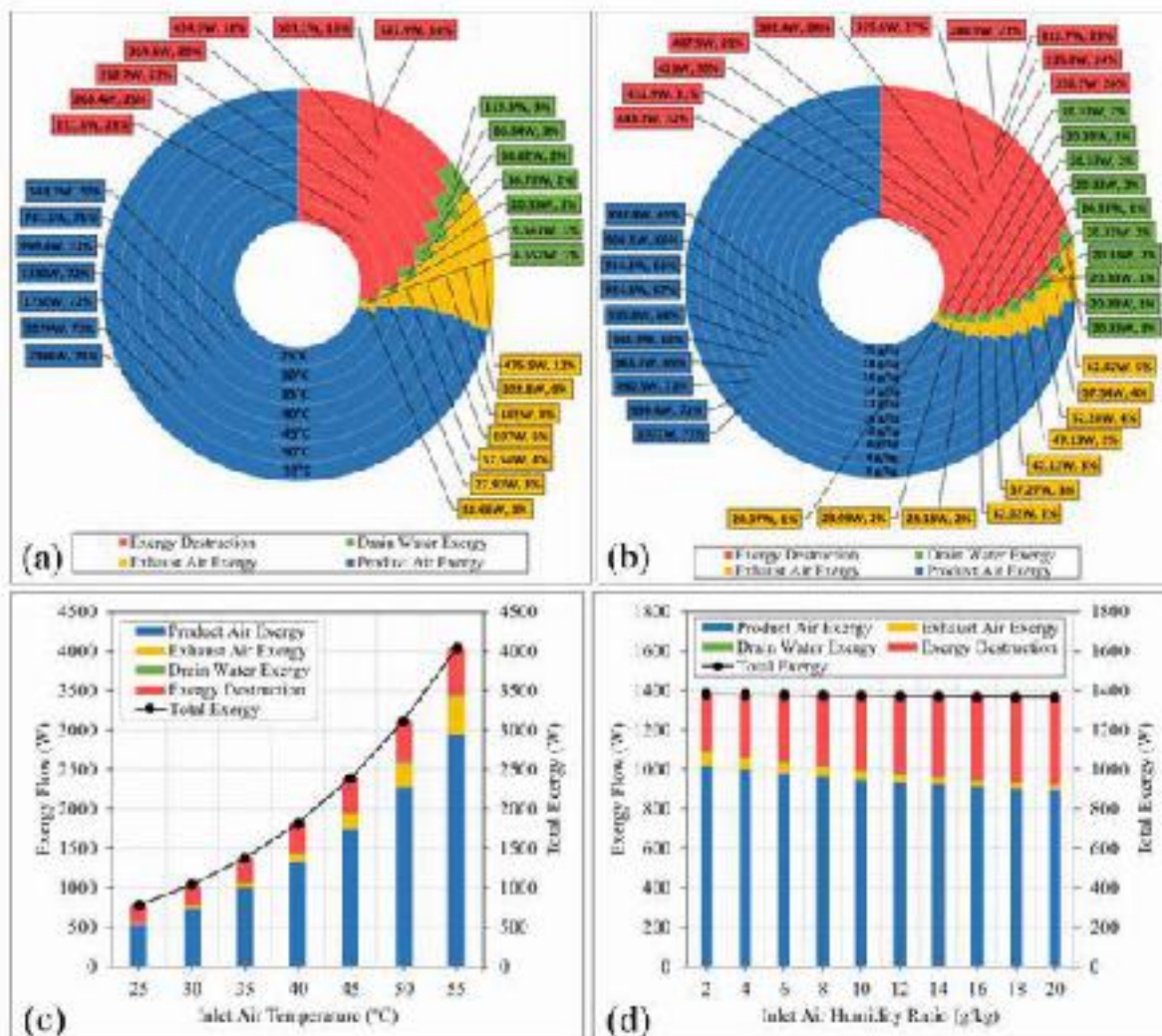


Fig. 5.36 (a) Effect of inlet air temperature on exergy flow; (b) Effect of inlet humidity ratio on exergy flow; (c) Variation of exergy flow and total exergy under effect of inlet air temperature; (d) Variation of exergy flow and total exergy under effect of inlet air humidity ratio

As can be seen, the total exergy is more sensitive to temperature variation than the humidity variation as it increased from 782 W to 4043 W when the inlet air temperature increased from 25°C to 55°C, while it marginally decreased from 1381 W to 1267 W when the inlet air humidity increased from 2 g/kg to 20 g/kg. Despite the slight variation in total input exergy under the variation of humidity ratio, yet, when the humidity ratio increased from 2 g/kg to 20 g/kg, the product air exergy noticeably diminished from 73% to 65% of the total exergy, while exergy destruction unfavorably grown by 11% (from 21% to 32% of the total exergy). This incidence badly affected the exergy efficiency of the cooler, as shown in Fig. 5.37(b).

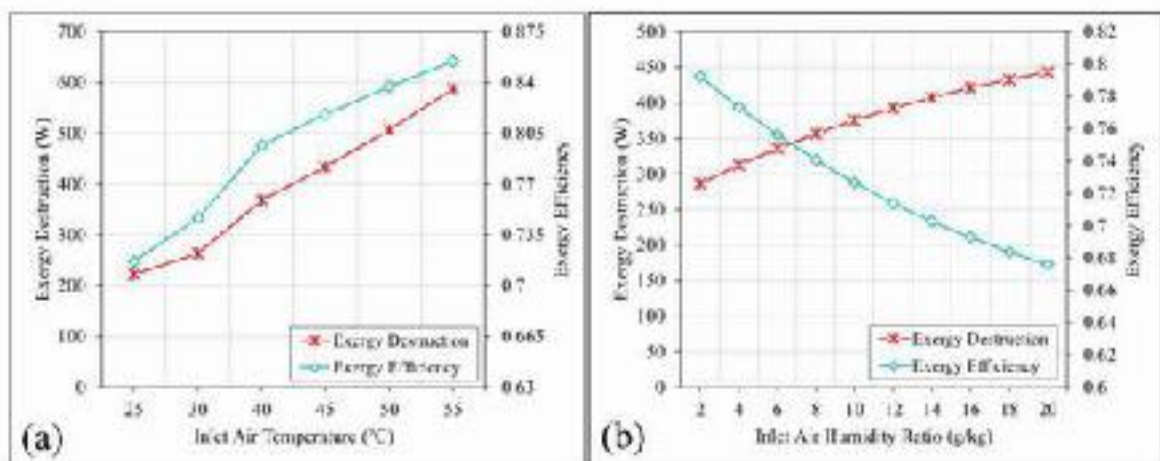


Fig. 5.37 Variation of exergy destruction and exergy efficiency under the influence of: (a) inlet air temperature; (b) inlet air humidity ratio

On the other hand, as illustrated in Fig. 5.36(a) and (c) and Fig. 5.37(a), with increasing the inlet air temperature, the exergy destruction has increased from 221.6 W to 587.9 W, while its rate in the total exergy has diminished from 28% to 14%, which is contributed in improving the exergy efficiency of the cooler that accounted for 13.79% improvement.

The entropy generation rate is directly proportional to the exergy destruction. The rate of entropy generation is considered as a fundamental thermodynamical

parameter from which the measure of the irreversibility can be observed. Inside an irreversible thermodynamic system, due to destruction of exergy, the entropy is generated. In addition, the sustainability analysis is an essential method of demonstrating how efficiently the system utilizes the resources and it is a function of exergy efficiency. The sustainability analysis for the proposed DPEC can be conducted by sustainability index (SI) method. The effect of inlet air temperature and humidity ratio on the entropy generation rate and sustainability index are shown in Fig. 5.38(a) and (b), respectively. With increasing the inlet air temperature and humidity, the entropy generation rate was continuously increased. The maximum recorded entropy generation was 1.79 W/K at maximum ambient temperature of 55°C, and 1.44 W/K at maximum ambient humidity ratio of 20 g/kg. In contrast, the sustainability of the proposed DPEC was improved with increasing temperature, however, it reduced with increasing humidity, which indicates that the cooler is more sustainable when operated under hot and dry ambient conditions. Consequently, through exergy analysis, it can be explained why operating such a system under humid climates will diminish its energy and thermal performances, while operating under hot and dry climates its energy and thermal performances improve.

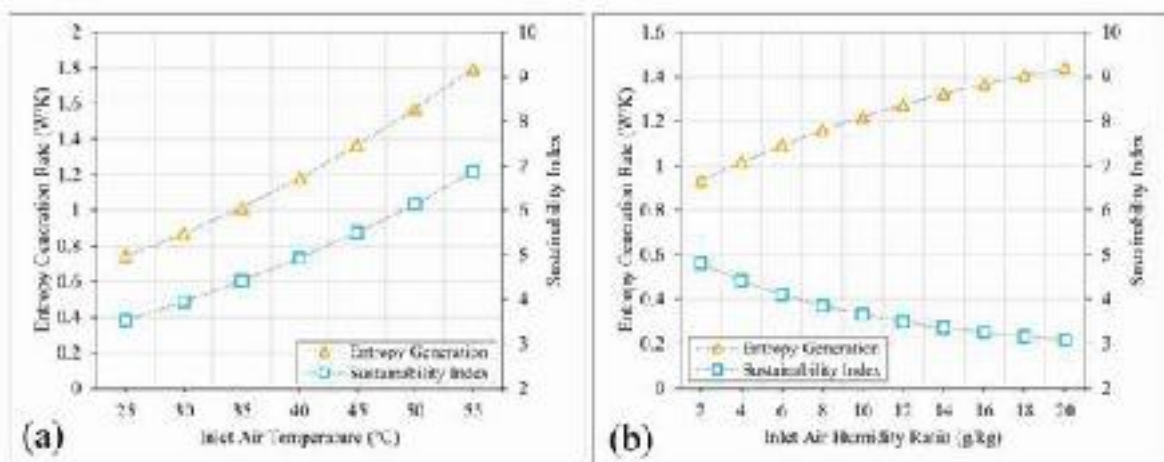


Fig. 5.38 Variation of entropy generation rate and sustainability index under influence of: (a) inlet air temperature; (b) inlet air humidity ratio

Overall, the DPEC is capable of converting huge amount of inlet air exergy to product air exergy under a wide range of inlet air temperature accounting for 2946 W out of 4043 W (71%) even when operated under sever ambient temperature as high as 55°C. This special merit is what distinguishes the DPEC from other air-conditioning systems and provides the cooler with significantly high energy efficiency (COP) and thermall effectiveness (ε_{dp} and ε_{wb}).

Furthermore, the influence of inlet air velocity and air ratio on the exergetic performance of the cooler are shown in Fig. 5.39. The rate of change of product air exergy and destructed exergy are more sensitive to the variation of air velocity than that of air ratio. For instance, the product air exergy and exergy destruction were merely varied from 71% to 73% and 22% to 24%, respectively, under the influence of inlet air velocity (refer to Fig. 5.39(a) and (c)), where as these two exergy rates severely varied from 24% to 85% and 13% to 50% under the influence of air ratio (refer to Fig. 5.39(b) and (d)), respectively.

Moreover, as it is evedence, the total available exergy significantly increaed from 731 W to 2260 W with increasing inlet air velocity, while it slightly increased from 1358 W to 1469 W with increasing air ratio, owing to that under the variation of inlet air velocity, the total air flow supply to the system increases, but when the air ratio increased, the total air flow supply to the system remains unchanged, therefore, the total inlet exergy slightly increase and the rate of this marginal increment is solely pertinent to the mechanical exergy. As the higher air ratio deems higher working air flow and lower primary air flow, and owing to more pressure reduction by working channels when compared to primary channels due to the effect of water surface, hence, more pressure reduction occures and more air resistance generates at the inlet of the HMX that will eventualll results in higher mechanical exergy.

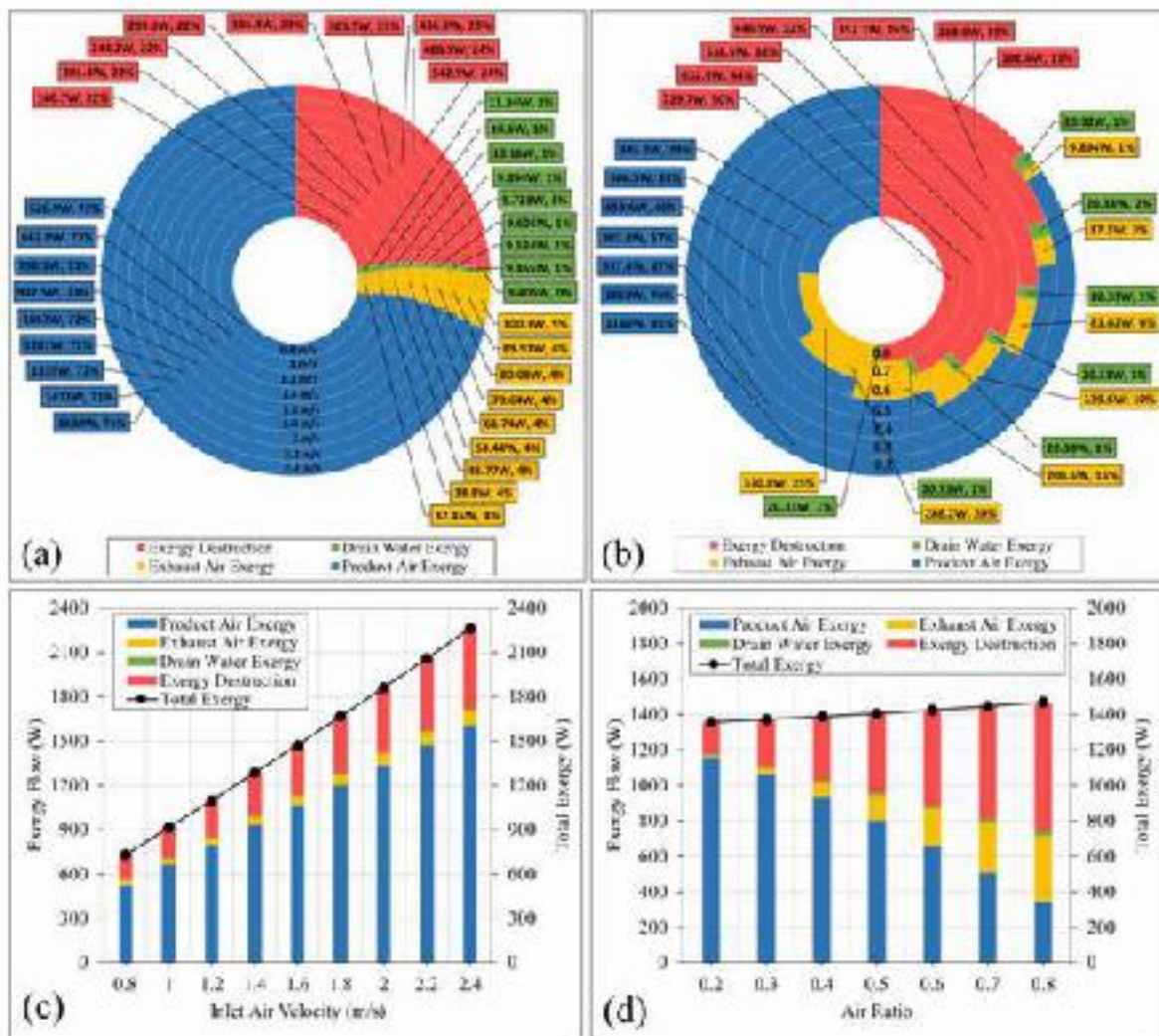


Fig. 5.39 (a) Effect of inlet air velocity on exergy flow; (b) Effect of air ratio on exergy flow; (c) Variation of exergy flow and total exergy under effect of inlet air velocity; (d) Variation of exergy flow and total exergy under effect of air ratio

Despite the slight alteration in total exergy under the influence of air ratio, yet the variations of each individual flow exergies are complicated. Regarding this matter, as illustrated in Fig. 5.39(b) and (d), as the air ratio increased from 0.2 to 0.8, greater amount of inlet air will be diverted to working channel which lessens the product air flow due to the degradation in the mechanical and thermal exergies. This air flow arrangement directly influence the variation of exergy flow, accordingly, the product air exergy dramatically decreased from 85% to 24%, in contrast, the exhaust air exergy significantly rised from 1% to

25%. This hugely resulted in elevating the exergy destruction from 13% to 50%. Consequently, the reduction in exergy efficiency is more noticeable under the effect of air ratio. The exergy efficiency was reduced from 78% to 75.9% when inlet air velocity rised from 0.8 m/s to 2.4 m/s, however, it was dramatically reduced from 86.5% to 50% when the air ratio rised from 0.2 to 0.8, as depicted in **Fig. 5.40(a)** and **(b)**, respectively.

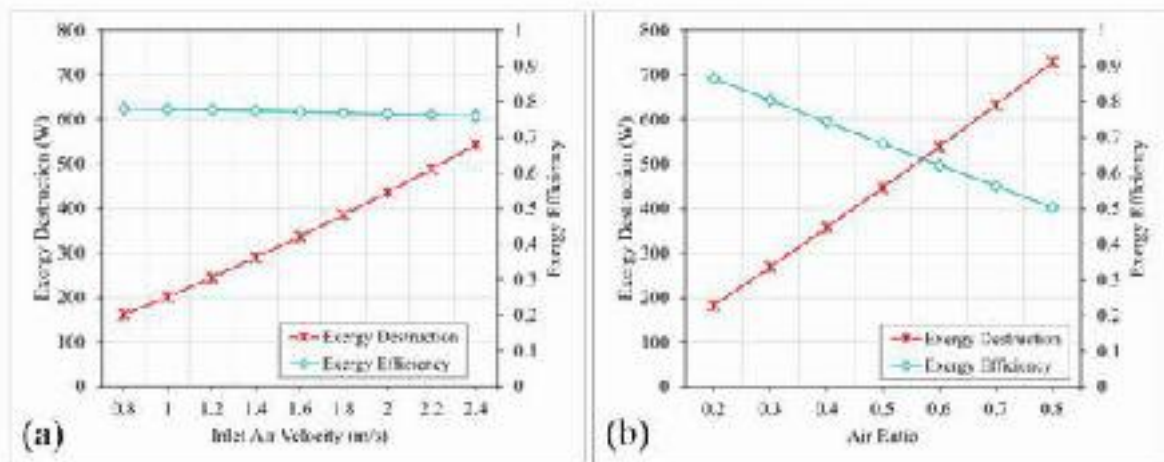


Fig. 5.40 Variation of exergy destruction and exergy efficiency under the influence of: (a) inlet air velocity; (b) air ratio

Same pattern of the aforementioned statements can be observed when it comes to entropy generation and sustainability analysis, as shown in **Fig. 5.41(a)** and **(b)**. The exergetic performance of the cooler is more stable under the influence of inlet air velocity than that of air ratio. The sustainability of the cooler, which is directly proportional to the exergy efficiency, is least affected by the influence of inlet air velocity which reduced only by 0.39, whereas it hugely affected by the air ratio variation as it diminished by upto 5.42. Regarding the entropy generation rate, at minimum air velocity and air ratio, the cooler generated about the same amount of exergy accounting for about 0.52 W/K, and the generation rate was considerably increased with increasing their values due increase in exergy destruction.

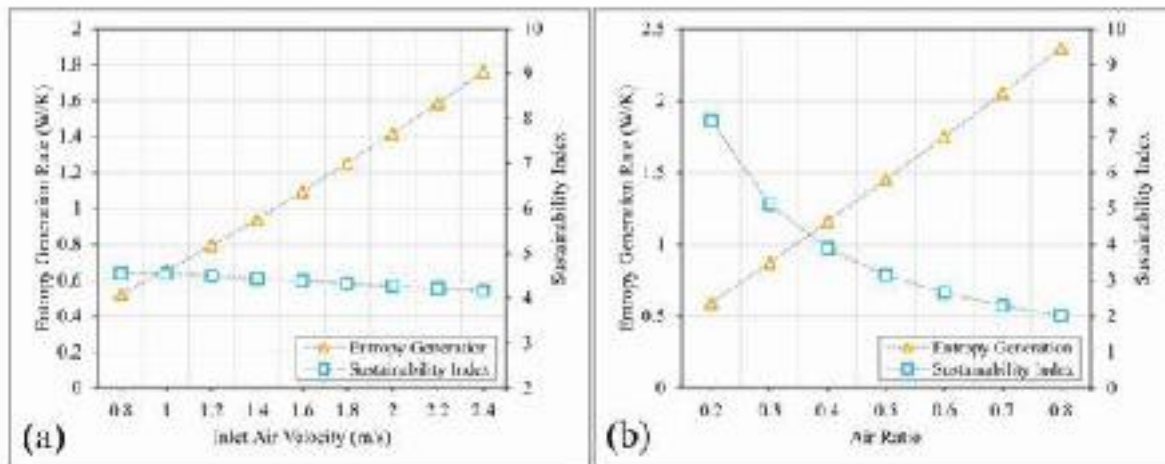


Fig. 5.41 Variation of entropy generation rate and sustainability index under influence of: (a) inlet air velocity; (b) air ratio

5.5.2 Influence of Geometrical Dimensions

The influence of the geometrical dimensions of the proposed DPEC, i.e., channel length and equivalent channel diameter, on the exergetic performance of the system are demonstrated and discussed in this section. As explained in Section 5.4.3, each time when channel diameter changed, the working channel height and total channel numbers changed as well. Fig. 5.42 illustrates the effect of the geometrical dimensions on exergy flow and total available exergy. It can be observed that the channel length has a marginal influence on flow exergies and total exergy.

It is worth mentioning that, over the span of channel length (from 40 cm to 220 cm), the total exergy only increased by 57 W (2% of total exergy), and the exergy destruction had a slight decrease of about 2% (from 24% to 22%). The small increment in total exergy with increasing channel length is due to increased air flow resistance that eventually contributes to the mechanical exergy. Likewise, with increasing the equivalent channel diameter from 0.39 cm to 1.11 cm, there were a marginal reduction regarding exergy flows and total exergy, but this time with a bit fluctuation between individual channel

diameters due to the reduction in air flow resistance (pressure drop) when the channel diameter increased.

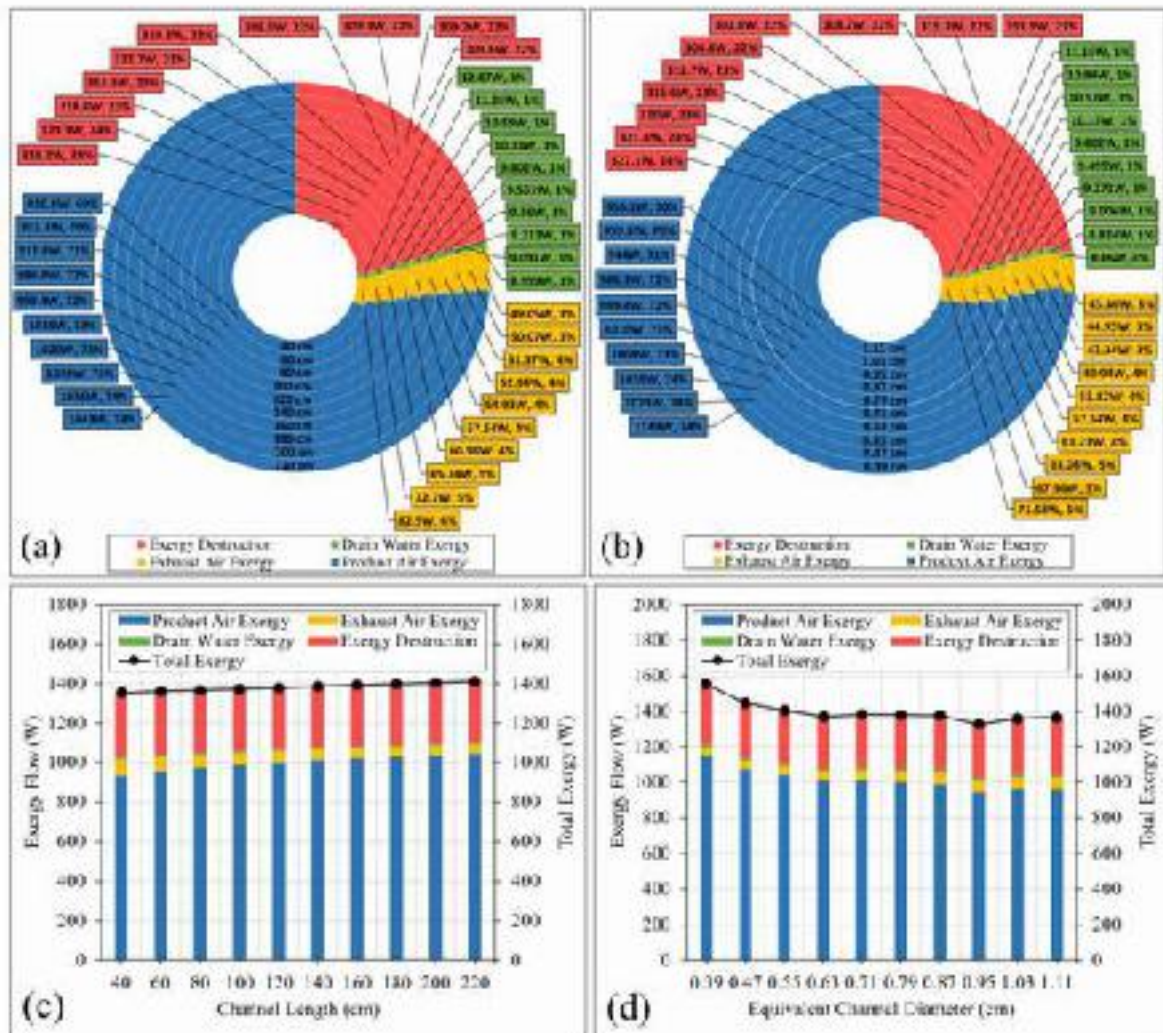


Fig. 5.42 (a) Effect of channel length on exergy flow; (b) Effect of equivalent channel diameter on exergy flow; (c) Variation of exergy flow and total exergy under effect of channel length; (d) Variation of exergy flow and total exergy under effect of equivalent channel diameter

In the mean time, as depicted in Fig. 5.43(a), the exergy efficiency slightly increased from 75.7% to 78.1% which increasing channel length owing to the marginal improvement in the product air exergy and slight reduction in the destructed exergy (refer to Fig. 5.42(a)). On the other hand, with increasing equivalent channel diameter, as shown in Fig. 5.43(b), the exergy efficiency

was gradually increased from 77.3% to 78.1% when the equivalent channel diameter increased from 0.39 cm to 0.55 cm, thereafter, it was slowly reduced to 76%. This indicates that 0.55 cm is the optimum equivalent channel diameter, after this value the available exergy of the working air is not efficiently used by the cooler to cool down the primary air.

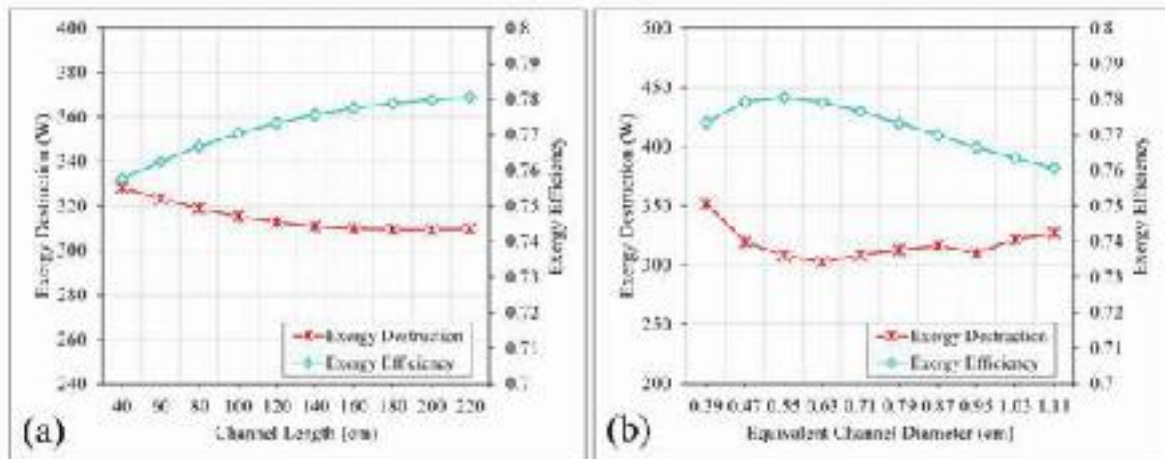


Fig. 5.43 Variation of exergy destruction and exergy efficiency under the influence of: (a) channel length; (b) equivalent channel diameter

The influence of geometrical dimensions on the entropy generation and sustainability of the cooler is shown in Fig. 5.44. The variation of entropy generation and sustainability are identical to that of exergy destruction and exergy efficiency under the influence of geometrical parameters, respectively. Consequently, the sustainability was slightly improved by upto 0.43 and entropy generation degraded by upto 0.06 W/K when channel length increased, while the sustainability was at its maximum value of 4.55 at equivalent channel diameter of 0.55 cm, and the entropy generation was somewhat flatuting between 1.14 W/K and 0.98 W/K. Overall, the influence of the geometrical parameters on the exergetic performance of the DPEC is rather small, with a bit more sensitive to the equivalent channel diameter.

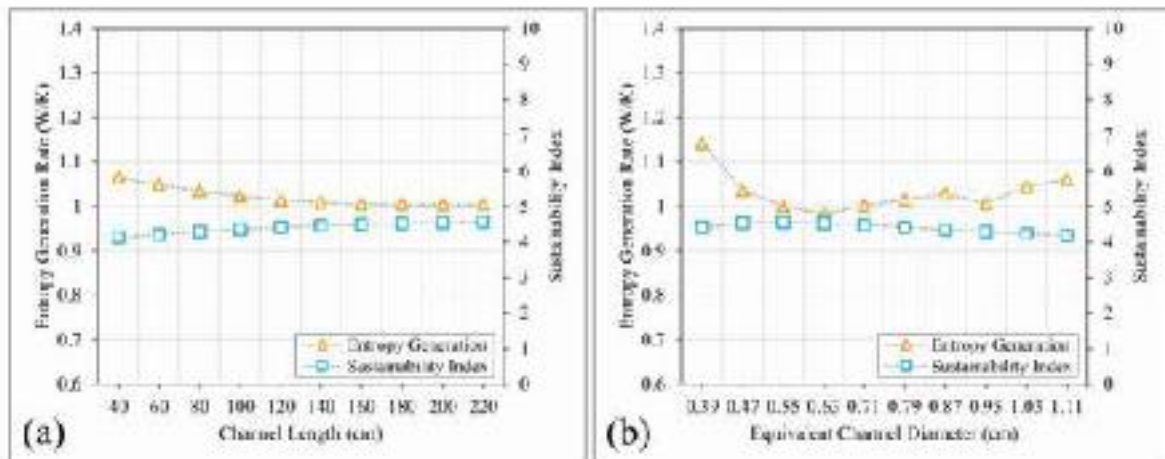


Fig. 5.44 Variation of entropy generation rate and sustainability index under influence of: (a) channel length; (b) equivalent channel diameter

5.6 CHAPTER SUMMERY

In this chapter, the numerical and experimental results obtained were investigated, compared, and discussed. First, the developed numerical simulation model has been validated with the experimental data from three published literatures. The comparison showed a good agreement with a maximum deviation of $\pm 4.4\%$. Thereafter, the parametrical analysis has been carried out to identify the optimum design parameters to be employed for the construction of the cooler. After the proposed DPEC has been manufactured, it was tested under series of experimentations at a wide range of varying inlet air temperature, humidity ratio, velocity, and air ratio.

The simulation model was further validated, this time with the experimental data acquired from the experimentations. Under all test conditions, the deviation rate was between $\pm 2.3\%$ and $\pm 5.1\%$. Through the validations conducted, the simulation model can be considered as reliable computational approach to be used to execute a deep parametrical analysis and evaluating the cooler's performance under any intended geometrical, operational, and meteorological conditions as well as different air-water flow configurations.

When the constructed unit tested experimentally, it could achieve a significantly high dew-point effectiveness of 99.6% and high wet-bulb effectiveness of 135%. These high thermal efficiency rates classify the cooler as super performing cooling device. Regarding the air velocity and air ratio, they had opposite effect on cooler's performance. With increasing the inlet air velocity, the product air temperature and cooling capacity of the coolers improved significantly, while they were noticeably diminished with increasing air ratio.

The analysis showed that the CF configuration could achieve a lower temperature product air than PF configuration (as low as 13°C), while the PF configuration achieved lower drain water temperature (as low as 9.2°C).

Under all test conditions, numerically and experimentally, the STX persistently outperformed the FPX in terms of thermal and energy performance, which indicates the superiority of the proposed STX.

Furthermore, exergy, entropy, and sustainability analysis has been carried out for STX-DPEC with CF configuration. The exergetic performance of the cooler varied differently under the effect of different operational and geometrical conditions. The system showed the highest and most stable exergy efficiency between 71.7% to 85.5% under the span of inlet air temperature (between 25°C to 55°C). Besides, the cooler was most sustainable when operated under hot and dry conditions. Whereas, it generated least exergy when operated at lower ambient temperature and humidity ratio and lower air flowrate. In another word, the cooler's irreversibility increased when operated under hotter and more humid ambient conditions and higher air flowrates.

CHAPTER 6

CONCLUSIONS AND FUTURE WORKS

6.1 CONCLUSIONS

In this dissertation, a novel dew point evaporative cooler has been proposed. The innovative cooler comprises of one shell and a bundle of tubes. The shell works as working channel, while the tube bundle works as primary channels. This neoteric design was first to be used as new geometry for DPEC. Through a comprehensive theoretical analysis and experimental investigation, it was found that the proposed DPEC continuously outperformed the conventional widely used flat-plate type DPEC under all test conditions in terms of thermal and energy performances. In addition, via shell and tube geometry, which has a simple and straight forward design, the design complexity of the heat and mass exchanger of previous DPECs was able to overcome which was one of the biggest impediment in globalization and mass production of such a high performance cooling machine.

The research started with a comprehensive literature review identifying all the limitations and shortcomings of the previously conducted research studies regarding DPECs. It was noticed that most of the former studies concentrated on improving cooler's performance through different numerical approaches theoretically, and employing different material types for evaporative surface and channels wall experimentally. Thus, improving the performance of the cooler via geometrical aspect was prominently underestimated. Thereafter, in this regard, several geometries were investigated, namely, circular-tube (i.e., shell and tube), square-tube, rectangular-tube, and triangular-tube. The tubes geometry representing the shape of the channels. Among all the geometries, the

cooler with shell and tube design performed the best, and thus it has been selected for the purpose of the current research study.

Thereafter, the proposed cooler has been further investigated through two different air-water flow configurations, namely, counter-flow and parallel-flow. For such an intensive theoretical investigation to be carried out, a dedicated numerical simulation model has been developed in Engineering Equation Solver (EES) environment. The simulation model characterized by being able to predict the thermal, energy, and exergy performance of the coolers with high accuracy, besides, one of the most distinct feature of the model is that it can calculate any operational and performance parameters at any point inside the HMX of the cooler. Based on the optimum geometrical parameters obtained from the simulation model, the system was constructed. The constructed system was tested under a wide range of operational conditions. The key findings from this work can be summarized in the following statements:

1. During the experimentations, the unit was able to achieve 99.6% dew-point effectiveness and 135% wet-bulb effectiveness when operated under inlet air temperature of 40°C and humidity ratio of 16.7 g/kg. This high level of performance ensures that the proposed system potentially can be considered as a superior alternative to high energy consuming vapor compression refrigeration systems for cooling of buildings.
2. When the constructed unit tested under extremely hot and dry weather condition of 53 °C temperature and 5.2 g/kg humidity ratio, which is similar to a critical Iraq's weather condition, the unit was able to achieve a cold air with 18.9°C (18.3°C numerically), or in another word, it could reduce the ambient temperature by up to 34.1 °C. Nonetheless, this super temperature reduction was achieved when the dew-point and wet-bulb effectiveness of the cooler was only 71.56% and 115.5%, respectively.

3. From the simulated results, it was observed that the dew-point/wet-bulb effectiveness of the system more sensitive to the inlet air temperature, velocity, humidity, air ratio, and geometrical sizes of the HMX, while less sensitive to feed water temperature and flowrate.
4. The effect of equivalent channel diameter was opposite to that of the channel length in terms of the cooler's thermal and energy performance owing to the fact that increasing channel length results in increasing surface area for heat and mass transfer process that will eventually contributes in improving cooler's performance, while increasing equivalent channel diameter will result in reducing the air flow velocity that directly reduces the heat and mass transfer coefficients causing reduction in cooling capability of the system.
5. During the experimentations, it was noticed that the cooling potential of the unit dramatically reduced when the air ratio gradually increased from 0.2 to 0.8. For instance, the cooling capacity was diminished from 135.1 W to 35.86 W, which accounted for 73.4% reduction in cooling potential.
6. For all the tests conducted on the DPECs in terms of air velocity and air ratio, the highest energy efficiency obtained when the air velocity spanning between 1.4 m/s to 2.2 m/s and air ratio ranged from 0.3 to 0.4, as within the range of this air ratio, the coolers acquired the best proportion between the cooling potential and power consumption.
7. The configuration between the primary channel air flow and downward flowing water significantly affects the drain water temperature. The parallel flow configuration distinguished by producing lower drain water temperature, while counter flow configuration distinguished by producing lower product air temperature. In average, the PF configuration was able to decrease drain water temperature by up to 17°C when compared to CF configuration, for all the proposed DPECs in general. In particular, the STX with PF configuration achieved lowest drain water temperature

ranging between 9.3 °C to 13.4 °C under the case of varying equivalent channel diameter.

8. The CF configuration is superior in producing colder air than PF configuration. However, under all conducted tests, the produced drain water temperature by CF configuration was between 21 °C to 32 °C, which is prominently elevated compared to the chill water temperature achieved by PF configuration.
9. In the PF configuration for both STX and FPX, condensation occurred near the end of working channels (at $z= 5$ cm). The occurrence of condensation at this location relates to higher working air's dew point temperature than the temperature of the channel wall.
10. The exhaust air from the DPECs was always fully saturated under all conducted tests experimentally and numerically as the relative humidity fluctuated between 99.4% to 100% during the experimentations while it was persistently 100% during simulations. This indicates efficient evaporation process inside the working channels of DPECs.
11. Under the variation of operational parameters, the proposed DPEC was able to achieve wet-bulb effectiveness of more than 100%, which indicates that the system can produce a cold air with its temperature lower than the wet-bulb temperature of entrance air and towards the dew-point temperature of ambient air.
12. Through exergy, entropy, and sustainability analysis, the STX-DPEC with CF configuration achieved the highest and most stable exergetic performance, in terms of exergy efficiency that was ranged between 71.7% to 85.5%, under the influence of inlet air temperature ranging between 25 °C to 55 °C.
13. The exergy destruction and entropy generation rates were minimum at lowest operational conditions (i.e., inlet air temperature, humidity ratio, inlet air velocity, and air ratio). However, both of these two rates were

noticeably increased with increasing operational conditions. This indicates that the irreversibility of the proposed DPEC increases when it operated under hotter, more humid, and higher air flowrate conditions.

14. The proposed DPEC recorded the highest sustainability index of about 7 at highest inlet air temperature of 55°C and lowest air ratio of 0.2. In addition, the air velocity, channel length, and equivalent channel diameter had the least contribution to the alteration of the sustainability of the cooler. Besides, the lowest sustainability recorded was 2.01 at air ratio of 0.8.

6.2 FUTURE WORKS

While this dissertation significantly contributed to the field of thermal mechanical engineering, there are several aspects that need further investigation:

1. To make the cooler sturdier, employing metallic tubes with thin walls suggested for investigation. In this regard, small diameter copper tube seems to be a promising candidate due to its high thermal conductivity corrosion resistant to water when compared to other metallic tubes. However, in this case, it must be decided between sturdiness and cost as the metallic tubes are not very economical and they are immensely more expensive than polycarbonate tubes.
2. During the experimental work, the water flowrate has been adjusted by the help of regulating valve. It would be better if a variable speed water pump employed to control the water flowrate via the alteration of input power to the pump. This technique will slightly contribute in reducing the overall power consumption by the cooler and improves its energy efficiency.
3. Due to conducting the current work in Iraq, it is preferred to test the proposed DPEC under the meteorological data of different cities of Iraq for

the cooling months of an entire year so as to assess the performance of the cooler and evaluate its acceptance rate at each city.

4. So as to extend the life span of the system, keeping the evaporation process running efficiently, and avoid contamination of the wet surface, it is proposed to use a water filter prior to the water storage tank to purify the water from any impurities, germs, minerals, and salt. As a fact, the evaporation process occurs in a higher rate for purified water when compared to a typical underground water.
5. By integrating the proposed DPEC with desiccant wheel, the inlet air can be dehumidified first before entering into the cooler. The air with less humidity will improve the coolers performance as it contributes in improved evaporation process. Consequently, more evaporation result in better cooling potential by the DPEC.

REFERENCES

- Abbood, A.W., Al-Obaidi, K.M., Awang, H., Abdul Rahman, A.M., 2015. Achieving energy efficiency through industrialized building system for residential buildings in Iraq. *International Journal of Sustainable Built Environment* 4, 78–90. <https://doi.org/10.1016/j.ijbsbe.2015.02.002>
- Afshari, A., Nikolopoulou, C., Martin, M., 2014. Life-cycle analysis of building retrofits at the urban scale-a case study in United Arab Emirates. *Sustainability* 6, 453–473. <https://doi.org/10.3390/su6010453>
- Akhlaghi, Y.G., Ma, X., Zhao, X., Shittu, S., Li, J., 2019. A statistical model for dew point air cooler based on the multiple polynomial regression approach. *Energy* 181, 868–881. <https://doi.org/10.1016/j.energy.2019.05.213>
- Al-Zubaydi, A.Y.T., Hong, G., 2019. Experimental study of a novel water-spraying configuration in indirect evaporative cooling. *Appl Therm Eng* 151, 283–293. <https://doi.org/10.1016/j.applthermaleng.2019.02.019>
- Anisimov, S., Pandelidis, D., Jedlikowski, A., Polushkin, V., 2014. Performance investigation of a M (Maisotsenko)-cycle cross-flow heat exchanger used for indirect evaporative cooling. *Energy* 76, 593–606. <https://doi.org/10.1016/j.energy.2014.08.055>
- ANSI/ASHRAE Standard 55, 2017. Thermal Environmental Conditions for Human Occupancy.
- ANSI/ASHRAE Standard 143, 2015. Method Of Test For Rating Indirect Evaporative Coolers. ASHRAE.
- Arun, B., Mariappan, V., 2019. Experimental study of an ultrasonic regenerative evaporative cooler for a desiccant cooling system. *Building Services Engineering Research and Technology* 40, 151–175. <https://doi.org/10.1177/0143624418810934>
- Baakeem, S.S., Orfi, J., Mohamad, A., Bawazeer, S., 2019. The possibility of using a novel dew point air cooling system (M-Cycle) for A/C application in Arab Gulf Countries. *Build Environ* 148, 185–197. <https://doi.org/10.1016/j.buildenv.2018.11.002>

- Baehr, H.D. (Hans D., Stephan, K. (Karl), 2006. Heat and mass-transfer. Springer.
- Bejan A., 2016. Advanced engineering thermodynamics. John Wiley & Sons.
- Benato, A., Stoppato, A., De Vanna, F., Schiro, F., 2021. Spraying Cooling System for PV Modules: Experimental Measurements for Temperature Trends Assessment and System Design Feasibility. *Designs (Basel)* 5, 25. <https://doi.org/10.3390/designs5020025>
- Bergman, T.L., Lavine, Adrienne., Incropera, F.P., 2017. Fundamentals of heat and mass transfer.
- Blanco-Marigorta, A.M., Tejero-González, A., Rey-Hernández, J.M., Velasco Gómez, E., Gaggioli, R., 2022. Exergy analysis of two indirect evaporative cooling experimental prototypes. *Alexandria Engineering Journal* 61, 4359–4369. <https://doi.org/10.1016/j.aej.2021.09.065>
- Boukhanouf, R., Ibrahim, H.G., Alharbi, A., Kanzari, M., 2014. Investigation of an Evaporative Cooler for Buildings in Hot and Dry Climates. *Journal of Clean Energy Technologies* 221–225. <https://doi.org/10.7763/JOCET.2014.V2.127>
- Buker, M.S., Riffat, S.B., 2016a. Performance Analysis of a Combined Building Integrated PV/T Collector with a Liquid Desiccant Enhanced Dew Point Cooler. *Energy Procedia* 91, 717–727. <https://doi.org/10.1016/j.egypro.2016.06.235>
- Buker, M.S., Riffat, S.B., 2016b. Performance Analysis of a Combined Building Integrated PV/T Collector with a Liquid Desiccant Enhanced Dew Point Cooler. *Energy Procedia* 91, 717–727. <https://doi.org/10.1016/j.egypro.2016.06.235>
- California Energy Commission, 2022. Building energy efficiency standards for residential and nonresidential buildings.
- Caliskan, H., Dincer, I., Hepbasli, A., 2012a. Exergoeconomic, enviroeconomic and sustainability analyses of a novel air cooler. *Energy Build* 55, 747–756. <https://doi.org/10.1016/j.enbuild.2012.03.024>
- Caliskan, H., Dincer, I., Hepbasli, A., 2012b. A comparative study on energetic, exergetic and environmental performance assessments of novel M-Cycle

- based air coolers for buildings. *Energy Convers Manag* 56, 69–79.
<https://doi.org/10.1016/j.enconman.2011.11.007>
- Caliskan, H., Hepbasli, A., Dincer, I., Maisotsenko, V., 2011. Thermodynamic performance assessment of a novel air cooling cycle: Maisotsenko cycle. *International Journal of Refrigeration* 34, 980–990.
<https://doi.org/10.1016/j.ijrefrig.2011.02.001>
- Çengel Y. A., Cimbala J. M., 2020. *Fluid Mechanics Fundamentals and Applications, Fourth Edition.* ed. Mc Graw Hill.
- Cengel, Y.A., Cimbala, J.M., Ghajar, A.J. (Afshin J., 2022. *Fundamentals of thermal-fluid sciences.*
- Chauhan, S.S., Rajput, S.P.S., 2016. Parametric analysis of a combined dew point evaporative-vapour compression based air conditioning system. *Alexandria Engineering Journal* 55, 2333–2344.
<https://doi.org/10.1016/j.aej.2016.05.005>
- Chen, Q., Ja, M.K., Burhan, M., Shahzad, M.W., Ybyraiymkul, D., Zheng, H., Ng, K.C., 2022. Experimental study of a sustainable cooling process hybridizing indirect evaporative cooling and mechanical vapor compression. *Energy Reports* 8, 7945–7956.
<https://doi.org/10.1016/j.egyr.2022.06.019>
- Chen, Q., Kum Ja, M., Burhan, M., Akhtar, F.H., Shahzad, M.W., Ybyraiymkul, D., Ng, K.C., 2021. A hybrid indirect evaporative cooling-mechanical vapor compression process for energy-efficient air conditioning. *Energy Convers Manag* 248, 114798.
<https://doi.org/10.1016/j.enconman.2021.114798>
- Chen, Y., Huang, X., Sun, T., Chu, J., 2021a. Experimental study of plant fiber-polymer composite for indirect evaporative cooler application. *Appl Therm Eng* 199, 117543.
<https://doi.org/10.1016/j.applthermaleng.2021.117543>
- Chen, Y., Huang, X., Sun, T., Chu, J., 2021b. Experimental study of plant fiber-polymer composite for indirect evaporative cooler application. *Appl Therm Eng* 199, 117543.
<https://doi.org/10.1016/j.applthermaleng.2021.117543>

- Chen, Y., Yang, H., Luo, Y., 2018. Investigation on solar assisted liquid desiccant dehumidifier and evaporative cooling system for fresh air treatment. *Energy* 143, 114–127. <https://doi.org/10.1016/j.energy.2017.10.124>
- Chengqin, R., Nianping, L., Guangfa, T., 2002a. Principles of exergy analysis in HVAC and evaluation of evaporative cooling schemes. *Build Environ* 37, 1045–1055. [https://doi.org/10.1016/S0360-1323\(01\)00104-4](https://doi.org/10.1016/S0360-1323(01)00104-4)
- Chengqin, R., Nianping, L., Guangfa, T., 2002b. Principles of exergy analysis in HVAC and evaluation of evaporative cooling schemes. *Build Environ* 37, 1045–1055. [https://doi.org/10.1016/S0360-1323\(01\)00104-4](https://doi.org/10.1016/S0360-1323(01)00104-4)
- Choi, J.-S., Kim, G.-C., Oh, M.-S., Kim, E.-J., 2023. Air-type photovoltaic thermal (PVT) system connected to heat recovery ventilators installed in typical classroom. *Energy Build* 298, 113535. <https://doi.org/10.1016/j.enbuild.2023.113535>
- Cook, J., 1979. *Cool houses for desert suburbs: optimizing heating & cooling for Arizona builders*. Phoenix: Arizona Solar Energy Commission.
- Cooper, G., 1998. *Air-Conditioning America: Engineers and the Controlled Environment 1900-1960*. Baltimore: Johns Hopkins University Press 176–178.
- Cui, X., Chua, K.J., Islam, M.R., Ng, K.C., 2015a. Performance evaluation of an indirect pre-cooling evaporative heat exchanger operating in hot and humid climate. *Energy Convers Manag* 102, 140–150. <https://doi.org/10.1016/j.enconman.2015.02.025>
- Cui, X., Chua, K.J., Islam, M.R., Ng, K.C., 2015b. Performance evaluation of an indirect pre-cooling evaporative heat exchanger operating in hot and humid climate. *Energy Convers Manag* 102, 140–150. <https://doi.org/10.1016/j.enconman.2015.02.025>
- Cui, X., Yang, C., Yan, W., Zhang, L., Wan, Y., Chua, K.J., 2023. Experimental study on a moisture-conducting fiber-assisted tubular indirect evaporative cooler. *Energy* 278, 128014. <https://doi.org/10.1016/j.energy.2023.128014>
- De Antonellis, S., Joppolo, C.M., Liberati, P., 2019. Performance measurement of a cross-flow indirect evaporative cooler: Effect of water nozzles and

- airflows arrangement. *Energy Build* 184, 114–121. <https://doi.org/10.1016/j.enbuild.2018.11.049>
- Delfani, S., Karami, M., 2020. Transient simulation of solar desiccant/M-Cycle cooling systems in three different climatic conditions. *Journal of Building Engineering* 29, 101152. <https://doi.org/10.1016/j.jobbe.2019.101152>
- Dincer I., Rosen M.A., 2020. *Exergy: energy, environment and sustainable development*. Elsevier Ltd.
- Dizaji, H.S., Hu, E., Chen, L., Pourhedayat, S., Wae-hayee, M., 2021. Proposing the concept of mini Maisotsenko cycle cooler for electronic cooling purposes; experimental study. *Case Studies in Thermal Engineering* 27, 101325. <https://doi.org/10.1016/j.csite.2021.101325>
- Dowdy, J., Karabash, N., 1987. Experimental determination of heat and mass transfer coefficients in rigid impregnated cellulose evaporative media. *ASHRAE Trans* 93, 382–95.
- Duan, Z., 2011. *Investigation of a Novel Dew Point Indirect Evaporative Air Conditioning System for Buildings*.
- Duan, Z., Zhan, C., Zhao, X., Dong, X., 2016a. Experimental study of a counter-flow regenerative evaporative cooler. *Build Environ* 104, 47–58. <https://doi.org/10.1016/j.buildenv.2016.04.029>
- Duan, Z., Zhan, C., Zhao, X., Dong, X., 2016b. Experimental study of a counter-flow regenerative evaporative cooler. *Build Environ* 104, 47–58. <https://doi.org/10.1016/j.buildenv.2016.04.029>
- Duan, Z., Zhao, X., Li, J., 2017a. Design, fabrication and performance evaluation of a compact regenerative evaporative cooler: Towards low energy cooling for buildings. *Energy* 140, 506–519. <https://doi.org/10.1016/j.energy.2017.08.110>
- Duan, Z., Zhao, X., Liu, J., Zhang, Q., 2019. Dynamic simulation of a hybrid dew point evaporative cooler and vapour compression refrigerated system for a building using EnergyPlus. *Journal of Building Engineering* 21, 287–301. <https://doi.org/10.1016/j.jobbe.2018.10.028>
- Duan, Z., Zhao, X., Zhan, C., Dong, X., Chen, H., 2017b. Energy saving potential of a counter-flow regenerative evaporative cooler for various

- climates of China: Experiment-based evaluation. *Energy Build* 148, 199–210. <https://doi.org/10.1016/j.enbuild.2017.04.012>
- Elsarrag, E., Igobo, O.N., Alhorr, Y., Davies, P.A., 2016. Solar pond powered liquid desiccant evaporative cooling. *Renewable and Sustainable Energy Reviews* 58, 124–140. <https://doi.org/10.1016/j.rser.2015.12.053>
- Farmahini-Farahani, M., Delfani, S., Esmaeelian, J., 2012. Exergy analysis of evaporative cooling to select the optimum system in diverse climates. *Energy* 40, 250–257. <https://doi.org/10.1016/j.energy.2012.01.075>
- Fouda, A., Melikyan, Z., 2011. A simplified model for analysis of heat and mass transfer in a direct evaporative cooler. *Appl Therm Eng* 31, 932–936. <https://doi.org/10.1016/j.applthermaleng.2010.11.016>
- Gao, F., Thu, K., Wang, S., Zhao, F., Lin, J., Wu, K., 2023. Numerical investigation of a novel tubular dew-point evaporative cooler. *Appl Therm Eng* 223, 120064. <https://doi.org/10.1016/j.applthermaleng.2023.120064>
- Ghosh, A., Bhattacharya, J., 2021a. A solar regenerated liquid desiccant evaporative cooling system for office building application in hot and humid climate. *Thermal Science and Engineering Progress* 22, 100804. <https://doi.org/10.1016/j.tsep.2020.100804>
- Ghosh, A., Bhattacharya, J., 2021b. A solar regenerated liquid desiccant evaporative cooling system for office building application in hot and humid climate. *Thermal Science and Engineering Progress* 22, 100804. <https://doi.org/10.1016/j.tsep.2020.100804>
- Goetzler W., Zogg R., Young J., Johnson C., 2014. Energy Savings Potential and RD&D Opportunities for Non-Vapor-Compression HVAC Technologies. U.S. Department of Energy Office of Energy Efficiency and Renewable Energy Building Technologies Office.
- Golizadeh Akhlaghi, Y., Badiei, A., Zhao, X., Aslansefat, K., Xiao, X., Shittu, S., Ma, X., 2020. A constraint multi-objective evolutionary optimization of a state-of-the-art dew point cooler using digital twins. *Energy Convers Manag* 211, 112772. <https://doi.org/10.1016/j.enconman.2020.112772>
- Guilizzoni, M., Milani, S., Liberati, P., De Antonellis, S., 2019. Effect of plates coating on performance of an indirect evaporative cooling system.

International Journal of Refrigeration 104, 367–375.
<https://doi.org/10.1016/j.ijrefrig.2019.05.029>

Habchi, C., Bou-Mosleh, C., Khaled, M., 2024. An experimental analysis of a hybrid photovoltaic thermal system through parallel water pipe integration. *International Journal of Thermofluids* 21, 100538.
<https://doi.org/10.1016/j.ijft.2023.100538>

Harrouz, J.P., Ghali, K., Ghaddar, N., 2021. Integrated solar – Windcatcher with dew-point indirect evaporative cooler for classrooms. *Appl Therm Eng* 188, 116654. <https://doi.org/10.1016/j.applthermaleng.2021.116654>

Hasan, A.A., 2012. Available Ways For Energy Conservation in Iraqi Residence Sector. *Al-Rafidain University College For Sciences* 29.

Hazi, A., Hazi, G., Grigore, R., Vernica, S., 2014. Opportunity to use PVT systems for water heating in industry. *Appl Therm Eng* 63, 151–157.
<https://doi.org/10.1016/j.applthermaleng.2013.11.010>

He, W., Huang, G., Markides, C.N., 2023. Synergies and potential of hybrid solar photovoltaic-thermal desalination technologies. *Desalination* 552, 116424. <https://doi.org/10.1016/j.desal.2023.116424>

Heidarinejad, G., Khalajzadeh, V., Delfani, S., 2010. Performance analysis of a ground-assisted direct evaporative cooling air conditioner. *Build Environ* 45, 2421–2429. <https://doi.org/10.1016/j.buildenv.2010.05.009>

Hosseini Motlagh, N., Mohammadrezaei, M., Hunt, J., Zakeri, B., 2020. Internet of Things (IoT) and the Energy Sector. *Energies (Basel)* 13, 494.
<https://doi.org/10.3390/en13020494>

IEA, 2021. Electricity Information: Overview, IEA, Paris [WWW Document]. URL <https://www.iea.org/reports/electricity-information-overview> (accessed 3.6.24).

IEA Iraq, 2021. International Energy Agency.

International Renewable Energy Agency, 2022. World energy transitions outlook.

Irshad, K., Rehman, S., Zahir, M.H., Khan, F., Balakrishnan, D., Saha, B.B., 2024. Analysis of photovoltaic thermoelectric air conditioning for

- personalized cooling in arid climate. *Journal of Building Engineering* 84, 108533. <https://doi.org/10.1016/j.jobe.2024.108533>
- Isah, A.S., Takaijudin, H.B., Singh, B.S.M., Abimbola, T.O., Muhammad, M.M., Sani, S.B., 2024. Photovoltaic-integrated advancements for sustainable water production: Developing and evaluating an enhanced hybrid solar desalination system. *Desalination* 579, 117453. <https://doi.org/10.1016/j.desal.2024.117453>
- Jia, L., Liu, J., Wang, C., Cao, X., Zhang, Z., 2019. Study of the thermal performance of a novel dew point evaporative cooler. *Appl Therm Eng* 160, 114069. <https://doi.org/10.1016/j.applthermaleng.2019.114069>
- Johnston, J.D., Cowger, A.E., Weber, K.S., 2022. Bioaerosol and microbial exposures from residential evaporative coolers and their potential health outcomes: A review. *Indoor Air* 32. <https://doi.org/10.1111/ina.13082>
- Jradi, M., Riffat, S., 2016. Testing and performance analysis of a hollow fiber-based core for evaporative cooling and liquid desiccant dehumidification. *Int J Green Energy* 13, 1388–1399. <https://doi.org/10.1080/15435075.2016.1183205>
- Junzeng, X., Qi, W., Shizhang, P., Yanmei, Y., 2012. Error of Saturation Vapor Pressure Calculated by Different Formulas and Its Effect on Calculation of Reference Evapotranspiration in High Latitude Cold Region. *Procedia Eng* 28, 43–48. <https://doi.org/10.1016/j.proeng.2012.01.680>
- Kashif Shahzad, M., Qadar Chaudhary, G., Ali, M., Ahmed Sheikh, N., Shahid Khalil, M., Rashid, T.U., 2018. Experimental evaluation of a solid desiccant system integrated with cross flow Maisotsenko cycle evaporative cooler. *Appl Therm Eng* 128, 1476–1487. <https://doi.org/10.1016/j.applthermaleng.2017.09.105>
- Kashyap, S., Sarkar, J., Kumar, A., 2022a. Experimental exergy, economic and sustainability analyses of the dual-mode evaporative cooler. *International Journal of Refrigeration* 135, 121–130. <https://doi.org/10.1016/j.ijrefrig.2021.12.005>
- Kashyap, S., Sarkar, J., Kumar, A., 2022b. Energy, exergy and economic assessments of the dual-mode evaporative cooler for various international

- climate zones. *Building Services Engineering Research and Technology* 43, 179–196. <https://doi.org/10.1177/01436244211044921>
- Kashyap, S., Sarkar, J., Kumar, A., 2022c. Energy, exergy and economic assessments of the dual-mode evaporative cooler for various international climate zones. *Building Services Engineering Research and Technology* 43, 179–196. <https://doi.org/10.1177/01436244211044921>
- Kashyap, S., Sarkar, J., Kumar, A., 2020a. Comparative performance analysis of different novel regenerative evaporative cooling device topologies. *Appl Therm Eng* 176, 115474. <https://doi.org/10.1016/j.applthermaleng.2020.115474>
- Kashyap, S., Sarkar, J., Kumar, A., 2020b. Exergy, economic, environmental and sustainability analyses of possible regenerative evaporative cooling device topologies. *Build Environ* 180, 107033. <https://doi.org/10.1016/j.buildenv.2020.107033>
- Khalid, O., Ali, M., Sheikh, N.A., Ali, H.M., Shehryar, M., 2016. Experimental analysis of an improved Maisotsenko cycle design under low velocity conditions. *Appl Therm Eng* 95, 288–295. <https://doi.org/10.1016/j.applthermaleng.2015.11.030>
- Kousar, R., Ali, M., Amjad, M.K., Ahmad, W., 2022. Energy, Exergy, Economic, Environmental (4Es) comparative performance evaluation of dewpoint evaporative cooler configurations. *Journal of Building Engineering* 45, 103466. <https://doi.org/10.1016/j.jobe.2021.103466>
- Kozak-Jagieła, E., Cisek, P., Ocio , P., 2023. Cooling techniques for PV panels: A review. *Scientiae Radices* 2, 47–68. <https://doi.org/10.58332/scirad2023v2i1a03>
- Kozubal, E., Woods, J., Judkoff, R., 2015. Indirect Evaporative Coolers with Enhanced Heat Transfer. US Patent No. 9,140,471 B2.
- Lacour, S.O.L., Trinquet, F., Vendee, P.E., Vallet, A., Delahaye, A., Fournaison, L., 2018. Assessment of the wet area of a heat exchanger exposed to a water spray. *Appl Therm Eng* 128, 434–443. <https://doi.org/10.1016/j.applthermaleng.2017.09.030>
- Lai, L., Wang, X., Kefayati, G., Hu, E., 2022. Performance evaluation of a solar powered solid desiccant evaporative cooling system with different

- recirculation air ratios. *Energy Build* 270, 112273.
<https://doi.org/10.1016/j.enbuild.2022.112273>
- Lee, J., Lee, D.-Y., 2013. Experimental study of a counter flow regenerative evaporative cooler with finned channels. *Int J Heat Mass Transf* 65, 173–179. <https://doi.org/10.1016/j.ijheatmasstransfer.2013.05.069>
- Lin, J., Bui, D.T., Wang, R., Chua, K.J., 2018a. The counter-flow dew point evaporative cooler: Analyzing its transient and steady-state behavior. *Appl Therm Eng* 143, 34–47.
<https://doi.org/10.1016/j.applthermaleng.2018.07.092>
- Lin, J., Bui, D.T., Wang, R., Chua, K.J., 2018b. The counter-flow dew point evaporative cooler: Analyzing its transient and steady-state behavior. *Appl Therm Eng* 143, 34–47.
<https://doi.org/10.1016/j.applthermaleng.2018.07.092>
- Lin, J., Bui, D.T., Wang, R., Chua, K.J., 2018c. On the exergy analysis of the counter-flow dew point evaporative cooler. *Energy* 165, 958–971.
<https://doi.org/10.1016/j.energy.2018.10.042>
- Lin, J., Thu, K., Bui, T.D., Wang, R.Z., Ng, K.C., Chua, K.J., 2016. Study on dew point evaporative cooling system with counter-flow configuration. *Energy Convers Manag* 109, 153–165.
<https://doi.org/10.1016/j.enconman.2015.11.059>
- Lin, J., Wang, R., Li, C., Wang, S., Long, J., Chua, K.J., 2020a. Towards a thermodynamically favorable dew point evaporative cooler via optimization. *Energy Convers Manag* 203, 112224.
<https://doi.org/10.1016/j.enconman.2019.112224>
- Lin, J., Wang, R., Li, C., Wang, S., Long, J., Chua, K.J., 2020b. Towards a thermodynamically favorable dew point evaporative cooler via optimization. *Energy Convers Manag* 203, 112224.
<https://doi.org/10.1016/j.enconman.2019.112224>
- Lin, J., Wang, R.Z., Kumja, M., Bui, T.D., Chua, K.J., 2017. Modelling and experimental investigation of the cross-flow dew point evaporative cooler with and without dehumidification. *Appl Therm Eng* 121, 1–13.
<https://doi.org/10.1016/j.applthermaleng.2017.04.047>

- Lin Jie, 2018. A NOVEL APPROACH TO AIR CONDITIONING VIA DECOUPLED LATENT AND SENSIBLE COOLING.
- Liu, Y., Akhlaghi, Y.G., Zhao, X., Li, J., 2019a. Experimental and numerical investigation of a high-efficiency dew-point evaporative cooler. *Energy Build* 197, 120–130. <https://doi.org/10.1016/j.enbuild.2019.05.038>
- Liu, Y., Li, J.M., Yang, X., Zhao, X., 2019b. Two-dimensional numerical study of a heat and mass exchanger for a dew-point evaporative cooler. *Energy* 168, 975–988. <https://doi.org/10.1016/j.energy.2018.11.135>
- Liu, Y., Yang, X., Li, J., Zhao, X., 2018. Energy savings of hybrid dew-point evaporative cooler and micro-channel separated heat pipe cooling systems for computer data centers. *Energy* 163, 629–640. <https://doi.org/10.1016/j.energy.2018.07.172>
- Lv, J., Xu, H., Xu, T., Liu, H., Qin, J., 2021. Study on the performance of a unit dew-point evaporative cooler with fibrous membrane and its application in typical regions. *Case Studies in Thermal Engineering* 24, 100881. <https://doi.org/10.1016/j.csite.2021.100881>
- Ma, X., Zeng, C., Zhu, Z., Zhao, X., Xiao, X., Akhlaghi, Y.G., Shittu, S., 2023. Real life test of a novel super performance dew point cooling system in operational live data centre. *Appl Energy* 348, 121483. <https://doi.org/10.1016/j.apenergy.2023.121483>
- Mahdi, A.H., Ali Aljubury, I.M., 2021. Experimental investigation of two-stage evaporative cooler powered by photovoltaic panels using underground water. *Journal of Building Engineering* 44, 102679. <https://doi.org/10.1016/j.jobbe.2021.102679>
- MAHJOUB, S., SALIMPOUR, M.R., SHOKOUHMAND, H., BAHRAMI, Z., 2014. Entropy generation analysis in an evaporative air-cooled heat exchanger. *Journal of Thermal Science and Technology* 9, JTST0004–JTST0004. <https://doi.org/10.1299/jtst.2014jtst0004>
- Mi, P., Ma, L., Zhang, J., 2020. Integrated optimization study of hot water supply system with multi-heat-source for the public bath based on PVT heat pump and water source heat pump. *Appl Therm Eng* 176, 115146. <https://doi.org/10.1016/j.applthermaleng.2020.115146>

- Min, Y., Chen, Y., Yang, H., 2019. Numerical study on indirect evaporative coolers considering condensation: A thorough comparison between cross flow and counter flow. *Int J Heat Mass Transf* 131, 472–486. <https://doi.org/10.1016/j.ijheatmasstransfer.2018.11.082>
- Min, Y., Shi, W., Shen, B., Chen, Y., Yang, H., 2021. Enhancing the cooling and dehumidification performance of indirect evaporative cooler by hydrophobic-coated primary air channels. *Int J Heat Mass Transf* 179, 121733. <https://doi.org/10.1016/j.ijheatmasstransfer.2021.121733>
- Montazeri, H., Blocken, B., Hensen, J.L.M., 2015. Evaporative cooling by water spray systems: CFD simulation, experimental validation and sensitivity analysis. *Build Environ* 83, 129–141. <https://doi.org/10.1016/j.buildenv.2014.03.022>
- Nasr, M.M., Hassan, M.S., 2009. Experimental and theoretical investigation of an innovative evaporative condenser for residential refrigerator. *Renew Energy* 34, 2447–2454. <https://doi.org/10.1016/j.renene.2009.03.008>
- Nateqi, M., Rajabi Zargarabadi, M., Rafee, R., 2021. Experimental investigations of spray flow rate and angle in enhancing the performance of PV panels by steady and pulsating water spray system. *SN Appl Sci* 3, 130. <https://doi.org/10.1007/s42452-021-04169-4>
- Oh, S.J., Ng, K.C., Thu, K., Chun, W., Chua, K.J.E., 2016. Forecasting long-term electricity demand for cooling of Singapore’s buildings incorporating an innovative air-conditioning technology. *Energy Build* 127, 183–193. <https://doi.org/10.1016/j.enbuild.2016.05.073>
- Olmü , U., Güzelel, Y.E., Büyükalaca, O., 2023. Seasonal analysis of a desiccant air-conditioning system supported by water-cooled PV/T units. *Energy Build* 291, 113101. <https://doi.org/10.1016/j.enbuild.2023.113101>
- P. Glanville, A. Kozlov, V. Maisotsenko, 2011. Dew Point Evaporative Cooling: Technology Review and Fundamentals. *ASHRAE Trans* 117.
- Pakari, A., Ghani, S., 2019. Comparison of 1D and 3D heat and mass transfer models of a counter flow dew point evaporative cooling system: Numerical and experimental study. *International Journal of Refrigeration* 99, 114–125. <https://doi.org/10.1016/j.ijrefrig.2019.01.013>

- Pandelidis, D., Anisimov, S., 2015. Numerical analysis of the selected operational and geometrical aspects of the M-cycle heat and mass exchanger. *Energy Build* 87, 413–424. <https://doi.org/10.1016/j.enbuild.2014.11.042>
- Pandelidis, D., Anisimov, S., Worek, W.M., Dr g, P., 2016. Comparison of desiccant air conditioning systems with different indirect evaporative air coolers. *Energy Convers Manag* 117, 375–392. <https://doi.org/10.1016/j.enconman.2016.02.085>
- Pandelidis, D., Cicho , A., Pacak, A., Anisimov, S., Dr g, P., 2018. Application of the cross-flow Maisotsenko cycle heat and mass exchanger to the moderate climate in different configurations in air-conditioning systems. *Int J Heat Mass Transf* 122, 806–817. <https://doi.org/10.1016/j.ijheatmasstransfer.2018.02.028>
- Pandelidis, D., Cicho , A., Pacak, A., Dr g, P., Dr g, M., Worek, W., Cetin, S., 2020a. Performance study of the cross-flow Maisotsenko cycle in humid climate conditions. *International Communications in Heat and Mass Transfer* 115, 104581. <https://doi.org/10.1016/j.icheatmasstransfer.2020.104581>
- Pandelidis, D., Pacak, A., Cicho , A., Dr g, P., Worek, W., Cetin, S., 2020b. Numerical and experimental analysis of precooled desiccant system. *Appl Therm Eng* 181, 115929. <https://doi.org/10.1016/j.applthermaleng.2020.115929>
- Pandelidis, D., Pacak, A., Cicho , A., Gizicki, W., Worek, W., Cetin, S., 2021. Experimental study of plate materials for evaporative air coolers. *International Communications in Heat and Mass Transfer* 120, 105049. <https://doi.org/10.1016/j.icheatmasstransfer.2020.105049>
- R. Chengqin, Y. Hongxing, 2006. An analytical model for the heat and mass transfer processes in indirect evaporative cooling with parallel/counter flow configurations. *Int J Heat Mass Transf* 617–627.
- Rasheed, S., Ali, M., Ali, H., Sheikh, N., 2022. Experimental Analysis of the Dew Point Indirect Evaporative Cooler Operating with Solar Panels, in: *The 1st International Conference on Energy, Power and Environment*. MDPI, Basel Switzerland, p. 90. <https://doi.org/10.3390/engproc2021012090>

- Ratlamwala, T.A.H., Dincer, I., 2013. Efficiency assessment of key psychometric processes. *International Journal of Refrigeration* 36, 1142–1153. <https://doi.org/10.1016/j.ijrefrig.2012.10.038>
- Ravajiri, E.S., Hasanloo, M., Jalali, A., Houshfar, E., 2024. Techno-economic analysis and tri-objective optimization of a novel HDH desalination with PVT and vapor-compression chiller for sustainable water supply in remote areas. *Sustain Cities Soc* 101, 105211. <https://doi.org/10.1016/j.scs.2024.105211>
- Reddy, S.R., Ebadian, M.A., Lin, C.-X., 2015. A review of PV–T systems: Thermal management and efficiency with single phase cooling. *Int J Heat Mass Transf* 91, 861–871. <https://doi.org/10.1016/j.ijheatmasstransfer.2015.07.134>
- Ren C., Yang H., 2006. An analytical model for the heat and mass transfer processes in indirect evaporative cooling with parallel/counter flow configurations. *Int J Heat Mass Transf* 49.
- REU, 2015. Renewable Energy Unit, Institute for Energy, Directorate-general joint research centre, European Commission, The European Code of Conduct on Data Centre Energy Efficiency’, version 3.0.
- Riangvilaikul, B., Kumar, S., 2010a. An experimental study of a novel dew point evaporative cooling system. *Energy Build* 42, 637–644. <https://doi.org/10.1016/j.enbuild.2009.10.034>
- Riangvilaikul, B., Kumar, S., 2010b. An experimental study of a novel dew point evaporative cooling system. *Energy Build* 42, 637–644. <https://doi.org/10.1016/j.enbuild.2009.10.034>
- Sadighi Dizaji, H., Hu, E.J., Chen, L., Pourhedayat, S., 2020. Analytical/experimental sensitivity study of key design and operational parameters of perforated Maisotsenko cooler based on novel wet-surface theory. *Appl Energy* 262, 114557. <https://doi.org/10.1016/j.apenergy.2020.114557>
- Sadighi Dizaji, H., Hu, E.J., Chen, L., Pourhedayat, S., 2019a. Comprehensive exergetic study of regenerative Maisotsenko air cooler; formulation and sensitivity analysis. *Appl Therm Eng* 152, 455–467. <https://doi.org/10.1016/j.applthermaleng.2019.02.067>

- Sadighi Dizaji, H., Hu, E.J., Chen, L., Pourhedayat, S., 2019b. Comprehensive exergetic study of regenerative Maisotsenko air cooler; formulation and sensitivity analysis. *Appl Therm Eng* 152, 455–467. <https://doi.org/10.1016/j.applthermaleng.2019.02.067>
- Sarntichartsak, P., Thepa, S., 2013. Modeling and experimental study on the performance of an inverter air conditioner using R-410A with evaporatively cooled condenser. *Appl Therm Eng* 51, 597–610. <https://doi.org/10.1016/j.applthermaleng.2012.08.063>
- Sarvar-Ardeh, S., Rashidi, S., Rafee, R., Li, G., 2024. Recent advances in the applications of solar-driven co-generation systems for heat, freshwater and power. *Renew Energy* 120256. <https://doi.org/10.1016/j.renene.2024.120256>
- Schulz, A., Akapiey, G.N., Shirkova, V.V., Rösler, H., Dmitriev, S.N., 2005. A new method of fabrication of heat transfer surfaces with micro-structured profile. *Nucl Instrum Methods Phys Res B* 236, 254–258. <https://doi.org/10.1016/j.nimb.2005.04.049>
- Shahzad, M.W., Lin, J., Xu, B. Bin, Dala, L., Chen, Q., Burhan, M., Sultan, M., Worek, W., Ng, K.C., 2021. A spatiotemporal indirect evaporative cooler enabled by transiently interceding water mist. *Energy* 217, 119352. <https://doi.org/10.1016/j.energy.2020.119352>
- Shi, W., Min, Y., Chen, Y., Yang, H., 2022a. Development of a three-dimensional numerical model of indirect evaporative cooler incorporating with air dehumidification. *Int J Heat Mass Transf* 185. <https://doi.org/10.1016/j.ijheatmasstransfer.2021.122316>
- Shi, W., Min, Y., Ma, X., Chen, Y., Yang, H., 2022b. Performance evaluation of a novel plate-type porous indirect evaporative cooling system: An experimental study. *Journal of Building Engineering* 48, 103898. <https://doi.org/10.1016/j.jobbe.2021.103898>
- Song, J., Sobhani, B., 2020. Energy and exergy performance of an integrated desiccant cooling system with photovoltaic/thermal using phase change material and maisotsenko cooler. *J Energy Storage* 32, 101698. <https://doi.org/10.1016/j.est.2020.101698>

- Stoitchkov, N.J., Dimitrov, G.I., 1998. Effectiveness of crossflow plate heat exchanger for indirect evaporative cooling. *International Journal of Refrigeration* 21, 463–471. [https://doi.org/10.1016/S0140-7007\(98\)00004-8](https://doi.org/10.1016/S0140-7007(98)00004-8)
- Sun, T., Huang, X., Chen, Y., Zhang, H., 2020a. Experimental investigation of water spraying in an indirect evaporative cooler from nozzle type and spray strategy perspectives. *Energy Build* 214, 109871. <https://doi.org/10.1016/j.enbuild.2020.109871>
- Sun, T., Huang, X., Qu, Y., Wang, F., Chen, Y., 2020b. Theoretical and experimental study on heat and mass transfer of a porous ceramic tube type indirect evaporative cooler. *Appl Therm Eng* 173, 115211. <https://doi.org/10.1016/j.applthermaleng.2020.115211>
- Sun, T., Sun, H., Tang, T., Yan, Y., Li, P., 2023. Experimental Study on the Thermal Performances of a Tube-Type Indirect Evaporative Cooler. *Fluid Dynamics & Materials Processing* 19, 2519–2531. <https://doi.org/10.32604/fdmp.2023.027118>
- Sverdlin, B., Tikhonov, A., Gelfand, R., 2011. THEORETICAL POSSIBILITY OF THE MAISOTSENKO CYCLE APPLICATION TO DECREASE COLD WATER TEMPERATURE IN COOLING TOWERS. *International Journal of Energy for a Clean Environment* 12, 175–185. <https://doi.org/10.1615/InterJEnerCleanEnv.2012005876>
- Taufiq, B.N., Masjuki, H.H., Mahlia, T.M.I., Amalina, M.A., Faizul, M.S., Saidur, R., 2007. Exergy analysis of evaporative cooling for reducing energy use in a Malaysian building. *Desalination* 209, 238–243. <https://doi.org/10.1016/j.desal.2007.04.033>
- Tejero-González, A., Andrés-Chicote, M., Velasco-Gómez, E., Rey-Martínez, F.J., 2013. Influence of constructive parameters on the performance of two indirect evaporative cooler prototypes. *Appl Therm Eng* 51, 1017–1025. <https://doi.org/10.1016/j.applthermaleng.2012.10.054>
- United Nations Framework Convention on Climate Change, 1998. Kyoto Protocol to the United Nations Framework Convention on Climate Change.
- Valeriy Maisotsenko, Leland E. Gillan, Timothy L. Heaton, Alan D. Gillan, 2003. Method and Plate Apparatus for Maisotsenko Dew Point

Evaporative Cooler. United States Patent. <https://doi.org/Patent No.: US 6,581,402 B2>

- Velasco Gómez, E., Tejero González, A., Rey Martínez, F.J., 2012. Experimental characterisation of an indirect evaporative cooling prototype in two operating modes. *Appl Energy* 97, 340–346. <https://doi.org/10.1016/j.apenergy.2011.12.065>
- Wan, Y., Lin, J., Chua, K.J., Ren, C., 2018. A new method for prediction and analysis of heat and mass transfer in the counter-flow dew point evaporative cooler under diverse climatic, operating and geometric conditions. *Int J Heat Mass Transf* 127, 1147–1160. <https://doi.org/10.1016/j.ijheatmasstransfer.2018.07.142>
- Wang, F., Sun, T., Huang, X., Chen, Y., Yang, H., 2017. Experimental research on a novel porous ceramic tube type indirect evaporative cooler. *Appl Therm Eng* 125, 1191–1199. <https://doi.org/10.1016/j.applthermaleng.2017.07.111>
- Wang, L., Zhan, C., Zhang, J., Zhao, X., 2019a. Optimization of the counter-flow heat and mass exchanger for M-Cycle indirect evaporative cooling assisted with entropy analysis. *Energy* 171, 1206–1216. <https://doi.org/10.1016/j.energy.2019.01.099>
- Wang, L., Zhan, C., Zhang, J., Zhao, X., 2019b. Optimization of the counter-flow heat and mass exchanger for M-Cycle indirect evaporative cooling assisted with entropy analysis. *Energy* 171, 1206–1216. <https://doi.org/10.1016/j.energy.2019.01.099>
- Wang, L., Zhan, C., Zhang, J., Zhao, X., 2018. The energy and exergy analysis on the performance of counter-flow heat and mass exchanger for M-cycle indirect evaporative cooling. *Thermal Science* 153–153. <https://doi.org/10.2298/TSCI171221153W>
- Wang, N., Wang, D., Dong, J., Wang, H., Wang, R., Shao, L., Zhu, Y., 2020. Performance assessment of PCM-based solar energy assisted desiccant air conditioning system combined with a humidification-dehumidification desalination unit. *Desalination* 496, 114705. <https://doi.org/10.1016/j.desal.2020.114705>

- Willink, R., 2022. An enhanced method for the evaluation of measurement uncertainty. *Measurement: Sensors* 24, 100373. <https://doi.org/10.1016/j.measen.2022.100373>
- Woods, J., Kozubal, E., 2013. A desiccant-enhanced evaporative air conditioner: Numerical model and experiments. *Energy Convers Manag* 65, 208–220. <https://doi.org/10.1016/j.enconman.2012.08.007>
- Wu, K., Wang, S., Lin, J., Shao, Y., Gao, F., Chua, K.J., 2024. The enhanced dew-point evaporative cooling with a macro-roughened structure. *Int J Heat Mass Transf* 219, 124898. <https://doi.org/10.1016/j.ijheatmasstransfer.2023.124898>
- Xu, P., Ma, X., Zhao, X., Fancey, K., 2017. Experimental investigation of a super performance dew point air cooler. *Appl Energy* 203, 761–777. <https://doi.org/10.1016/j.apenergy.2017.06.095>
- Xu, P., Ma, X., Zhao, X., Fancey, K.S., 2016. Experimental investigation on performance of fabrics for indirect evaporative cooling applications. *Build Environ* 110, 104–114. <https://doi.org/10.1016/j.buildenv.2016.10.003>
- Xu, P., Mu, X., Chen, H., Ma, X., Zhao, X., 2024. Experimental and numerical investigation of the temperature and humidity distribution inside the channels for a regenerative indirect evaporative cooler. *Appl Therm Eng* 236, 121586. <https://doi.org/10.1016/j.applthermaleng.2023.121586>
- Y. A. Cengel, M. A. Boles, M. Kanoglu, 2019. *Thermodynamics: an engineering approach*. McGraw-Hill Education.
- Yang, C., Lin, J., Miksik, F., Miyazaki, T., Thu, K., 2024. Dew-point evaporative cooling of PV panels for improved performance. *Appl Therm Eng* 236, 121695. <https://doi.org/10.1016/j.applthermaleng.2023.121695>
- Z. Duan, C. Zhan, X. Zhang, M. Mustafa, X. Zhao, B. Alimohammadisagvand, A. Hasan, 2012. Indirect evaporative cooling: Past, present and future potentials. *Renewable and Sustainable Energy Reviews* 16, 6823–6850.
- Zanchini, E., Naldi, C., 2019. Energy saving obtainable by applying a commercially available M-cycle evaporative cooling system to the air conditioning of an office building in North Italy. *Energy* 179, 975–988. <https://doi.org/10.1016/j.energy.2019.05.065>

- Zhan, C., Duan, Z., Zhao, X., Smith, S., Jin, H., Riffat, S., 2011. Comparative study of the performance of the M-cycle counter-flow and cross-flow heat exchangers for indirect evaporative cooling – Paving the path toward sustainable cooling of buildings. *Energy* 36, 6790–6805. <https://doi.org/10.1016/j.energy.2011.10.019>
- Zhang, C., Shen, C., Wei, S., Wang, Y., Lv, G., Sun, C., 2020. A Review on Recent Development of Cooling Technologies for Photovoltaic Modules. *Journal of Thermal Science* 29, 1410–1430. <https://doi.org/10.1007/s11630-020-1350-y>
- Zhao, X., Liu, S., Riffat, S.B., 2008. Comparative study of heat and mass exchanging materials for indirect evaporative cooling systems. *Build Environ* 43, 1902–1911. <https://doi.org/10.1016/j.buildenv.2007.11.009>
- Zhou, X., 2021. Thermal and energy performance of a solar-driven desiccant cooling system using an internally cooled desiccant wheel in various climate conditions. *Appl Therm Eng* 185, 116077. <https://doi.org/10.1016/j.applthermaleng.2020.116077>
- Zhu, G., Chen, W., Zhang, D., Wen, T., 2023a. Performance evaluation of counter flow dew-point evaporative cooler with a three-dimensional numerical model. *Appl Therm Eng* 219, 119483. <https://doi.org/10.1016/j.applthermaleng.2022.119483>
- Zhu, G., Chen, W., Zhang, D., Wen, T., 2023b. Performance evaluation of counter flow dew-point evaporative cooler with a three-dimensional numerical model. *Appl Therm Eng* 219, 119483. <https://doi.org/10.1016/j.applthermaleng.2022.119483>
- Žižak, T., Domjan, S., Medved, S., Arkar, C., 2022. Efficiency and sustainability assessment of evaporative cooling of photovoltaics. *Energy* 254, 124260. <https://doi.org/10.1016/j.energy.2022.124260>

APPENDIX A1

Developed Simulation Program for DPEC in EES software (Only for Shell and Tube Type DPEC with CF Configuration)

```
"NUMERICAL SIMULATION MODEL OF DPHMX"  
"CONCENTRIC TUBES"
```

```
$Keyboard US  
$UnitSystem SI C kPa kJ Mass Rad  
$Tabstops 0.50 2.5 7.62 9.00 12.00  
$Include HMX.DPEC_Preference.PRF  
$Include HMX.DPEC_UnitsList.unt  
$Array on
```

```
"-----ENTRY LENGTH BY FUNCTIONS AND LOGIC STATEMENTS-----"
```

```
"-----FOR AIR FLOW INSIDE PRIMARY CHANNEL-----"
```

```
Function h_local(L,B,Xt,Nod,Re,Pr,Dh,h0,mu_f,mu_w,kappa)
```

```
If (Nod*L/B<Xt) Then "entry undeveloped region"
```

```
Gz=(Dh/(Nod*L/B))*Re*Pr
```

```
Nu=((7.54/(tanh(2.264*Gz^(-1/3)+(1.7*Gz^(-2/3))))))
```

```
+(0.0499*Gz*tanh(Gz^(-1)))/tanh(2.432*Pr^(1/6)*Gz^(-1/6))
```

```
h=Nu*kappa/Dh
```

```
Else
```

```
If (Nod*L/B=Xt) Then
```

```
Nu=((7.54/(tanh(2.264*Gz^(-1/3)+(1.7*Gz^(-2/3))))))
```

```
+(0.0499*Gz*tanh(Gz^(-1)))/tanh(2.432*Pr^(1/6)*Gz^(-1/6))
```

```
h=Nu*kappa/Dh
```

```
Else
```

```
If (Nod*L/B>Xt) Then "fully developed region"
```

```
h=h0
```

```
Endif
```

```
Endif
```

```

    Endif

h_local=h

End

"Function of Local Convection Heat Transfer"
Function q_local(L,B,Xt,Nod,Re,Pr,Dh,h0,mu_f,mu_w,kappa,
T_f,T_w,As)
q_local=h_Local(L,B,Xt,Nod,Re,Pr,Dh,h0,mu_f,mu_w,kappa)*As*(T
_f-T_w)
End

"-----FOR AIR FLOW INSIDE WORKING CHANNEL-----"

Function h|wc_local(L,B,Xt,Nod,Re,Pr,Prs,Dh,h0,mu_f,mu_w,kappa)

    If (Nod*L/B<Xt) Then                                "entry undeveloped region"
Nu=0.27*((Re^0.63)*(Pr^0.36))*((Pr/Prs)^0.25))
h=Nu*kappa/Dh

    Else

    If (Nod*L/B=Xt) Then
Nu=0.27*((Re^0.63)*(Pr^0.36))*((Pr/Prs)^0.25))
h=Nu*kappa/Dh

    Else

    If (Nod*L/B>Xt) Then                                "fully developed region"
h=h0

    Endif
Endif
Endif

h|wc_local=h

End

"Function of Local Convection Heat Transfer"
Function q|wc_local(L,B,Xt,Nod,Re,Pr,Prs,Dh,h0,mu_f,mu_w,
kappa,T_f,T_w,As)
q|wc_local=h|wc_Local(L,B,Xt,Nod,Re,Pr,Prs,Dh,h0,mu_f,mu_w,
kappa)*As*(T_f-T_w)
End

"-----RELATED FUNCTIONS-----"

```

"Function of Moist Air Enthalpy in Working Channel"

```
Function enth_wet(Tair,HR)
Cpa=1.005
enth_dryair=Cpa*Tair
enth_fg=2449
Cpv=1.868
enth_vapor=enth_fg+Cpv*Tair
enth_wet=enth_dryair+HR*enth_vapor
End
```

"Function of Enthalpy of Water Vapor in the atmosphere/moist-air"

```
Function enth_vap(Twater)
enth_fg=2449
Cpv=1.868
enth_vap=enth_fg+Cpv*Twater
End
```

"Function of Heat and Mass Transfer Analogy - Inside Working Channel"

```
Function hm_local(rho,Cp,kappa,T_wm,enth)
Dm_r= 0.000026
Dm_c=Dm_r*((T_wm+T_zero#)/298)^(3/2)
alpha=kappa/(rho*Cp*1000[W/kW])
Le=alpha/Dm_c
hm_local=enth*Le^(-2/3)/(rho*Cp*1000[W/kW])
End
```

"Function of RH"

```
Function rh_air(tempd,humidity)
P_infinity=101.325
rh_air=relhum(AirH2O,T=tempd,P=P_infinity,w=humidity)
End
```

"Function of Major Loss for Air Flow"

```
Function deltap_majair(f,L,Dh,Rho,u)
deltap_majair=f*(L/Dh)*((Rho*u^2)/2)
End
```

"Function of Minor Loss for Air Flow"

```
Function deltap_minair(CL,Rho,u)
deltap_minair=CL*((Rho*u^2)/2)
End
```

"-----THE NUMERICAL PARAMETERS-----"

"Pre-Set Operating Conditions"

```
HR_infinity=0.004    "ambient air humidity ratio"
```

```

RH_infinity=0.1146    "ambient air relative humidity"
T_infinity=35        "ambient air dry-bulb temperature"
u_dry=1.5            "interring air velocity to dry channel"
T_waterin=23        "interring water temperature"
m_watertot=60       "total inlet mass flow rate of water"
Length=1.2          "length of the channels"
AR=0.35             "working to primary air ratio"
HR_infinity=humrat(AirH2O,T=T_infinity,R=RH_infinity,P=P_infinity)
RH_infinity=relhum(AirH2O,T=T_infinity,w=HR_infinity,P=P_infinity)
P_infinity=101.325

```

```
GrAc=9.8
```

"Channel Wall Properties"

```

delta_wall=0.2 [mm]*convert(mm,m)
kappa_wall=190

```

"Water Film Properties"

```

delta_water=0.1 [mm]*convert(mm,m)
Cp_water=4.182

```

"Water Line Properties"

```

f_watline=64/Re_watline
Dh_watline=7.5 [mm]*convert(mm,m)
Ac_watline=pi#*(Dh_watline/2)^2
Length_watline=2.3

```

"Related Propetries"

```

Eta_fan=0.6
Dh_perforation=2 [mm]*convert(mm,m)
Ac_perforation=pi#*(Dh_perforation/2)^2

```

"Water Flow in Supply Water Line"

```

Re_watline=Rho_watline*u_watline*Dh_watline/Mu_watline
Rho_watline=density(Water,T=T_waterin,P=P_infinity)
Mu_watline=viscosity(Water,T=T_waterin,P=P_infinity)
u_watline=m_watertot/3600/Ac_watline/Rho_watline
Vf_watline=u_watline*Ac_watline
kappa_water=conductivity(Water,T=T_waterin,P=P_infinity)

```

"Ambient Air Properties"

```

Tdp_infinity=dewpoint(AirH2O,T=T_infinity,P=P_infinity,w=HR_infinity)
Twb_infinity=wetbulb(AirH2O,T=T_infinity,P=P_infinity,w=HR_infinity)
Rho_infinity=density(AirH2O,T=T_infinity,P=P_infinity,w=HR_infinity)

```

"Mesh Setup"

B=450 "number of elements per channel"

"-----VARIABLE PARAMETERS-----"

"-----SHELL and TUBE type HMX-----"

"Geometry Specifications"

channels|sat=3025 [-] "total number of HMX channels"
D|sat_dc=0.79808[cm]***convert**(cm,m) "diameter of dry channel inner surface"
H_e=1 [cm]***convert**(cm,m) "height of one computational element"
W_e=H_e "width of one computational element"}
}

Dh|sat_dc=D|sat_dc
r|sat_dc=D|sat_dc/2
Ac|sat_dc=pi#*r|sat_dc^2
As|sat_dc=2*pi#*r|sat_dc*(Length/B)
P|sat_dc=2*pi#*r|sat_dc
Dh|sat_wc=4*Ac|sat_wc/P|sat_wc
P|sat_wc=P|sat_po+((2*W_e)+(2*H_e))
P|sat_po=2*pi#*r|sat_po
r|sat_po=r|sat_dc+delta_wall
Ac|sat_wc=(W_e*H_e)-Ac|sat_pdc
Ac|sat_pdc=pi#*r|sat_po^2
As|sat_po=2*pi#*r|sat_po*(Length/B)
r|sat_pi=r|sat_dc
Ac|sat_p=pi#*(r|sat_po^2-r|sat_pi^2)
r|sat_watero=r|sat_dc+delta_wall+delta_water
r|sat_wateri=r|sat_dc+delta_wall
Dh|sat_watfilm=(2*r|sat_watero-2*r|sat_wateri)
As|sat_water=2*pi#*r|sat_watero*(Length/B)

"Flow Conditions"

f|sat_dry=64/Re|sat_dry
f|sat_wet={0.6686}{0.044+((0.08*(H_e/D|sat_dc)))/((((H_e-D|sat_dc)/D|sat_dc)^(0.43-(1.13*(D|sat_dc/H_e)))))*(((Rho|sat_wet*({(H_e)/(H_e-D|sat_dc))*u|sat_wet)*D|sat_dc)/(0.00001080))^(-0.15))
Nu0|sat_dry=4.36 [-]
Nu0|sat_wet=3.61 [-]
Nu|sat_water=4.86

"-----h0 IN FULLY DEVELOPED REGION-----"

"h0 Inside Dry Channel - for Fully Developed Condition"

"air properties:"

```

Mu | sat_dry=viscosity(AirH2O, T=T | sat_dry, P=P_infinity, w=HR | sat_
dry)
Cp | sat_dry=specheat(AirH2O, T=T | sat_dry, P=P_infinity, w=HR | sat_
dry)
Kappa | sat_dry=conductivity(AirH2O, T=T | sat_dry, P=P_infinity, w=HR | sat_
dry)
Rho | sat_dry=density(AirH2O, T=T | sat_dry, P=P_infinity, w=HR | sat_
dry)
Pr | sat_dry=6randtl(Air, T=T | sat_dry)
Mu | sat_sd=viscosity(AirH2O, T=T | sat_water, P=P_infinity, R=1)

```

```

"flow properties:"

```

```

m | sat_dry=u_dry*Ac | sat_dc*Rho_infinity
Xt | sat_dry=0.05*Re | sat_dry*Pr | sat_dry*Dh | sat_dc "thermal
entry length of dry channel"
Re | sat_dry=Rho | sat_dry*u_dry*Dh | sat_dc/Mu | sat_dry
h0 | sat_dry=Nu0 | sat_dry*kappa | sat_dry/Dh | sat_dc "for fully
developed region"

```

```

"h0 Inside Wet Channel"

```

```

"air properties:"

```

```

Rho | sat_wet=density(AirH2O, T=T | sat_wet, P=P_infinity, w=HR | sat_
wet)
Mu | sat_wet=viscosity(AirH2O, T=T | sat_wet, P=P_infinity, w=HR | sat_
wet)
Cp | sat_wet=specheat(AirH2O, T=T | sat_wet, P=P_infinity, w=HR | sat_
wet)
Kappa | sat_wet=conductivity(AirH2O, T=T | sat_wet, P=P_infinity, w=HR | sat_
wet)
Pr | sat_wet=6randtl(Air, T=T | sat_wet)
Pr | sat_wetsat=prandtl(Air, T=T | sat_water)
Mu | sat_sw=viscosity(AirH2O, T=T | sat_water, P=P_infinity, R=1)

```

```

"flow properties:"

```

```

m | sat_wet=m | sat_dry*AR "mass flow rate in wet channel"
Vf | sat_dry=u_dry*Ac | sat_dc
Vf | sat_wet=Vf | sat_dry*AR
u | sat_wet=Vf | sat_wet/Ac | sat_wc
Xt | sat_wet=0.05*Re | sat_wet*Pr | sat_wet*Dh | sat_wc
"thermal entry length for dry channel"
Re | sat_wet=Rho | sat_wet*u | sat_wet*Dh | sat_wc/Mu | sat_wet
h0 | sat_wet=Nu0 | sat_wet*Kappa | sat_wet/Dh | sat_wc
"for fully developed region"

```

```

"Water Film Convection and Plate Conduction"

```

```

R | sat_plate=ln(r | sat_po/r | sat_pi)/(2*pi#*kappa_wall*(Length/B))
R | sat_water=1/(h | sat_water*2*pi#*r | sat_po*(Length/B))
h | sat_water=(Nu | sat_water*kappa_water)/Dh | sat_watfilm

```

```

"-----BOUNDARY CONDITIONS-----"

```

```

"for dry channels"

```

```
T|sat_dry[0]=T_infinity
HR|sat_dry=HR_infinity
T|sat_dry=(T|sat_dry[1]+T|sat_dry[B])/2
```

"for wet channels"

```
T|sat_wet[B+1]=T|sat_dry[B]
HR|sat_wet[B+1]=HR|sat_dry
T|sat_wet=(T|sat_wet[1]+T|sat_wet[B+1])/2
HR|sat_wet=(HR|sat_wet[1]+HR|sat_wet[B+1])/2
```

"for water film"

```
T|sat_water[B+1]=T_waterin
T|sat_water=(T|sat_water[1]+T|sat_water[B+1])/2
m|sat_water[B+1]=m_watertot/channels|sat/3600
```

"-----NUMERICAL SIMULATION (Array [I,j])-----"

"-----Duplicate - Channel J-----"

"Numerical calculation throughout the entire numerical domain"

Duplicate j=1,B

```
HR|sat_water[j]=humrat(AirH2O,T=T|sat_water[j],P=P_infinity,R=1
```

"THE GOVERNING EQUATIONS:"

"ENERGY BALANCE OF DRY CHANNEL"

```
Q|sat_dry[j]=q_local(Length,B,Xt|sat_dry,j,Re|sat_dry,Pr|sat_dry,Dh|sat_dc,h0|sat_dry,Mu|sat_dry,Mu|sat_sd,Kappa|sat_dry,T|sat_dry[j],T|sat_pi[j],As|sat_dc)
Q|sat_dry[j]=m|sat_dry*Cp|sat_dry*1000[W/kW]*(T|sat_dry[j]-T|sat_dry[j+1])
```

"ENERGY BALANCE OF PLATE WALL"

```
Q|sat_condplate[j]=(T|sat_pi[j]-T|sat_po[j])/R|sat_plate
Q|sat_condplate[j]=Q|sat_dry[j]
```

"ENERGY BALANCE OF WATER FILM"

```
Q|sat_convwater[j]=(T|sat_po[j]-T|sat_water[j])/R|sat_water
Q|sat_convwater[j]=Q|sat_condplate[j]
Q|sat_water[j]=m|sat_water[j]*Cp_water*1000[W/kW]*(T|sat_water[j]-T|sat_water[j+1])
Q|sat_water[j]=Q|sat_convwater[j]-Q|sat_wet[j]-Q|sat_evap[j]
```

"ENERGY BALANCE OF WET CHANNEL"

```
Q|sat_wet[j]=-q|wc_local(Length,B,Xt|sat_wet,j,Re|sat_wet,Pr|sat_wet,Pr|sat_wetsat,Dh|sat_wc,h0|sat_wet,Mu|sat_wet,Mu|sat_sw,Kappa|sat_wet,T|sat_wet[j],T|sat_water[j],As|sat_water)
```

$Q|_{\text{sat_evap}[j]} = m|_{\text{sat_evap}[j]} * 1000 [W/kW] * \text{enth_vap}(T|_{\text{sat_water}[j]})$

$\text{DELTAenth}|_{\text{sat_wet}[j]} = m|_{\text{sat_wet}[j]} * 1000 [W/kW] * (\text{enth_wet}(T|_{\text{sat_wet}[j]}, \text{HR}|_{\text{sat_wet}[j]}) - \text{enth_wet}(T|_{\text{sat_wet}[j+1]}, \text{HR}|_{\text{sat_wet}[j+1]}))$

$\text{DELTAenth}|_{\text{sat_wet}[j]} = Q|_{\text{sat_evap}[j]} + Q|_{\text{sat_wet}[j]}$

"MASS BALANCE OF WET CHANNEL"

$m|_{\text{sat_evap}[j]} = \text{hm_local}(\text{Rho}|_{\text{sat_wet}}, \text{Cp}|_{\text{sat_wet}}, \text{Kappa}|_{\text{sat_wet}}, T|_{\text{sat_water}[j]}, \text{h}|_{\text{wc_local}}(\text{Length}, \text{B}, \text{Xt}|_{\text{sat_wet}}, j, \text{Re}|_{\text{sat_wet}}, \text{Pr}|_{\text{sat_wet}}, \text{Pr}|_{\text{sat_wetsat}}, \text{Dh}|_{\text{sat_wc}}, \text{h0}|_{\text{sat_wet}}, \text{Mu}|_{\text{sat_wet}}, \text{Mu}|_{\text{sat_sw}}, \text{Kappa}|_{\text{sat_wet}}) * \text{As}|_{\text{sat_water}} * \text{Rho}|_{\text{sat_wet}} * (\text{HR}|_{\text{sat_water}[j]} - \text{HR}|_{\text{sat_wet}[j]})$

$\text{hm}|_{\text{sat33}[j]} = \text{hm_local}(\text{Rho}|_{\text{sat_wet}}, \text{Cp}|_{\text{sat_wet}}, \text{Kappa}|_{\text{sat_wet}}, T|_{\text{sat_water}[j]}, \text{h}|_{\text{wc_local}}(\text{Length}, \text{B}, \text{Xt}|_{\text{sat_wet}}, j, \text{Re}|_{\text{sat_wet}}, \text{Pr}|_{\text{sat_wet}}, \text{Pr}|_{\text{sat_wetsat}}, \text{Dh}|_{\text{sat_wc}}, \text{h0}|_{\text{sat_wet}}, \text{Mu}|_{\text{sat_wet}}, \text{Mu}|_{\text{sat_sw}}, \text{Kappa}|_{\text{sat_wet}}) * \text{As}|_{\text{sat_water}} * \text{Rho}|_{\text{sat_wet}} * (\text{HR}|_{\text{sat_water}[j]} - \text{HR}|_{\text{sat_wet}[j]})$

$m|_{\text{sat_evap}[j]} = m|_{\text{sat_wet}[j]} * (\text{HR}|_{\text{sat_wet}[j]} - \text{HR}|_{\text{sat_wet}[j+1]})$

"MASS BALANCE OF WATER FILM"

$m|_{\text{sat_evap}[j]} = m|_{\text{sat_water}[j+1]} - m|_{\text{sat_water}[j]}$

$m|_{\text{sat_evap}[j]} = m|_{\text{sat_water}[j]} - m|_{\text{sat_water}[j+1]}$

$Q|_{\text{sat_dry}[j]} = \text{DELTAenth}|_{\text{sat_wet}[j]} + Q|_{\text{sat_water}[j]}$

$\text{RH}|_{\text{sat_wet}[j]} = \text{rh_air}(T|_{\text{sat_wet}[j]}, \text{HR}|_{\text{sat_wet}[j]})$

$\text{RH}|_{\text{sat_dry}[j]} = \text{rh_air}(T|_{\text{sat_dry}[j]}, \text{HR}|_{\text{sat_dry}[j]})$

End

"-----SYSTEM PERFORMANCE EVALUATION-----"

$T|_{\text{sat_product}} = T|_{\text{sat_dryout}}$

$\text{RH}|_{\text{sat_product}} = \text{rh_air}(T|_{\text{sat_dry}[B]}, \text{HR}|_{\text{sat_dry}[B]})$

$\text{HR}|_{\text{sat_product}} = \text{HR}|_{\text{sat_dry}[B]}$

$T|_{\text{sat_dryin}} = T_{\text{infinity}}$

$T|_{\text{sat_dryout}} = T|_{\text{sat_dry}[B]}$

$T_{\text{dp}}|_{\text{sat_dryin}} = T_{\text{dp_infinity}}$

$T_{\text{wb}}|_{\text{sat_dryin}} = T_{\text{wb_infinity}}$

$T|_{\text{sat_waterout}} = T|_{\text{sat_water}[1]}$

$T|_{\text{sat_exhaust}} = T|_{\text{sat_wet}[1]}$

$\text{RH}|_{\text{sat_exhaust}} = \text{rh_air}(T|_{\text{sat_wet}[1]}, \text{HR}|_{\text{sat_wet}[1]})$

$\text{HR}|_{\text{sat_exhaust}} = \text{HR}|_{\text{sat_wet}[1]}$

$V_f|_{\text{sat_supply}} = V_f|_{\text{sat_dry}}$

$V_f|_{\text{sat_exhaust}} = V_f|_{\text{sat_supply}} * \text{AR}$

$V_f|_{\text{sat_product}} = (V_f|_{\text{sat_supply}}) * (1 - \text{AR})$

"Pressure Losses of Air Flow"

$\text{DELTA}P|_{\text{sat_drymaj}} = \text{deltap_majair}(f|_{\text{sat_dry}}, \text{Length}, \text{Dh}|_{\text{sat_dc}}, \text{Rho}|_{\text{sat_dry}}, u_{\text{dry}})$

```

DELTAP|sat_wetmaj=deltap_majair(f|sat_wet,Length,Dh|sat_wc,Rho
o|sat_wet,u|sat_wet)
DELTAP|sat_drymin=deltap_minair(CL|sat_1,Rho|sat_dry,u|sat_dr
y1)+deltap_minair(CL|sat_2,Rho|sat_dry,u|sat_dry2)+deltap_min
air(CL|sat_3,Rho|sat_dry,u|sat_dry3)

```

"loss coefficients"

```

CL|sat_1=0.8
CL|sat_2=0.9
CL|sat_3=2
u|sat_dry1=u_dry
u|sat_dry2=u_dry
u|sat_dry3=u_dry*(1-AR)
DELTAP|sat_wetmin=(deltap_minair(CL|sat_4,Rho|sat_wet,u|sat_w
et1)*6)+(deltap_minair(CL|sat_5,Rho|sat_wet,u|sat_wet2)*6)+de
ltap_minair(CL|sat_6,Rho|sat_wet,u|sat_wet2)
CL|sat_4=2
CL|sat_5=1.5
CL|sat_6=2
u|sat_wet1=(Vf|sat_wet/6)/Ac_perforation
u|sat_wet2=u|sat_wet

```

```

DELTAP|sat_dry=DELTAP|sat_drymaj+DELTAP|sat_drymin
DELTAP|sat_wet=(DELTAP|sat_wetmaj+DELTAP|sat_wetmin)*3
DELTAP|sat_Air=(DELTAP|sat_dry+DELTAP|sat_wet)/1000
    "[kPascal]"

```

"Theoretical Power Consumption"

```

W|sat_fan=(Vf|sat_supply*DELTAP|sat_Air*channels|sat)/Eta_fan
    "[kW]" "power consumption of air fan"

```

"Water system pressure lose"

```

W|sat_pump=((Massflow_wat*GrAc*Hwater_tot)/eff_pump)/1000
    "[kWatts]"

```

```

Massflow_wat=m_watertot*(0.00028)
Hwater_tot=H_valve+H_gravity+H_friction+(H_nozzle)
H_valve=1.5
H_gravity=3
H_nozzle=1.5
H_friction=(64/Re_watline)*(Length_watline/Dh_watline)*((Vf_w
atline^2)/(2*GrAc))
eff_pump=0.6

```

"Performance Evaluation"

"DP effectiveness"

```

EPSILON|sat_DewPoint=((T|sat_dryin-|sat_dryout)/(T|sat_dryin-
Tdp|sat_dryin))*100

```

"WB effectiveness"

```

EPSILON|sat_WetBulb=((T|sat_dryin-T|sat_dryout)/(T|sat_dryin-
Twb|sat_dryin))*100

```

"water evaporated per channel"

```

Evaporation|sat_water=m|sat_water[B+1]-m|sat_water[1]
"total evaporated water"
Evaporation|sat_Total=Evaporation|sat_water*channels|sat*3600
"[Kg/hr]"

"Cooling capacity and cooling flux"
Q|sat_cooling=m|sat_dry*(1-AR)*Cp|sat_dry*(T|sat_dryin-
T|sat_dryout)*channels|sat "[kW]"
Qc|sat_flux=((m|sat_dry*(1-AR)*Cp|sat_dry*(T|sat_dryin-
T|sat_dryout))/As|sat_dc)*1000 "[W/m2]"
"Energy Efficiency (COP)"
COP|sat=Q|sat_cooling/((W|sat_fan+W|sat_pump)*1.8)

"dew point temperature of exhaust air - to study condensation
potential"
Asdc|sat_exchanger=2*pi#*r|sat_dc*Length*channels|sat
Asdc|sat_tube=2*pi#*r|sat_dc*Length
Aswc|sat_exchanger=2*pi#*r|sat_po*Length*channels|sat
Aswc|sat_tube=2*pi#*r|sat_po*Length

"-----EXERGY, ENTROPY, AND SUSTAINABILITY ANALYSIS-----"

"Exergy Analysis:"

Ra=0.287 "specific gas constant for air"
Rv=0.4615 "specific gas constant for water vapor"
Cpa=cp(Air,T=T_amb)
Cpv=cp(H2O,T=T_amb)

"Inlet Conditions:"
T_amb=T_infinity
HR_amb=HR_infinity
P_amb=P_infinity

"Dead State (0):"
T_0=T_amb
HR_0=humrat(AirH2O,T=T_0,R=RH_0,P=P_amb) "saturation state"
RH_0=1 "saturation state"
P_0=P_amb

"Pressure Drops"
DELTAP_primarych=(DELTAP|sat_dry/1000)
DELTAP_workingch=(DELTAP|sat_wet/1000)
P_intrance=P_amb+DELTAP_primarych+DELTAP_workingch
P_product=P_amb+DELTAP_workingch
P_exhaust=P_amb

"Saturation Properties"
P|ex_satWatVap=p_sat(Steam,T=T_0)
h|0_satWatVap=enthalpy(Steam,T=T_0,P=(P|ex_satWatVap-0.001))
h|wi_satWat=enthalpy(Water,T=T_waterin,P=P_amb)

```

```

h|wo_satWat=enthalpy(Water,T=T|sat_waterout,P=P_amb)
s|0_satWatVap=entropy(Steam,T=T_0,P=(P|ex_satWatVap-0.001))
s|wi_satWat=entropy(Water,T=T_waterin,P=P_amb)
s|wo_satWat=entropy(Water,T=T|sat_waterout,P=P_amb)
P|_satWatLiqin=p_sat(Water,T=T_waterin)
P|_satWatLiqout=p_sat(Water,T=T|sat_waterout)
v|wi_satWatLiq=volume(Water,T=T_waterin,P=P_amb)
v|wo_satWatLiq=volume(Water,T=T|sat_waterout,P=P_amb)

```

"Exergy Model"

```

mf=1.608*HR_amb                                "mole fraction"
mf_0=1.608*HR_0                                "mole fraction at dead state - saturated"
m_water=m_watertot/3600

```

"Inlet Exergies:"

"Exergy of primary channel inlet (pi)"

```

ex|pi_t=(Cpa)*(T_0+273.15)*(((T_amb+273.15)/(T_0+273.15))-1-
(ln((T_amb+273.15)/(T_0+273.15))))
ex|pi_m=(1)*Ra*(T_0+273.15)*ln(P_inrance/P_0)
ex|pi_c=Ra*(T_0+273.15)*(((1)*ln((1+mf_0))))

```

```

ex|pi_Total=ex|pi_t+ex|pi_m+ex|pi_c

```

```

Ex|inlet_Air=ex|pi_Total*(m|sat_dry*channels|sat)

```

"Exergy of water inlet (wi)"

```

ex|wi_Water=(h|wi_satWat-h|0_satWatVap)-((s|wi_satWat-
s|0_satWatVap)*(T_0+273.15))+((P_product-P|_satWatLiqin)*
v|wi_satWatLiq)-(Rv*(T_0+273.15)*ln(RH_0))

```

```

Ex|inlet_Water=ex|wi_Water*m_water

```

"Outlet Exergies:"

"Exergy of Product air - Primary channel Output (po)"

```

ex|po_t=(Cpa)*(T_0+273.15)*(((T|sat_product+273.15)/(T_0+273.
15))-1-(ln((T|sat_product+273.15)/(T_0+273.15))))
ex|po_m=(1)*Ra*(T_0+273.15)*ln(P_product/P_0)
ex|po_c=Ra*(T_0+273.15)*(((1)*ln((1+mf_0))))
ex|po_Total=ex|po_t+ex|po_m+ex|po_c
m|sat_product=m|sat_dry*(1-AR)

```

```

Ex|out_product=ex|po_Total*(m|sat_product*channels|sat)

```

"Exergy of Exhaust air - Working channel Output (wo)"

```

mf|wo=1.608*HR|wo
HR|wo=HR|sat_exhaust
ex|wo_t=(Cpa+(HR|wo*Cpv))*(T_0+273.15)*(((T|sat_exhaust+273.1
5)/(T_0+273.15))-1-(ln((T|sat_exhaust+273.15)/(T_0+273.15))))

```

$$\text{ex}|_{\text{wo}_m} = (1 + \text{mf}|_{\text{wo}}) * \text{Ra} * (T_0 + 273.15) * \ln(P_{\text{exhaust}}/P_0)$$

$$\text{ex}|_{\text{wo}_c} = \text{Ra} * (T_0 + 273.15) * ((1 + \text{mf}|_{\text{wo}}) * \ln((1 + \text{mf}_0) / (1 + \text{mf}|_{\text{wo}})) + (\text{mf}|_{\text{wo}} * \ln(\text{mf}|_{\text{wo}}/\text{mf}_0)))$$

$$\text{ex}|_{\text{wo_Total}} = \text{ex}|_{\text{wo}_t} + \text{ex}|_{\text{wo}_m} + \text{ex}|_{\text{wo}_c}$$

$$\text{m}|_{\text{sat_exhaust}} = \text{m}|_{\text{sat_dry}} * (\text{AR})$$

$$\text{Ex}|_{\text{out_exhaust}} = \text{ex}|_{\text{wo_Total}} * (\text{m}|_{\text{sat_exhaust}} * \text{channels}|_{\text{sat}})$$

"Exergy of water outlet (wo)"

$$\text{ex}|_{\text{wo_Water}} = (h|_{\text{wo_satWat}} - h|_{0_satWatVap}) - ((s|_{\text{wo_satWat}} - s|_{0_satWatVap}) * (T_0 + 273.15)) + ((P_{\text{amb}} - P|_{\text{satWatLiqout}}) * v|_{\text{wo_satWatLiq}} - (Rv * (T_0 + 273.15) * \ln(\text{RH}_0)))$$

$$\text{Ex}|_{\text{out_Water}} = \text{ex}|_{\text{wo_Water}} * (\text{m}_{\text{water}} - (- \text{Evaporation}|_{\text{sat_Total}} / 3600))$$

"Fan Exergy"

$$\text{Ex}_{\text{fan}} = (\text{DELTA}P_{\text{primarych}} * (Vf|_{\text{sat_dry}} * \text{channels}|_{\text{sat}})) + (\text{DELTA}P_{\text{workingch}} * (Vf|_{\text{sat_wet}} * \text{channels}|_{\text{sat}}))$$

"Exergy Loss"

$$\text{Ex}_{\text{loss}} = Q|_{\text{sat_cooling}} * (1 - (T_0/T_{\text{infinity}}))$$

"Exergetic Efficiency"

$$\text{Ex}|_{\text{Total_in}} = \text{Ex}|_{\text{inlet_Air}} + \text{Ex}|_{\text{inlet_Water}}$$

$$\text{Ex}|_{\text{Total_out}} = \text{Ex}|_{\text{out_product}} + \text{Ex}|_{\text{out_exhaust}} + \text{Ex}|_{\text{out_Water}}$$

$$\text{eff_Ex1} = \text{Ex}|_{\text{Total_out}} / \text{Ex}|_{\text{Total_in}}$$

"Irreversibility = Exergy Destruction"

$$\text{Ex}_{\text{destr}} = \text{Ex}|_{\text{Total_in}} - \text{Ex}|_{\text{Total_out}} - \text{Ex}_{\text{loss}}$$
 "irreversibility"

"Exergetic COP = Exergy efficiency ratio"

$$\text{COP}_{\text{Ex1}} = \text{COP}|_{\text{sat}} * (1 - (T_0/T_{\text{infinity}}))$$

$$\text{COP}_{\text{Ex2}} = (\text{Ex}|_{\text{out_product}} - (\text{Ex}|_{\text{inlet_Air}} * (1 - \text{AR}))) / \text{Ex}_{\text{fan}}$$

"Entropy Generation (S_gen)"

$$S_{\text{gen}} = \text{Ex}_{\text{destr}} / (T_0 + 273.15)$$

"Entropy generation number (NS)"

$$\text{NS}_{\text{gen}} = (S_{\text{gen}} * (T_0 + 273.15)) / Q|_{\text{sat_cooling}}$$

"Sustainability"

$$\text{SI} = 1 / (1 - \text{eff_Ex1})$$

APPENDIX A2

(Calibration of the Instrumentations)

1. Thermocouples

The utilized type K thermocouples were calibrated using the fundamentals of temperature measurement apparatus (WL202 by GUNT) at Sulaimani Polytechnic University, as depicted in **Fig. A2.1**.



Fig. A2.1 WL202 fundamentals of temperature measurement (GUNT)

The calibrated Type K thermocouple was employed in GUNT's WL202 apparatus for fundamental temperature measurements. It also offers a straightforward approach for calibrating uncalibrated Type K thermocouples.

Fig. A2.2 illustrates the deviations among these thermocouples, with the maximum recorded deviation of 0.5 °C.

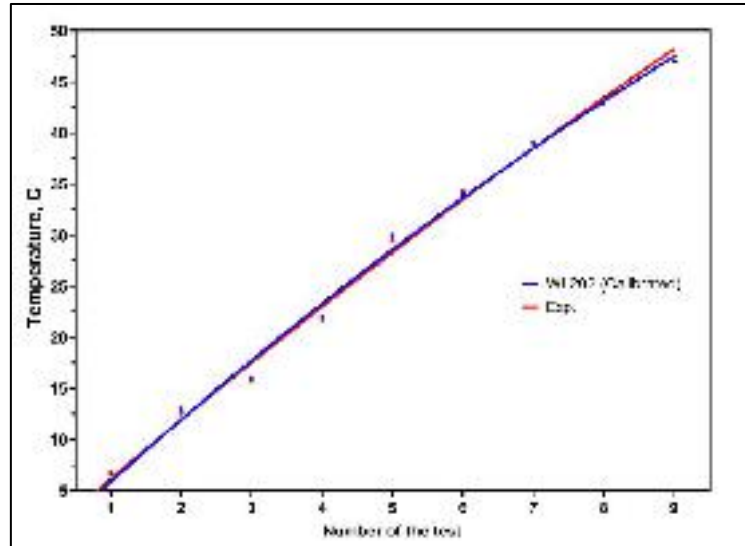


Fig. A2.2 Calibration result

2. Hygrometers

The humidity measuring instruments (hygrometers) were utilized for measuring relative humidity at inlet, product, and exhaust locations of the cooler. To assess the accuracy of the employed hygrometers, they were put under a test. As shown in **Fig. A2.3**, the hygrometer put in an enclosed chamber alongside with a humidifier. It has been waited until the chamber reached full saturation (100% actual relative humidity). Thereafter, the hygrometer's accuracy tested by observing the data viewer from the measuring instrument for about 30 minutes and observing for any fluctuation in the reading. Throughout 30 minutes testing, the sensor was most of the time measured 100% relative humidity with a slight alteration between 99.6% and 100% at rare occasions. This stable measurement indicates high accuracy measuring instrument.

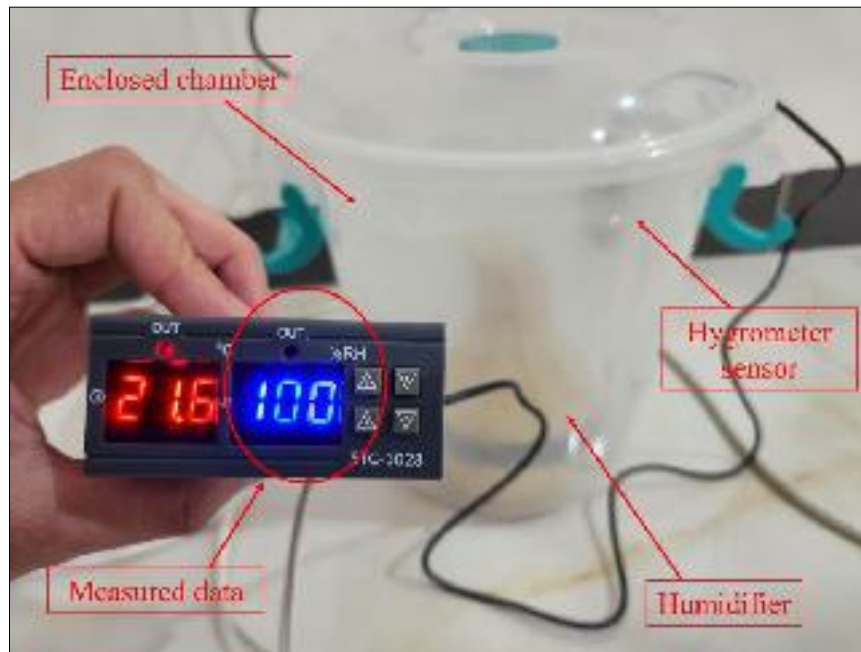


Fig. A2.3 Calibration of the humidity measuring instrument

3. Anemometers

For the purpose of velocity measurement, vane type anemometer has been utilized. To calibrate this type of measuring instrument, a special set of velocity calibration apparatus is required which was hard to acquire. As an alternative, so as to measure a reasonable magnitude of velocity, each time to measure the velocity of airflow, three anemometers (as shown in **Fig. A2.4**) were employed for the data measurement, thereafter the average of these three measurements has been recorded as the final measurement for the intended test. Throughout the course of the experimentations, the maximum deviation observed between the anemometers for each test were about 0.1 m/s.



Fig. A2.4 Employed anemometers for velocity measurement

4. Rotameter

Regarding the water flow measurement, a variable area type rotameter has been employed. Prior to the experimentations, the accuracy of utilized rotameter has been evaluated by comparing the actual measured data with the calculated data at different water flowrates. The results from the comparison are presented in **Table A2.1**. The maximum deviation recorded was about $\pm 2.25\%$.

Table A2.1 comparison between measured and calculated data

Test	Experimental period (minute)	Measured flowrate (L/m)	Calculated flowrate (L/m)	Deviation
1	10	1.3	1.33	$\pm 2.25\%$
2	10	1.63	1.66	$\pm 1.84\%$
3	10	1.95	2.00	$\pm 2.5\%$
4	10	2.30	2.33	$\pm 1.28\%$
5	10	2.60	2.66	$\pm 2.25\%$
6	10	2.95	3.00	$\pm 1.66\%$
7	10	3.25	3.33	$\pm 2.4\%$

APPENDIX A3

List of Publications

Journal Papers (Published)

- [1] Mohammed, A.S., Ahmed, M.A., Hasan, H.F., Benim, A.C., Anjal, H.A. (2023), “Performance Analysis of Novel Dew Point Evaporative Cooler with Shell and Tube Design Through Different Air-Water Flow Configurations”. *Energy* 289, 129922. <https://doi.org/10.1016/j.energy.2023.129922>
- [2] M. A. Sulaiman, A. M. Adham (2023), “New Dew Point Evaporative Cooler Heat and Mass Exchanger Design with Different Geometries”. *Building Services Engineering Research and Technology*. (Research Trend, 44(44)). <https://doi.org/10.1177/01436244231179456>

Conference Papers (Accepted and Reviewed, Waiting for Publication)

- [3] M. A. Sulaiman, A. M. Adham, G. F. Abdullah (2023), “Energy Performance Analysis of Dew Point Evaporative Cooler with Novel Heat and Mass Exchanger Design”. *14th International Conference on Computational Heat and Mass Transfer, Düsseldorf, Germany, 4-8 September 2023*.
- [4] M. A. Sulaiman, A. M. Adham, G. F. Abdullah (2023), “Assessing the Performance of Novel Dew Point Evaporative Cooler Considering the Climatic Conditions of Different Cities in Iraq”. *14th International Conference on Computational Heat and Mass Transfer, Düsseldorf, Germany, 4-8 September 2023*.

- [5] Mohammed A. Sulaiman, Ahmed M. Adham, Hasan F. Hasan, Gazinga F. Abdullah (2024), "Creating a Typical Weather Data File for Analyzing and Estimating Energy Generation from Renewable Energy Systems in Five Cities in Iraq". *5th International Conference on Communication Engineering and Computer Science, Erbil Iraq, 24-25 April, 2024.*

On-going Manuscripts

- [6] Mohammed, A.S., Ahmed, M.A., (2024), "Energy, Exergy, Entropy, Environmental, and Economical (5Es) Analysis of Neoteric Dew Point Evaporator with Innovative Geometrical Design: Experimental and Numerical Studies".
(At finalization and submission stage: targeted for journal publication)
- [7] Mohammed, A.S., Ahmed, M.A., (2024), "Experimental Study of Super Performance Novel Shell and Tube Design Dew Point Evaporative Cooler".
(At finalization and submission stage: targeted for journal publication)
- [8] Mohammed, A.S., Ahmed, M.A., (2024), "A Thorough Review on the Latest Advances in Dew Point Evaporative Cooling Technologies".
(At writing stage)



Performance analysis of novel dew point evaporative cooler with shell and tube design through different air-water flow configurations

Muhammed A. Sulaiman^{a,*}, Ahmed M. Arham^a, Hasan F. Hasan^b, Ali C. Benim^c, Hassan A. Anjal^d

^a Department of Industrial Mechanics and Design Engineering, BUI Technical Engineering College, BUI Technical University, Bui 44321, Iraq

^b Faculty of Engineering, Qadisi University-QADISI, 50644001, Iraq

^c Faculty of Mechanical and Process Engineering, University of Applied Sciences, Dinslaken 49075, Germany

^d Department of Engineering Technology, College of Technical Engineering, Al-Furat Al-Awsat, 31004, Iraq

ARTICLE INFO

Handling Editor: Wojciech Szlach

Keywords

Dew point evaporative cooler
CFD simulation
Performance analysis
Air-water flow

ABSTRACT

The complex design of a dew point evaporative cooler (DPEC) is the largest impediment to the global uptake of such a high-performance system. Therefore, in this paper, we introduce a new design for the DPEC which eliminates the complexity barrier and significantly improves the system's performance. The new design consists of a shell and a bank of tubes. The shell shell works as a working stream, while the tubes work as primary streams. A solid mathematical model has been developed to allow prediction of the system's performance with high accuracy, as has been validated against flow experimental results. Through this analysis, the energy and thermal performance of the current model has been compared to the conventional DPEC with flat plate design for two air-water flow configurations, namely parallel and counter air-water flow configurations. It was found that, under a wide range of operational and geometrical conditions, the new cooler consistently outperformed the flat plate type cooler by producing colder air by about 0.1 °C, and improving energy efficiency by about 12.2%. Moreover, the parallel air-water flow configuration produced much colder water than the counter configuration, accounting for 15.75 °C (140 %) colder.

1. Introduction

Over the years, evaporative cooling, in general, has been considered as one of the most consistent and reliable sources of cooling in buildings and industries owing to its simplicity, low-cost, and non-toxic nature. Besides, compared to space cooling refrigeration systems (SCRSs), it lacks hydrofluorocarbon (HFC) that have been banned over the past several years, such working fluids must be pressurized and de-pressurized to transport heat from one area to another and produce cooling. This process consumes a high amount of electrical energy that eventually contributes to the global warming phenomenon through the emission of greenhouse gases [1,2]. In 2021 alone, the SCRSs approximately accounted for 12 % of overall electricity consumption and 8% of overall greenhouse gas emissions worldwide [3]. In consequence, the SCRSs such as high electricity bills, high leaks, and maintenance costs, and severe environmental damage [4,5]. Therefore, the environmentally friendly characteristics of the evaporative cooler led many researchers to study such a system and attempt to improve its performance through

many approaches [6–11]. The limitation of high humidity content and wet bulb temperature of product air are two of the common impediments of the direct evaporative system [12,13]. However, in 2003, a group of researchers [14] was able to overcome these impediments and boost the system's performance by introducing a direct and indirect evaporative (DPEI) with novel design from which the air was cooled to meet the minimum dew point temperature, yet keeping the humidity ratio unchanged. This system was named the Masabheko cycle (M-cycle). It distinguished from direct evaporative cooler by providing the air within the cooler inside the primary channel before directing to the working channel.

Since its first invention, the performance of such a system has been continuously improving through the endeavors of many researchers, and it came with other names such as dew point and regenerative evaporative cooler. Such studies include experimental-based, computational-based, and combined studies. Such as employing a different aspect, i.e. geometrical investigation, air-flow configurations, mathematical approaches, weather assessment, and structural material. Xu et al. [15] employed a corrugated stripe plate as a new design for the

* Corresponding author.

E-mail address: mahmeds@bui.edu.iq (M.A. Sulaiman).

Evaluation of new dew point evaporative cooler heat and mass exchanger designs with different geometries

Building Serv. Eng. Res. Technol.
2021, Vol. 0(0) 1–18
© The Author(s) 2021
Article reuse guidelines:
sagepub.com/journals-permissions
DOI: 10.1177/1753435221101955
journals.sagepub.com/home/bse


Mohammed A Sulaiman  and Ahmed M Adham 

Abstract

In this study four new geometries of heat and mass exchanger for dew point evaporative cooling are investigated and their performance is compared to that of the commonly used flat plate and corrugated plate exchangers. In the proposed exchangers, each dry channel is completely enclosed by its adjacent wet channels, and each wet channel is completely enclosed by its adjacent dry channels (related detailed information is presented graphically in this paper). In addition, a robust numerical model was developed and is examined under various operational and geometrical conditions. The analysis showed that the proposed dew point evaporative coolers improve the chilled air temperature, water consumption, cooling capacity, and energy efficiency. In particular, the circular concentric tube exchanger, under certain operating conditions (inlet air temperature, humidity ratio, and velocity of 40°C, 6 g/kg, and 3 m/s, respectively), could produce the lowest chilled air temperature of 9.6°C and the highest wetbulb and dew point effectiveness of 140% and 99%, respectively. Additionally, water consumption is reduced to 1.34 L/hr for an inlet air velocity of 1 m/s. A triangular tube exchanger achieved the highest cooling capacity and coefficient of performance, but consumed the largest amount of water. Our geometrical analysis demonstrates that the overall performance of dew point evaporative cooling systems can be improved by employing new geometries for heat and mass exchanger channels.

Practical application: The dew point evaporative cooler is an environmentally friendly air conditioning system used in buildings. It is considered the strongest candidate to replace vapour-compression refrigeration systems because it consumes considerably less electricity while achieving high performance. Our research demonstrates that through revised geometry it is possible to further improve the performance of the system leading to improved energy and water efficiency.

Keywords

Air conditioning, dew point evaporative cooler, heat and mass transfer, numerical simulation

Received 11 January 2021; Revised 2 May 2021; Accepted 7 May 2021

Department of Technical Mechanical and Energy Engineering, Erbil Technical Engineering College, Erbil Polytechnic University, Erbil, Iraq

Corresponding author:

Mohammed A Sulaiman, Department of Technical Mechanical and Energy Engineering, Erbil Technical Engineering College, Erbil Polytechnic University, Kurdistan Region, Erbil 44001, Iraq.
Email: mohammed.sulaiman@teu.edu.iq

Paper III

Energy Performance Analysis of Dew Point Evaporative Cooler with Novel Heat and Mass Exchanger Design

Mohammed A. Sulaiman¹ and Ahmed M. Acham¹

¹ Department of Technical Mechanical and Energy Engineering, Erbil Technical Engineering College, Erbil Polytechnic University, Kurdistan Region, Erbil 44011, Iraq
mohammed.a.sulaiman@epu.edu.iq

Abstract. This paper investigates the energy performance of a novel dew point evaporative cooler (DPEC) with a new shell and tube design heat and mass exchanger. The shell is assigned as a wet channel, and the tubes are assigned as dry channels. The results obtained from the numerical simulation have been validated against the experimental data and compared to the conventional DPEC, namely, flat-plate type DFEC, under a wide range of operational and geometrical conditions. The obtained results revealed that, when compared to the conventional flat-plate type, the energy efficiency has significantly improved (as high as 35%) due to a significant decrease in pressure drop, which eventually led to lower power consumption for the same amount of air flow rate alongside with the increase in heat and mass transfer potential. In addition, it was found that the new cooler recorded the best performance when the channel diameter was smallest (about 1.5 mm); meanwhile, the channel length of 1.3 m, air velocity of 1.7 m/s, and air ratio of 0.3 are found to be the optimum values which resulted in the best energy performance for the proposed cooler.

Keywords: Heat and Mass Transfer, Dew Point Evaporative, Numerical Simulation.

1 Introduction

The building and housing sector accounts for 26.6% of the total energy consumption worldwide [1]. This rate is considerably high, and to minimize it, it has to be done by either utilizing renewable energy sources, improving the thermal insulation, or enhancing the energy and thermal performances of the air-conditioning systems. In general, many air-conditioning systems are available. However, the most efficient and commonly used types are vapor compression systems (VCS) and evaporative coolers. The VCS are considered as high thermal performance systems due to high cooling capacity, while the evaporative coolers are considered as high energy performance systems with COP ranging from 15 to 20 due to low energy consumption characteristics. In addition, when compared to VCS, the evaporative coolers are considered environmentally friendly systems owing to the utilization of water as a working fluid rather than hydrofluorocarbon refrigerants, which eventually contribute to global warming and ozone depletion [2, 3].

Paper IV

Assessing the Performance of Novel Dew Point Evaporative Cooler Considering the Climatic Conditions of Different Cities in Iraq

Mohammed A. Sulaiman¹ORCID:0000-0001-2165-1165, Ahmed M. Adhame¹ORCID:0000-0001-0281-7710, Cezayirli F. Abdulkhalil¹ORCID:0000-0002-2185-0021

¹ Department of Technical Mechanical and Energy Engineering, Erbil Technical Engineering College, Erbil Polytechnic University, Kurdistan Region, Erbil (44001), Iraq
msulaiman@pu.edu.iq

Abstract. In recent years, performance enhancement of dew point evaporative cooler (DPEC) has been thrust due to its high performance and low energy consumption. In this study, a new idea for designing the heat and mass exchanger, which is the core of DPEC, has been introduced and its performance has been evaluated under the climatic conditions of Iraq. The new system consisted of one shell and a bundle of tubes. The shell is assigned as the wet channel, and the tube bundle is assigned as the dry channel. The weather data files for five different cities in Iraq were taken from the National Aeronautics and Space Administration (NASA). Therefore, we created a typical weather data file for each city by averaging the last five years' weather data (from 2018 to 2022) so as to become a base for the numerical simulation. It was found that, under the climate condition of Basra, the DPEC reduced the dry bulb temperature by almost 30 °C (from 48 °C to 18.13 °C in July). Under Erbil climate, the system stopped operating in a stable condition, as it kept supplying air around 17.5 °C on average throughout the summer season. The system achieved the highest yearly average cooling capacity of about 721 W when it was operated under Basra climate, while it achieved the lowest rate of about 477 W when it was operated under Ha-Osama climate.

Keywords: Dew Point Evaporative Cooler, Air Conditioning, Weather Data.

1 Introduction

The global electrical energy generation has increased by 6.2% in 2021 alone as a consequence of the growth in population. Energy consumed by the residential sector accounts for 26.2% of overall energy consumption [1]. Typically, a significant part of energy consumption in buildings is used by heating, ventilation, air-conditioning, and refrigeration (HVAC&R) systems. For instance, HVAC&R systems account for about 57.5%, 4.5%, and 55% of the total residential energy usage in the United Arab Emirates, the United States, and China, respectively [2, 3]. More energy consumption means emitting more carbon dioxide emissions, which will eventually contribute to worsening the global warming impact and ozone layer depletion [4]. Therefore, new-

Paper V

Creating a Typical Weather Data File for Analyzing and Estimating Energy Generation from Renewable Energy Systems in Five Cities in Iraq

Mohammed A. Sulaiman^{1*}, Ahmed M. Adham¹, Hasna F. Hasan², Gazinga F. Abdallah

¹Department of Technical Mechanical and Energy Engineering, Erbil Technical Engineering College, Erbil Polytechnic University, Kurdistan Region, Erbil, Iraq

²Faculty of Engineering, Cihan University-Erbil, Erbil 44031, Iraq

*Corresponding author, E-mail: mohammed.sulaiman@epu.edu.iq

Abstract

In this research, we present creating a typical weather data file for different Iraqi cities and use it for planning to allocate suitable kinds of renewable systems to be installed in different parts of Iraq. To create typical weather data for five Iraqi cities, the daily, monthly, and yearly weather data for the last five years are averaged. We obtained the data from Power Data Access Viewer, which is operated by the National Aeronautics and Space Administration (NASA). We used this typical weather data to estimate the amount of daily clean real energy that a typical solar PV panel and a typical wind turbine can generate in each of the five cities over the span of a year. In the analysis, it was found that Basra has the highest daily solar irradiance availability during the winter and spring seasons. Hefi Omran possessed the highest solar availability during the summer season. The seasonal and spatial difference in solar irradiance was reflected in the amount of daily electrical energy generated by solar PV panels in each of the selected cities. Regarding the correlation between wind speed and energy generated by the wind turbines, the highest amount of electrical energy can be generated from turbines installed in Basra, followed by Baghdad. Moreover, our analysis inferred that since Sulaymaniyah has the highest precipitation rate, as high as 5 mm/day, it can be a good place for generating clean energy through hydroelectric power plants.

Keywords: energy generation, renewable energies, weather data analysis

1. Introduction

Weather data plays a significant role in the design stage in many engineering applications. For example, engineers need to use weather data to estimate the annual energy demand of buildings or energy that renewable energy plants can generate (P.fookaboni et al., 2021; Segarra et al., 2020). In fact, weather data are embedded in all simulation software that is used for selecting, designing, and sizing heating, ventilation, air conditioning, and refrigeration (HVAC&R) systems (Adham et al., 2017; Shakir et al.,

.)dew point evaporative cooler (DPEC)(

DPEC

(

)



Design and Implementation of Dew Point Evaporative Cooler: Theoretical and Experimental Investigation